APPLIED COMPUTATIONAL ELECTROMAGNETICS SOCIETY JOURNAL

September 2022
Vol. 37 No. 9
ISSN 1054-4887

The ACES Journal is abstracted in INSPEC, in Engineering Index, DTIC, Science Citation Index Expanded, the Research Alert, and to Current Contents/Engineering, Computing & Technology.

The illustrations on the front cover have been obtained from the ARC research group at the Department of Electrical Engineering, Colorado School of Mines

Published, sold and distributed by: River Publishers, Alsbjergvej 10, 9260 Gistrup, Denmark

SEPTEMBER 2022 REVIEWERS

Layla H. Abood
Djelloul Aissaoui
Rezaul Azim
Syed Sabir Hussain Bukhari
Mahendran C.
Xiaoming Chen
Merit Cisneros-Gonzalez
Yogesh Kumar Coukiker
Arkaprovo Das
Tanmaya Kumar Das
Mona Elhelbawy
Piotr Gas
Bernhard J. Hoenders
Muyu Hou
I. Kathir
Wang-Sang Lee
Yingsong Li
Biswa Binayak Mangaraj
Ali Madani Mohammadi
Weidong Mu
Amjad Omar
Balendu Kumar Pandey
Andrew Peterson
Natarajamani S.
Sayidmarie
Fusun Oyman Serteller
Marsellas Waller
Lu Wang
Steven Weiss
Gaobiao Xiao
Wentao Yuan
Xiaoyan Zhang
Yun-Qi Zhang

THE APPLIED COMPUTATIONAL ELECTROMAGNETICS SOCIETY JOURNAL

Vol. 37 No. 9 September 2022

TABLE OF CONTENTS

Analysis of Transmission Characteristics of EBG Structures by Subgridding Unconditionally Stable FETD Method
Yixin Wang, Bing Wei, and Kaihang Fan 921

A New Approach of Applying Chebyshev Distribution of Series Fed Microstrip Antenna Array for Radar Applications
Mohammed S. Salim, Tareq A. Najm, Qusai Hadi Sultan, and Adham M. Saleh 933

Reduction of Random Variables in EMC Uncertainty Simulation Model
Jinjun Bai, Yixuan Wan, Ming Li, Gang Zhang, and Xin He 941

Parametric Modeling and Optimization of Switched Reluctance Motor for EV
Lijun Liu, Yu Huang, Mingwei Zhao, and Yi Ruan 948

Design of a Wideband CPW Fed Fractal Antenna for Satellite Communication
Varnikha Nanthagopal and Jothilakshmi Paramasivam 959

Decoupling Technique Based on Field Distribution on Ground Plane for WLAN MIMO Antenna Applications
Zicheng Zhou, Xiao-Yu Ma, Zi-Yu Pang, Guan-Long Huang, Rui-Sen Chen, and Changqing Gu 970

Bandwidth Enhancement of Slot Antenna Using Fractal Shaped Isosceles for UWB Applications
Djelloul Aissaoui, Abdelhalim Chaabane, Noureddine Boukli-Hacene, and Tayeb A. Denidni 977

On the Coupling Imbalance of the UWB BLC in the 5G Low Noise Amplifier Design
Tamer G. Abouelnaga and Esmat A. Abdallah 986

A Novel Compact Filtering Antenna for 5.0-GHz WLAN Communication System
Shujia Yan, Chongqi Zhang, Qiang Chen, and Mei Song Tong 996

A Novel Comb-line Leaky-wave Antenna for 77 GHz FMCW Automotive Radar System and Comparison with Buttler Beamformers
Masoud Sarabi and Warren F. Perger 1005

Analysis of Transmission Characteristics of EBG Structures by Subgridding Unconditionally Stable FETD Method

Yixin Wang[1], Bing Wei[1,*], and Kaihang Fan[2]

[1]School of Physics
Xidian University, Xi'an, 710071, China

[2]School of Information and Communications Engineering
Xi'an Jiaotong University, Xi'an, 710049, China
[*]bwei@xidian.edu.cn

***Abstract* –** Subgridding unconditionally-stable finite-element time-domain method based on spatial modes filtering (SSMF-FETD) is combined with the Floquet theorem and used to analyze the transmission characteristics of 2-D dielectric pillar-array electromagnetic bandgap (EBG) structures with cross-section shapes of square and H. The computational stress is effectively reduced by exploiting the periodicity of the EBG structure and subgridding technique. Through the spatial modes filtering (SMF) method, the subgridding FETD (S-FETD) method is developed into the SSMF-FETD with larger time steps and higher computational efficiency. The effect of geometric and electromagnetic parameters on transmission characteristics of EBG structures are analyzed and compared in detail, the conclusions are as follows: the optimal filling ratio of the dielectric square-pillar EBG structure is 0.5, the composite H-pillar EBG structure has multiple bandgaps and can effectively save metal materials while satisfying the design requirements. The effect of electromagnetic parameters can be uniformly analyzed from the perspective of the average relative permittivity; with its increase, the central frequency of the bandgap becomes lower. It should be noted that the bandgap distribution and variation of composite H-pillar EBG structure are related to how its dielectric parameters change and combine. The results can serve as a reference for similar structures design.

***Index Terms* –** electromagnetic bandgap (EBG), finite-element time-domain (FETD), Floquet theorem, spatial modes filtering (SMF), subgridding technique.

I. INTRODUCTION

Electromagnetic bandgap (EBG) is a type of electromagnetic structure that can prevent electromagnetic wave propagation in specific frequency ranges [1]. Similar to the photonic band gap (PBG) structures in the optical band, EBG structures can be directly composed of various dielectrics, metals, or other hybrid materials which are arranged periodically in a vacuum, or implanted into the base material. Due to the obvious bandgap characteristic, EBG structures have been applied in many fields in recent years [2, 3]. It can be used to design microwave devices such as broad band-stop filters and high-Q resonators [4, 5], improve antenna performance [6–8] or design multi-frequency antennas [9, 10], increase the efficiency and output power of power amplifiers and be used as frequency selection surfaces[11, 12], etc. For the numerical simulation of 2-D EBG structures with regular geometric shapes, the finite-difference time-domain (FDTD) method [13–15] is used more frequently than the finite-element time-domain (FETD) method [16, 17]. The principle of FDTD is simple and it's easy to implement by programming. At the same time, FETD is suitable for dealing with complex media [18] and its discretization schemes are more flexible and convenient. However, if the EBG structure contains complex and fine structures, the space step size will be very small to capture them accurately when discretizing the computational domain, which will increase the number of grids and memory demand by a considerable amount. At the same time, both FDTD and FETD are limited by the stability condition [19]. The time step is restricted by the minimum space step and has to be very small, which leads to long calculation time and low efficiency. These present a great challenge to the traditional FDTD and FETD method.

Recently, the spatial modes filtering (SMF) method has been proposed and introduced to FDTD and FETD [20–22] to break through the stability condition by filtering out the spatial modes that are unstable under the given larger time step from the numerical system, which substantially improves the computation efficiency. Later, the SMF-FETD method based on subgridding technique (SSMF-FETD) is proposed in [23].

Submitted On: July 01, 2022
Accepted On: November 09, 2022

https://doi.org/10.13052/2022.ACES.J.370901

The use of subgridding technique can not only ensure the discretization quality required by fine structures but also avoid over-division in the region without fine structures. At present, the researches on EBG structures mainly focus on the multifunctional design of metal patch EBG structures and their applications in microstrip structures [2–5, 14–16], etc. However, there are insufficient research on the effect on electromagnetic characteristics of EBG structures composed of multiple material pillars caused by cross-section shapes, combination ways, and electromagnetic parameters.

In this paper, the SSMF-FETD method [23], which has natural advantages in simulating EBG structures, is used to conduct a numerical analysis on a dielectric square-pillar EBG structure and a composite H- pillar EBG structure. In the spatial domain, due to the regular geometric shape of EBG structures, discretizing the computational domain with rectangular grids is enough to ensure modeling accuracy. Using refined rectangular grids to capture the fine structures in EBG structure not only increases the discrete flexibility but also avoids creating excessively unnecessary unknowns in other regions. Besides, the computational domain is reduced by introducing the Floquet periodic boundary condition. In the time domain, the time step of FETD is effectively expanded through the SMF method, thus the time domain iteration pressure is reduced, and the calculation time is shortened.

Through analyzing the influence of geometric and electromagnetic parameters on the transmission characteristics of EBG structures, it can be seen that the optimal filling ratio of the dielectric square-pillar EBG structure is 0.5, the composite H-pillar EBG structure has multiple bandgaps and can effectively save metal materials on the basis of satisfying design requirement. The influence of electromagnetic parameters on EBG structures can be uniformly analyzed from the perspective of the average relative permittivity as: with its increase, the central frequency of bandgap becomes lower. It should be noted that the bandgap distribution and variation of the composite H-pillar EBG structure are related to how its dielectric parameters at the grooves on both sides change and combine.

II. CALCULATION MODEL AND NUMERICAL METHOD

A. Calculation model of EBG Structure

A 2-D EBG structure composed of dielectric square pillars periodically arranged in a vacuum is shown in Fig. 1 (a). There are N layers of pillars in the x-direction and infinite layers in the y-direction. The cross-section side length of the pillar is a, the relative permittivity is ε_r, and the periodic length of EBG unit is r.

The relevant boundary condition settings of a calculation periodic unit T when N=6 are shown in Fig. 1 (b). The absorbing boundary condition (ABC) is set in the x-direction, and the Floquet theorem $f(x,y+T,t)=f(x,y,t))$ can be used to introduce the periodic boundary condition (PBC) and simplify the calculation because there are infinite layers in the y-direction. The planar differential Gaussian pulse is set at the position of the excitation source. The line integral of the transmitted fields is obtained at the observing position, as E_{t1} for the presence of dielectric pillars and E_{t0} for the absence. The transmission coefficient of the EBG structure is calculated by the ratio of E_{t1} and E_{t0} after Fourier transform as:

$$\text{Transmissioncoefficient} = \frac{\text{FFT}(E_{t1})}{\text{FFT}(E_{t0})}.$$

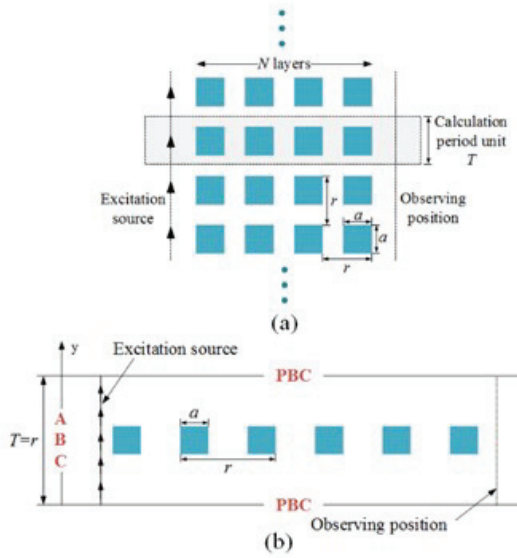

Fig. 1. (a) The 2-D dielectric square-pillar EBG structure. (b) Boundary condition settings of a calculation periodic unit T.

B. Numerical method

The traditional FETD discretization scheme generally requires conforming grids to divide the whole domain [24], and the scale is Δ usually determined by the incident wave as:

$$\Delta \le \frac{\lambda}{10} = \frac{\lambda_0}{10\sqrt{\varepsilon_r \mu_r}},$$

where ε_r and μ_r are the electromagnetic parameters of the target domain, λ and λ_0 are the wavelength of the incident wave in the target domain and in a vacuum respectively. For the 2-D EBG structure model shown in Fig. 1, the space step required by dielectric pillars is obviously smaller than that required by the vacuum background, which would lead to an unnecessarily over-fine

discretization of the vacuum domain. In this scenario, the introduction of the subgridding technique can create a more rational discretization scheme with fewer spatial elements in the computational domain.

As shown in Fig. 2, suppose the dielectric pillar is uniformly divided by fine grids of scale l_f and the remaining vacuum domain is divided by coarse grids of scale l_c. The coarse-to-fine ratio is defined as $Ratio = \frac{l_c}{l_f}$. Dealing with the discontinuous field values caused by the different number of edges at the coarse-fine boundary is the core of the subgridding FETD (S-FETD). Taking the edges at the upper coarse-fine boundary as an example, the electric fields are denoted as $E_5 - E_9$ at the fine boundary, as E_1 at the coarse boundary in Fig. 2. The electric fields at the coarse-fine boundary have to be interpolated [23], the $E_5 - E_9$ are respectively equal to $\frac{1}{Ratio}$ of E_1, so the continuity of the fields is ensured and repeated calculation is avoided.

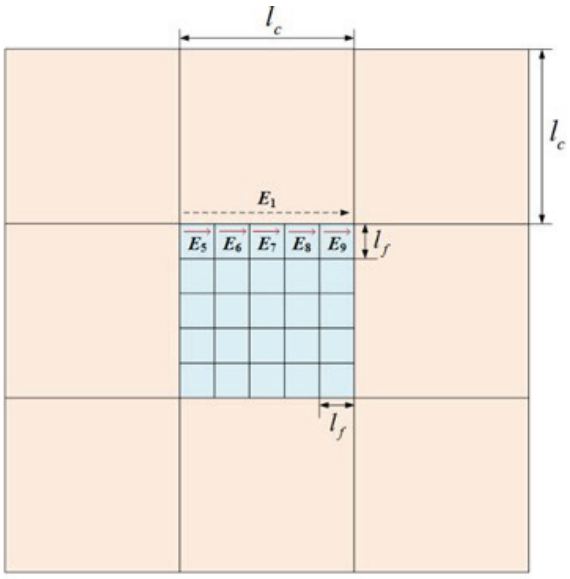

Fig. 2. Electric fields at the upper coarse-fine boundary of subgridding element.

The actual computation starts with processing the edge basis functions which are associated with edge lengths. The fine-edge basis functions at the boundary can be directly written as the 1/Ratio of the coarse-edge basis function [23]. Subsequently, the coarse and fine regions are respectively constructed into a system matrix, where the coarse region is in the order of first the inside edges and then the boundary edges, and the fine region is in the order of first the boundary edges and then the inside edges. After completion, the two system matrices are combined into a complete system matrix T and S in the order of first coarse region and then fine region. However, the T and S matrix both contain the related items that represent the coupling relationship between the coarse boundary edges. For ensuring the continuity of the fields, it is necessary to delete them and only retain their corresponding fine-edge-related items in the calculation [23]. Then the S-FETD system equation can be obtained as follows [23]:

$$T_{new}\frac{d^2 e_{new}}{dt^2} + S_{new} e_{new} = h_{new},$$

where T_{new} and S_{new} are the new system mass matrix and stiffness matrix without the items that relate to the coarse boundary edges, e_{new} is the correlation coefficient vector of the edge basis function, h_{new} is the excitation vector.

Although the S-FETD method can reduce the number of grids, its time step is still limited by the stability condition. Since the system matrices established after the introduction of subgridding technique in the finite-element framework still maintain the characteristics of symmetric positive definite or symmetric semi-positive definite [23], the SMF method can be directly applied to S-FETD to break through the limitation of the time step Δ_t by the minimum spatial step. By solving the generalized eigenvalue problem of the system, and then excluding the unstable eigenmodes from the basic numerical system, the simulation stability under the given large time step can be guaranteed [22]. The unstable modes are required to satisfy [22]:

$$\lambda_i^2 \geq \frac{4}{\Delta t^2},$$

where λ_i^2 is the ith eigenvalue of the system matrix, and the column vectors of matrix Φ_h are the eigenvectors of unstable modes. Then the S-FETD can be developed into SSMF-FETD with a new system without unstable modes through simple modification, and the system matrix equation is changed into [23]:

$$\mathrm{T}_{new}\frac{d^2 e_{new}}{dt^2} + \mathrm{S}_{new}\left(\mathrm{I} - \Phi_h \Phi_h^T \mathrm{T}_{new}\right) e_{new} = h_{new}.$$

III. TRANSMISSION CHARACTERISTIC ANALYSIS OF THE SQUARE-PILLAR EBG STRUCTURE

In this section, the efficiency and accuracy of the SSMF-FETD method are verified by calculating the transmission coefficient of the square-pillar EBG structure. Meanwhile, the effect of geometric and electromagnetic parameters on its transmission characteristics is analyzed.

A. Efficiency and accuracy verification of SSMF-FETD

The parameters of the dielectric square-pillar are as follows: cross-section side length is a=0.01 m, periodic length of EBG unit is r=0.02 m, relative permittivity is $\varepsilon_r = 14$. The coarse and fine grids are of scale $l_f = 0.0004$ m and $l_c = 0.002$ m. The pulse width is $\tau = 2 \times 10^{-10}$s and the pulse peak value is at $t_0 = \tau$.

Figure 3 shows the transmission coefficient of the 2-D dielectric square-pillar EBG structure obtained from FETD, S-FETD, and SSMF-FETD respectively, and the calculation results are in good agreement. It can be seen from Table 1 that compared with the FETD which has 63175 unknowns, the S-FETD effectively reduces the number of unknowns by nearly 84% through the subgridding technique. On this basis, the SSMF-FETD adopts the SMF method to expand the time step and reduces the time occupied by time marching. Although it takes some time and memory to solve the generalized eigenvalue problem, SSMF-FETD still improves the calculation efficiency overall. The results show that the SSMF-FETD method is efficient and accurate in EBG structure simulation.

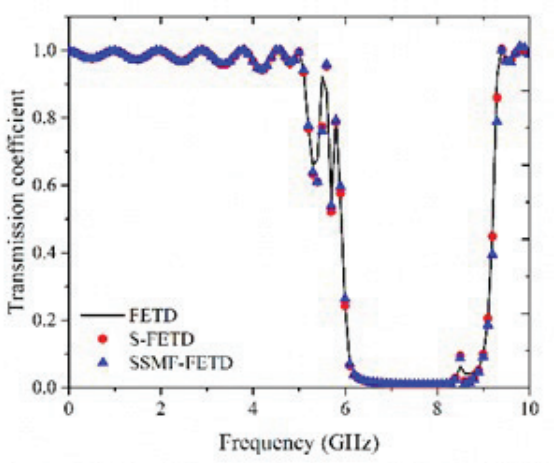

Fig. 3. Transmission coefficient of EBG structure obtained from different methods.

Table 1: Simulation parameters of different methods

Methods	Size of the System Matrix	Time Step (s)	Time for Eigenvalue Analysis (s)	Time for Time Marching (s)	Memory (MB)
FETD	63175	5×10^{-13}	Null	1786.60	72.79
S-FETD	10075	5×10^{-13}	Null	311.84	18.54
SSMF-FETD	10075	3.25×10^{-12}	33.18	161.03	4655.00

B. Effect of geometric parameters

Figures 4 and 5 respectively show the effect of the side length a and periodic length r on transmission coefficient when $\varepsilon_r = 14$. When r = 0.020 m, as a increases, the central frequency of bandgap gradually becomes lower, the bandwidth increases at first and then decreases, and reaches the maximum when a=0.010 m. When a=0.010 m, as r increases, the central frequency of bandgap becomes lower, the bandwidth increases at first and then decreases, and reaches the maximum when r=0.020m. As r increases continuously, the EBG structure gradually exhibits dual-band characteristics. Through Fig. 4 and Fig. 5, it can be verified that for such a square-pillar EBG structure, the bandgap width is the widest when the filling ratio ($\frac{a}{r}$) is 0.5.

C. Effect of electromagnetic parameters

The effect of the relative permittivity ε_r of the dielectric pillar on the EBG structure is shown in Fig. 6, where f_1 and f_h denote the lowest and highest frequency of the bandgap satisfied $S_{21} < -20dB$, f_0 and BW denote the central frequency and bandwidth. It can be seen that as ε_r increases, the central frequency of the bandgap becomes lower and the bandwidth becomes narrower.

Suppose there is a more complex and practical composite dielectric square-pillar EBG structure that contains two different dielectric materials on the basis of the above structure. A dielectric square pillar with side length b and dielectric constant ε_{r2} is surrounded by a layer of dielectric material with ε_{r3} outside. The structural parameters of the composite dielectric square-pillar EBG are still a=0.01 m and r=0.02 m. The coarse grids shown in Fig. 7 (a) cannot accurately describe the pillar. However, the subgridding discretization scheme shown in Fig. 7 (b) can satisfy the requirements of geometric and dielectric parameters on space step at the same time.

When a and r remain unchanged, the effect of changing b, or the relative permittivity ε_{r2}, ε_{r3} on transmission characteristics of the EBG structure, can be attributed to the change of the average relative permittivity ε_r' of the composite dielectric pillar. It is clear that ε_r' is a function of ε_{r2}, ε_{r3} and dielectric-pillar area as follow:

$$\varepsilon_r' = \frac{S_b}{S_a}(\varepsilon_{r2} - \varepsilon_{r3}) + \varepsilon_{r3},$$

where $S_b = b^2$ is the internal area, $S_a = a^2$ is the overall area of the composite pillar.

The change of average relative permittivity ε_r' caused by the electromagnetic parameters (shown in Fig. 8 (a) and Fig. 8 (b)) and geometric parameters (shown in Fig. 8 (c) and Fig. 8 (d)) can affect the central frequency and bandwidth of the composite square-pillar EBG structure. It can be seen that ε_r' can be increased by increasing $\varepsilon_{r2}, \varepsilon_{r3}$ or the filling area with the larger relative permittivity. In the four different cases shown in Fig. 8, as ε_r' increases, the central frequency of the bandgap becomes lower and the bandwidth becomes narrower. This rule is also applicable to the composite square-pillar EBG structure has more layers of dielectric materials.

In fact, ε_r of the single-dielectric square pillar shown in Fig. 1 is equivalent to ε_r'. Then, whether it is a single-dielectric or multi-dielectric square-pillar EBG structure, by increasing or decreasing the ε_r', the central frequency of the bandgap can become lower or higher, also the bandwidth can become wider or narrower.

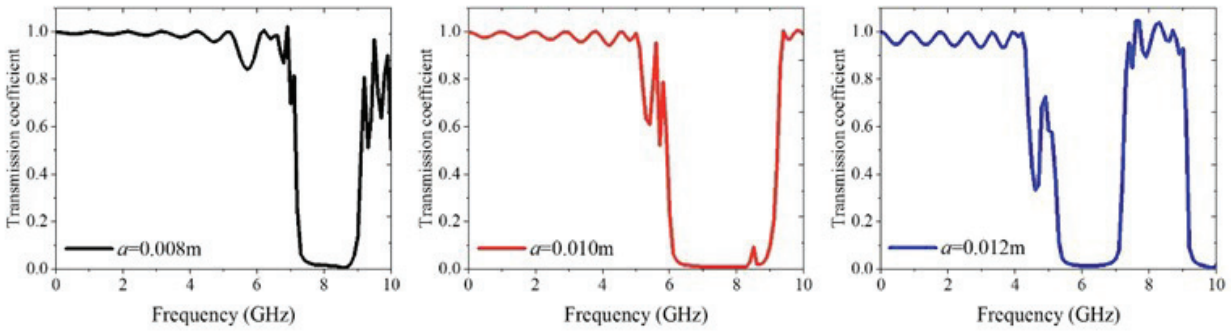

Fig. 4. Effect of a on transmission coefficient when r=0.020m.

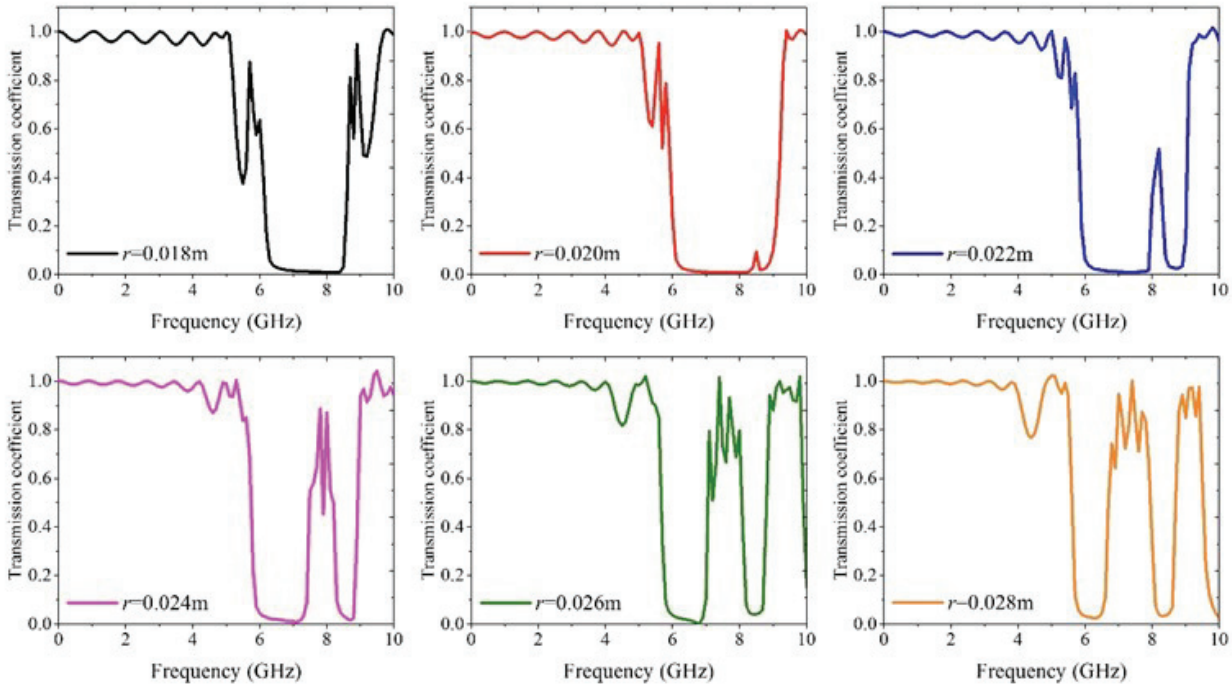

Fig. 5. Effect of r on transmission coefficient when a=0.010 m.

The effects of the geometric and electromagnetic parameters on the transmission coefficient of the dielectric square-pillar EBG structure are analyzed in this section. It is verified that the optimal filling ratio of the square-pillar EBG structure is 0.5. Also, as the average relative permittivity increases, the central frequency of the bandgap becomes lower and the bandwidth becomes narrower.

IV. TRANSMISSION CHARACTERISTIC ANALYSIS OF THE COMPOSITE H-PILLAR EBG STRUCTURE

In this section, a composite H-pillar EBG structure that can satisfy the design requirements and save metal materials is proposed. The effects of geometric and electromagnetic parameters on transmission characteristics are analyzed respectively by adjusting the size and relative permittivity of the grooves on both sides of the H-pillar.

A. Design requirements

The periodic arrangement of metal materials or hybrid materials in a vacuum can also produce EBG structures. The excitation source parameters are $\tau = 8 \times 10^{-10}s$ and $t_0 = \tau$, under this situation, it is required to design an EBG structure whose frequency range of bandgap satisfied $S_{21} < -20dB$ is not less than 1.28∼1.50 GHz. If the square pillar shown in Fig. 1 is

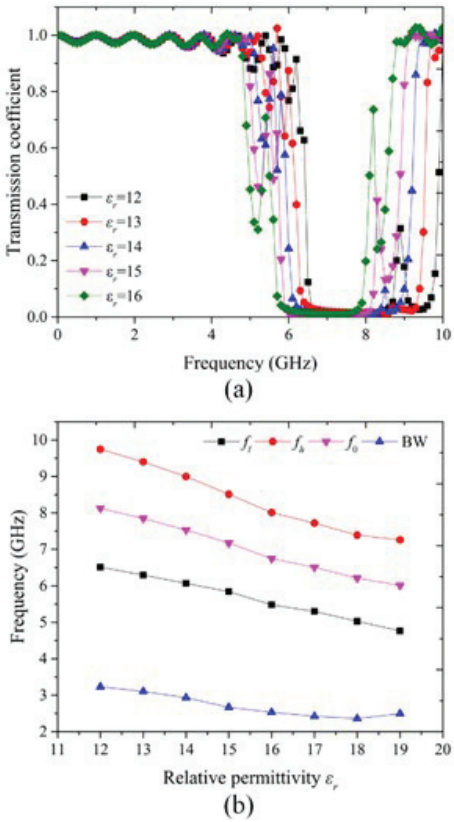

Fig. 6. Effect of relative permittivity ε_r (a) on transmission coefficient, (b) on central frequency and bandwidth.

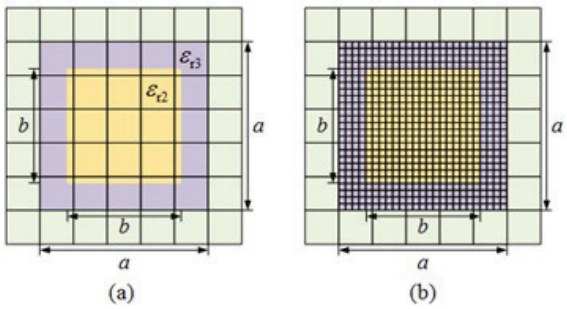

Fig. 7. Mesh model of the composite dielectric square pillar. (a) The coarse mesh scheme. (b) The subgridding scheme.

made of metal, the bandgap of the metal square-pillar EBG structure with a = 0.04 m and r = 0.10 m can satisfy the design requirement.

However, it will be extremely expensive to design with precious metal materials, which are scarce in the Earth's crust and difficult to explore, mine, and refine. For the purpose of saving materials and reducing costs, parts of the metal square pillar can be symmetrically hollowed out and filled with dielectric materials to form a composite H-pillar, and then a composite H-pillar EBG structure. The length of the groove in the H-pillar is p, the width is q, and the dielectric parameters at the grooves on both sides are ε_{r1} and ε_{r2} respectively. As shown in Fig. 9 (a), the spatial grids with a scale of $l_c = 0.01$ m determined by the incident wave cannot describe the structure accurately, but it can be solved by using the fine grids $l_f = 0.002$ m to refine the 4×4 coarse grids occupied by the composite H-pillar as Fig. 9 (b). For simplifying the calculation, the metal material is regarded as the perfect electric conductor (PEC).

Figure 10 shows the transmission characteristics (S_{21} parameter) of the metal square-pillar EBG structure and composite H-pillar EBG structures without dielectric material ($\varepsilon_{r1} = \varepsilon_{r2} = 1$). The geometric parameters of the 'H-pillar_1' case are p = 0.016 m and q = 0.008 m, and the 'H-pillar_2' case corresponds to p = 0.010 m and q = 0.036 m. Compared with the square-pillar case, the bandwidth of the two H-pillar EBG structures are slightly increased, and the performance is improved. Table 2 shows the detailed bandgap parameters of these three EBG structures. It can be seen that the design requirements are satisfied, indicating that the H-pillar EBG structure can save materials effectively while maintaining the performance of the metal square-pillar EBG structure. The cross-sectional area filled with metal materials has been reduced by 16% and 45% respectively, which is of great significance for saving precious metal materials and costs.

The composite H-pillars without dielectric material in both grooves actually construct a pure metal EBG structure. However, when grooves are filled with dielectric materials, the H-pillar EBG structure becomes a multi-band electromagnetic structure, which exhibits the double-bandgap or triple-bandgap characteristic. The first bandgap of them still satisfies the design requirement of 1.28∼1.50 GHz, but the propagation of electromagnetic waves in a certain high-frequency range is also prevented because of the second or third bandgap. It is significant for the design of multi-frequency and frequency-selective working devices.

B. Effect of geometric parameters

Figure 11 (a) and Fig. 11 (b) respectively show the effect of p and q on the transmission characteristics (S_{21} parameter) when $\varepsilon_{r1} = \varepsilon_{r2} = 4$. The EBG structure presents the dual-band characteristic at this time. When q = 0.008 m, as p increases from 0.014 m to 0.018 m, the performance of the first bandgap is slightly improved, the central frequency of the second bandgap becomes lower, and its bandwidth becomes narrower. When p = 0.016 m, as q increases from 0.004 m to 0.012 m, the performance of the first bandgap is improved, the cen-

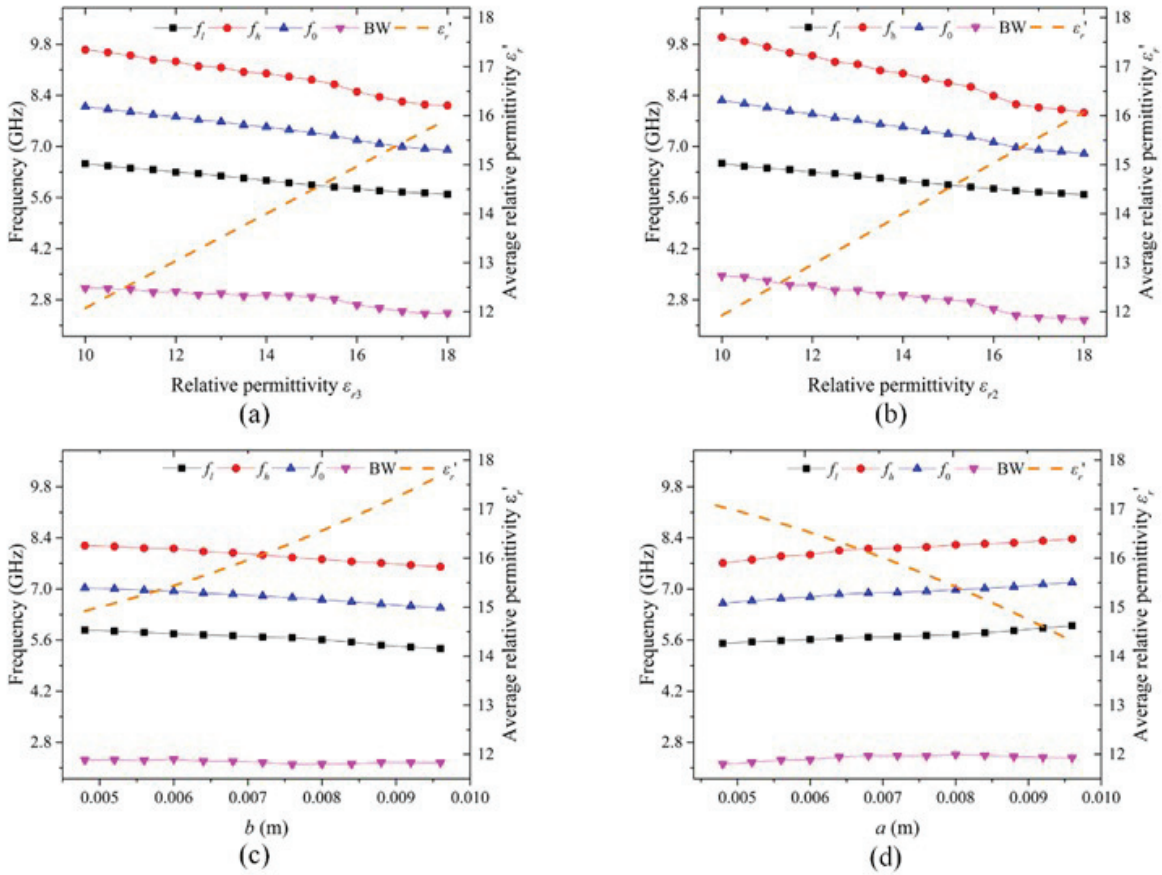

Fig. 8. Effect of average relative permittivity on the central frequency and bandwidth of bandgap. (a) Caused by ε_{r3} (When $b = 0.0072\ m,\ \varepsilon_{r2} = 14$). (b) Caused by ε_{r2} (When $b = 0.0072\ m,\ \varepsilon_{r3} = 14$). (c) Caused by b (When $\varepsilon_{r2} = 18,\ \varepsilon_{r3} = 14$). (d) Caused by b (When $\varepsilon_{r2} = 14,\ \varepsilon_{r3} = 18$).

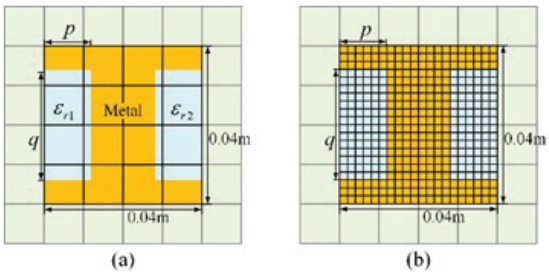

Fig. 9. Mesh model of the composite H-pillar. (a) The coarse mesh scheme. (b) The subgridding scheme.

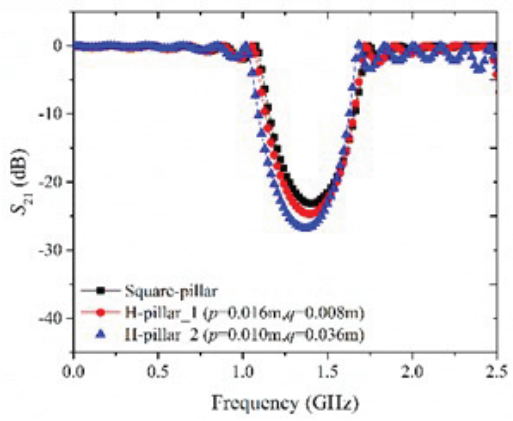

Fig. 10. Transmission characteristics (S_{21} parameter) of metal EBG structures with different cross-section shapes.

tral frequency becomes lower, and the bandwidth is basically unchanged; the performance of the second bandgap is improved, and its central frequency becomes lower while its bandwidth is obviously increased, meanwhile the pass-band between the two bandgaps becomes narrower.

Table 3 further shows the effect of q on central frequency and bandwidth when p = 0.016 m, where the suffixes 1-3 indicate the serial number of bandgaps, and the BW-total denotes the sum of all bandwidths. It

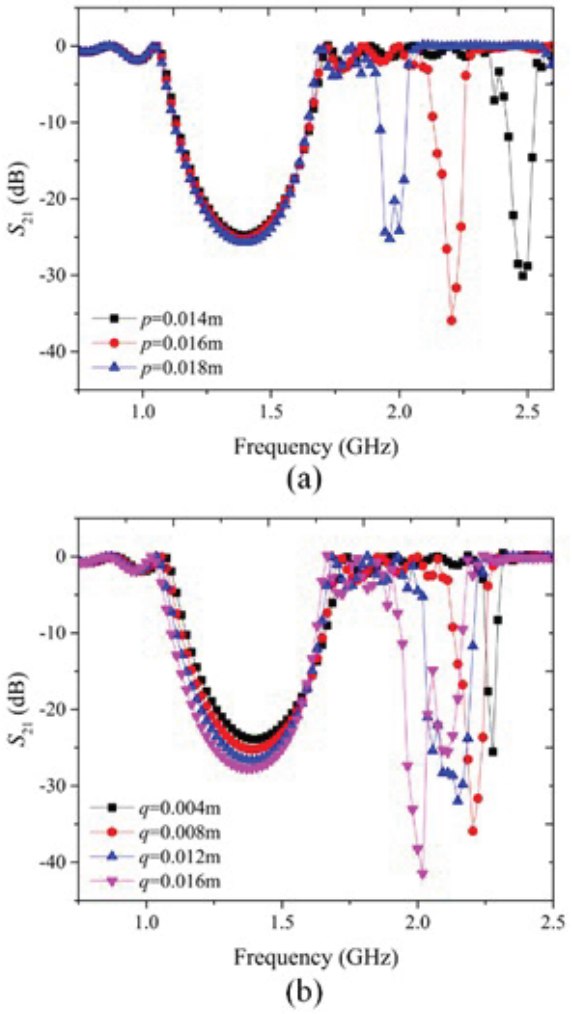

Fig. 11. The effect of geometric parameters on transmission characteristics. (a) Caused by p. (b) Caused by q.

Table 2: Bandgap parameters of metal EBG structures with different cross-section shapes

	Requirements	Square-pillar	H-pillar_1	H-pillar_2
f_l(GHz)	≤ 1.28	1.27451	1.23632	1.18103
f_h(GHz)	≥ 1.50	1.53956	1.55438	1.54754

can be seen that the EBG structure has three bandgaps when $q \geq 0.016$ m. As q increases, the central frequency of the first bandgap becomes lower and its bandwidth becomes narrower, but the design requirements are still satisfied; the central frequency and bandwidth of the second bandgap become lower and wider respectively; the central frequency and bandwidth of the third bandgap become higher and wider respectively. Overall, as q increases, the total bandwidth of bandgaps increases.

Table 3: The effect of q on central frequency and bandwidth of bandgaps

q/m	f_0-1 (GHz)	BW-1 (GHz)	f_0-2 (GHz)	BW-2 (GHz)	f_0-3 (GHz)	BW-3 (GHz)	BW-total (GHz)
0.016	1.370	0.392	1.997	0.085	2.105	0.074	0.551
0.020	1.355	0.405	1.920	0.091	2.072	0.075	0.572
0.024	1.343	0.415	1.904	0.113	2.071	0.079	0.607
0.028	1.329	0.405	1.908	0.134	2.100	0.098	0.636
0.032	1.317	0.409	1.892	0.149	2.101	0.103	0.660
0.036	1.302	0.404	1.869	0.170	2.106	0.099	0.673

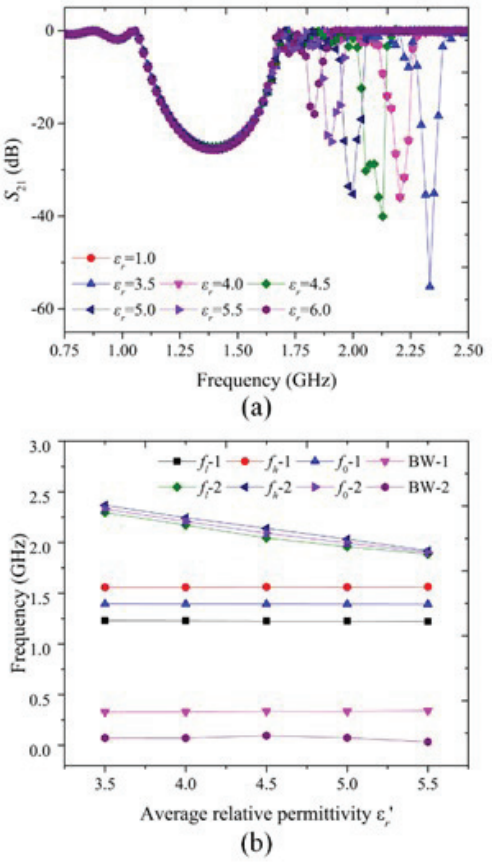

Fig. 12. Effect of ε_r' on transmission characteristics when $\varepsilon_{r1} = \varepsilon_{r2}$. (a) S_{21} parameter. (b) Central frequency and bandwidth.

By analyzing the effect of geometric parameters on transmission characteristics of the composite H-pillar EBG structure, it can be known that adjusting the size of the H-pillar grooves can control the generation of the second, and third bandgap and the movement of their central frequencies.

C. Effect of electromagnetic parameters

The average relative permittivity of the dielectric regions in the composite H-pillar is $\varepsilon_r' = (\varepsilon_{r1} + \varepsilon_{r2})/2$ and the geometric parameters of H-pillar are p = 0.016 m and q = 0.008 m. Figure 12 shows the effect of ε_r' on

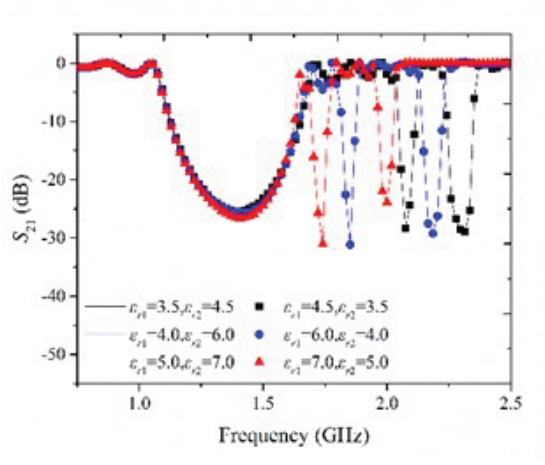

Fig. 13. Effect of ε_r' on transmission characteristics when $\varepsilon_{r1} \neq \varepsilon_{r2}$.

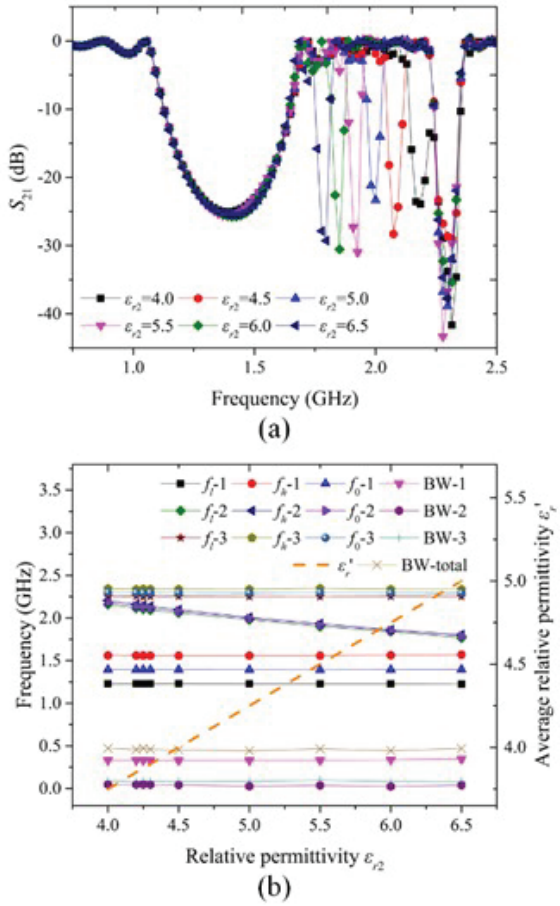

Fig. 14. Effect of ε_r' on transmission characteristics when ε_{r1} is constant. (a) S_{21} parameter. (b) Central frequency and bandwidth.

transmission characteristics when $\varepsilon_{r1} = \varepsilon_{r2}$. As ε_r' increases from 3.5 to 6.0, the first bandgap remains practically unchanged, the central frequency of the second bandgap becomes lower and its performance decreases, and the widest bandwidth appears when $\varepsilon_r' = 4.5$.

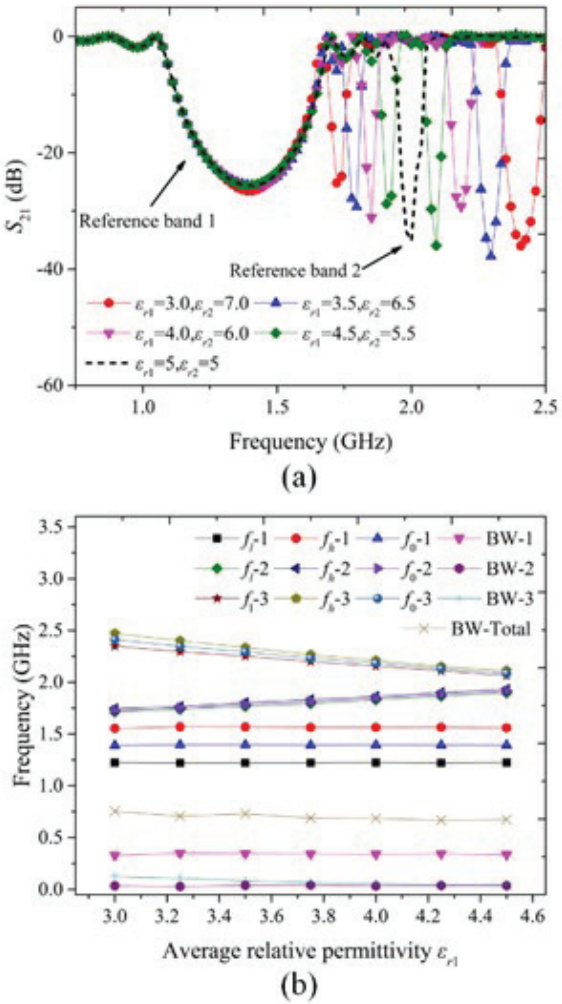

Fig. 15. Effect of ε_{r2} and ε_{r2} on transmission characteristics when $\varepsilon_r' = 5$. (a) S_{21} parameter. (b) Central frequency and bandwidth.

The effect of ε_r' on the transmission characteristics when $\varepsilon_{r1} \neq \varepsilon_{r2}$ is shown in Fig. 13. It can be seen that the EBG structure exhibits the triple-band characteristic when the dielectric parameters in grooves are different. Moreover, the exchange of the left and right dielectric parameters does not affect the transmission characteristics. As ε_r' increases, the central frequency of the first bandgap remains unchanged while the second and third bandgaps become lower.

Figure 14 shows the effect of ε_r' by adjusting ε_{r2} on the transmission characteristics when $\varepsilon_{r1} = 3.5$. As ε_{r2} increases from 4.0 to 6.5, ε_r' increases, the central frequency, and bandwidth of the first and third bandgaps

remain practically unchanged, the central frequency of the second bandgap gradually becomes lower and approaches the first bandgap, and its bandwidth remains unchanged. Combining the results shown in Fig. 13 and Fig. 14, it can be seen that the increase of dielectric parameters in both grooves may cause the central frequency of the second and third bandgap both become lower, and the increase of one-side dielectric parameter only affects the central frequency of the second bandgap.

The influence of simultaneous change in ε_{r1} and ε_{r2} on transmission characteristics when $\varepsilon_r' = 5$ is shown in Fig. 15. We defined the bandgap with lower central frequency as reference bandgap 1 and the higher central frequency as reference bandgap 2 when $\varepsilon_{r1} = \varepsilon_{r2} = 5$ (the black dash line in Fig. 15). It can be seen that the EBG structure exhibits a triple-band characteristic when $\varepsilon_r' = 5$ but $\varepsilon_{r1} \neq \varepsilon_{r2}$, the second and third bandgaps are distributed on both sides of the reference band 2. Meanwhile, the closer the values of ε_{r1} and ε_{r2} are, the closer the second and third bandgaps are to the reference bandgap 2, and the narrower the bandwidth of the third bandgap is.

The influence of electromagnetic parameters on transmission characteristics of the composite H-pillar EBG structure is analyzed by changing the average relative permittivity ε_r'. First of all, for the dual-band situation with $\varepsilon_{r1} = \varepsilon_{r2}$, the increase of ε_r' has little effect on the first bandgap but causes the central frequency of the second bandgap obviously becomes lower. Secondly, for the triple-band situation when $\varepsilon_{r1} \neq \varepsilon_{r2}$, the increase of ε_r' caused by the simultaneous increase of ε_{r1} and ε_{r2} causes the central frequency of the second and third bandgaps to decrease, the increase of the dielectric parameter on one side (ε_{r1}orε_{r2}) only causes the central frequency of the second band becomes lower. Finally, when the second bandgap of the EBG structure with $\varepsilon_r' = \varepsilon_{r1} = \varepsilon_{r2} = 5$ is defined as the reference band, as the value of ε_{r1} and ε_{r2} change simultaneously and get closer but ε_r' remains unchanged, the second and third bandgaps are distributed on both sides of the reference band but become closer to it.

In conclusion, the composite H-pillar EBG structure can effectively save metal materials on the basis of satisfying the design requirements. By adjusting the geometric and electromagnetic parameters, the EBG structure can exhibit dual- or triple-band characteristics while maintaining the characteristics of the first bandgap constant. The central frequency of the second and third bandgaps are adjustable, which increases the total bandgap width of the EBG structure and can prevent the propagation of electromagnetic waves in multiple frequency ranges.

V. CONCLUSION

In this paper, the transmission characteristics of a dielectric square-pillar EBG structure and a composite H-pillar EBG structure are analyzed. The Floquet theorem is combined with the SSMF-FETD method to simulate the periodically arranged 2-D pillar-array EBG structures while the subgridding technique and the periodicity of the EBG structure are used to reduce the calculation. The influence of geometric and electromagnetic parameters on EBG structures with different cross-section shapes and materials are compared in detail through the transmission coefficient and S_{21} parameters. From the analysis of geometric parameters, it is verified that the optimal filling ratio of the dielectric square-pillar EBG structure is 0.5, and the composite H-pillar EBG structure is effective in saving metal materials while satisfying the design requirements and exhibits dual- or triple-bandgap characteristic. The analysis of the electromagnetic parameters leads to the conclusion that the central frequency of the bandgap decreases as the average relative permittivity increases, the changes are more obvious in the high-frequency bandgaps of the composite H-pillar EBG structure. The electromagnetic parameters are also the factors that affect the number of bandgaps. The EBG structure exhibits triple-bandgap characteristics when the dielectric parameters on both grooves are different. The change of one-side dielectric parameter only affects the central frequency of the second bandgap, but for both sides, the central frequency and bandwidth of the second and third bandgaps are affected simultaneously. The work of this paper can provide references for the design and development of EBG structures.

REFERENCES

[1] A. Pirhadi, H. Bahrami, and A. Mallahzadeh, "Electromagnetic band gap (EBG) superstrate resonator antenna design for monopulse radiation pattern," *Applied Computational Electromagnetics Society (ACES) Journal*, vol. 27, no. 11, pp. 908-917, Nov. 2012.

[2] S. D. Assimonis, T. M. Kollatou, T. V. Yioultsis, and C. S. Antonopoulos, "Absorbing surfaces using EBG structures," *IEEE Trans. Magn.*, vol. 50, no. 2, pp. 197-200, Feb. 2014.

[3] M. Kim, "A compact EBG structure with wideband power/ground noise suppression using meander-perforated plane," *IEEE Trans. Electromag. Compat.*, vol. 57, no. 3, pp. 595-598, Jun. 2015.

[4] N Yang, Z. N. Chen, Y. Y. Wang, and M. Y. W. Chia. "A two-layer compact electromagnetic bandgap (EBG) structure and its applications in microstrip filter design," *Microw. Opt. Technol. Lett.*, vol. 37, no. 1, pp. 62-64, Apr. 2003.

[5] M. Y. Koledintseva, S. Radu, and J. Nuebel, "EBG common-mode 20-GHz microstrip and stripline filters: sensitivity to design parameters," *IEEE Trans. Electromag. Compat.*, vol. 62, no. 5, pp. 1989-2001, Oct. 2020.

[6] J. Y. Lee, S. H. Kim, and J. H. Jang, "Reduction of mutual coupling in planar multiple antenna by using 1-D EBG and SRR structures," *IEEE Trans. Antennas Propag.*, vol. 63, no. 9, pp. 4194-4198, Sep. 2015.

[7] H. H. Park, "Reduction of electromagnetic noise coupling to antennas in metal-framed smartphones using ferrite sheets and multi-via EBG structures," *IEEE Trans. Electromag. Compat.*, vol. 60, no. 2, pp. 394-401, Apr. 2018.

[8] P. Bora, P. Pardhasaradhi, and B. Madhav. "Design and analysis of EBG antenna for Wi-Fi, LTE, and WLAN applications," *Applied Computational Electromagnetics Society (ACES) Journal*, vol. 35, no. 9, pp. 1030-1036, Sep. 2020.

[9] W. Q. Cao, B. N. Zhang, A. J. Liu, T. B. Yu, D. S. Guo, and X. F. Pan, "Multi-frequency and dual-mode patch antenna based on electromagnetic band-gap (EBG) structure," *IEEE Trans. Antennas Propag.*, vol. 60, no. 12, pp. 6007-6012, Aug. 2012.

[10] L. Peng, C. L. Ruan, and J. Xiong, "Compact EBG for multi-band applications," *IEEE Trans. Antennas Propag.*, vol. 60, no. 9, pp. 4440-4444, Sep. 2012.

[11] V. Radisic and Y. Qian, "Broad-band power amplifier using dielectric photonic bandgap structure," *IEEE Microw. Guided Wave Lett.*, vol. 8, no. 1, pp. 13-14, Jan. 1998.

[12] Y. J. Lee, J. Yeo, R. Mittra, and W. S. Park, "Design of a high-directivity Electromagnetic band gap (EBG) resonator antenna using a frequency-selective surface (FSS) superstrate," *Microw. Opt. Technol. Lett.*, vol. 43, no. 6, pp. 462-467, Dec. 2004.

[13] A. R. Weily, K. P. Esselle, T. S. Bird, and B. C. Sanders, "Linear array of woodpile EBG sectoral horn antennas," *IEEE Trans. Antennas Propag.*, vol. 54, no. 8, pp. 2263-2274, Aug. 2006.

[14] Y. F. Mao, B. Chen, R. Xiong, Z. Cai, and Q. Chen, "A novel weakly conditionally stable FDTD method for periodic structures," *IEEE Antennas Wireless Propag. Lett.*, vol. 11, pp. 164-167, Feb. 2012.

[15] F. Yang and Y. Rahmat-Samii, "Microstrip antennas integrated with electromagnetic band-gap (EBG) structures: a low mutual coupling design for array applications," *IEEE Trans. Antennas Propag.*, vol. 51, no. 10, pp. 2936-2946, Oct. 2003.

[16] S. D. Assimonis, T. V. Yioultsis, and C. S. Antonopoulos, "Computational investigation and design of planar EBG structures for coupling reduction in antenna applications," *IEEE Trans. Magn.*, vol. 48, no. 2, pp. 771-774, Feb. 2012.

[17] M. N. Vouvakis, Z. Cendes, and J. F. Lee, "A FEM domain decomposition method for photonic and electromagnetic band gap structures," *IEEE Trans. Antennas Propag.*, vol. 54, no. 2, pp. 721-733, Feb. 2006.

[18] J. F. Lee, R. Lee, and A. Cangellaris, "Time-domain finite-element methods," *IEEE Trans. Antennas Propag.*, vol. 45, no. 3, pp. 430-442, Mar. 1997.

[19] D. Jiao and J. M. Jin, "A general approach for the stability analysis of the time-domain finite-element method for electromagnetic simulations," *IEEE Trans. Antennas Propag.*, vol. 50, no. 11, pp. 1624-1632, Nov. 2002.

[20] J. Yan and D. Jiao, "Fast explicit and unconditionally stable FDTD method for electromagnetic analysis," *IEEE Trans. Microw. Theory Tech.*, vol. 65, no. 8, pp. 2698-2710, Aug. 2017.

[21] S. H. Zhao, B Wei, X. B. He, Y. W. Li, and X. L. Wei, "Hybrid FDTD algorithm for electromagnetic analysis of fine structures," *Results Phys.,* vol. 31, pp. 105017, Dec. 2021.

[22] W. Lee and D. Jiao, "An alternative explicit and unconditionally stable time-domain finite-element method for electromagnetic analysis," *IEEE J. Multiscale Multiphys. Comput. Tech.*, vol. 3, pp. 16-28, Mar. 2018.

[23] K. H. Fan, B. Wei, and X. B. He, "A subgridding unconditionally stable FETD method based on local eigenvalue solution," *IEEE Trans. Antennas Propag*, vol. 69, no. 8, pp. 4695-4705, Aug. 2021.

[24] F. L. Teixeira, "Time-domain finite-difference and finite-element methods for Maxwell equations in complex media," *IEEE Trans. Antennas Propag.*, vol. 56, no. 8, pp. 2150-2166, Aug. 2008.

Yixin Wang was born in Xi'an, Shaanxi, China, in 1995. She received her B.S. degree in Electromagnetic Wave Propagation And Antennas from Xidian University, Xi'an, China, in 2017. She is currently pursuing a Ph.D. degree in Radio Science at the School of Physics, Xidian University. Her current research interests include the finite element time-domain method and its related methods.

Bing Wei was born in Tianshui, Gansu, China, in 1970. He received a B.S. degree in Physics from Beijing Normal University, Beijing, China, in 1993, and a Ph.D. degree in Radio Science from Xidian University, Xi'an, China, in 2004. From 1993 to 1998, he was a Physics professor at Tianshui Normal University, Tianshui, China. From 1998 to 1999, he was a Physics professor at Baoji University of Arts and Science, Baoji, China. Since 2004, he was been with Xidian University. Currently, he is also a professor at Xidian University. His research interests include investigations of electromagnetic field theory, numerical field computation, and short pulse interactions on complex objects.

Kaihang Fan was born in Linfen, Shanxi, China, in 1990. She received a B.S. degree in Electronic Information Science And Technology and a Ph.D. degree in Radio Science from Xidian University, Xi'an, China, in 2014 and 2021, respectively. She is currently working as a postdoctoral researcher at the School of Information and Communications Engineering, Xi'an Jiaotong University, Xi'an, China. Her current research interests include the finite element time-domain method and the multiphysics problem.

A New Approach of Applying Chebyshev Distribution of Series Fed Microstrip Antenna Array for Radar Applications

Mohammed S. Salim, Tareq A. Najm, Qusai Hadi Sultan, and Adham M. Saleh

Department of Communications Engineering
Ninevah University, Mosul, Iraq
mohammed.salim@uoninevah.edu.iq, tareq.najm@uoninevah.edu.iq,
qusai.sultan@uoninevah.edu.iq, adham.saleh@uoninevah.edu.iq

***Abstract* –** In this paper a new method of applying Chebyshev distribution for series fed antenna array was proposed for radar applications. The first part of this study consists of applying the proposed method on antenna arrays working at 2.3 GHz (S-band radar applications) with 6, 8, 10, 14, and 28 elements, whereas the second part of the study is applying the method on antenna arrays working at 5.2 GHz (C-band radar applications) with the same number of elements. The achieved sidelob level is around (19.6- 24 dB).The obtained antenna gain is around (10-17.4 dB) depending on the number of elements. Whereas the horizontal half-power beam width is around (7° – 20°).

***Index Terms* –** Antenna array, Chebyshev distribution, series fed, side lob level.

I. INTRODUCTION

Radars can be used in many fields such as marine applications, air traffic control, and military fields. There are many frequency bands dedicated to radar applications, for example, X-band (8.5-10.5 GHz), S-band (2.3-2.38 GHz), and C- band (5.2-5.8 GHz) [1].

In general, antennas play a significant role in radar systems and they affect the performance of the radar systems. There are many types of antennas used in radars applications such as parabolic antennae, horn antennae, and microstrip antennae. The accuracy of radar detection depends on several antenna parameters for instance side lobe level, HPBW, polarization, and gain. Microstrip antenna arrays are widely used in radar applications, due to their unique features such as high gain, low cost, lightweight, and low profile, and can accurately control the radiation patterns [2]. The desired radiation pattern of the antenna array can be formed depending on the spacing between the elements. It is also relying on the excitation's distribution of the elements. The most popular methods of amplitude distribution are uniform, Chebyshev and Binomial distribution. Feeding of microstrip patch antenna array can be achieved by single feed or multiple ports. Because of the simplicity of a single feed port, it is widely used in radar antennas. Chebyshev method was chosen to apply to the series feed array antenna with single.

Reducing the side lobe of antenna arrays has attracted much research in recent years [3–8]. Designing a series-fed microstrip array antenna for x-band Indonesian maritime radar was proposed by Hajian M. et al. In the mentioned work, the researchers designed an 8- and 16element antenna array and they used the spacing between elements as a parametric study to optimize the radiation pattern [9]. Chen Z. and Otto S. studied a taper optimization of a microstrip patch antenna array [10]. A 2*16-element antenna array working at 9.35 GHz for marine radar applications were proposed by Kuo F. Y. and Hwang R. B. [11]. The researchers used s-parameter analysis to find the values of main feed line impedances by which the Chebyshev distribution is achieved [11]. Milijić M. et al studied the influence of feeding structure on the side lobe level [12]. A 4*4 non-uniform antenna array working at 0.9 GHz was designed by Inserra D., Hu W., and Wen G. They used a sequentially rotated series power divider to apply a Chebyshev tapering [13]. Toan, Tran, and Giang proposed a double-sided printed dipole linear array antenna working at 5.5 GHz for WLAN outdoor applications. The proposed antenna consists of 10-element double side; also the researchers used series-fed Chebyshev tapering [14].

The main idea behind this paper is to examine a new analysis method to apply Chebyshev distribution for a series-fed microstrip antenna array. The distribution of amplitude excitations of the array elements is controlled by changing the width of the main feed line. The variation of the width was evaluated depending on the impedance values, which were calculated by the proposed method. By applying this method of analysis, a wider feed line was obtained as compared to other works. This technique allows more power to be transmitted through the antenna array due to the fact that

Submitted On: April 20, 2022
Accepted On: September 23, 2022

https://doi.org/10.13052/2022.ACES.J.370902

impedance values are reduced with increasing the width of the feed line. In addition, the increased width of the feed lines is an advantage from the manufacturing perspective since less fabrication accuracy is needed. Furthermore, the proposed method in this work has shown that the variation of the feed line's impedance is too small where the impedance values are ranging from 43 to 70 Ω, which in fact doesn't necessitate the use of $\lambda/4$ transform. All these advantages of the proposed technique cause the proposed antenna arrays to exhibit low complexity and low fabriction cost in addition to handling higher power while maintaining the standard acceptable performance.

II. THEORETICAL ANALYSIS

The analysis of the feeding network was achieved by considering each feed line of the elements as a tee junction, which is denoted by T1, T2....T6 as shown in Fig. 1, [11]. The distance between the two elements was chosen to be one wavelength λ, whereas the length of the feeding line of each element is $\lambda/4$ see Fig. 1. The power ratio between the tee junction ports is depending on the characteristic impedance of the microstrip lines. The impedances of the main feed line are denoted by Zi, where i = 1, 2...7 as explained in Fig. 2. The value of Z_1 was assumed to be 70 Ω. The impedances of the feed lines of all the elements were assumed to be the same and denoted by Z = 50 Ω except element 7, which was assumed to be 45 Ω. The values of $Z_{(in,1)}$ to $Z_{(in,6)}$ which represent the impedances seen after i-th tee junction were calculated depending on the power divider relation. For example, to calculate $Z_{(in,1)}$, at tee junction 1 the power divider relationship is given by [13]:

$$P_{in}Z_1 = P_{in,1}Z_{in,1}. \quad (1)$$

Where: P_{in} is the total power fed to the one side of the feeding network. $P_{in,1}$ is the power delivered to port 2 of the first tee junction and it is given by Eq. 2.

$$P_{in,1} = P_{in} - P_1. \quad (2)$$

Where P_1, P_2 ..... P_i is the power fed to each element of the array, which was calculated according to the Chebyshev distributions. Therefore, the values of $Z_{(in,1)}$ to $Z_{(in,6)}$ were evaluated using Eq. 1. To calculate the values of Z_i, a reverse impedance analysis was applied. The values of the calculated Z_i are listed in Table 1. Depending on the assumed values of Z_1 and Z,

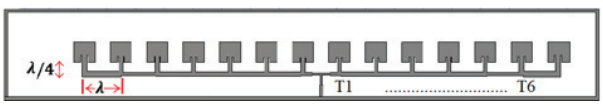

Fig. 1. The proposed antenna array configuration (14 elements).

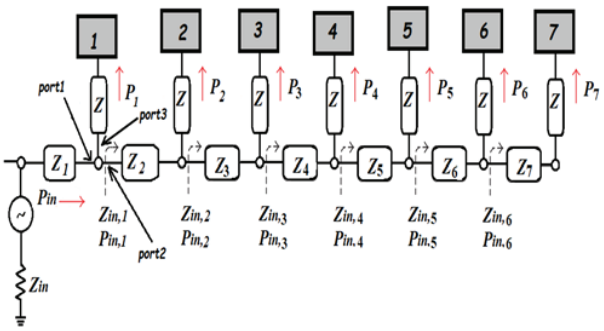

Fig. 2. Equivalent circuit of the right side 14-element antenna array.

Table 1: Values of calculated impedances of the main feed line

Impedance	Value of the Impedance Ω	Width of the Line (mm)
Z_1 (assumed)	70	1.5
Z_2	49.5	3
Z_3	51.1	2.85
Z_4	51.7	2.8
Z_5	52.5	2.7
Z_6	61	2.04
Z_7	43	3.8

the obtained range of Z_i is extended from 43 to 70 Ω. On the other hand, this assumption excludes the use of $\lambda/4$ transform between the elements but only one $\lambda/4$ transform is used in the feed that separates both sides of the antenna array.

III. ANTENNA DESIGN

A rectangular microstrip antenna was chosen to be the basic element of the array. The width (W) and length (L) of the elements were optimized to satisfy the desired frequency bands. At the S-band, the dimensions of the patch antenna is W = 39.18 mm and L = 30.4 mm, whereas W = 17.1 mm and L = 12.8 mm at the C-band.

At the beginning, a 14-element antenna array working on 2.3 GHz was designed. The array is divided into two symmetrical parts each part contains 7 elements as shown in Fig. 1. The proposed antenna array was implemented on FR4 substrate with relative dielectric constant ε_r = 4.3, thickness of 1.6 mm and tangent loss δ=0.025.

The feeding network was designed according to the Chebyshev distribution. The amplitude excitation of each element was calculated based on the Chebyshev method [1] and listed in Table 2. To validate the proposed method of feeding network analysis, two steps were applied. The first step is to change the number of elements (6, 8 and 10) for the proposed antenna array at 2.3 GHz. The second step of validation is to redesign the same antenna

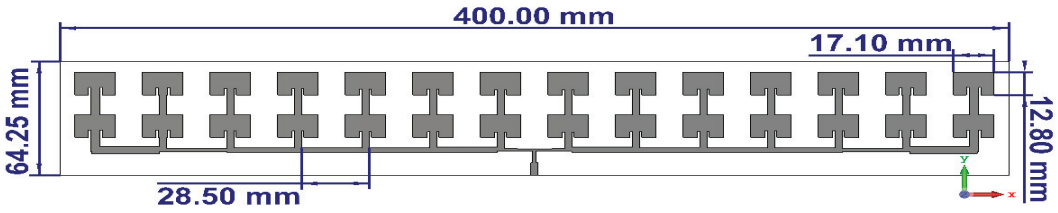

Fig. 3. Geometry of the 2*14-element antenna array at C-band.

Table 2: Calculated Chebyshev amplitude excitation

Amplitude Excitation of the i-th Element	6 Elements	8 Elements	10 Elements	14 Elements
a_1	1	1	1	1
a_2	0.72	0.818	0.89	0.786
a_3	0.37	0.544	0.706	0.496
a_4	——	0.33	0.485	0.266
a_5	——	——	0.357	0.138
a_6	——	——	——	0.077
a_7	——	——	——	0.0065

arrays (6, 8, 10 and 14 elements) at different frequency band (5.2 GHz). To increase the gain of the array, the number of elements was duplicated as shown in Fig. 3 to be a 2∗14-element antenna array.

IV. RESULTS ANALYSIS

This section presents the simulated results of the proposed antenna arrays in terms of reflection coefficient (S11), surface current distribution, half power beam width (HPBW), antenna gain and sidelobe level at two frequency bands (S and C band). These simulated results are obtained by CST software package. The simulated reflection coefficients for the two arrays are explained in Figs. 4 (a) and (b). Each array is simulated with different number of elements (6, 8, 10, 14 and 28 elements) to show their effect on the bandwidth. It is clear from figures that the obtained bandwidth fluctuated when increasing the number of elements in both bands. These fluctuations can be related to the effect of the feeding network. By increasing the number of elements the feeding network becomes more complex and the overall impedance of the antenna array will change. This will affect the S11 and bandwidth results. Additionally, it can be noticed that there is a small shift in the operating frequency bands. This shift happened because of the change of the total physical length of the array antenna due to the change in the number of elements in each array.

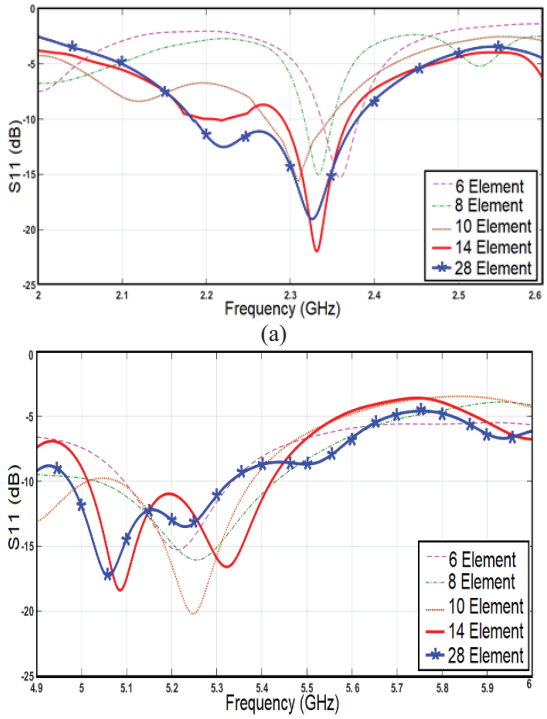

Fig. 4. S11 of the designed antenna arrays at: (a) S-band. (b) C-band.

Furthermore, the 2D-Normalized antenna array patterns in xz-plane were plotted in Fig. 5 while the antenna parameters of the presented antennas like HPBW, antenna gain and side lob level were listed in Tables 3 and 4. These tables show the natural trend of decreasing HPBW with increasing the number of radiating elements in 1-D antenna array [2]. This means compressing the radiation pattern in the xz-plane (horizontal) and expanding the radiation pattern in the yz-plane (vertical). The only exception for the previous scenario is in the case of the 2∗14 element where the horizontal HPBW is slightly increased approximately by 2°. This increase is resulted from duplicating the number of elements from 14 to 2*14 element, which leads to compress the pattern in elevation and expand the pattern in the horizontal plane.

Table 3: HPBW, Gain and SLL of array antennas at 2.35 GHz

No. of Elements	HPBW (deg.) xz-Plane	HPBW (deg.) yz-Plane	BW (MHz)	Gain (dB)	SLL (dB)
6	20.3	78	44	10	−22
8	19.5	79	40	10.8	−20
10	17	81	76	11.3	−23
14	7.4	89	169	14.5	−20
2*14	9.1	86	199	17.4	−21.5

Table 4: HPBW, Gain and SLL of array antennas at 5.2 GHz

No. of Elements	HPBW (deg.) xz-Plane	HPBW (deg.) yz- Plane	BW (MHz.)	Gain (dB)	SLL (dB)
6	20.4	79	240	10.1	−19.7
8	20	79	387	10.3	−19.6
10	13.1	82	290	11.4	−21.9
14	8.4	85	408	13.2	−20.1
2*14	10.8	83	357	17	−23.1

Moreover, the tables indicate that the gain of antenna arrays are increased with increasing the number of elements. A 3dB gain enhancement was obtained by duplicating the radiating elements from 14 to 28. Regarding to the achieved side lob level, it is approximately -19 down to -25 dB. On the other hand, the surface current distribution for the 2*14-element antenna array is shown in Fig. 6. It evident that the radiating elements at the center of the arrays have higher amplitude excitation compared to the elements at the edges of the arrays as shown in the amplitude excitation values in Table 2. Finally, the 3D and 2D radiation patterns for 28 elements were illustrated in Fig. 7 and Fig. 8 at the two bands.

V. EXPERIMENTAL RESULTS

To validate the simulation results, 14 and 28-element prototype antenna arrays at 5.2GHz were created on a PCB board as shown in Fig. 9. A vector network analyzer (VNA) was used to test the S-parameter of the printed antennas. Comparisons between the simulated and measured outcomes for the two proposed antennas are depicted in Fig. 10. It is clear from these comparisons that the results of the 2*14-element antenna array have the same tendency whereas some differences were noticed in the results of the 14-element antenna array.

The radiation pattern is another significant parameter that should be tested practically inside the anechoic chamber to show the side lobes levels and compare it

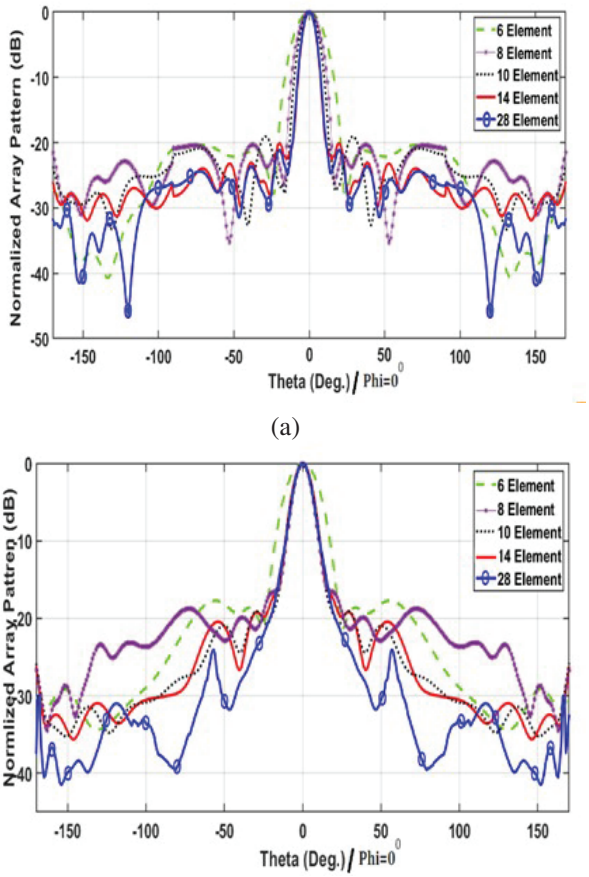

(a)

(b)

Fig. 5. 2D Radiation pattern in x-z plane of the designed antenna arrays at: (a) 2.35 GHz; (b) 5.2 GHz.

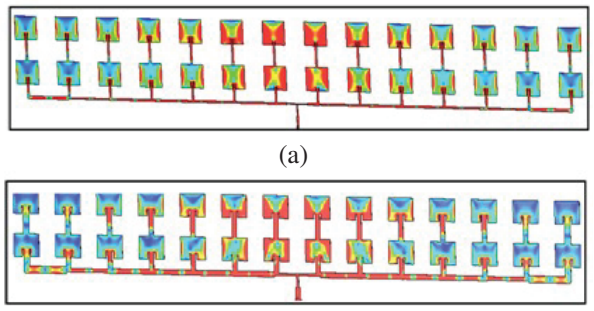

(a)

(b)

Fig. 6. Surface current distribution of 28 element at: (a) 2.35 GHz; (b) 5.2 GHz.

with the simulation ones. The x-y plane radiation pattern was plotted. Figure 11 shows the comparison of the x-y plane radiation pattern of the theory with the simulated and measured results. The theory results were obtained using the equations listed in [1]. The array fac-

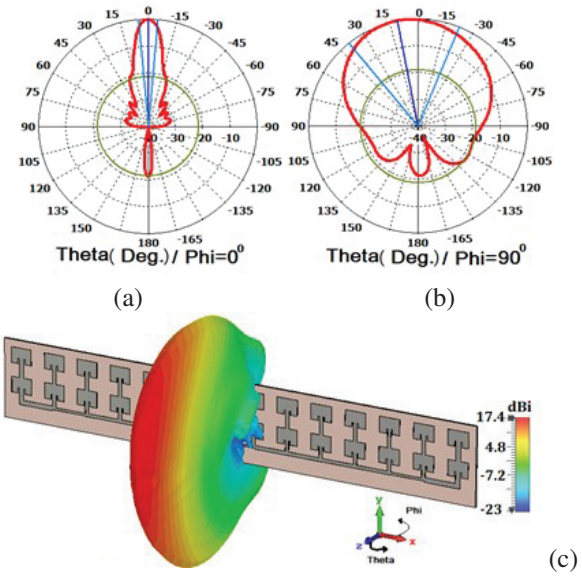

Fig. 7. Far-field radiation pattern of the antenna array at 2.35 GHz.: (a) H-plane; (b) E-plane; (c) 3D pattern.

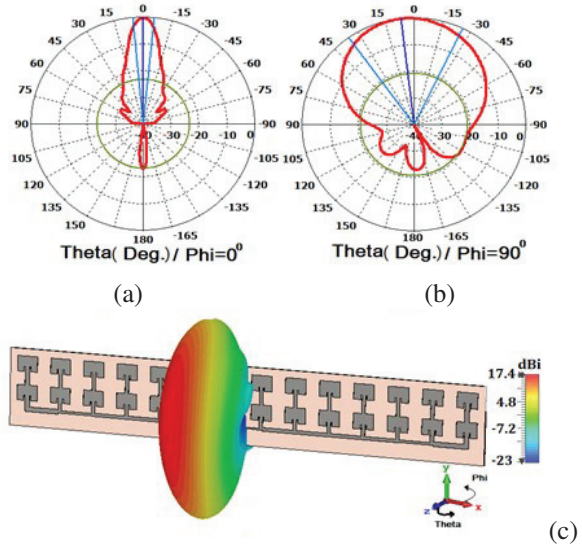

Fig. 8. Far-field radiation pattern of the antenna array at 5.2 GHz: (a) H-plane; (b) E-plane; (c) 3D pattern.

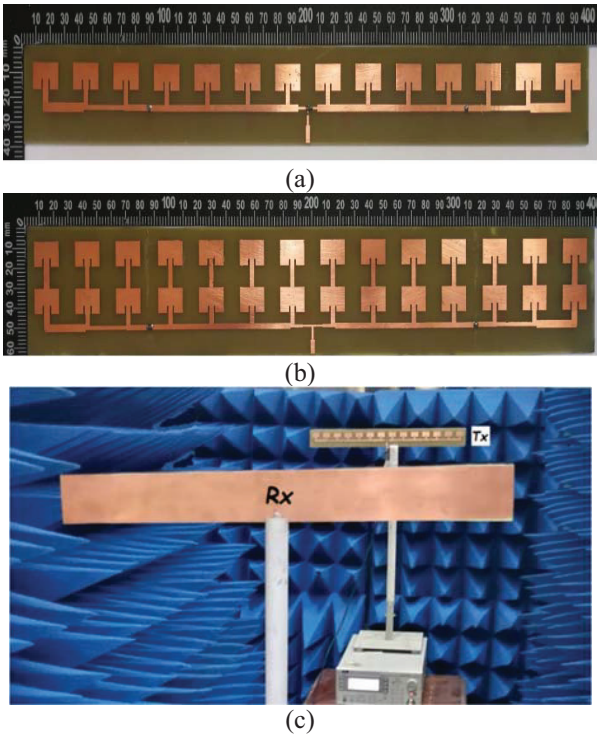

Fig. 9. Fabricated antenna arrays and experimental setup. (a) 14-elements fabricated antenna array. (b) 28-elements fabricated antenna array. (c) experimental setup.

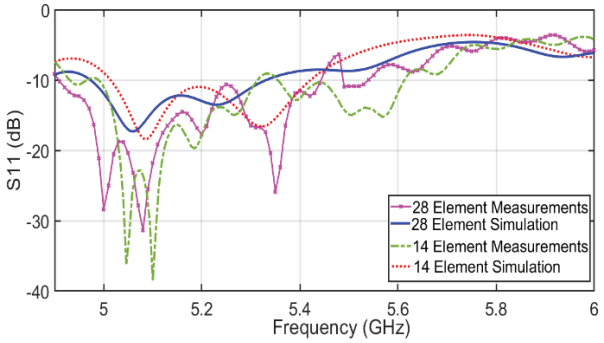

Fig. 10. Comparison of S11 results between Simulation and Measurements at C-band.

tor was calculated first and then multiplied with the radiation pattern of the single-element antenna. It is clear from Fig. 11 that a good agreement is achieved between simulated and measured results for the two proposed antenna arrays. All the obtained results are summarized in Table 5. It is clear from the table that the experimental results have the same trend as those obtained by simulation with small differences.

Finally, the differences between simulation and measurements results in Figs. 10 and 11 can be related to the assumed values of the ε_r of the substrate and the effect of non-ideal environment of the Lab. In addition, due to the toleration of manufacturing and soldering, there are some deviations between the measured and simulated data. In general, the proposed antennas have achieved the expected SLL. The differences between the theory against the simulation and measurement results can be related to the fact that the theory does not take into account the effect of mutual coupling between the elements.

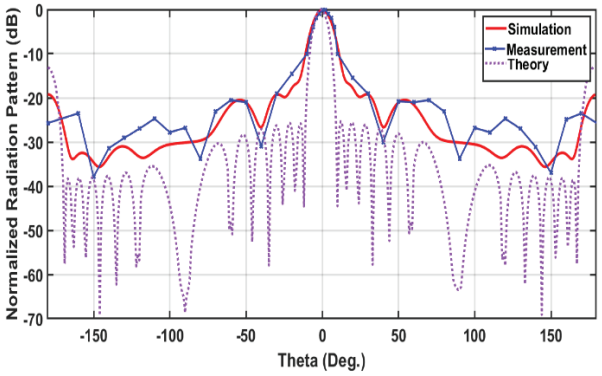

(a)

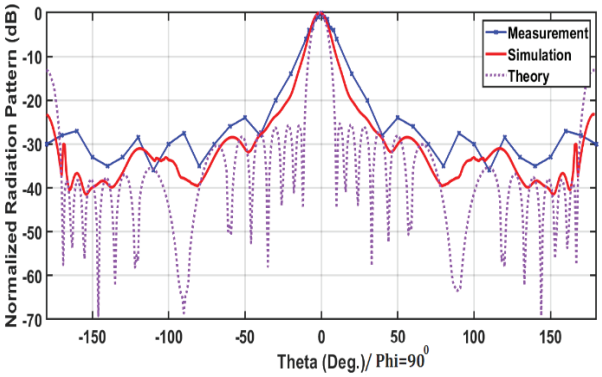

(b)

Fig. 11. Comparison of xy-plane results for the printed antenna array at 5.2 GHz. (a) 14-elements. (b) 28-elements.

Table 5: HPBW, gain and SLL of array antennas at 5.2 GHz of the simulated and measurement results

No. of Elements	HPBW (deg.) xz plane	BW (MHz)	Gain (dB)	SLL (dB)
14 Simulated	8.4	408	13.2	−20.1
14 Measured	12	318	12.1	−20
2*14 Simulated	10.8	357	17	−23.1
2*14 Measured	10	540	15.7	−24

VI. COMPARESION WITH OTHER WORKS

Table 6 shows a comparison between the obtained results of the proposed antenna arrays in this article with other works. To make a fair comparison, the performance of the antenna array was compared with other works in literature that have the same number of elements. It was observed that a good agreement with such works is obtained in terms of HPBW and SLL. However, the values of BW that are obtained in this work outperform other reported works. In addition, there are some differences in gain values, which can be related to the number of elements or to the geometry of the antenna array as shown below. Finally, the overall agreement between the obtained results and the other works validate the proposed method of applying the Chebyshev distribution with gaining the advantage of less complexity and cost.

Table 6: Comparing with results from other works

	This work Sim.	This work Sim.	This work Meas.	[10]	[14]	[11]
No. of Elements	1*10	2*14	2*14	1*10	1*10	2*16
Freq/GHz	5.2	5.2	5.2	5.8	5.5	9.35
HPBW/ 0	13.1	10.8	10	10	10.4	5.3
BW/ MHz	290	357	540	90	212	100
Gain / dB	11.4	17	15.7	—-	17.5	22
SLL / dB	−21.9	−25.6	−24	−20	−26	−26.4

By comparing the design of 10 elements with a reference [10], a good correlation was observed between the results. In [10], a symmetric 10-element antenna array with a Chebyshev tapering operating at 5.8 GHz has been designed by two methods of tapering. The first is the patch width tapering method and the second is the feed line tapering method [10]. As compared to [14], there is a difference in the results of the SLL and gain for the design of 10-element antenna array at the C-band. The difference of the gain values is due to the effect of the driven element, which is found above each element in the array reported in [14]. Whereas the difference of the SLL can be related to the methodology of the design and the type of the material (Roger RT /Duroid). The main difference between this work and [14] is the methodology of the design. Shunt stubs were added to the main feed line to achieve Chebyshev tapering with calculated values of the impedances of these stubs ranging from 45-178 Ω whereas in this work they are from 43-70 Ω. In addition, in [14] the value of the higher impedance is 178 Ω and the width of the strip line less than 0.8mm, which represent weakness when using high power. In [11] the researchers designed a 2*16-element antenna array. They used the width of the main feed line to achieve the Chebyshev distribution. They considered each junction of the feed line of the element as a tee junction then they found the s-matrix of the tee junction. Depending on the analysis of the s-matrix, they found the impedances of the main feed line. In addition, they considered the impedance value of feed lines of the elements to be equal to 100 Ω. It can be noticed that they use a $\lambda/4$ transformer after each junction. Referring to [11], the SLL results of the design of the 2*14-element antenna array is approximately equal. On the other hand, the gain values of this work are lower by 5dB. This difference in the gain values is caused by the effect of two metallic plates

bounding the antenna array in [11], which acts as a director. It is true that the gain was improved by using such a director, but this gain is at the price of complexity and reliability. Thus, careful consideration should be paid to such tradeoffs.

VII. CONCLUSION

A new method of applying Chebyshev distribution on a microstrip antenna array is produced. The method is tested by designing two sets of antenna arrays that work at the S-band and C-band respectively. As mentioned previously, the values of the impedances of the main feed line is around (43-70 Ω) which means the quarter wavelength transformers are not needed. The feed line of the proposed array is wider than the previous designs of the other researchers, which allows more power to be transmitted through it. The practical measurements show an agreement with the simulation results. The proposed antenna (2*14 Element) is suggested for radar applications.

REFERENCES

[1] ITU Recommendation V431-8, "Nomenclature of the frequency and wavelength bands wsed in telecommunications," Aug. 2015.

[2] C. A. Balanis, *Antenna Theory Analysis and Design, 3rd edition*, John Wiley & Sons, 2005.

[3] K. H. Sayidmarie and Q. H. Sultan, "Synthesis of wide beam array patterns using random phase weights," *International Conference of Electrical, Communication, Computer, Power and Control Engineering ICECCPCE*, vol. 13, pp. 52-57, Dec. 17-18, 2013.

[4] H. Luo, Y. Xiao, W. Tan, L. Gan, and H. Sun. "A W-band dual-polarization slot array antenna with low sidelobe level," *Applied Computational Electromagnetics Society (ACES) Journal*, vol. 34, pp. 1711-1718, Nov. 2019.

[5] M. R. Sarker, M. M. Islam, M. T. Alam, and M. H. E-Haider, "Side lobe level reduction in antenna array using weighting function," *International Conference on Electrical Engineering and Information & Communication Technology ICEEICT*, Bangladesh, pp. 1-5, Apr. 2014.

[6] J. R. Mohammed and K. H. Sayidmarie, "Sidelobe cancellation for uniformly excited planar array antennas by controlling the side elements," *IEEE Antennas and Wireless Propagation Letters*, vol. 13, pp. 987-990, 2014.

[7] H. Singh and S. K. Mandal, "Side lobe levels reduction in digitally optimized time modulated linear arrays using particle swarm optimization technique," *Students Conference on Engineering and Systems*, India, pp. 1-4, May 2014.

[8] E. Kurt, S. Basbu, and K. Guney, "Linear antenna array synthesis by modified seagull optimization algorithm," *Applied Computational Electromagnetics Society (ACES) Journal*, vol. 36, pp. 1552-1562, Dec. 2022.

[9] M. Hajian, J. Zijderveld, A. A. Lestari, and L. P. Ligthart, "Analysis, design and measurement of a series-fed microstrip array antenna for X-Band Indra: the indonesian maritime radar," *European Conference on Antennas and Propagation*, Berlin, Germany, pp. 1154-1157, Mar. 2009.

[10] Z. Chen and S. Otto, "A taper optimization for pattern synthesis of microstrip series-fed patch array antennas," *European Wireless Technology Conference*, Rome, Italy, Sep. 2009.

[11] F. Y. Kuo and R. B. Hwang, "High-isolation X-band marine radar antenna design," *IEEE Transactions on Antennas and Propagation*, vol. 62, no. 5, pp. 2331-2337, May 2014.

[12] M. Milijić, A. Nešić, B. Milovanović, N. Dončov, and I. Radnović, "Feeding structure influence on side lobe suppression of printed antenna array with parallel reflector," *12th International Conference on Telecommunication in Modern Satellite, Cable and Broadcasting Services (TELSIKS)*, Nis, Serbia, Oct. 2015.

[13] D. Inserra, W. Hu, and G. Wen, "Design of a microstrip series power divider for sequentially rotated nonuniform antenna array," *International Journal of Antennas and Propagation*, vol. 2017, Jan. 2017.

[14] M. T. Nguyen and V. B. Giang Truong, "A novel chebyshev series fed linear array with high gain and low sidelobe level for WLAN outdoor systems." *Applied Computational Electromagnetics Society (ACES) Journal*, vol. 34, no. 8, Aug. 2019.

Mohammed Sameer Salim was born in Mosul, Iraq in 1987. He received a B.Sc. degree in Communications Engneering in 2007, then completed his M.Sc. study in Ccommuncation Engineering at the College of Electronics Engineering, Ninevah university (2013). Currently, he works as an assistant lecturer at the same collage. His reserch interests include antenna design, antenna arrays, and wave propagation.

Tareq A. Najm was born in Mosul, Iraq, in 1984. He received B.Sc. and M.Sc. degrees from Ninevah University, Iraq in 2006 and 2013, respectively, in Communications Engineering. He has been a Lecturer at Ninevah University since 2013. His current research interests include MIMO antenna design, filter design, ultrawide band antennas (UWB), and multi-band antenna techniques.

Qusai Hadi Sultan was born in Mosul, Iraq, in 1979. He received B.Sc. and M.Sc. degrees from Mosul University, Iraq in 2007 and 2014, respectively, in Communications Engineering. He has been a Lecturer at Ninevah University since 2008. His current research interests include antenna array, reflect antenna array, fractal antenna design, and multi-band antenna techniques.

Adham Maan Saleh was born in Mosul, Iraq, in 1984. He received B.Sc. and M.Sc. degrees from Ninevah University, Iraq in 2006 and 2012, respectively, all in Communication Engineering. After that, he received a Ph.D. degree from the University of Bradford, West Yorkshire, UK, in 2020 in Antennas Engineering He has been a Lecturer at Ninevah University since 2012. His current research interests include MIMO antenna design, defected ground structures (DGS), neutralization techniques, reflectarray antennas, and multiband antennas techniques.

Reduction of Random Variables in EMC Uncertainty Simulation Model

Jinjun Bai[1], Yixuan Wan[1], Ming Li[2], Gang Zhang[3], and Xin He[3]

[1]Department of Electrical Engineering
Dalian Maritime University, Dalian, 116026, China
baijinjun@dlmu.edu.cn, wanyixuan90@163.com

[2]Aviation Industry Corporation of China (AVIC)
AVIC Aero Polytechnol Estab, Beijing 100028, Peoples R China
liming_mse_buaa@163.com

[3]Harbin Inst Technol, Sch Elect Engn & Automat
Harbin Institute of Technology,Harbin 150001, Peoples R China
zhang_hit@hit.edu.cn,19s106116@stu.hit.edu.cn

Abstract **–** To improve the reliability of simulation results, uncertainty analysis methods were developed in the Electromagnetic Compatibility (EMC) field. Random variables are used to describe random events. The more random variables you have, the less efficient the simulation is. Therefore, many high-accuracy methods have the problem of dimensional disaster, which means the calculation efficiency decreases exponentially with the increase of the number of random variables. A random variable reduction strategy based on sensitivity analysis method is proposed in this paper, so as to improve the computational efficiency of the global uncertainty analysis method.

Index Terms **–** dimensional disaster, electromagnetic compatibility, random variable, sensitivity analysis method, uncertainty analysis method.

I. INTRODUCTION

To describe random events and unknown parameters in a practical engineering environment, the uncertainty analysis method is becoming popular in the EMC field. The random variable model is used to describe the actual uncertainty factors instead of the deterministic values.

Uncertainty analysis methods can be divided into two categories. In one class, some of the methods need to change the original solver, such as the Perturbation Method [1], the Stochastic Galerkin Method [2, 3], and the Stochastic Testing Method [4]. In general, to describe complex electromagnetic compatibility problems in practical engineering environment, the finite element analysis method is used to construct model parameters, and then commercial simulation software is needed. The software is not open source, and cannot change the original internal solver. Therefore, this class of uncertainty analysis method is not competitive in the EMC field.

Another class of methods does not need to change solver, represented by the Monte Carlo Method [5, 6], the Stochastic Reduced Order Models [7], the Moment Method [8], and the Stochastic Collocation Method (SCM) [9, 10]. They are suitable for different EMC simulation situations. The Monte Carlo Method has high accuracy and low computational efficiency. It is suitable for uncertainty analysis with a short simulation time. For complex problems, it will lose competitiveness because of its low computational efficiency. The advantage of the Stochastic Reduced Order Models and the Moment Method is high computational efficiency. However, in most cases, their accuracy is not as good as other methods. The Stochastic Reduced Order Models have low accuracy due to the lack of an appropriate convergence criterion. The Moment Method assumes that the simulation input and simulation output are linear, which leads to its low accuracy. The advantages of the SCM combine computational efficiency and accuracy, but it is trapped in the problem of dimension disaster. This means that the number of collocation points increases exponentially with the number of random variables. Many scholars have improved the SCM to alleviate the dimension disaster problem slightly [11]. To completely solve this problem, it is still necessary to fundamentally reduce the number of random variables.

Based on the thoughts of the Moment Method, this paper proposes a fast sensitivity calculation method, which directly transfers the random variables with low sensitivity to the average values. It can be predicted that the longer single EMC simulation time, the more

Submitted On: December 13, 2021
Accepted On: August 13, 2022

https://doi.org/10.13052/2022.ACES.J.370903

significant the improvement of computing efficiency will be.

II. SENSITIVITY ANALYSIS BASED ON THE RICHARDSON EXTRAPOLATION METHOD

When the EMC simulation model is in the form of random variables, the output will present uncertainty. The contribution of each random variable to the uncertainty of simulation output is different. If the contribution can be expressed quantitatively, the random variable with a smaller contribution can be replaced by its average value, so as to achieve the reduction of the random variables.

The contribution can be described by means of sensitivity analysis, while all uncertainty analysis methods can realize sensitivity analysis by calculating standard deviation. It should be noted that the sensitivity analysis method proposed in this paper is a pre-processing step of the uncertainty analysis method, so its solving speed must be far better than that of the uncertainty analysis method, otherwise, the reduction of random variables will be meaningless.

In the Moment Method, the sensitivity analysis of each random variable is used to estimate variance values. The sensitivity calculation process is shown below:

$$\begin{aligned} S(i) &= \frac{dy_\xi}{d\xi_i} \\ &= \frac{U_{EMC}\left(\overline{\xi_1},\cdots,\overline{\xi_i}+\delta_i,\cdots,\overline{\xi_n}\right)}{\delta_i} \\ &\quad - \frac{U_{EMC}\left(\overline{\xi_1},\cdots,\overline{\xi_i},\cdots,\overline{\xi_n}\right)}{\delta_i}. \end{aligned} \tag{1}$$

Among them, $\overline{\xi_i}$ represents the mean value of random variable ξ_i, and $U_{EMC}\left(\overline{\xi_1},\cdots,\overline{\xi_i},\cdots,\overline{\xi_n}\right)$ represents the EMC simulation result at a certain point $(\overline{\xi_1},\overline{\xi_i},\cdots,\overline{\xi_n})$. δ_i is a small perturbation, and S(i) is the sensitivity analysis result corresponding to random variable ξ_i. Its principle is to transform the differential formula into a difference formula.

The selection of perturbation is based on the uniform distribution. Suppose that the uncertainty parameter is $k(\xi_i) = A + B \times \xi_i$, where ξ_i is the uniform distribution variable of the interval [-1,1] . In this case, the perturbation is $\delta_i = \frac{B}{A}$. However, not all uncertain parameters are in the form of uniform distribution, thus it is necessary to convert them into an equivalent uniform distribution. It is assumed that the mean value of uncertain parameters is k_M, the variance of that is k_σ. The equation can be converted as follow:

$$\begin{cases} k_M = A \\ k_\sigma = \frac{1}{3}B^2. \end{cases} \tag{2}$$

Therefore, the perturbation is $\delta_i = \frac{\sqrt{3k_\sigma}}{k_M}$.

Reference [8] mentions that the Moment Method does not achieve very good accuracy, which is mainly due to the following two reasons. On one hand, the Moment Method assumes that the input and output are in a linear relationship, which leads to calculation error of sensitivity S(i) in formula (1). On the other hand, this formula only considers the disturbance quantity when it is greater than the average value, the sensitivity estimated does not represent the whole situation at this time. To solve this nonlinear problem, the Richardson extrapolation method is proposed to improve the different processes in formula (1), as shown below:

$$\begin{aligned} IS_{pos}(i) &= \frac{dy_\xi}{d\xi_i} \\ &= 2 \times \frac{U_{EMC}\left(\overline{\xi_1},\cdots,\overline{\xi_i}+\frac{\delta_i}{2},\cdots,\overline{\xi_n}\right)}{\frac{\delta_i}{2}} \\ &\quad - 2 \times \frac{U_{EMC}\left(\overline{\xi_1},\cdots,\overline{\xi_i},\cdots,\overline{\xi_n}\right)}{\frac{\delta_i}{2}} \\ &\quad - \frac{U_{EMC}\left(\overline{\xi_1},\cdots,\overline{\xi_i}+\delta_i,\cdots,\overline{\xi_n}\right)}{\delta_i} \\ &\quad + \frac{U_{EMC}\left(\overline{\xi_1},\cdots,\overline{\xi_i},\cdots,\overline{\xi_n}\right)}{\delta_i}, \end{aligned} \tag{3}$$

$$\begin{aligned} IS_{neg}(i) &= \frac{dy_\xi}{d\xi_i} \\ &= 2 \times \frac{U_{EMC}\left(\overline{\xi_1},\cdots,\overline{\xi_i}-\frac{\delta_i}{2},\cdots,\overline{\xi_n}\right)}{\frac{\delta_i}{2}} \\ &\quad - 2 \times \frac{U_{EMC}\left(\overline{\xi_1},\cdots,\overline{\xi_i},\cdots,\overline{\xi_n}\right)}{\frac{\delta_i}{2}} \\ &\quad - \frac{U_{EMC}\left(\overline{\xi_1},\cdots,\overline{\xi_i}-\delta_i,\cdots,\overline{\xi_n}\right)}{\delta_i} \\ &\quad + \frac{U_{EMC}\left(\overline{\xi_1},\cdots,\overline{\xi_i},\cdots,\overline{\xi_n}\right)}{\delta_i}. \end{aligned} \tag{4}$$

The proposed algorithm considers both sides, that is, there are positive sensitivity $IS_{pos}(i)$ and negative sensitivity $IS_{neg}(i)$. The mathematical derivation of the

Richardson extrapolation method is as follows. The complete calculation formula corresponding to formula (1) is:

$$\frac{dy_\xi}{d\xi_i} = \frac{U_{EMC}\left(\overline{\xi_1},\cdots,\overline{\xi_i}+\delta_i,\cdots,\overline{\xi_n}\right)}{\delta_i} - \frac{U_{EMC}\left(\overline{\xi_1},\cdots,\overline{\xi_i},\cdots,\overline{\xi_n}\right)}{\delta_i} - \frac{\delta_i}{2}\times y''_\xi + o(\delta_i). \tag{5}$$

When using formula (1) to calculate sensitivity, the error is $\frac{\delta_i}{2}\times y''_\xi$.

By changing the perturbation in formula (5) into $\frac{\delta_i}{2}$, formula (6) can be obtained:

$$\frac{dy_\xi}{d\xi_i} = \frac{U_{EMC}\left(\overline{\xi_1},\cdots,\overline{\xi_i}+\frac{\delta_i}{2},\cdots,\overline{\xi_n}\right)}{\frac{\delta_i}{2}} - \frac{U_{EMC}\left(\overline{\xi_1},\cdots,\overline{\xi_i},\cdots,\overline{\xi_n}\right)}{\frac{\delta_i}{2}} - \frac{\delta_i}{4}\times y''_\xi + o(\delta_i). \tag{6}$$

Multiplying formula (6) by 2 and subtracting formula (5), formula (7) is presented:

$$\frac{dy_\xi}{d\xi_i} = 2\times\frac{U_{EMC}\left(\overline{\xi_1},\cdots,\overline{\xi_i}+\frac{\delta_i}{2},\cdots,\overline{\xi_n}\right)}{\frac{\delta_i}{2}} - 2\times\frac{U_{EMC}\left(\overline{\xi_1},\cdots,\overline{\xi_i},\cdots,\overline{\xi_n}\right)}{\frac{\delta_i}{2}} - \frac{U_{EMC}\left(\overline{\xi_1},\cdots,\overline{\xi_i}+\delta_i,\cdots,\overline{\xi_n}\right)}{\delta_i} + \frac{U_{EMC}\left(\overline{\xi_1},\cdots,\overline{\xi_i},\cdots,\overline{\xi_n}\right)}{\delta_i} + o(\delta_i). \tag{7}$$

By means of approximation, formula (3) results. Similarly, negative sensitivity shown in formula (4) can also be derived. Obviously, the approximate error is $o(\delta_i)$, which is better than $\frac{\delta_i}{2}\times y''_\xi$ in formula (5).

A comprehensive index of both sides can be obtained by adding absolute values directly.

$$IS(i) = \left|IS_{pos}(i)\right| + \left|IS_{neg}(i)\right|. \tag{8}$$

The contribution of each random variable is represented by the percentage as follow:

$$P(i) = \frac{IS(i)}{\sum_{i=1}^{N} IS(i)}. \tag{9}$$

III. ALGORITHM VALIDATION

This section presents a benchmark calculating example in [10] to verify the accuracy of random variable reduction algorithm. It is a crosstalk simulation example with 6 uncertain parameters shown in Fig. 1. There is crosstalk source voltage $U_m(\xi)$, the height of two parallel cables $h_1(\xi)$ and $h_2(\xi)$, length of parallel cables $l(\xi)$, resistance value at load side $R_1(\xi)$ and $R_2(\xi)$.

$$U_m(\xi) = 1.05 + 0.05\times\xi_1 \text{ V}, \tag{10}$$
$$h_1(\xi) = 0.04\times(1.1+0.1\times\xi_2)\text{ m}, \tag{11}$$
$$h_2(\xi) = 0.03\times(1.15+0.15\times\xi_3)\text{ m}, \tag{12}$$
$$l(\xi) = 1.1+0.1\times\xi_4\text{ m}, \tag{13}$$
$$R_1(\xi) = 50\times(1.05+0.05\times\xi_5)\,\Omega, \tag{14}$$
$$R_2(\xi) = 50\times(1.04+0.04\times\xi_6)\,\Omega. \tag{15}$$

Among them,ξ_1, ξ_2, ξ_3, ξ_4, ξ_5 and ξ_6 are all uniform distribution random variables in the interval [-1,1]. The horizontal distance between the two cables is 0.05m, and the frequency of crosstalk results is in 50MHz. The other detailed information of the model is completely consistent with reference [10].

Table 1 shows the sensitivity calculation results of the random variables. It can be seen that the sum weight of the random variables ξ_5 and ξ_6 is only 1.7%, thus the average values can be adopted to replace them, as shown below.

$$R_1(\xi_5=0) = 50\times1.05 = 52.5\Omega, \tag{16}$$
$$R_2(\xi_6=0) = 50\times1.04 = 52\Omega. \tag{17}$$

In this case, there are only four random variables left in the simplified EMC model.

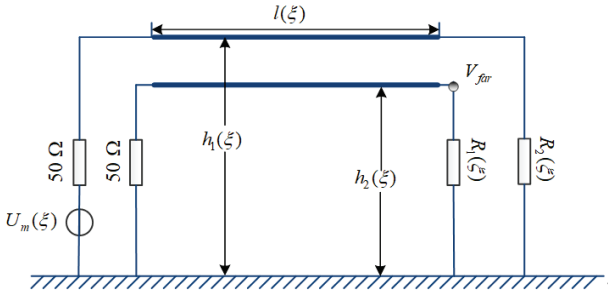

Fig. 1. Benchmark calculating example in [10].

Table 1: Sensitivity analysis results of random variables

Variable	Sensitivity
ξ_1	22%
ξ_2	16.9%
ξ_3	24.3%
ξ_4	35.1%
ξ_5	1%
ξ_6	0.7%

Taking the SCM as an example, the uncertainty analysis results of voltage crosstalk in load side are calculated in both original model and simplified model respectively. According to the SCM, uniform distribution random variable in the interval [-1,1] is corresponding to the Legende orthogonal polynomial. If the probability density function is arbitrary, the chaotic polynomial form can be obtained by the three-term polynomial recursive formula in the Stieltjes Procedure. For details, please refer to literature [12].

Zero points of the 7th-order Legendre orthogonal polynomial are considered as the collocation points, they are shown as follows.

$$P_{\xi_i} = \{0.9491, 0.7415, 0.4058, 0, \\ -0.4058, -0.7415, -0.9491\}. \tag{18}$$

In multiple random variables situation, the selection of collocation points takes the form of tensor product:

$$P_{\xi_i} \otimes P_{\xi_i} \otimes P_{\xi_i} \otimes P_{\xi_i} \otimes P_{\xi_i} \otimes P_{\xi_i}. \tag{19}$$

Multivariate Lagrange interpolation at the collocation points is implemented, the result in the form of random variables polynomial will be obtained.Through statistical sampling, the final uncertainty analysis results can be got, such as expectation, standard deviation and probability density curve.

Figures 2 and 3 show the Probability Distribution Function (PDF) results and the Cumulative Distribution Function (CDF) results of crosstalk voltage values respectively. The results of 4-variables model and original model variables model are given at the same time. It is clearly seen that two curves are almost exactly the same in both Figs. 2 and 3, and it means that the reduction has no impact on accuracy. For quantitative comparison, the mean value calculated by original model is 0.01506 V, and the standard deviation is 9.8058×10^{-4} V. For 4-variables model, the mean value is 0.01506 V and the standard deviation is 9.7870×10^{-4} V.

The Mean Equivalent Area Method (MEAM) is a validity evaluation method of uncertainty analysis results. The MEAM can evaluate the accuracy of simulation results by quantifying the similarity between simulation results and standard data. When the MEAM value of the simulation result is better than 0.95, its accuracy is considered "Excellent" [13]. For random variable reduction problem in this paper, the uncertainty analysis results of the original model are taken as the standard data, and the uncertainty analysis results of 4-variables model must be at the level of "Excellent", so that the reduction is meaningful. In Figs. 2 and 3, the MEAM value of 4-variables model is 0.9981, which proves that the effect of reduction is good.

According to the generalized polynomial chaos theory [4], the original model requires the number of deterministic simulations is $7^6 = 117649$. As a comparison, the number of pre-processing simulations in 4-variables model is $4 \times 6 + 1 = 25$, that of deterministic simulations is $7^4 = 2401$ Thus, in 4-variables model, a total of 2426 deterministic simulations are required. It means that the calculation amount of 4-variables model is only 2% of that of the original model. It is worth noting that the longer the single simulation time, the better the improvement of computational efficiency.

In summary, by comparing the required single simulation times, it is verified that the proposed reduction method in this paper improves the efficiency of the uncertainty analysis method. The validity of the reduction method is verified by comparing the expected value, standard deviation and MEAM value. Thus, it is proved that the reduction method can alleviate the dimension disaster of the SCM to some extent.

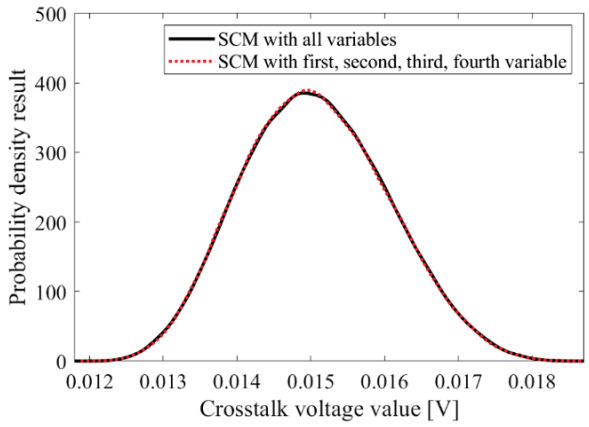

Fig. 2. PDF results of 4-variables model.

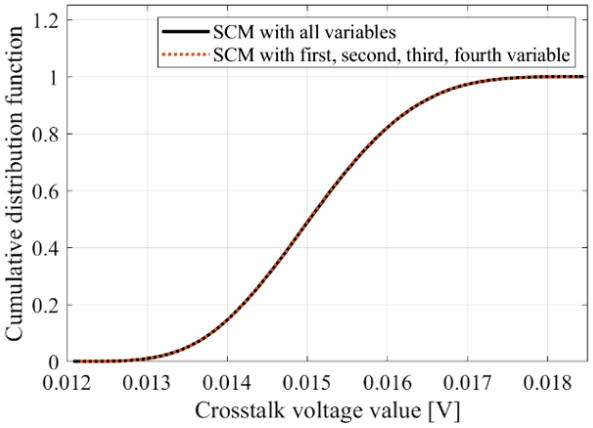

Fig. 3. CDF results of 4-variables model.

IV. DISCUSSION OF THE WEIGHT THRESHOLD

In Table 1, the percentage of ξ_5 and ξ_6 is small, so they can obviously be reduced. The effectiveness of reduction has been proved in Section III. If another random variable is reduced too, the computational efficiency will inevitably increase, but with the risk of accuracy decline. In this section, the weight threshold of percentage sum of retained random variables is quantitatively determined. As shown in Table 1, the percentage of ξ_1 and ξ_2 is the next smallest, two new simplified models are proposed. One is with the random variables ξ_1, ξ_3 and ξ_4. The other is with ξ_2, ξ_3 and ξ_4.

Figures 4 and 5 show PDF results and CDF results under random variables ξ_1, ξ_3 and ξ_4. The mean value of the result is 0.01507 V, and the standard deviation of that is 9.2107×10^{-4} V. The MEAM value is 0.9393, which is less than 0.95, but still in the acceptable range.

Figures 6 and 7 show PDF results and CDF results in random variables ξ_2, ξ_3 and ξ_4. The mean value of this model is 0.01507 V, and the standard deviation is

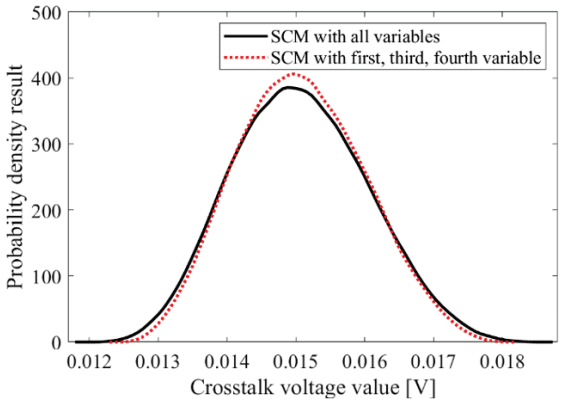

Fig. 4. PDF results of the model with ξ_1, ξ_3 and ξ_4.

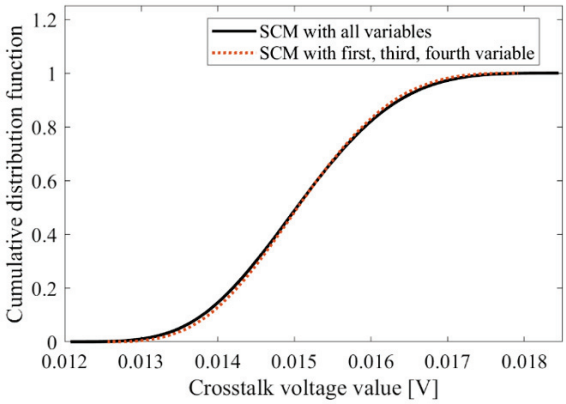

Fig. 5. CDF results of the model with ξ_1, ξ_3 and ξ_4.

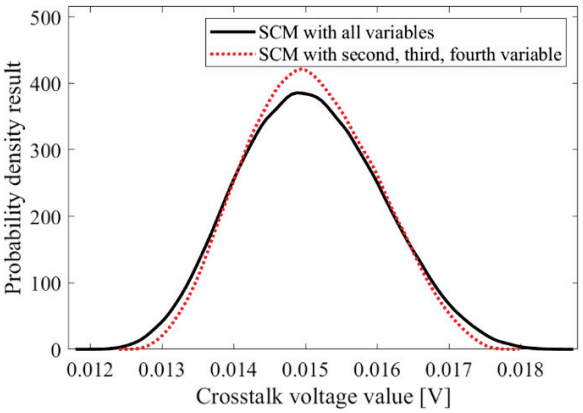

Fig. 6. PDF results of the model with ξ_2, ξ_3 and ξ_4.

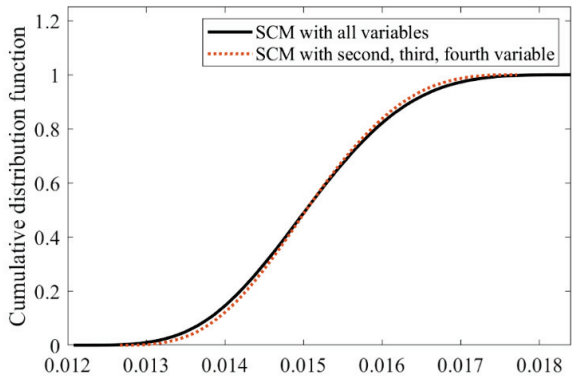

Fig. 7. CDF results of the model with ξ_2, ξ_3 and ξ_4.

8.8981×10^{-4} V. The MEAM value is 0.9074, which has a gap of 0.95. In this case, the error of reduction is identified as large, so it is not acceptable.

After quantitative comparison of these two simplified models, the former one is barely acceptable, while the latter one is unacceptable. The weight threshold of them is 22% + 24.3% + 35.1% = 81.4% and 16.9% + 24.3% + 35.1% = 76.3%. It can be seen that when the weight threshold is below 85%, the uncertainty analysis results of the reduction model are not satisfactory. To ensure, it is better to set the weight threshold within the range of 90% to 95% in practical application, so as to ensure that the MEAM value can be maintained above 0.95, in an "Excellent" level.

V. CONCLUSION

Based on the Richardson extrapolation method, a sensitivity analysis method to evaluate the contribution of random variables is proposed to improve the EMC uncertainty simulation computational efficiency. The effectiveness of the proposed reduction method is verified by using a benchmark simulation example. On

the premise of maintaining the original accuracy, the proposed method greatly improves the computational efficiency of the SCM, and the time required is only 2% of the previous time. It is proved that the reduction strategy can alleviate the dimension disaster problem of the SCM to a certain extent. Finally, through quantitative calculation by using the MEAM, it is determined that from 90% to 95% is a reasonable selection range of weight threshold.

REFERENCES

[1] Y. Zhang, C. Liao, R. Huan, Y. Shang, and H. Zhou, "Analysis of nonuniform transmission lines with a perturbation technique in time domain," *IEEE Transactions on Electromagnetic Compatibility*, vol. 62, no. 2, pp. 542-548, 2020.

[2] P. Manfredi, D. Ginste, I. Stievano, D. De Zutter, and F. Canavero, "Stochastic transmission line analysis via polynomial chaos methods: An overview," *IEEE Electromagnetic Compatibility Magazine*, vol. 6, no. 3, pp. 77-84, 2017.

[3] P. Manfredi, D. Vande. Ginste, D. De Zutter, and F. G. Canavero, "Generalized decoupled polynomial chaos for nonlinear circuits with many random parameters," *IEEE Microwave & Wireless Components Letters*, vol. 25, no. 8, pp. 505-507, 2015.

[4] Z. Zhang, T. A. EI-Moselhy, I. M. Elfadel, and L. Daniel, "Stochastic testing method for transistor-level uncertainty quantification based on generalized polynomial chaos," *IEEE Transactions on Computer-Aided Design of Integrated Circuits and Systems*, vol. 32, no. 10, pp. 1533-1545, 2013.

[5] S. A. Pignari, G. Spadacini, and F. Grassi, "Modeling field-to-wire coupling in random bundles of wires," *IEEE Electromagnetic Compatibility Magazine*, vol. 6, no. 3, pp. 85-90, 2017.

[6] H. Xie, J. F. Dawson, J. Yan, A. C. Marvin, and M. P. Robinson, "Numerical and analytical analysis of stochastic electromagnetic fields coupling to a printed circuit board trace," *IEEE Transactions on Electromagnetic Compatibility*, vol. 62, no. 4, pp. 1128-1135, 2020.

[7] Z. Fei, Y. Huang, J. Zhou, and Q. Xu, "Uncertainty quantification of crosstalk using stochastic reduced order models," *IEEE Transactions on Electromagnetic Compatibility*, vol. 59, no. 1, pp. 228-239, 2016.

[8] R. S. Edwards, A. C. Marvin, and S. J. Porter, "Uncertainty analyses in the finite difference time domain method," *IEEE Transactions on Electromagnetic Compatibility*, vol. 52, no. 1, pp. 155-163, 2010.

[9] T. Wang, Y. Gao. L. Gao, C. Liu, J. X. Wang, and Z. Y. An, "Statistical analysis of crosstalk for automotive wiring harness via the polynomial chaos method," *Journal of the Balkan Tribological Association*, vol. 22, no. 2, pp. 1503-1517, 2016.

[10] J. Bai, G. Zhang, D. Wang, A. P. Duffy, and L.Wang, "Performance comparison of the sgm and the scm in emc simulation," *IEEE Transactions on Electromagnetic Compatibility*, vol. 58, no. 6, pp. 1739-1746, Apr. 2016.

[11] J. Bai, G. Zhang, A. P. Duffy, and L. Wang, "Dimension-reduced sparse grid strategy for a stochastic collocation method in emc software," *IEEE Transactions on Electromagnetic Compatibility*, vol. 60, no. 1, pp. 218-224, 2018.

[12] D. Xiu, E. Karniadakis, and George, "The wiener-askey polynomial chaos for stochastic differential equations," *SIAM Journal on Scientific Computing*, vol. 24, no. 2, pp. 619-644, 2002.

[13] J. Bai, L. Wang, D. Wang, A. P. Duffy, and G. Zhang, "Validity evaluation of the uncertain emc simulation results," *IEEE Transactions on Electromagnetic Compatibility*, vol. 59, no. 3, pp. 797-804, Jun. 2017.

Jinjun Bai received his B.Eng. degree in Electrical Engineering and Automation in 2013, and a Ph.D. degree in electrical engineering in 2019 from the Harbin Institute of Technology, Harbin, China.

He is now a lecturer at Dalian Maritime University. His research interests include uncertainty analysis methods in EMC simulation, EMC problem of electric vehicles, and the validation of CEM.

Yixuan Wan is working toward a Master's Degree in Electrical Engineering. Her current research on simulation of electromagnetic radiation is related to electric vehicles. She is now engaged in electric vehicle cable harness crosstalk simulation.

Ming Li was born in Tai'an, China, in 1982. He received B.Sc. and Ph.D.degrees from Beihang University, Beijng, China, in 2004 and 2010, respectively. He is currently a senior engineer at AVIC Aero Polytechnology Establishment, Beijing, China. His research interests include equipment environmental effects analysis and simulation.

Gang Zhang was born in Tai'an, China, in 1984. He received a B.Sc. in Electrical Engineering from China University of Petroleum, Dongying, China, in 2007, and M.Sc. and Ph.D. degrees in Electrical Engineering from Harbin Institute of Technology (HIT), Harbin, China, in 2009 and 2014, respectively.

He is currently an Associate Professor in electrical engineering at Harbin Institute of Technology, Harbin, China, and a Visiting Professor at University of L'Aquila, L'Aquila, Italy. His research interests include electrical contact theory, uncertainty analysis of electromagnetic compatibility, and the validation of CEM.

Xin He was born in Wenshan, China, in 1996. He received B.S. and M.Sc. degrees in Electrical Engineering from Harbin Institute of Technology, China, in 2019 and 2021, respectively, where he is currently pursuing a Ph.D. degree. His research interests include cable fault detection and location, and finite element simulation.

Parametric Modeling and Optimization of Switched Reluctance Motor for EV

Lijun Liu[1,2], Yu Huang[2], Mingwei Zhao[1,2*], and Yi Ruan[1]

[1]School of Electromechanical Engineering and Automation
Shanghai University, Shanghai, 200444, China
xznu_llj@163.com, xznu_zmw@163.com

[2]School of Electrical Engineering and Automation
Jiangsu Normal University, Xuzhou, 221116, China
1819931958@qq.com, yraun@mail.shu.edu.cn

Abstract – To meet the high- performance requirements of new energy vehicle drive, the optimization design of 8/6 Switched Reluctance Motor is realized based on finite element parametric modeling of the motor. Firstly, the initial design of motor structure parameters is carried out based on the mathematical model of Switched Reluctance Motor, and the simulation model of the motor is built using RMxprt platform, and the debugging of the characteristics of the wide speed range of the motor is finished. Then, the parametric finite element model of the motor is generated, and the stator and rotor pole arc coefficients of the motor are selected as the optimization variables, and the multi-objective compromise optimization of the torque characteristics and efficiency of the motor is carried out by using the Quasi-Newton method weighting method. Finally, the magnetic field distribution, torque characteristics, efficiency and speed range characteristics before and after optimization are compared, proving that the optimized Switch Reluctance Motor can achieve multi-objective performance optimization. The motor designed by this modeling optimization method can improve the requirements of vehicle driving better.

Index Terms – multi-objective performance optimization, parametric finite element modeling, Switched Reluctance Motor, wide speed regulation characteristics.

I. INTRODUCTION

In order to meet the requirements of various working conditions of new energy vehicles, the drive system has higher performance requirements. Switched Reluctance Motor (SRM) has the advantages of large starting torque, wide speed range, strong load capacity, high operation efficiency and high reliability [1], making it one of the best driving options for electric vehicles. However, due to its double salient pole structure and magnetic saturation nonlinearity, the torque pulsation is large. In addition, there are still high losses such as iron core loss and copper loss, which reduce the operating efficiency of the motor [2]. Therefore, it is necessary to further improve the modeling accuracy of SRM and optimize its electromagnetic performance.

A parameter analysis model of the motor should be established first to optimize the performance of the motor drive system. Look-up data tables-based modeling of SRM was realized by Memon et.al [3], but the storage of magnetization curve data requires a lot of hardware resources. The function fitting method [4] adopted the appropriate functional analytical formula to fit or model the relationship between flux or torque, phase current, and rotor position according to the modeling accuracy in practical application, but the parameters must be optimized and determined based on the family of magnetization curves obtained from experiments and finite element analysis. In [5], SRM rapidly converged to the optimal design in different aspects such as loss, cost, and weight with the help of Magnetic Equivalent Circuit (MEC) analysis;, the MEC method was fast, but it involved the assumption of magnetic flux, so the calculation results may not be accurate. Although the computation time of Finite Element Analysis (FEA) [6] was long, it could realize higher precise multi-physical domain simulations such as electric, magnetic, and noise, and comprehensively test and optimize the performance of the motor and drive system.

In addition, the optimization of motor model parameters is one of the effective methods for realizing motor performance optimization. In [6–8], the torque ripple and efficiency optimization of SRM was realized based on the finite element method, but the power speed range was not considered. Three evaluation indexes of SRM performance for electric vehicles were proposed, and the performance of motors such as torque, copper loss, and torque ripple was optimized by a multi-objective control

Submitted On: August 20, 2022
Accepted On: October 30, 2022

https://doi.org/10.13052/2022.ACES.J.370904

strategy in [9]. However, only the influence of turn-on and turn-off Angles on performance was considered, and the influence of structural parameters of the motor on performance was not considered.

An 8/6 structure SRM model suitable for a new energy vehicle drive system is designed based on the finite element parametric modeling method in this paper. Quasi-newton method and weighting method are used to optimize the efficiency, torque, and torque ripple of the motor. The comparison of motor performance before and after optimization proves that the optimized motor model can achieve the comprehensive optimization of torque ripple, speed range, and lose efficiency.

II. MATHEMATICAL MODEL OF SRM

SRM operates on the principle of least reluctance, where the flux closes according to the magnetic circuit with the lowest reluctance [10]. Due to the non-uniform distribution of the flux at the end of the motor, the nonlinearity of the flux density, and the depth saturation of the magnetic circuit, the parameters of the flux Ψ, inductance, L and current i of the motor phase winding will change periodically with the rotor position angle θ and meet the nonlinear relationship. According to the theory of electromagnetic field, the conversion relationship between electrical, magnetic, and mechanical energy of SRM is presented [11]. It can be expressed by the following equation.

A. Circuit equation

Assuming that the four-phase structure of the motor is symmetric, the balance equation of Phase K is:

$$U_k = R_k i_k + \frac{d\Psi_k}{dt}, \tag{1}$$

where U_k, R_k, i_k, and $\Psi_k$are the applied voltage, resistance, current, and flux of the K- phase winding.

The phase inductance $L_k(i_k,\theta)$ is a function of the phase current i_k and the rotor position angle θ due to the double salient pole structure of the SRM and the saturation effect of the magnetic circuit. Ignoring the hysteresis effect, eddy current effect, and phase-phase mutual inductance of SRM, the phase winding flux $\Psi_k$is the product of phase inductance $L_k(i_k,\theta)$ and phase current i_k, and the flux equation can be obtained as:

$$\Psi_k(i_k,\theta) = L_k(i_k,\theta)i_k. \tag{2}$$

Take the derivative of the left and right sides of equation (2)and substitute it into equation (1) to get:

$$U_k = R_k i_k + i_k \frac{\partial L_k}{\partial \theta}\frac{d\theta}{dt} + (i_k \frac{\partial L_k}{\partial i_k} + L_k)\frac{di_k}{dt}. \tag{3}$$

B. Electromechanical relation equation

As a speed regulating system, the key to the control of SRD is the control of electromagnetic torque, which is the electromechanical coupling term generated by SRM through the coupling magnetic field at the mechanical port. If the influence of mutual inductance between windings is not considered, the electromagnetic torque generated by the motor when one phase works independently is:

$$T_k = \frac{\partial W(i_k,\theta)}{\partial \theta} \mid i_k = const, \tag{4}$$

where T_k is the instantaneous electromagnetic torque of one phase, and the magnetic common energy $W'(i_k,\theta)$ of the phase winding is expressed as:

$$W'(i_k,\theta) = \int_0^{ik} \Psi(i_k,\theta)di_k = \int_0^{i_k} L_k(i_k,\theta)i_k, di_k. \tag{5}$$

Substitute equation (5) into equation (4) to obtain:

$$T_k = \frac{\partial W'(i_k,\theta)}{\partial \theta}|i_k = const = \int_0^{i_k} \frac{\partial L_k(i_k,\theta)}{\partial \theta} i_k di_k. \tag{6}$$

The direction of SRM torque depends on the trend of the inductance curve, but has nothing to do with the direction of the current.

The total electromagnetic torque T_e of SRM can be obtained by:

$$T_e = \sum_{k=1}^{m} T_k. \tag{7}$$

where m is the phase number of the motor.

C. Mechanical equation

According to the relevant mechanical knowledge, the mechanical equation of the rotor can be expressed as:

$$J\frac{d\varpi}{dt} = T_e - T_L - D\varpi, \tag{8}$$

where ϖ is rotor angular velocity, and $\varpi = \frac{d\theta}{dt}$.

III. DESIGN AND ESTABLISHMENT OF SRM MODEL

In this design, the SRM rating parameters used in electric vehicles are set as shown in Table 1.

Table 1: Motor rating parameter settings

Parameter	Value	Parameter	Value
Rated speed (rpm)	1500	Rated output power (kW)	10
Voltage rating (V)	330	Operating temperature (cel)	120

A. Model parameters of motor initialization design

The selection of motor parameters is determined by the designer according to the motor performance and process production requirements, combined with their own design experience [12]. Table 2 lists the specific structural parameters of SRM.

In addition, the stator and rotor of SRM are made of silicon steel sheets laminated, and air gaps are unavoidable. Different silicon steel sheet materials have different magnetization curves, resulting in different magnetic

Table 2: SRM structural parameter

Parameter	Value	Parameter	Value
Number of stator	8	Number of rotor	6
D_{os} (Stator outer diameter) (mm)	240	D_{or} (Rotor outer diameter) (mm)	126.4
D_{is} (Stator inner diameter) (mm)	127.2	D_{ir} (Rotor inner diameter) (mm)	40
H_{cs} (Stator yoke height) (mm)	13	H_{cr} (Rotor yoke height (mm)	20
β_s (Stator pole arc) (deg)	21	β_r (Rotor pole arc) (deg)	21
Stator core length (mm)	140	Rotor core length (mm)	140
Winding turns (turns)	40	Advance conduction angle (degrees)	20
Upper and lower current (A)	80-78	Pulse width (deg)	110

load performances [13]. DW310_35 type silicon steel sheet is used in this design. Figure 1 shows its magnetization curve and the magnetic flux density B can be expressed as:

$$B = J + \mu_0 H, \tag{9}$$

where J is the magnetization strength, μ_0 is the vacuum permeability, H is the magnetic field strength.

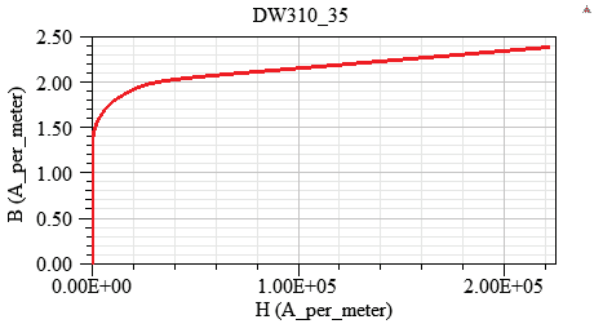

Fig. 1. Magnetization curve of silicon steel sheet DW310_35.

When the magnetic field intensity H reaches the order of 10^5, the magnetization curve enters the saturation phase. However, since the magnetic induction intensity $\mu_0 H$ in the space occupied by the medium doesn't saturate and rises slowly, the synthesized magnetization curve shows that B still increases slightly with the increase of H.

B. Establishment of SRM simulation model

After determining the parameters of each part, simulation modeling of the designed SRM is carried out as shown in Fig. 2 below.

The SRM simulation model established in RMxprt is shown in Fig. 2 (a), where the main structural parameters of the motor are marked. Figure 2 (b) is the 2D finite element model of SRM with mesh division imported into Maxwell. The rotation region and boundary of the model are respectively set, and the model is discretized by mesh division for a finite element solution.

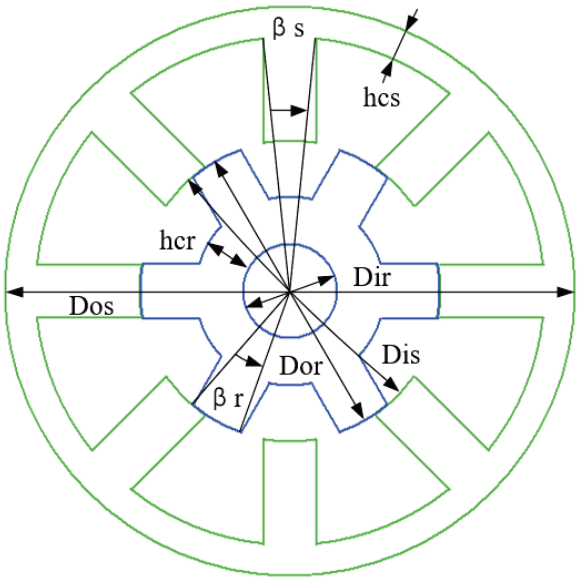

(a)

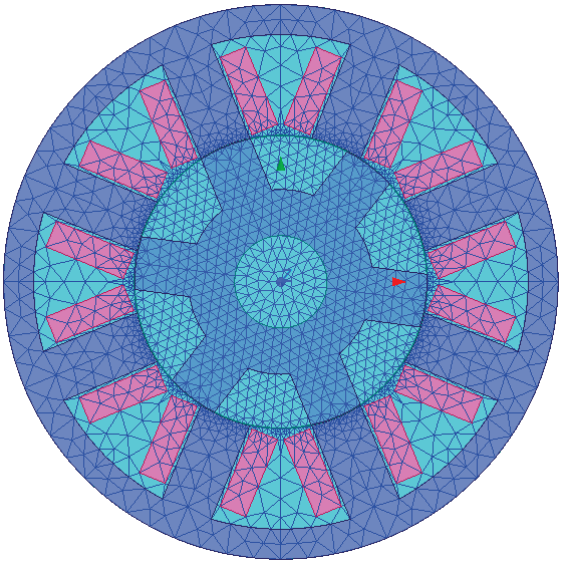

(b)

Fig. 2. Simulation model of SRM. (a) RMxprt simulation model. (b) Maxwell 2D finite element model.

IV. DEBUGGING OF SRM WIDE SPEED REGULATION CHARACTERISTICS

The speed control characteristics of SRM is shown in Fig. 3, where ω_r is the base speed of SRM and ω_{sc} is the highest speed in the constant power region [10]. Current Chopper Control (CCC) is used when the rotor angular velocity ω_r is in the range of $0 \sim \omega_b$, which makes the motor obtain the constant torque speed regulation characteristic. When ω_r is in the range of $\omega_b \sim \omega_{sc}$, SRM adopts Angle Position Control (APC), so that the motor can obtain constant power speed regulation characteristic. In addition, SRM works in series excitation characteristic when $\omega_r > \omega_{sc}$.

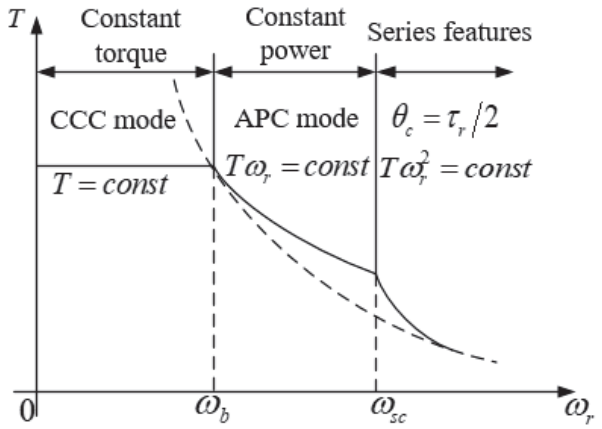

Fig. 3. Speed control characteristics of SRM.

A. Constant torque speed control characteristics below base speed ($0 < \omega_r < \omega_b$)

The rated speed of the motor is set as $\omega_b = 1500rmp$. CCC control is used and the upper and lower amplitude of the current is set to $80A$ $78A$ in the speed range of $0 < \omega_r < \omega_b$. The rated phase current and air gap inductance waveform of SRM below base speed is shown in Fig 4. The simulation results show that the output power is 9756.25 W and the rated torque is 62.1102 N.m, corresponding to excitation voltage $U_s = 330V$ and rated speed $\omega_b = 1500rmp$. The constant torque speed regulation characteristic of SRM can be achieved by maintaining. $U_s\omega_r$ during the debugging.

B. Constant power speed regulation characteristics above base speed ($\omega_b < \omega_r < \omega_{sc}$)

APC control is used above base speed, and the constant power characteristics can be achieved by adjusting the turn-on angle $\theta_{on}$and the turn-off angle θ_{off} of the switch devices. The value of ω_{sc} needs to be determined first. It can be seen from the current waveform in Fig. 4 (a) that the abscissa electrical angle of the point m1, where the phase current drops to 0A, is 156^o, and the abscissa electrical angle of the point m2, where the phase current begins to conduct in advance, is 340^o. According to the torque waveform in Fig. 4 (b), the point m3, where the inductance rises to the maximum value, corresponds to an electric angle of 181^o on the abscissa, while the point m4, where the inductance drops to 0 mH, corresponds to an electric angle of 316^o on the abscissa. The current should be turned on at the moment when the inductance is 0 mH, so that the current reaches the maximum value before the inductance rises, and it should also fall to 0A before the inductance rises to the maximum value, so as to avoid negative torque of the motor [6]. Therefore, the angle corresponding to current conduction in advance can be further advanced by 25^o, and the width of current can be further increased by 25^o.

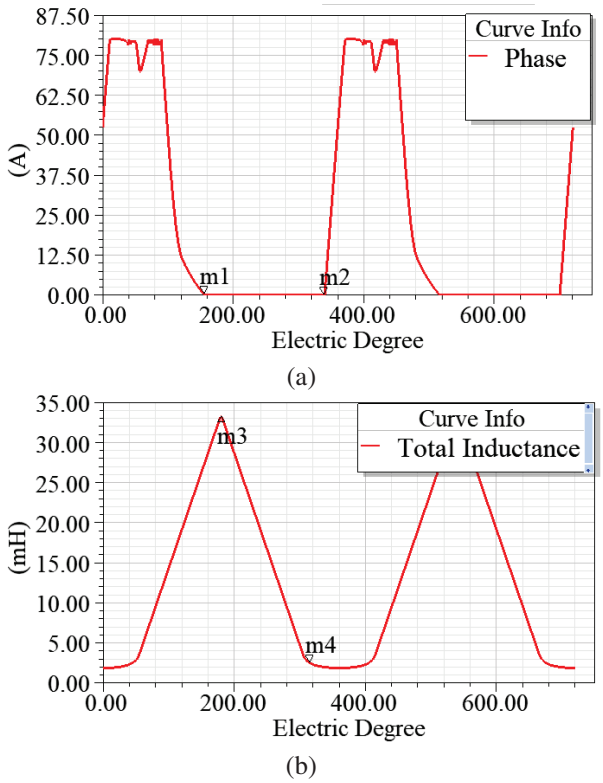

Fig. 4. Waveform of rated phase current and airgap inductance of SRM below base speed. (a) Rated current waveform of SRM below base speed. (b) Air gap inductance waveform of SRM below base speed.

According to the above conclusion, the advance conduction angle and opening width of the switch devices are adjusted accordingly. The simulation results show that, at that time of $\omega_{sc} = 6900rpm$, the output power is 9764.48 W and the output torque is 13.5136 N.m, that is, SRM can achieve the constant power operation characteristics in the wide speed regulation range of

1500rpm∼6900rpm. The phase current waveform of SRM corresponding to ω_{sc} is shown in Fig. 5.

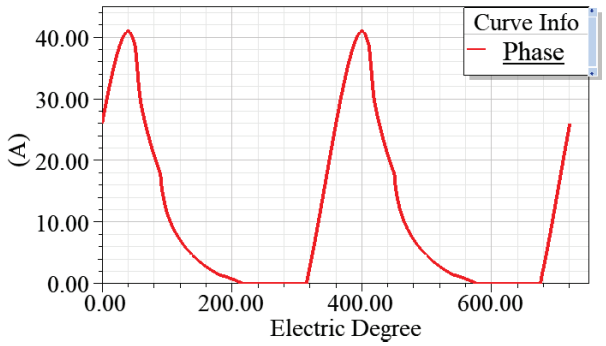

Fig. 5. Phase current waveform of SRM corresponding toω_{sc}

C. Series excitation speed regulation characteristics above base speed ($\omega_r > \omega_{sc}$)

When the motor speed $\omega_r > \omega_{sc} = 6900rpm$, the corresponding data of the speed, output power and output torque obtained from the simulation results are shown in Table 3. The output torque of SRM will decreases by ω_r^{-2} with the decrease of the speed to realize the serial-excitation operation characteristics.

Table 3: Speed and output power of SRM corresponding to $\omega_r > \omega_{sc}$

Rotor Speed	Power Output	Output Torque
7000 rpm	9618.24 W	13.1211 N.m
8000 rpm	8347 W	9.9635 N.m
9000 rpm	7370.38 W	7.82022 N.m
10000 rpm	6605.74 W	6.30801 N.m

The debugging results show that SRM can achieve constant power speed regulation in the range of the speed ω_r of 1500rpm ∼ 6900rpm above the base speed, which can reach 2∼3 times of the rated speed, and meet the performance requirements of wide speed regulation range of electric vehicle driving motor.

V. FINITE ELEMENT PARAMETERIZATION OPTIMIZATION OF SRM

The structural parameters optimal design of SRM can improve motor performance and prolong motor life. The Quasi-Newton method is used to optimize the finite element parametric model of SRM in this design. Figure 6 shows the specific optimization steps of finite element optimization.

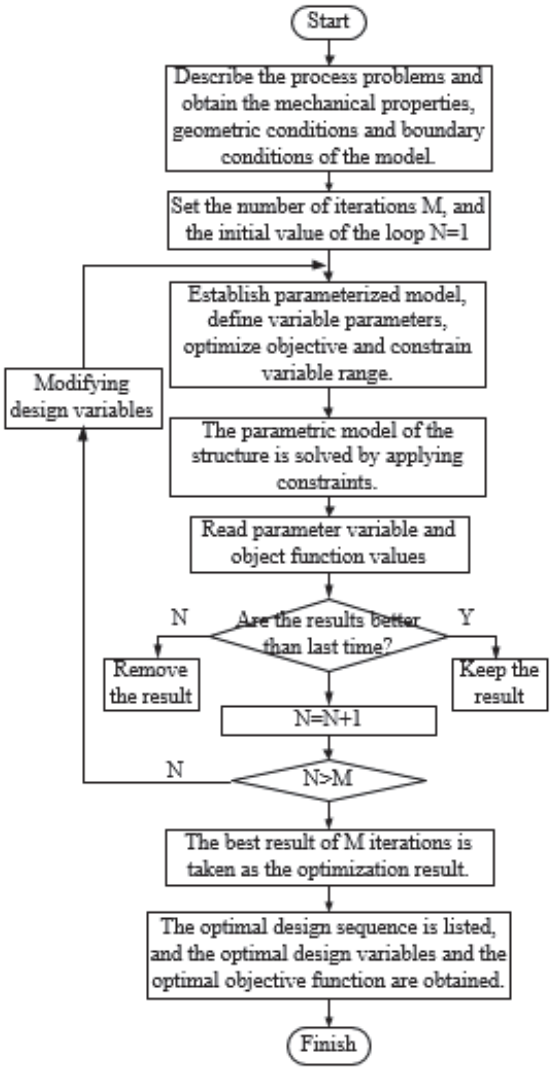

Fig. 6. Specific steps of Quasi-Newton optimization.

A. Optimization performance evaluation index of SRM

Based on the wide speed range characteristics of SRM obtained in previous section, SRM should achieve large working torque and small torque ripple as much as possible under the condition of high efficiency. The optimization performance evaluation indexes of SRM are represented by average torque, torque ripple coefficient and efficiency, which are defined as follows.

(1) Average torque

According to the principle of electromechanical conversion, the average torque T_{av} of SRM when it is in steady state operation is defined as:

$$T_{av} = \frac{1}{\theta}\sum_{k=1}^{m}\int^{(\theta_{on}+\theta_p)} T_k(\theta,i)d\theta, \qquad (10)$$

where θ_p represents the period of phase current, m represents the number of phases, and T_k represents the phase torque and θ_{on} represents the turn-on angle of the switch device. The larger T_{av} is, the higher the average torque of SRM is.

(2) Torque ripple coefficient

The torque ripple of SRM can be characterized by the torque ripple coefficient K_p and is defined as:

$$K_p = \frac{T_{max} - T_{min}}{T_{av}} \tag{11}$$

where $T_{max}$is the maxmum of torque, and $T_{min}$is the minimum of torque. The smaller K_p is, the smaller the torque ripple of SRM is.

(3) Efficiency

SRM roughly includes three kinds of losses, namely, core loss, winding copper loss, additional loss. The total loss of the motor can be obtained after each loss of the motor is solved, and then the efficiency of the motor can be judged. The efficiency of SRM can be characterized by E_i and defined as:

$$E_i = \frac{P_2}{P_2 + P_{core} + P_{Cu} + P_{fw} + P_s} = \frac{T_{av}\omega}{T_{avg}\omega + P_{total}}, \tag{12}$$

where P_2, P_{core}, P_{Cu}, P_{fw}, P_s and P_{totla} represent output power, core loss, copper loss, mechanical loss, stray loss and total loss respectively [12]. The mechanical loss P_{fw} generally includes the frictional loss and windage loss. The stray loss P_s denotes power loss in semiconductors (diodes and IGBTs), conduction, and switching losses separately [14]. The larger the evaluation index E_i is, the higher the efficiency of SRM.

B. Selection and constraints of design variables

The pole arcs of the stator and rotor of SRM are ones of the important parameters affecting the performance of the motor, the saturation degree of magnetic circuit and the mechanical strength of the rotor. Therefore, the stator pole-arc coefficient *ebs* and rotor pole-arc coefficient *ebr* of the motor are selected as the optimization design variables, which can be expressed as:

$$\begin{cases} ebs = \frac{\beta_s}{2\pi/N_s} \\ ebr = \frac{\beta_r}{2\pi/N_r}, \end{cases} \tag{13}$$

where N_s and N_r are the pole number of the stator and rotor of SRM.

In order to realize the self-starting of the motor, it is necessary to ensure that the adjacent salient poles of the stator and rotor have the overlapping regions when the salient pole axis of the stator and rotor are critically aligned [15]. The pole arcs of the stator and rotor need to meet the following condition [1]:.

$$\begin{cases} min(\beta_s, \beta_r) \geq \frac{2\pi}{mN_r} \\ \beta_s + \beta_r \leq \frac{2\pi}{N_r}. \end{cases} \tag{14}$$

Based on the mechanical design requirements of the motor and the above constraints, the pole arc coefficients ranges of stator and rotor of the four-phase 8/6 structure SRM are determined. The value ranges of the optimization design variables *ebs* and *ebr* are [0.45, 0.65] and [0.35, 0.6], respectively.

C. Torque performance optimization of SRM

ebs and *ebr* are changed to optimize the average torque and torque ripple [7]. Figure 7 shows the optimized 3D diagram of the average torque and torque ripple of SRM. According to the analysis of Fig. 7 (a) and Fig. 7 (b), when the values of *ebs* and *ebr* are 0.55 and 0.4 respectively, $maxT_{av}$ of SRM is 66.3714N.m, and the torque ripple coefficient K_p is 1.37889. When the values of *ebs* and *ebr* are 0.5 and 0.45 respectively, $minK_p$ of SRM is 1.35036, and the average torque T_{av} is 66.1522 N.m.

D. Efficiency optimization of SRM

As illustrated in Fig. 8, the efficiency of SRM varies from 84% to 89% with the increase of the optimization design variables *ebs* and *ebr*, and both *ebs* and *ebr* have a great influence on the motor efficiency. As can be seen from Fig. 8 (a), with the increase of the rotor pole arc coefficient *ebr*, the efficiency E_i of SRM increases first and then decreases. When *ebr* is 0.55, $maxE_i$ = 0.895. It can be seen from Fig. 8 (b) that the efficiency increases with the increase of the stator pole-arc coefficient *ebs*.

ebs and *ebr* are changed to optimize motor efficiency. Figure 9 shows the optimized 3D diagram of the efficiency of SRM. When *ebs* and *ebr* are 0.55 and 0.5 respectively, $maxE_i$ of SRM is 89.66%.

E. Multi-objective optimization of SRM

From the results of single objective optimization, the pole-arc coefficients of the stator and rotor have different optimal values respectively, which make the efficiency and average torque maximum and the torque ripple coefficient minimum. Therefore, a multi-objective optimization function is proposed in this paper, which is defined by using three weight factors and three base values. When the multi-objective function is maximized, an appropriate tradeoff among efficiency, average torque, and torque ripple coefficient can be obtained. The multi-objective optimization function can be expressed as:

$$W = \omega_E \frac{E_i}{E_b} + \omega_T \frac{T_{av}}{T_b} + \omega_k \frac{1}{K_p K_b}, \tag{15}$$

$$T_b = maxTav, \tag{16}$$

$$K_b = max1/Kp, \tag{17}$$

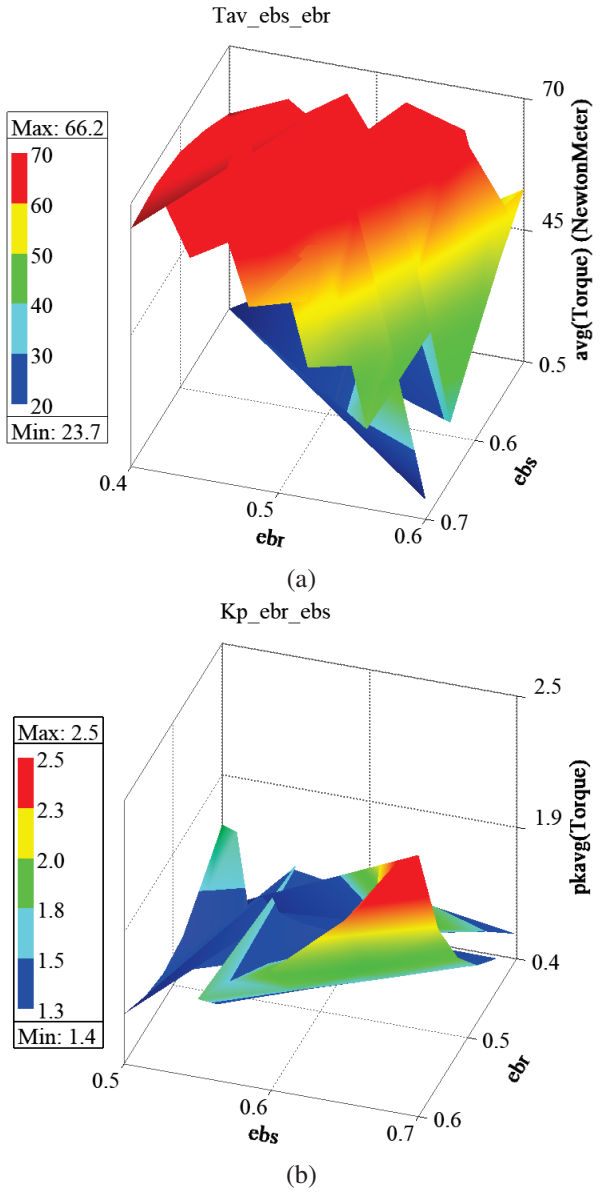

Fig. 7. Optimized 3D diagram of average torque and torque ripple. (a) Optimized 3D diagram of the average torque. (b) Optimized 3D diagram of torque ripple.

$$E_b = maxE_i, \tag{18}$$

$$\omega_T + \omega_k + \omega_E = 1, \tag{19}$$

where, W is the designed multi-objective function, ω_T,ω_K and ω_E are the weighting factors of average torque, torque ripple coefficient and efficiency respectively, whose values are 0.4, 0.4 and 0.2. T_b, K_b, and E_b are the base values of average torque, torque ripple coefficient, and efficiency respectively, and are the maximum values determined by single objective optimization.

According to the multi-objective optimization curve family in Fig. 10, when the values of *ebs* and *ebr* are

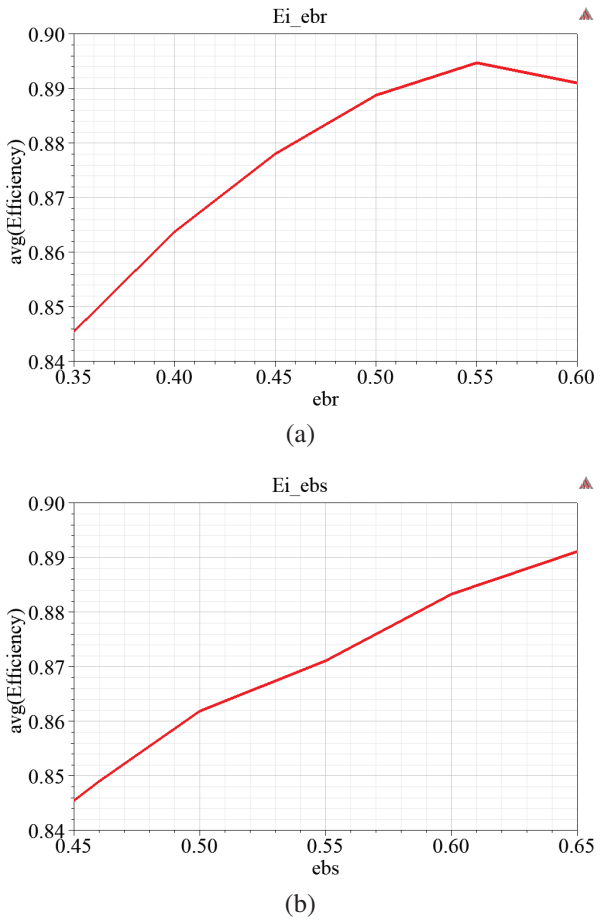

Fig. 8. Curve family of E_i as a function of optimization variables. (a) Curve of E_i as a function of *ebr*. (b) Curve of E_i as a function of *ebs*.

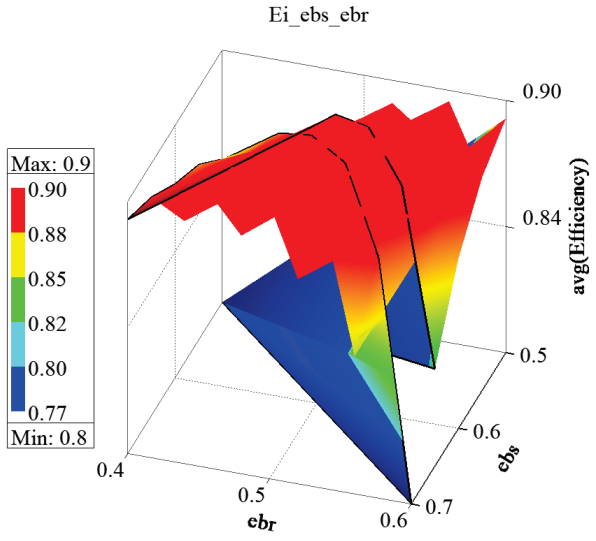

Fig. 9. Optimized 3D diagram of E_i.

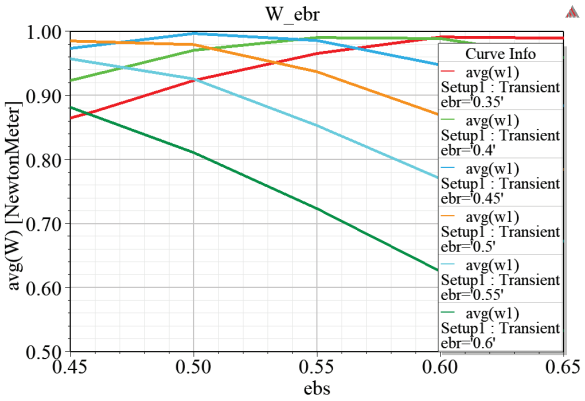

Fig. 10. Multi-objective optimization curve family of SRM.

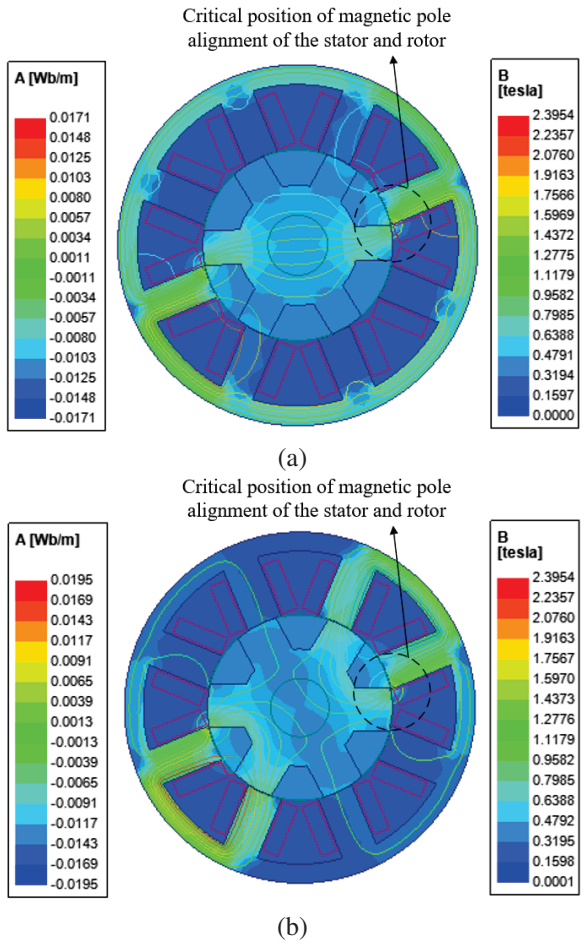

Fig. 11. Comparison of magnetic field distribution of SRM before and after optimization. (a) Magnetic field distribution of SRM before optimization. (b) Magnetic field distribution of SRM after optimization.

0.5 and 0.45, respectively, the maximum value *maxW* of the multi-objective weighting function is 0.9958, and the corresponding objective function values of average torque, torque ripple coefficient, and efficiency are 66.1522 N.m, 1.35036, and 89%.

VI. MOTOR PERFORMANCE COMPARISON BEFORE AND AFTER OPTIMIZATION

The optimized pole-arc parameters of SRM were brought into the motor model, and the limiting current controlled by CCC was reduced to meet the corresponding rated power requirements. Then, the magnetic field distribution, torque characteristics, and efficiency Map calculation results were analyzed and compared between the two motor models before and after optimization in a wide speed range.

A. Comparison of SRM magnetic field distribution before and after optimization

By comparing Fig. 11 (a) and Fig. 11 (b), it can be seen that the flux leakage at the critical position, where the salient poles of the stator and rotor coincide, is significantly reduced after optimization. In addition, the color representing the size of magnetic flux density *B* is obviously lighter at the pole tip where the salient poles of the stator and rotor coincide, which means that the saturation degree of the magnetic circuit is significantly reduced after optimization, so the torque ripple caused by the switching point in the torque overlap area will be significantly reduced [8].

B. Comparison of torque characteristics before and after optimization

The average torque and torque ripple coefficient were calculated in the time range of 2ms∼8ms. The comparison of torque characteristics before and after optimization is shown in Fig. 12.

The average torque decreases slightly before and after optimization, but the ripple coefficient decreases greatly from 1.2093 to 0.8965, which proves that increasing the stator and rotor pole-arc coefficients of SRM can improve the torque ripple performance of the motor effectively [16].

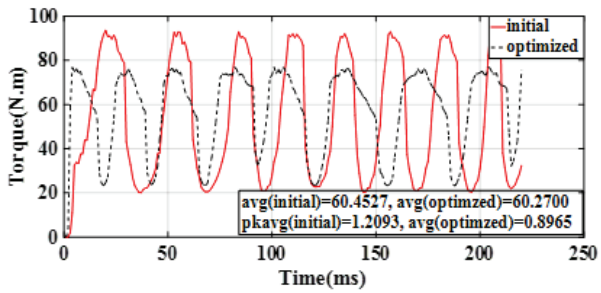

Fig. 12. Torque comparison of the motor model before and after optimization.

C. Efficiency comparison before and after optimization

The RMxprt model rated load performance comparison of SRM before and after optimization is shown in Table 4. Due to the obvious reduction of copper loss in the optimized model, the motor efficiency is increased from 89.9% to 91.5%, which proves that the stator and rotor pole arc coefficients also have a great impact on the motor efficiency.

Table 4: Comparison of efficiency at rated load before and after pole arc coefficient optimization of SRM

Indicators	Initial	Optimized
Iron loss (W)	282.578	314.449
Copper loss (W)	895.011	685.805
Efficiency (%)	89.9018	91.4525

D. Comparison of speed range before and after optimization

The stator and rotor pole-arc coefficients of SRM are increased, and the lower and upper limits of chopper current are adjusted to 69 and 71, to keep the rated output power almost the same before and after optimization. According to the comparison of the two output power map calculations of the motor model in Fig. 13, the constant power speed range of the motor is reduced after optimization, but the highest speed ω_{sc} in the constant power region is still satisfied with 2 to 3 times of the rated speed, which can fully meet the operation requirements of the wide speed regulation range for the driving motor in EV.

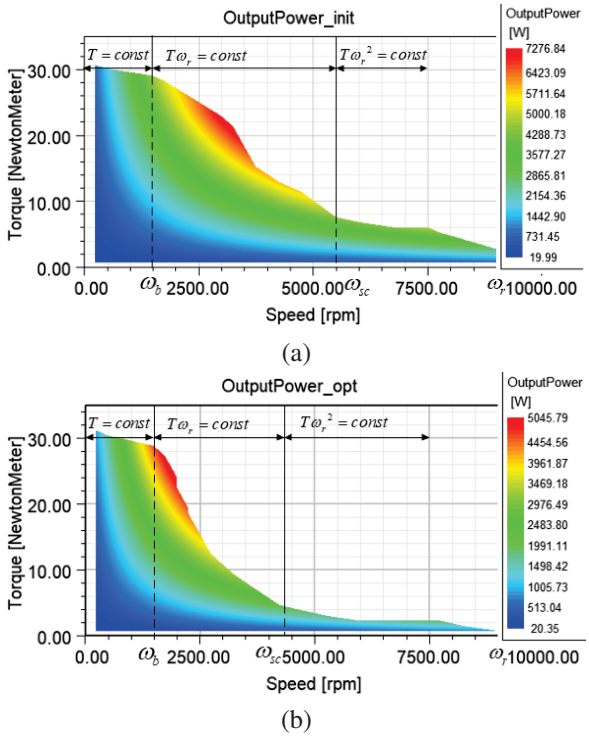

Fig. 13. Comparison of output power Map calculation of motor model before and after optimization. (a) SRM output power Map before optimization. (b) Output power Map of SRM after optimization.

VII. CONCLUSION

Because SRM has the advantages of large starting torque, wide speed range, strong load capacity, and high efficiency, it is especially suitable for new energy vehicle driving. According to the design requirements of the new energy vehicle drive, a 10 kW 8/6 structure SRM motor model is designed, and the wide speed range debugging of the motor model and the optimization of the motor performance based on parametric modeling is completed in this paper.

It can be seen from the performance comparison of the SRM model before and after optimization that the average torque of the optimized SRM model is basically unchanged, but the torque ripple coefficient is greatly reduced under the condition of meeting the design power requirements. The optimization of motor structure parameters also plays a role in optimizing the efficiency of the motor. The comparison of the output power Map before and after optimization shows that the increase of the pole-arc coefficients makes the constant power range of the motor smaller, but it can better meet the requirements of electric vehicles for the speed range. In the future, more structural parameters of the motor should be considered, and more performance optimization should be realized, including power density, vibration noise, etc.

ACKNOWLEDGMENT

The authors would like to thank the National Natural Science Foundation of China (Grant no. 62173165) and the Modern Education Technology Research Project of Jiangsu Province (Grant no. 2021-R-91852) for providing funds and equipment for this research.

REFERENCES

[1] Y. Y. Zhu, C. T. Yang, and Y. Yue, "Design and optimisation of an in-wheel switched reluctance motor for electric vehicles," *IET Intelligent Transport Systems*, vol. 13, no. 2, pp. 175-182, 2019.

[2] H. Cheng, H. Chen, and Z. Yang, "Design indicators and structure optimization of switched reluctance motor for electric vehicles," *IET Electric Power Application*, vol. 9, no. 4, pp. 319-331, 2015.

[3] A. A. Memon, M. M. Shaikh, S. S. H. Bukhari, and J. -S. Ro, "Look-up data tables-based modeling of Switched Reluctance Machine and experimental validation of the static torque with statistical analy-

sis," *Journal of Magnetics*, vol. 25, no. 2, pp. 233-244, 2020.

[4] X. D. Sun, K. K. Diao, and G. Lei, "Direct torque control based on fast modeling method for a segmented-rotor switched reluctance motor in HEV application," *IEEE Journal of Emerging and Selected Topics in Power Electronics*, vol. 9, no. 1, pp. 232-241, Feb. 2021.

[5] F. E. Fleming and C. S. Edrington, "Real-time emulation of switched reluctance machines via magnetic equivalent circuits," *IEEE Transactions on Industry Magnetic*, vol. 63, no. 6, pp. 3366-3376, June. 2016.

[6] C. Ma and L. Y. Qu, "Design considerations of switched reluctance motors with bipolar excitation for low torque ripple applications," *IEEE Energy Conversion Congress and Exposition*, Denver, CO, USA, pp. 926-933, 2013.

[7] J. Q. Chen, H. L. Xian, and F. C. LAN, "Structural torque ripple suppression method for switched reluctance motor," *Journal of Mechanical Engineering*, vol. 56, no. 20, pp. 106-119, Oct. 2020.

[8] Z. Li, L. Zheng, and W. Yang, "Research on torque ripple and structure optimization design of switched reluctance motor," *Electric Machines and Control*, vol. 22, no. 6, pp. 11-21, Jun. 2018.

[9] X. D. Xue, K. W. E. Cheng, and J. K. Lin, "Optimal control method of motoring operation for SRM drives in electric vehicles," *IEEE Transactions On Vehicular Technology*, vol. 59, no. 3, pp. 1191-1204, Mar. 2010.

[10] H. H. Wang, *Speed Control Technology of Switched Reluctance Motor*, China Machine Press, Beijing, Apr. 2014.

[11] L. J. Liu, M. W. Zhao, and X. B. Yuan, "Direct instantaneous torque control system for switched reluctance motor in electric vehicles," *J. Eng*, vol. 2019, no. 16, pp. 1847-1852, 2019.

[12] H. X. Wu, *Theory and Control Technology of Switched Reluctance Motor System*, China Electric Power Press, Beijing, Jul. 2010.

[13] J. W. Zhang, H. H, Wang, and L. Chen, "Multi-objective optimal design of bearingless switched reluctance motor based on multi-objective genetic particle swarm optimizer," *IEEE Transactions on Magnetics*, vol. 54, no. 1, Jan. 2018.

[14] A. A. Memon, S. S. H. Bukhari, and J. -S. Ro, "Experimental determination of equivalent iron loss resistance for prediction of iron losses in a Switched Reluctance Machine," *IEEE Transactions on Magnetics*, vol. 58, no. 2, pp. 1-4, Feb. 2022.

[15] B. Anvari, H. A. Toliyat, and B Fahimi, "Simultaneous optimization of geometry and firing angles for in-wheel switched reluctance motor drive," *IEEE Transactions on Transportation Electrification*, vol. 4, no. 1, pp. 322-329, Mar. 2018.

[16] X. M. Deng, R. Li, L. Hao, A. K. Zhang, and J. H. Zhou, "Design and finite element analysis of a novel permanent magnet assisted reluctance synchronous motor," *Applied Computational Electromagnetics Society (ACES) Journal*, vol. 35, no. 9, pp. 1012-1021, Sep. 2020.

Lijun Liu was born in Shanxi, China, in 1977. She received her M.S. degree in Power Electronics and Power Drive from China University of Mining and Technology, Xuzhou, China, in 2006, and is currently pursuing a Ph.D. degree in Power Electronics and Power Drive from Shanghai University, Shanghai, China.

She is currently a lecturer at the School of Electrical Engineering and Automation, Jiangsu Normal University, Xuzhou, China. She has published more than 10 articles. Her research interests include the design and optimization of new energy-electric drive systems, and industrial motion control systems, etc.

Yu Huang was born in Jiangsu, China. He received his B. S. degree in Electric Engineering from Jiangsu Normal University, Xuzhou, China, in 2022, and is currently pursuing an M.S. degree in Power Systems from North China Electric Power University, Baoding, China. His research interests include the design and optimization of new energy electric drive systems, and high voltage techniques, etc.

Mingwei Zhao was born in Shandong China, in 1975. He received anthe M.S. degree in Power Electronics and Power Drive from Nanjing University of Aeronautics and Astronautics, Nanjing, China, in 2012, and is currently pursuing a Ph.D. degree in Control Science and Control Engineering from Shanghai University, Shanghai, China.

Since 2006, he has been an experiment lecturer with the school of Electrical Engineering and Automation, Jiangsu Normal University, Xuzhou, China. He is the author of 10 articles. His research interests include the robot dynamic drive and cooperative control, and industrial motion control system, etc.

Yi Ruan was born in Shanghai, China, in 1955. He received an M.S. degree in Shanghai University of Technology, Shanghai, China, in 1989, and a Ph.D. degree in Power Electronics and Power Drive from Shanghai University, Shanghai, China, in 1996.

From1989 to 2015, he has been a professor of the Electromechanical Engineering and Automation, Shanghai University, Shanghai, China. He once served as the chairman of the Special Committee Of Variable Frequency Power Supply And Electric special committee of variable frequency power supply and electric drive of the Power Supply Society of China. His research interests include the power electronics and power drive, control and power conversion technology of new energy, etc.

Design of a Wideband CPW Fed Fractal Antenna for Satellite Communication

Varnikha Nanthagopal and Jothilakshmi Paramasivam

Department of Electronics and Communication Engineering
Sri Venkateswara College of Engineering, Sriperambudur, 602105, India
varnikavidesh@gmail.com, jothi@svce.ac.in

Abstract – A novel 'T' square wideband fractal antenna is proposed for satellite communication. The Wideband is achieved through the 'T' square fractal design and CPW feed. At first, a conventional square-shaped patch antenna is designed. Then the square-shaped patch is replaced by a Type-I fractal to achieve wideband. Finally, a Type-II fractal with an L-Shaped boundary is used to enhance the bandwidth to a greater extent. The gain of the proposed antenna ranges from 4 dB to 6.3 dB for the entire frequency range of 6.2 GHz to 14 GHz. The radiation efficiency of the antenna is noticed up to 84%. The fractal antenna resonates well throughout the entire frequency range with a VSWR of less than 2. The antenna having such a wide band characteristic can be found suitable for a wide range of applications like earth exploration satellites, fixed satellites, radiolocation, maritime radio navigation, and aeronautical radio navigation. A metal reflector is also introduced at the bottom of the antenna to produce a unidirectional radiation pattern. This increases the gain up to 9.8 dBi and a front-to-back ratio is noticed above 20 dB. The design is fabricated and the measurement results are found to be in good agreement with the simulation results.

Index Terms – CPW fed antenna, fractal antenna, reflector, satellite application, 'T' Square fractal, wideband.

I. INTRODUCTION

Satellite communication carries an important aspect of the global telecommunication system. A satellite device consists of an antenna, transponders to receive and retransmit signals, a propulsion unit, and a power grid. The cost of launching the satellite is very high and it depends on its weight. Hence, lightweight satellites are preferable nowadays. Due to this reason, low-profile and lightweight microstrip patch antennas are the best candidates for the purpose. These conformal antennas have the ability to operate in more than one band to be selected for a wide range of satellite communications. Narrow bandwidth is the major concern in conventional microstrip antennas. Many methods are available in the literature for improving the impedance bandwidth of microstrip patch antennas so that a single antenna can be used for many applications. These methods include using a thick dielectric material with low dielectric constants, coupling the feed instead of connecting it directly to the patch, etching different shaped slots in the patch, using a single layer metamaterial superstrate, using a defected ground structure, etc. The bandwidth of Microstrip patch antennas can be enhanced by increasing substrate thickness [1]. The increase in the thickness of the substrate results in the excitation of the surface waves which affects the performance of the antenna. By decreasing the dielectric constant of the substrate [2] also wider bandwidth can be achieved, but it increases the overall size of the antenna. In [3], an inverted U-shaped slot was implemented on the radiating patch to improve the impedance bandwidth to 17.8%. In [4], although the microstrip antenna with a stacked structure provides a very wider bandwidth, it is having a very complex structure. Similarly, wideband is achieved with U-shaped parasitic elements in [5]. Using the metamaterial-based technique, a wider fractional bandwidth of 30% is achieved in [6]. But again, it cannot fulfill the requirement of a wider range of satellite communications. Most of the prevailing methods can increase the impedance bandwidth to some extent, however, it is necessary to further enhance the bandwidth to meet the needs of broadband wireless communication systems. In [7], the narrow band property of the conventional microstrip antenna is improved by adding a gap between the substrate and ground, which further decreases the effective permittivity of the substrate. This results in achieving improved bandwidth of up to 58% along with the use of defected ground structure. In [8], a simple structure of singly-fed wideband dielectric resonator antenna (DRA) is designed. This DRA has one rectangular and two half-split cylindrical dielectric resonators with excitation via a stair-shaped slot. The multiple orthogonal mode pairs are excited and an impedance bandwidth of 49.67% is achieved by tuning and merging the orthogonal mode pairs.

Along with the other methods, wider bandwidth can also be achieved by the use of fractal antennas. Fractals are self-similar geometry at different scales used in patch antennas to achieve miniaturization, multi-band, and wideband due to their self-similar and space-filling

Submitted On: November 8, 2021
Accepted On: October 5, 2022

https://doi.org/10.13052/2022.ACES.J.370905

nature. Complex shapes of fractals generate many electric current modes or distinct current distributions which further give rise to radiation. Hence, fractal antennas can have a wider bandwidth than conventional antennas. There are many deterministic fractals available such as Minkowski, Sierpinski, Koch, cantor set, etc., which can be used to achieve wideband, multiband, and miniaturized antennas. In [9], a printed Cantor monopole multiband antenna with a reduced size covering multiple applications has been proposed. In [10], the Fractal concept based on a square ring structure using circular ring elements is developed for multiband applications. Three iterations of the antenna have been designed and investigated. The last iteration shows better results in terms of antenna bandwidth. This improvement along with multiband characteristics for the fractal antenna makes it a suitable candidate for different wireless applications. In [11], a rectangular dielectric resonator antenna with Minkowski and Sierpinski fractals is used for wideband applications. The fractal antenna offers a wide bandwidth of 66%. In [12], for bandwidth improvement of a fractal monopole antenna, a compact Grounded CPW feeding method is proposed. This feeding technique changes the multiband behavior of fractal elements to the wideband property. But a comparatively lesser gain is noticed in the designed antenna. In [13], a wideband antenna is designed using Sierpinski fractal geometry. Even though it could achieve an impedance bandwidth of 120%, the gain was only 3.35 dB and the radiation pattern was also not unidirectional. Microstrip-line-fed printed wide-slot antenna is proposed in [14] to increase the bandwidth with a fractal structured slot. After etching the fractal slot, it can be observed that the impedance bandwidth is improved significantly. In [15], a wideband fractal slot antenna is proposed and fabricated. The broadband characteristic is achieved by implementing a Sierpinski fractal into a square slot without increasing the overall size of the antenna. It is also observed that the number of resonances increases with the increase in fractal iterations in the slot. In [16], fractal Minkowski curves are used to design a compact dual-band microstrip ring antenna. The sides of the ring have been replaced with the first and second iterations of the fractal geometry to design the compact antenna with dual-band operations. Although the use of fractals in the above-discussed articles enhances the bandwidth to some extent, other performance parameters of the antenna are not up to mark for their use in satellite communication. Hence, a novel method is proposed here combining two different fractal types to achieve a bandwidth of up to 76% with balanced performance parameters.

In this article, a novel 'T' square wideband fractal antenna is proposed for satellite communication. CPW feed is used here to have an impedance matching over the entire bandwidth. At first, a conventional square-shaped patch antenna is designed. Then the square-shaped patch is replaced by a Type-I fractal to achieve wideband. Finally, a Type-II fractal with an L-Shaped boundary is used to enhance the bandwidth to a greater extent.

II. ANTENNA DESIGN AND ANALYSIS

A. Antenna geometry

The design procedure of a microstrip antenna starts with selecting the proper substrate and feeding technique to achieve the required specifications. Here, in particular, the design goal is to improve the bandwidth of the antenna. To achieve wider bandwidth in our case, a CPW feed is used [17]. The feed, radiating patch, and ground plane are positioned on the same side of the substrate. FR4 with dielectric constant 4.3 is used as the substrate with a height of 1.6 mm. The dimension of the substrate is kept at 35 mm x 30 mm to accommodate the radiating patch and the ground plane. Figure 1 shows the proposed CPW-fed wideband fractal antenna. The dimensions of the same antenna are tabulated in Table 1.

The proposed antenna geometry consists of a T-square fractal geometry and is designed in two different stages. In the first stage, a plus-shaped radiator is generated from a conventional square patch antenna. The conventional square patch antenna is considered here as Design 1 and the antenna with a plus-shaped radiator is named Design 2. In the next stage, each square of the

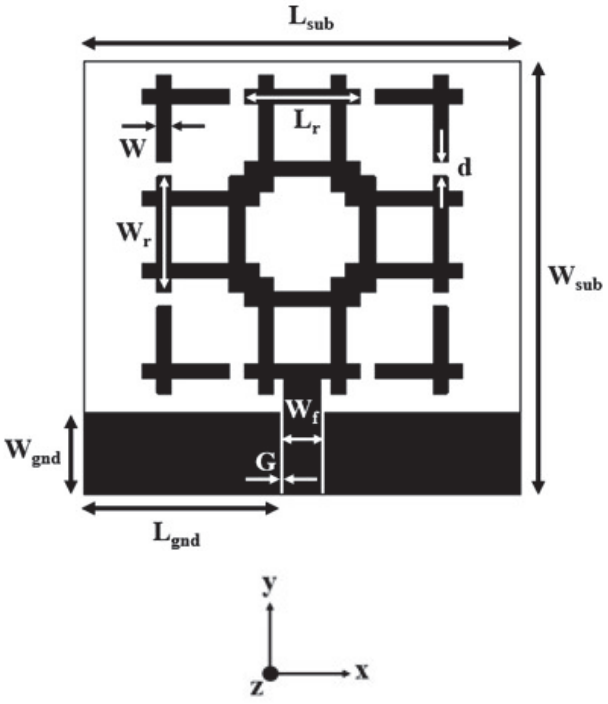

Fig. 1. Geometry of the proposed fractal antenna.

Table 1: Dimensions of the proposed antenna

Parameters	Description	Value (mm)
Lr	Length of the radiating square	8
Wr	Width of the radiating square	8
W	Width of rectangle strip	1
Wf	Width of CPW feedline	2.4
G	Gap of CPW line	0.4
Lsub	Length of Substrate	30
Wsub	Width of Substrate	35
Lgnd	Length of the Ground	13.4
Wgnd	Width of the Ground	5.7
-d	Gap between radiating elements	1

plus-shaped patch is replaced with a wired structure having a strip width of 1 mm and length of 8 mm for Design 3. Then following the space-filling property of fractal two L-shaped strips are added at the top corners and named Design 4. Finally, two more L-shaped strips are added to the structure at the bottom corners for the final Design 5. Two finite ground planes of the same dimensions are positioned symmetrically on both sides of the CPW feed. The dimension of the ground plane of the coplanar waveguide is 6.5 mm x 13.4 mm. The length of the feed is taken as 8 mm with a width of 2.4 mm. A gap of 0.4 mm is maintained between the coplanar ground plane and the signal strip used to feed the radiating patch. The detailed design procedure of the proposed fractal antenna along with the generator and initiator descriptions are given in the next section.

B. Design procedure

In this section, the complete design procedure for the proposed fractal antenna is described in five different design stages. In the first stage, a conventional square-shaped radiator is designed with dimensions of 22 mm x 22 mm, as shown in Fig. 2 (a). This square-shaped patch antenna is designated as Design 1 and yields a simulated bandwidth of 2.7 GHz from 11 GHz to 13.7 GHz. In the next stage, Design 2 is generated from Design 1 by replacing the initiator with the generator structure as shown in Fig. 2. Here, the square patch is considered as the initiator whereas, four square slots in the four corners with a center square slot is etched out as the Type-I generator structure for Design 2. This modified antenna gives a wider bandwidth from 7.8 GHz to 11 GHz compared to Design 1. The simulated S_{11} vs. frequency graph is plotted in Fig. 4.

From Fig. 4, it can be seen that the s_{11} curve of Design 2 is not perfectly matched. The resonating frequency is shifted towards the left due to the increase in the current path length. Hence, to improve the impedance matching, a 'T' square fractal is introduced in Design 3 as the third stage. Again, in Design 3 all the square shapes of the plus-shaped initiator are replaced with a Type-II generator structure as shown in Fig. 3. The Type-II generator structure consists of four rectangular strips with a width of 1 mm and a length of 8 mm.

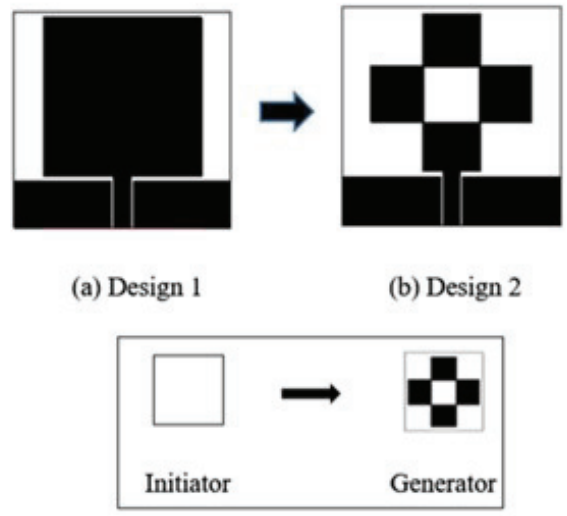

Fig. 2. Construction of Design 2 from Design 1 with initiator and generator structure.

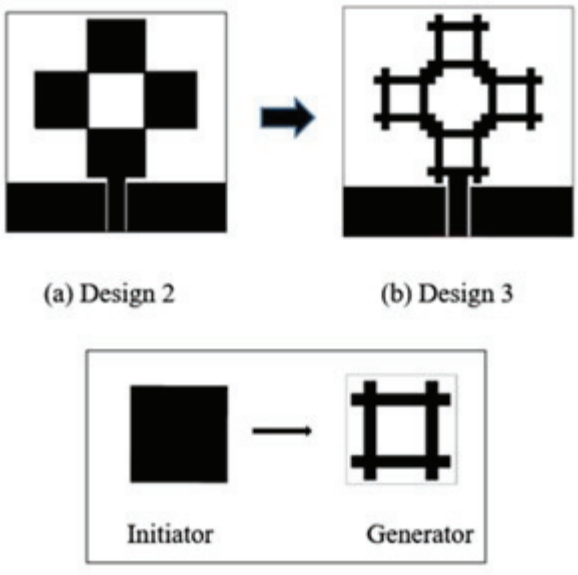

Fig. 3. Construction of Design 3 from Design 2 with initiator and generator structure.

The scaling dimension relation is used here to determine the dimension of the fractal design. The first it-

eration of the fractal is three times wide and three times taller than the generator. So, it is said to be scaled by a factor of 3. To construct iteration 1, four copies of the original generator are required. Design 3 is formed by combining four copies of the generator.

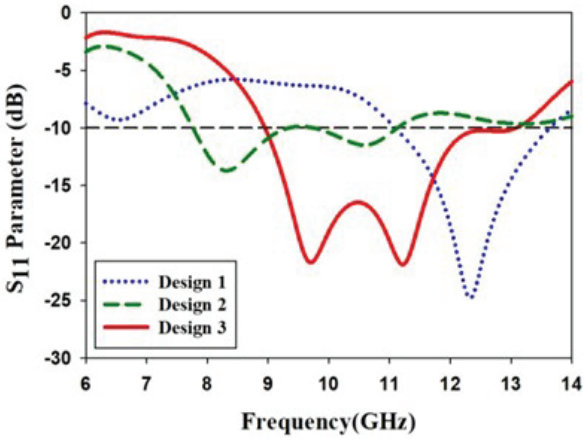

Fig. 4. S_{11} vs. frequency graphs of Design 1, 2, and 3.

Using scaling dimension relation [18],

$$C = S^d,$$
$$\text{Number of copies} = scaling\ factor^{dimensiom}$$
$$4 = 3^d$$
$$\log 4 = \log 3^d$$
$$d = \log 4/\log 3$$
$$d = 1.26.$$

The dimension of the above-designed fractal antenna is 1.26. After introducing the 'T' square fractal in Design 3, the antenna resonates from 9 GHz to 12 GHz. The s_{11} value has also improved up to -21 dB which can also be observed from Fig. 4. In Design 2, the two resonances are wide apart but in Design 3 both the resonances came closer to behaving as a single wide band. The Fractals with self-similar properties help in achieving this wider bandwidth in Design 3.

Although we have achieved a wider bandwidth of 3 GHz in Design 3, to improve the impedance bandwidth further, two L-shaped elements are introduced in the fourth stage at the top corners in Design 4 as shown in Fig. 5 (a). These L-shaped elements maintain a coupling gap with the radiator which results in improved impedance bandwidth. The coupling gap gives the capacitive effect and the inductive effect is compensated by this capacitive effect to get a wideband impedance matching characteristic from 8.7 GHz to 12 GHz in Design 4. The bandwidth of this antenna can be improved further if the antenna utilizes efficiently the available area, with its geometrical configuration. This is known as the space-filling property of fractal. Hence, to satisfy this property of fractal, in the last stage, two more L-shaped elements are added at the bottom corners of the radiator in Design 5 which is shown in Fig. 5 (b). This further increases the bandwidth from 8.4 GHz to 14 GHz. However, the s_{11} curve degrades and touches the -10 dB line at 12 GHz. The comparison among S_{11} curves of Design 3, 4, and 5 is shown in Fig. 6 over the wide range of frequency. To get a perfect impedance matching in Design 5, the parametric optimization method is adopted. Detailed procedure of the parametric optimization and its results are discussed in the coming section.

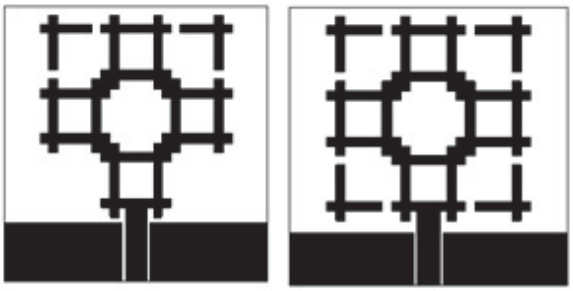

Fig. 5. (a) Design 4, (b) Design 5.

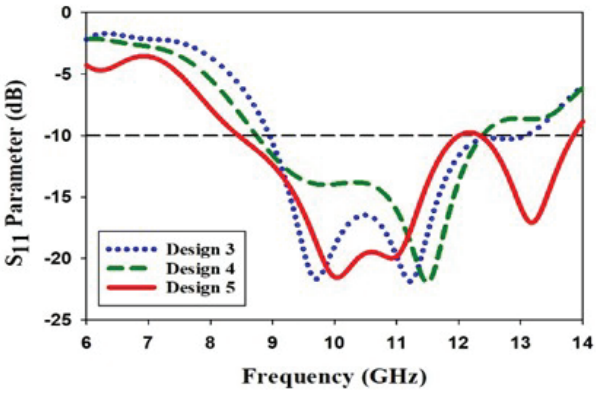

Fig. 6. S_{11} vs. frequency graphs for Design 3, 4, and 5.

C. Parametric analysis

A parametric analysis method is adopted here, for the optimization of the proposed antenna. At first, the sensitivity of the design parameters is examined over the resonance properties of the antenna. Then two design parameters, d and Wgnd are selected for the optimization process due to their impact on the antenna performance over other design parameters.

Here d is the gap between the L-shaped element and the 'T' square fractal and Wgnd is the width of the CPW ground. At first, the gap between the L-shaped element and the radiator, d is varied from 0.1 to 1 with a gap of 0.5 mm by keeping the width of the ground Wgnd, constant. The same process is repeated for 3 different values of Wgnd, 6.3 mm, 6 mm, and 5.7 mm.

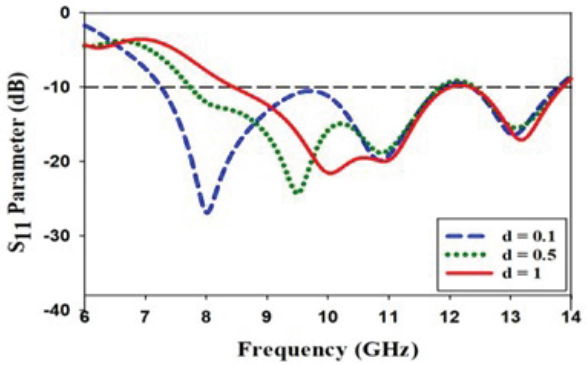

Fig. 7. S_{11} vs. frequency graphs for the variation of 'd' for Wgnd = 6.3 mm.

The variations of S_{11} for different values of 'd' are plotted in Fig. 7 for Wgnd of 6.3 mm. The same variations of S_{11} are plotted in Figs. 8 and 9, for the values of Wgnd 6 mm and 5.7 mm, respectively. It can be clearly observed from all these three figures that the bandwidth is increasing with good impedance matching when the gap d is increased from 0.1 mm to 1 mm for a constant value of Wgnd. Variation in d doesn't have any effect on the upper resonant frequency. However, it helps in increasing the bandwidth by dropping the lower resonant frequency of the proposed fractal antenna. So, from here one can conclude that the S_{11} graph for the proposed antenna performs well for the maximum value of

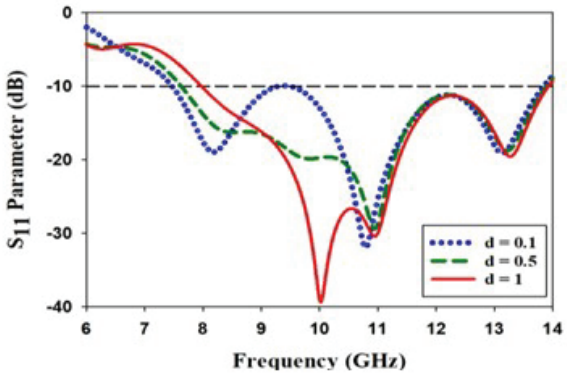

Fig. 8. S_{11} vs. frequency graphs for the variation of 'd' for Wgnd = 6 mm.

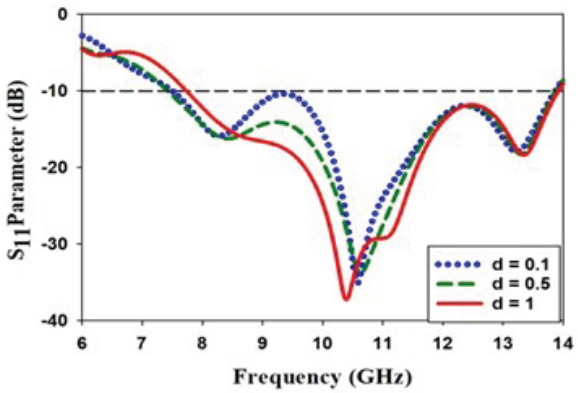

Fig. 9. S_{11} vs. frequency graphs for the variation of 'd' for Wgnd = 5.7 mm.

d i.e., 1 mm, for a constant value of Wgnd. Hence, in the next step of parametric analysis, S_{11} graphs are compared in Fig. 10 for different values of Wgnd by keeping d constant as 1 mm. The values of ground plane width Wgnd, is varied by 6.3 mm, 6 mm, and 5.7 mm for this comparison.

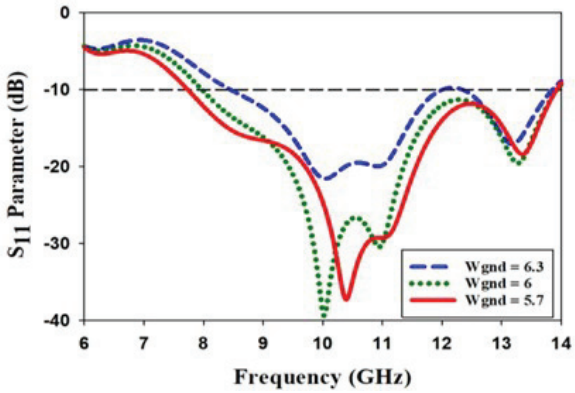

Fig. 10. S_{11} vs. frequency graphs for the variation of 'Wgnd' for d = 1 mm.

From Fig. 10, it can be seen that all the s_{11} curves are well below the −10 dB line and the impedance bandwidth is also improved compared to the last parametric analysis. The bandwidth is increasing here while decreasing the width of the ground plane from 6.3 mm to 5.7 mm. Hence, we can conclude that Wgnd = 5.7 mm and g = 1 mm gives the optimum result with a wider bandwidth from 7.7 GHz to 14 GHz and a good matching throughout this wide range of resonating frequencies. Figure 11 shows the S_{11} comparison plot for the proposed antenna before and after its optimization. An improvement in bandwidth and impedance matching can be observed in the optimized result compared to the unoptimized one.

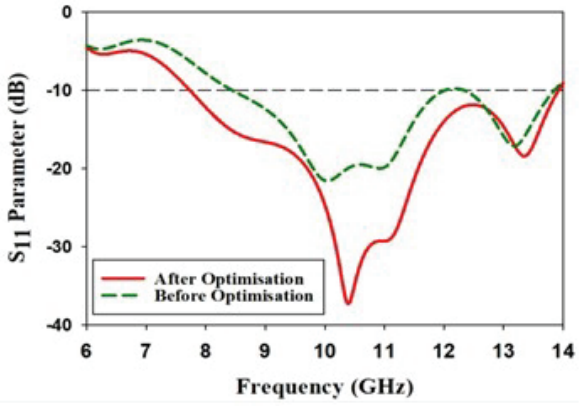

Fig. 11. S_{11} vs. frequency graphs for the proposed design before and after optimization.

Impedance also plays a vital role in verifying the reflection characteristics and their matching for the antenna. The characteristic impedance has two components, the real part, and the imaginary part. The real part includes the resistance, whereas, the imaginary part is the reactance. To have a better insight into the reflection characteristics of the antenna, both the real and imaginary parts of the impedance are plotted in Fig. 12. It includes the impedance plots of the design before and after optimization. The simulated Z_{11} characteristics of the design in Fig. 12 elucidate that, for the whole range of the operating band, the impedance graphs are maintaining their values near the 50-ohm impedance line for the real part and 0 Ω reactance line for the imaginary part in both before and after optimization. However, compared to the unoptimized one, a wider bandwidth is found in the design after optimizing the design parameters d and Wgnd for the antenna.

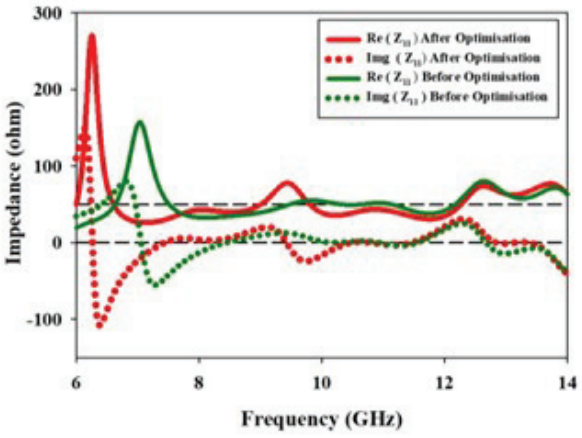

Fig. 12. Re, Img (Z_{11}) vs. frequency plot of the proposed antenna before and after optimization.

Although the proposed optimized antenna shows good reflection characteristics throughout a whole range of frequencies, the radiation patterns of the proposed wideband antenna need to be examined at different resonant frequencies. The radiation patterns for the optimized design at different frequencies are plotted in Fig. 13.

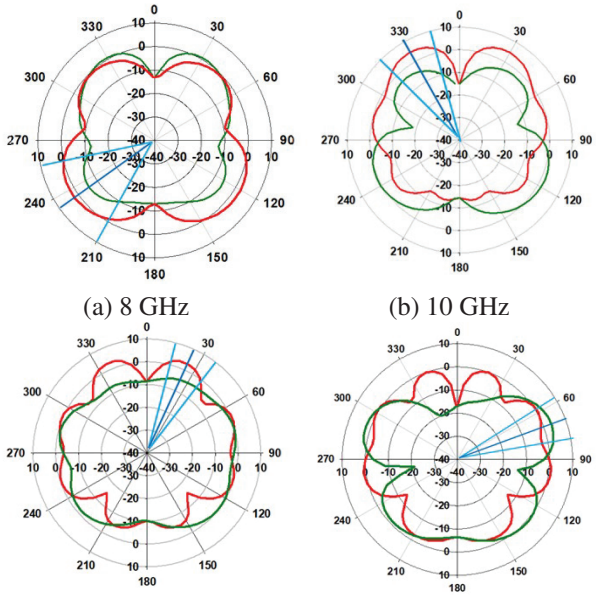

(a) 8 GHz (b) 10 GHz

(c) 12 GHz (d) 13 GHz

Fig. 13. Radiation pattern at (a) 8 GHz, (b) 10 GHz, (c) 12 GHz, and (d) 13 GHz without a reflector.

The XZ and YZ-plane radiation patterns are plotted at 4 different frequencies, 8 GHz, 10 GHz, 12 GHz, and 13 GHz for the optimized wideband antenna. From Fig. 13, it can be observed that the radiation patterns at all the frequencies have adequate gain values. However, from the application point of view, satellite antennas need to be unidirectional to radiate in a particular direction. But it can be seen from Fig. 13, the radiation patterns of the wideband antenna are not unidirectional. Hence, to fulfill this criterion of satellite communication, a reflector is introduced at the back of the radiator to change its radiation pattern to unidirectional. This will also improve the gain and front-to-back ratio of the proposed antenna.

III. ANTENNA WITH REFLECTOR

The antenna proposed here is designed with the help of the time domain (transient) solver of CST Microwave Studio. This solver makes use of Finite Integration Technique (FIT) as a computational method to solve extremely large, complex, and detailed simulations. It uses a hexahedral mesh type to analyze the designed antenna. Method on-demand approach of CST to allocate suitable

solver and mesh to best fit the problem, make it more efficient and accurate for the design and analysis. Perfect boundary approximation further simplifies the analysis process. Adaptive mesh refinement, parallelization of time domain solver, automatic parametric studies, and inbuilt optimization methods can be availed in CST Microwave Studio to successfully design the 3D model and analyze the reflection and radiation properties of the antenna. For simplification of the design procedure, CST also allows us to define the properties of the background material. Pre-loaded structure templates, and excitation settings help us in the easy realization of the simulation. The hexahedral mesh view for the proposed antenna is shown in Fig. 14 for the reference of the reader. Figure 14 shows the top and side view of the proposed fractal antenna with a metal reflector below the substrate along with its mesh view for xy-and yz-planes. The reflector is used here below the substrate to reduce the back radiation. The distance between the antenna and the reflector plays an important role in creating a 180^0 phase shift in the back radiations, which ultimately produces a unidirectional pattern. To achieve this, the gap between the antenna and reflector (g) should be $\lambda/4$. Since the proposed antenna is resonating over a wideband ranging from 6.2 to 14 GHz, the center frequency of 10 GHz is considered for calculating the gap $\lambda/4$.

$$g = \frac{c}{4f} = 7.5\ mm. \tag{2}$$

The size (length and width) of the reflector is taken as two times lambda.

For Centre frequency 10 GHz, $\lambda = 30\ mm$. Hence, $2\lambda = 60\ mm$.

The above-designed reflector acts as an infinite ground plane and reflects back the radiations to the frontal lobe for the whole wide range of frequencies. This results in a unidirectional pattern for the proposed antenna at all operating frequencies.

Figure 15 shows the radiation pattern for the proposed antenna after the addition of the reflector. From this figure, a clear indication can be noticed in the change in back lobes after adding the reflector at the back of the antenna. This further produces a unidirectional radiation pattern in the proposed antenna by diverting the back lobes toward the front of the radiator, which helps in increasing the overall gain of the antenna.

The antenna proposed here is linearly polarized. The axial ratio of the proposed antenna is found to be 40 dB, which confirms the linear polarization. Linear polarization can offer significant advantages over circular polarization. At high-frequency bands, linear polarized antennas perform well with respect to atmospheric effects such as rain attenuation. Hence, for the frequency bands where atmospheric effects are dominant and when maximum frequency re-use is needed, the advantages of linear

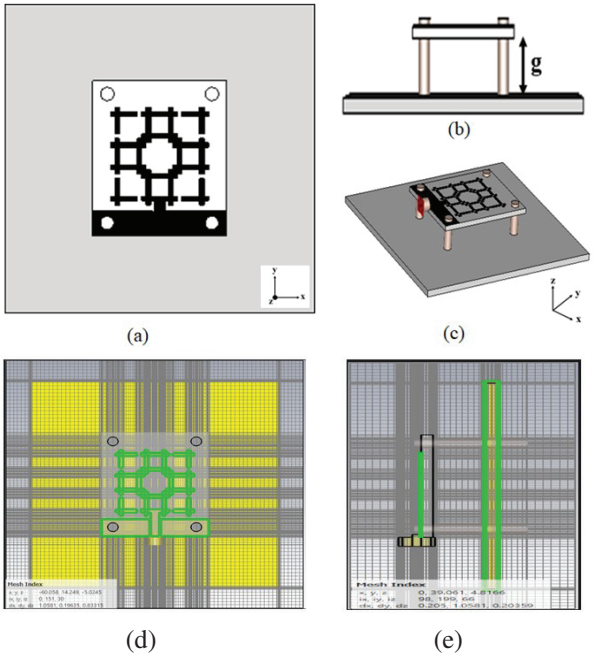

Fig. 14. (a) Top view, (b) Side view, and (c) trimetric view of the proposed fractal antenna with reflector. (d) Mesh view of the proposed antenna in xy-plane and (e) Mesh view of the proposed antenna in yz-plane.

polarization can be utilized [19]. Further, in linear polarization, co-polar side-lobe suppression and cross-polar discrimination can also be achieved in the receiving antenna.

FBR has a huge impact on the directivity of the antenna. It is the ratio of the magnitude of directional radiation in a single direction divided by the radiation wasted by the antenna in other unwanted directions. Antennas with a higher front-to-back ratio can improve the signal to noise plus interference ratio efficiently which increases the overall performance of the antenna. The higher the ratio, the antenna is more directional. A directional antenna should have a front-to-back ratio of a minimum 15 dBi to accommodate itself in high-range communications [20]. Always a high front-to-back ratio is preferred as in this case less energy radiates behind the antenna in unwanted directions. The proposed antenna proves to be more efficient with a front-to-back ratio of more than 20 dB having a unidirectional pattern and a signal-to-noise plus interference ratio. As it can be seen from Fig. 16, the FBR of the antenna without a reflector is below 20 dB and when the reflector is added to the design, it increases up to 40 dB with an average FBR of 30 dB.

Figure 17 shows the gain of the fractal antenna with and without the reflector. The reflector helps in improving the gain of the antenna from 6.3 dBi to 10 dBi. The

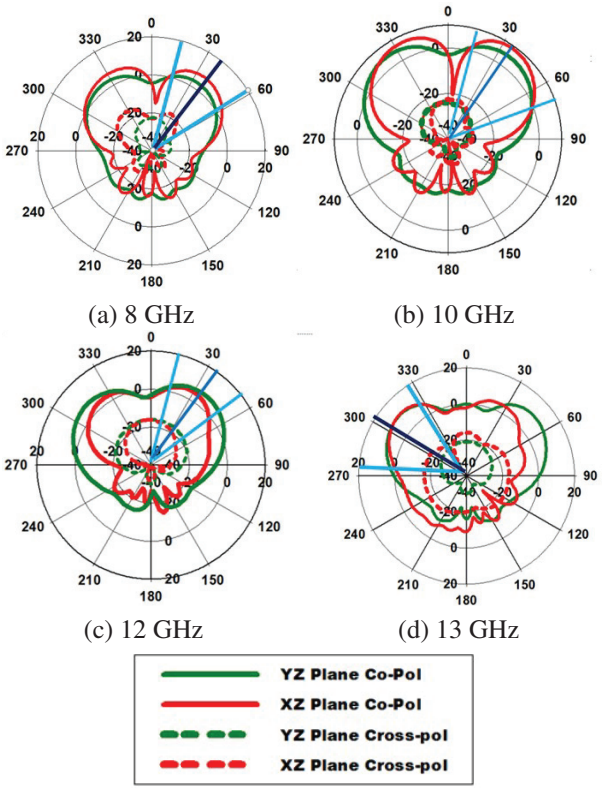

Fig. 15. Radiation pattern at (a) 8 GHz, (b) 10 GHz, (c) 12 GHz, and (d) 13 GHz, with reflector.

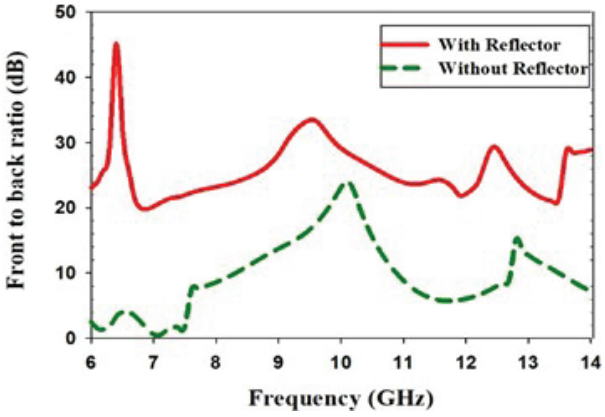

Fig. 16. FBR of the proposed antenna with and without a reflector.

average gain of the antenna was found to be 3.5 dBi higher after the addition of the reflector.

The radiation efficiency of antennas is the ratio of total power radiated by an antenna to the total input power received from the generator. In the case of an antenna with low radiation efficiency, the input power mostly dissipated because of internal losses such as metal conduction, dielectric, and magnetic losses within the antenna.

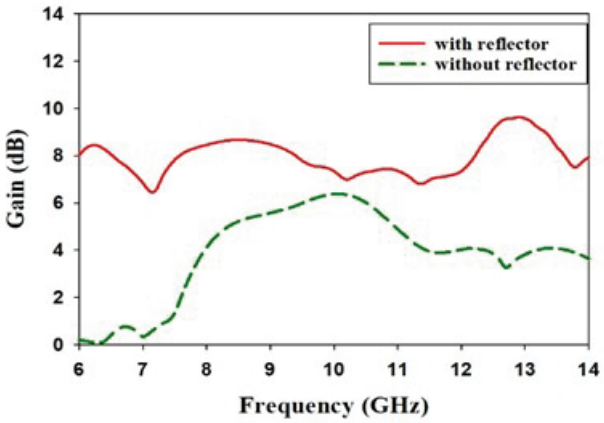

Fig. 17. Gain of the proposed antenna with and without a reflector.

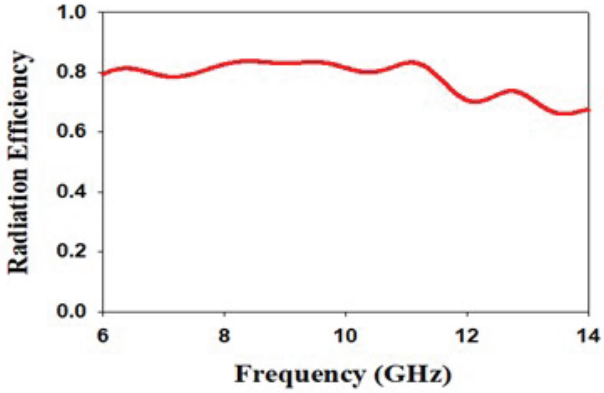

Fig. 18. Radiation efficiency of the proposed antenna.

Figure 18 shows the Radiation efficiency plot of the proposed antenna. The fractal antenna is radiating well with a maximum Radiation efficiency of 84% and average Radiation efficiency of 80% throughout the operating band. From CST Microwave Studio, an accepted power of 0.498 W and radiated power of 0.404 W is found for our proposed antenna at 10 GHz. Hence, the radiation efficiency is found to be 0.81 at 10 GHz for the proposed antenna. The remaining 0.094 W is dissipated in terms of Dielectric loss, metal loss, and magnetic losses.

The comparison of FBR, gain, sidelobe level, and Radiation efficiency of the antenna with and without a reflector is presented in Table 2. It is seen from the comparison table that the sidelobe level is also decreased while using a reflector.

IV. EXPERIMENTAL RESULTS AND DISCUSSION

The Antenna is fabricated on an FR4 dielectric substrate with the reflector. At first, the reflection charac-

Table 2: Comparison of antenna performance parameters with and without the reflector

Performance Parameters	Without Reflector	With Reflector
FBR (dB)	22	45
GAIN (dBi)	6.3	9.8
SLL (dB)	−11.6	−21.8
Radiation efficiency (%)	82	84

teristics of the proposed antenna are measured in VNA. Then the radiation pattern of the fabricated antenna prototype is measured in an anechoic chamber. A horn antenna having an operating frequency range of 1-20 GHz is taken as a reference at the transmitter side, whereas the proposed T-shaped fractal antenna is placed at the receiver end as an antenna under test (AUT) for the radiation pattern measurement. A minimum distance of $2D^2/\lambda$ is maintained to accommodate the far-field distance between the transmitter and the receiver. The radiation patterns of the fabricated antenna are measured for both XZ- and YZ-planes.

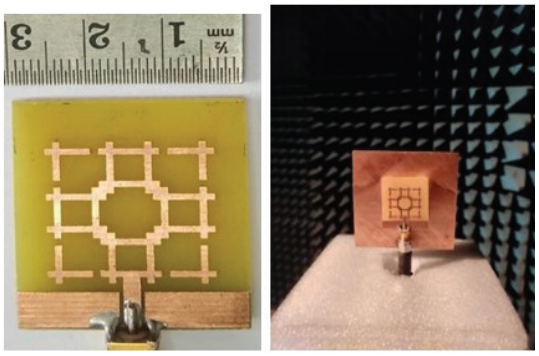

(a) (b)

Fig. 19. (a) Fabricated antenna prototype. (b) Antenna with reflector in an anechoic chamber.

The measured results need to be verified with the simulated results. The magnitude of S_{11} parameters measured using the VNA is presented in Fig. 20. A good agreement is found between the simulated and measured results. The simulated and measured radiation patterns of the proposed antenna are plotted at 8 GHz, 10 GHz, 12 GHz, and 13 GHz frequencies for both $\varphi = 0^\circ$ and $\varphi = 90^\circ$ and shown in Figs. 21 (a), (b), (c), and (d) respectively. It can be observed from the figure, that the measured radiation patterns follow the simulated trend and a slight mismatch can be found due to minor fabrication errors.

A performance comparison is carried out for the proposed antenna with other antennas from various literature in Table 3. All the antennas are compared

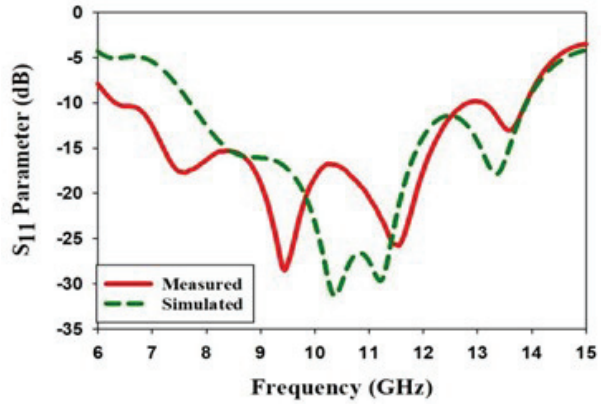

Fig. 20. Simulated and measured S_{11} Vs. frequency for the proposed antenna.

according to three important performance parameters, bandwidth, antenna gain and size of the antenna. After the application of the fractal technique, the proposed antenna exhibits a high gain of 6.3 dBi with a bandwidth of 7550 MHz. Dwivedi et al have designed an antenna in [13], having the highest fractional bandwidth of 120% than other designs. However, the same antenna has a low gain of 3.35 dBi compared to our antenna gain of 6.3 dBi. The antenna reported by Boualem et al. in [22], has a very small size but again the gain and bandwidth of this antenna are low compared to our design. After going through all the parameters of the comparison table, it is inferred that the proposed fractal antenna reported here is superior among all, in terms of its size, gain, and other performances. The proposed fractal antenna miniaturization technique is one of the simplest methods to achieve size reduction and other improved performance parameters. The antenna having such a wide band characteristic can be found suitable for a wide range of applications like earth exploration satel-

Table 3: Comparison of antenna performance parameters with other literature

Design	Res. Freq (GHz)	Fractional Bandwidth (%)	Dimension (mm^3)	Bandwidth (MHz)	Gain (dBi)
[7]	11.75	58.7	60×60×1.6	6900	6.5
[13]	6.25	**120**	27×28×1.6	7500	3.35
[21]	8.12	64	50×50×1.6	5200	4.9
[22]	8.6	37.2	24×22×0.25	3200	4
[23]	11	32	50×50	3280	4.7
[24]	9.4	37.5	25×30×9.8	3600	6
[25]	11	29	35×35×4.5	3200	4.78
[26]	4.65	71	26×47×1	3300	5
Proposed Antenna	**10**	**76**	**30×30×1.6**	**7550**	**6.3**

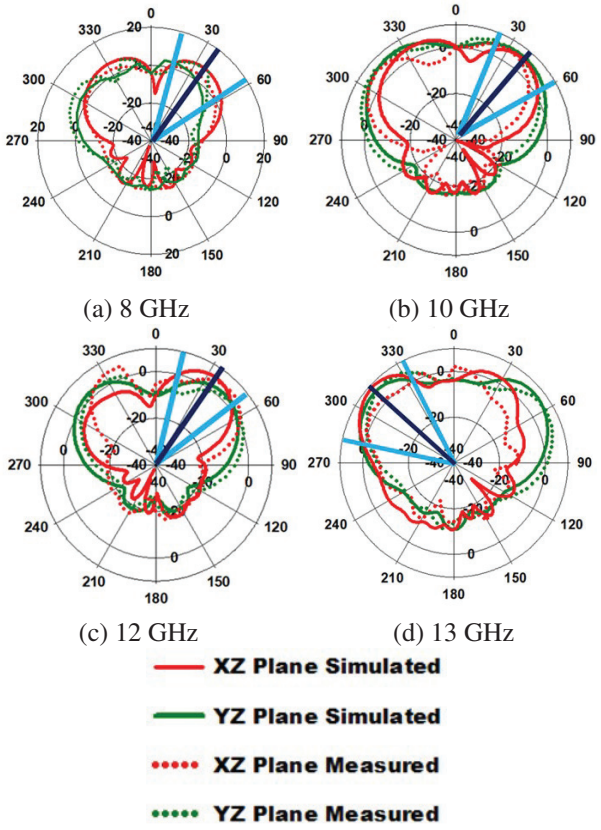

Fig. 21. Simulated and measured radiation pattern at (a) 8 GHz, (b) 10 GHz, (c) 12 GHz, and (d) 13 GHz.

lite, fixed satellite, radiolocation, maritime radio navigation, and aeronautical radio navigation.

V. CONCLUSION

A CPW fed 'T' square fractal antenna is designed for C, X, and Ku Band applications using CST Microwave Studio Software. The antenna is resonating from 6.2 GHz to 14 GHz with VSWR less than 2. Such wideband is achieved here by the use of a 'T' square fractal patch in combination with CPW feed. Due to the application of fractal, miniaturization is also achieved and the antenna performs well throughout the wideband with moderate gain from 6.3 to 10 dBi. A metallic reflector is incorporated in the design to make its radiation pattern unidirectional, thereby enhancing the Front-to-back ratio and the gain by minimizing backward radiations. The fractal antenna can be found suitable for many satellite applications with its balanced performance characteristics.

REFERENCES

[1] M. Kara, "The resonant frequency of rectangular microstrip antenna elements with various substrate thicknesses," *Microwave and Optical Technology Letters,* vol. 11, no. 2, pp. 55-59, 1996.

[2] M. Hasan and A. Suman, "Substrate height and dielectric constant dependent performance analysis of circular microstrip patch array antennas for broadband wireless access," *American Academic and Scholarly Research Journal,* vol. 4, no. 6, pp. 43-49, 2012.

[3] A. Singh and S. Singh, "Miniaturized wideband aperture coupled microstrip patch antenna by using inverted U-slot," *International Journal of Antennas and Propagation,* vol. 2014, Article ID 306942, pp. 7, 2014.

[4] S. D. Targonski, R. B. Waterhouse, and D. M. Pozar, "Design of wideband aperture-stacked patch microstrip antennas," *IEEE Trans. Antennas Propag.,* vol. 46, pp. 1245-1251, Sep. 1998.

[5] S. H. Wi, Y. S. Lee, and J. G. Yook, "Wideband microstrip patch antenna with U-shaped parasitic elements," *IEEE Trans. Antennas Propag.,* vol. 55, no. 4, pp. 1196-1199, Apr. 2007.

[6] W. Liu, Z. Chen, X. Qing, J. Shi, and F. Lin, "Miniaturized wideband metasurface antennas," *IEEE Transactions on Antennas and Propagation,* vol. 65 no. 12, pp. 7345-7349, 2017.

[7] T. Sarkar, A. Ghosh, l. L. K. Singh, S. Chattopadhyay and C. Sim, "DGS-integrated air-loaded wideband microstrip antenna for X- and Ku-band," *IEEE Antennas and Wireless Propagation Letters,* vol. 19, no. 1, pp. 114-118, Jan. 2020.

[8] G. Varshney, V. S. Pandey, R. S. Yaduvanshi, and L. Kumar, "Wide band circularly polarized dielectric resonator antenna with stair-shaped slot excitation," *IEEE Transactions on Antennas and Propagation,* vol. 65, no. 3, pp.1380-1383, Mar. 2017.

[9] B. Manimegalai, S. Raju, and V. Abhaikumar, "A multifractal cantor antenna for multiband wireless applications," *IEEE Antennas and Wireless Propagation Letters,* vol. 8, pp. 359-362, 2009.

[10] G. Bharti and J. Singh, "A design of multiband nested square shaped ring fractal antenna with circular ring elements for wireless applications," *Progress in Electromagnetics Research C*, vol. 108, pp. 115-125, 2021.

[11] D. V. Kiran, D. Sankaranarayanan, and B. Mukherjee, "Compact embedded dual-element rectangular dielectric resonator antenna combining sierpinski and minkowski fractals," *IEEE Transactions on Components, Packaging and Manufacturing Technology,* vol. 7, no. 5, pp. 786-791, 2017.

[12] M. N. Jahromi, A. Falahati, and R. M. Edwards, "Bandwidth and impedance-matching enhancement of fractal monopole antennas using compact grounded coplanar waveguide," *IEEE Transactions*

on Antennas and Propagation, vol. 59, no. 7, pp. 2480-2487, Jul. 2011.

[13] R. P. Dwivedi and U. K. Kommuri, "Compact high gain UWB antenna using fractal geometry and UWB-AMC," *Microwave Optical Technology Letters,* vol. 61, pp. 787-793, 2019.

[14] W. Chen, G. Wang, and C. Zhang, "Bandwidth enhancement of a microstrip-line-fed printed wide-slot antenna with a fractal-shaped slot," *IEEE Transactions on Antennas and Propagation,* vol. 57, no. 7, pp. 2176-2179, Jul. 2009.

[15] Y. J. Sung, "Bandwidth enhancement of a wide slot using fractal-shaped sierpinski," *IEEE Transactions on Antennas and Propagation,* vol. 59, no. 8, pp. 3076-3079, Aug. 2011.

[16] K. Vinoy and A. Pal, "Dual-frequency characteristics of Minkowski-square ring antennas," *Microwaves, Antennas & Propagation, IET*, vol. 4, no. 2, pp. 219-224, Feb. 2010.

[17] R. Garg, P. Bhartia, I. J. Bahl, and A. Ittipiboon, *Microstrip Antena Design Handbook*, Artech House, Norwood, MA, USA, 2001.

[18] C. Balanis, *Antenna Theory: Analysis and Design*, Wiley, Hoboken, NJ, USA, 2005.

[19] Recommendation ITU-R BO.791, Choice of polarization for the broadcasting-satellite service.

[20] B. Wen, L. Peng, X. Li, K. Mo, X. Jiang, and S. Li, "A low-profile and wideband unidirectional antenna using bandwidth enhanced resonance-based reflector for fifth generation (5G) systems applications," *IEEE Access,* vol. 7, pp. 27352-27361, 2019.

[21] S. Dhar, R. Ghatak, B. Gupta, and D. R. Poddar, "A wideband minkowski fractal dielectric resonator antenna," *IEEE Transactions on Antennas and Propagation,* vol. 61, no. 6, pp. 2895-2903, Jun. 2013.

[22] B. Mekimah, T. Djerafi, A. Messai, and A. Belhedri, "Broadband circularly polarized CPW-fed asymmetrically-shaped slot patch antenna for X band applications," *Progress in Electromagnetics Research Letters,* vol. 91, pp. 137-143, Jan. 2020.

[23] E. Vinodha and S. Raghavan, "A Low-profile wide band "S" shaped rectangular dielectric resonator antenna for "X" band application," *IETE Journal of Research,* vol. 67, no. 4, pp. 485-490, 2021.

[24] A. Majeed, A. Abdullah, F. Elmegri, K. Sayidmarie, R. Abd-Alhameed, and J. Noras, "Dual-segment s-shaped aperture-coupled cylindrical dielectric resonator antenna for X-band applications," *IET Microwave Antennas & Propagation,* vol. 9, no. 15, pp. 1673-1682, 2015.

[25] J. M. Lee, S.-J. Kim, G. Kwon, C. M. Song, Y. Yang, K.-Y. Lee, and K. C. Hwang, "Circularly polarized semi-eccentric annular dielectric resonator antenna for X-Band applications," *IEEE Antennas and Wireless Propagation Letters,* vol. 14, pp. 1810-1813, 2015.

[26] A. Bhattacharya, B. Roy, S. Chowdhury, and A. Bhattacharjee, "Design and analysis of a koch snowflake fractal monopole antenna for wideband communication," *Applied Computational Electromagnetics Society (ACES) Journal,* vol. 32, no. 6, pp. 548-554, 2017.

Varnikha Nanthagopal received her BE from Satyabhama University in 2013, and ME from Anna University in 2016. She is pursuing a Ph.D. from Anna University, Chennai, India. Her research articles are published in many International conferences and journals. Her research interests include fractal antennas, RF, and microwave and communication.

P. Jothilakshmi completed her B.E. degree in Electronics and Communication Engineering from the University of Madras, in 1996 and her M.E. degree in Communication Systems from Madurai Kamaraj University, in 2000. She completed her Ph.D. Degree from Anna University, Chennai, India. She is serving as a lecturer from 1996 onwards. She is currently serving as a Professor in ECE at Sri Venkateswara College of Engineering, Chennai, India. She is an active fellow in professional societies ISTE, IETE, and IAENG. She led several numbers of B.E., M.E., and Ph.D.-level projects. She has published several SCI indexed; Scopus indexed international journal papers. She presented and published papers at international and national conferences. Her research area is Microwave antenna design and wireless communication.

Decoupling Technique Based on Field Distribution on Ground Plane for WLAN MIMO Antenna Applications

Zicheng Zhou[1], Xiao-Yu Ma[2*], Zi-Yu Pang[2], Guan-Long Huang[3*], Rui-Sen Chen[3], and Changqing Gu[1]

[1]College of Electronic and Information Engineering
Nanjing University of Aeronautics and Astronautics, Nanjing, P. R. China

[2]College of Electronics and Information Engineering
Shenzhen University, Shenzhen, P. R. China
*xiaoyu_ma@foxmail.com

[3]School of AI - Guangdong & Taiwan
Foshan University, Foshan, P. R. China
*hgl@fosu.edu.cn

Abstract **–** An efficiently-decoupling method for multiple-input multiple-output (MIMO) antenna systems is proposed in this paper. A planar-modified monopole antenna operating at the WLAN band is chosen as the antenna unit. The antenna structure is based on the printed circuit board technique. By observing and analyzing the ground plane's field distribution generated by high-order modes, it is found that several stable minimum current points can be excited along the edges of the ground plane. In doing so, a high isolation can be obtained if the other antenna is placed at one of these points. The measured results and simulated results have a good agreement with each other, which well validates the proposed design concept. In addition, compared with the traditional decoupling technology, this method can improve the isolation between antennas without adding additional structures, which has excellent practicality in wireless communication system applications.

Index Terms **–** decoupling, MIMO, wireless communication system, WLAN.

I. INTRODUCTION

Nowadays, multiple-input multiple-output technology (MIMO) has been widely applied to modern wireless communication systems [1, 2]. However, as limited by internal space in some specific terminal devices, the mutual coupling of MIMO antennas will inevitably incur in these devices [3]. If the mutual coupling problem is not resolved properly, the antenna's radiation efficiency will be significantly influenced, which will largely deteriorate the communication performance.

To reduce the mutual coupling between adjacent antennas, a lot of decoupling methods have been proposed [4–10] and one of the effective methods is to place a defective ground structure (DGS) between two adjacent antennas [11]. To further reduce the degree of mutual coupling, parasitic loading is introduced to generate contrary coupling, while [12] has proposed the technique of embedding non-radiating elements between antenna elements to alter the current distribution that results in affecting the antenna radiation and achieves the purpose of reducing the mutual coupling. However, the above methods [11, 12] usually require enough spacing among antenna units, increasing the whole size of the antenna system. Thus, to reduce the size and simplify the decoupling network, another effective technique to achieve good mutual decoupling is introducing a decoupling network using reactive lumped elements [13]. Although this method can obtain good impedance matching, as well as high port-to-port isolation of the entire antenna system, the introduction of the reactive lumped components will produce parasitic effects, and the antenna efficiency will not be very high.

Even though all the aforementioned methods can achieve good mutual decoupling between adjacent antennas, they also have some limitations and complications. For example, if the ground size of the two-antenna MIMO system is relatively small, it will be very challenging for the antenna engineer to select the optimized positions that can yield the best isolation level between the antennas. Thus, it is imperative to seek a method with a lesser complex design, applicable to smaller ground plane sizes, and not involve any additional decoupling network. This paper proposes

Submitted On: July 14, 2022
Accepted On: September 8, 2022

https://doi.org/10.13052/2022.ACES.J.370906

a method of achieving good mutual decoupling between two adjacent monopole antennas without the need to load any additional complicated decoupling network. The monopole antennas are placed at the selected minimum points generated by one of MIMO antenna while observing along the edges of the ground plane, and a high isolation between the two adjacent monopole antennas can be obtained in a small space (or ground size), which can achieve a compact size of the WLAN terminals (like routers), as well as a high radiation efficiency.

II. ANTENNA STRUCTURE

For easy illustration, the MIMO antenna system is simplified, as shown in Fig. 1. It is mainly composed of the ground plane and the monopole antennas, which are placed perpendicularly to the ground plane. To form a dual-antenna MIMO system with the proposed decoupling technique, after Antenna 1 (Ant. 1) is fixed on the ground plane, Antenna 2 (Ant. 2) can be freely placed on the platform. In particular, Ant. 2 is sequentially moved from points ① to ⑥ on the ground plane during the design investigation. The points' positions are the same as those shown in Fig. 2 (a). According to the dimensions marked in Fig. 3 (b), the size of the ground plane is: L = 170 mm and W = 80 mm, and the dimensions of the

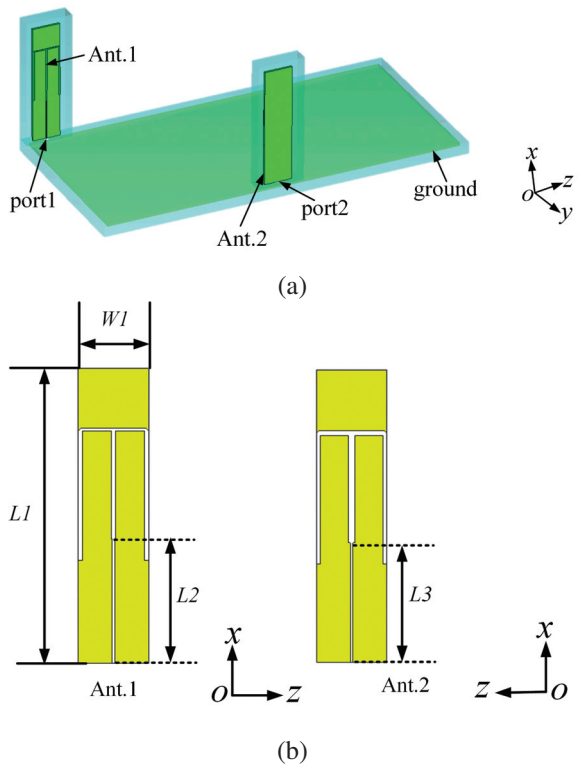

Fig. 1. Physical structure of the proposed MIMO antenna. (a) 3-D view of the whole antenna. (b) The detailed structure of the two antennas.

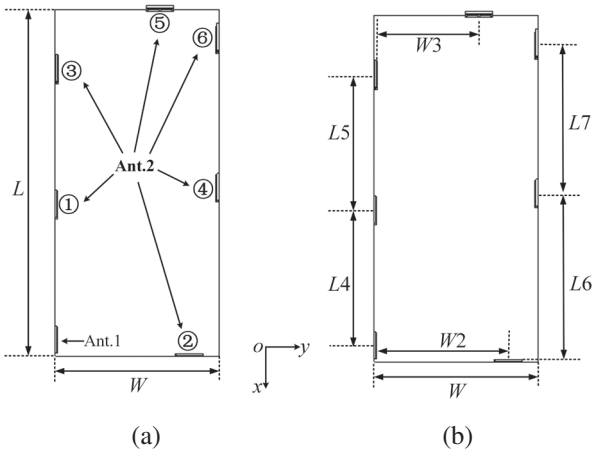

Fig. 2. Configuration of the proposed MIMO antenna system. (a) Positions of Ant. 2. (b) Dimensional parameters.

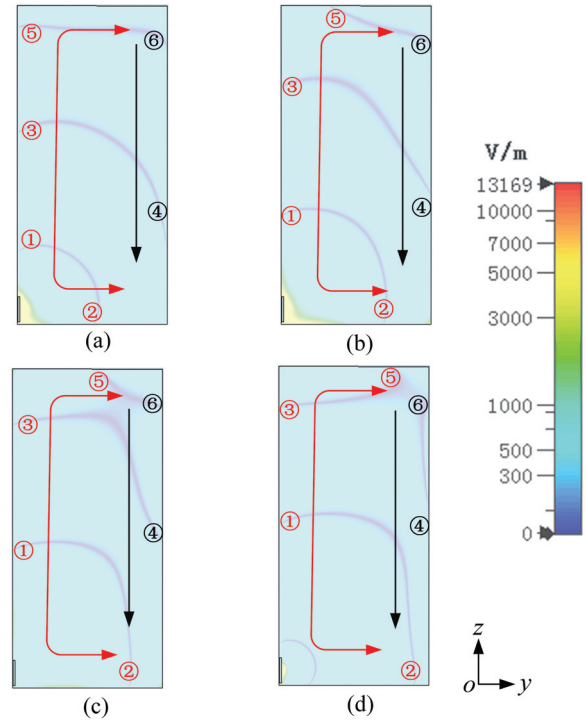

Fig. 3. Simulated E-field distribution on the ground plane at different phases. (a) 0°. (b) 45°. (c) 90°. (d) 135°.

monopole antenna are $L1$ = 50 mm and $W1$ = 13 mm. The physical dimension of Ant. 1 and Ant. 2 are identical. The dimensions are $L4$ = 66 mm, $W2$ = 64 mm, and $L5$ = 66 mm when Ant. 2 is placed at points ①-③. In the case that Ant. 2 is located at points ④-⑥, the dimensions are $L6$ = 74 mm, $W3$ = 50 mm, and $L7$ = 73 mm. The monopole antenna is designed using FR-4 PCB board with a thickness of 1.0 mm (ε_r = 4.4, tanδ =

0.02). In addition, the ground plane is also made up of an FR-4 substrate with 1.6 mm thickness. Table 1 tabulates the optimized dimensions of the proposed MIMO antenna system.

Table 1: Dimensions of the antenna system

Parameter	Value	Parameter	Value
L	170 mm	*L5*	66 mm
W	80 mm	*L6*	74 mm
L1	50 mm	*L7*	73 mm
W1	13 mm	*W2*	64 mm
L2	24 mm	*W3*	50 mm
L3	23 mm	*H1*	1.0 mm
L4	66 mm	*H2*	1.6 mm

III. WORKING MECHANISM OF THE PROPOSED DESIGN

A. Minimum point of field distribution on ground

As is well known, a monopole antenna can excite two traveling waves on the ground plane, which propagate in opposite directions along the edges [14], [15]. When these two traveling waves overlap with each other at the edges of the ground plane, an extra standing wave region can appear between the two traveling wave regions. The standing wave region contains a stable minimum point, while the traveling wave one contains a propagation minimum point.

The simulated electric field (E-field) distribution on the ground plane at 2.4 GHz at four different phases is shown in Fig. 3. It can be observed that six field amplitude minima are found on the ground plane marked by ①, ②, ③, ④, ⑤, and ⑥, respectively. Black color numbers refer to stable minimum points under the conditions of different phases, while the red ones refer to the unstable minimum points, which move along with the phases. Besides, the direction of the minimum traveling points is represented by the red arrows. While the black ones show the area covering the stable minimum points. The minimum points ① and ③ are placed at the left edge of the ground plane, and they propagate along the edge from the bottom to the top when the phase of the E-field changes. The minimum point ② is placed at the bottom edge of the ground plane and moves from left to right along the bottom edge of the ground plane. The minimum point ⑤ is placed at the upper edge of the ground plane and moves from left to right along it. On the contrary, the minimum points ④ and ⑥ are placed at the right edge of the ground plane, these points remain unchanged with the variation of the phase of the E-field.

B. Performance of MIMO antenna system

The configuration of the proposed MIMO antenna system is provided in Fig. 2. Two monopole antennas operating at 2.4 GHz, i.e., Ant. 1 and Ant. 2, are utilized in this system. The E-field distribution on the ground plane is influenced by following factors: the antenna's size, the antenna's position, the shape of the ground plane, and the size of the ground plane. To obtain better isolation in the MIMO antenna system while Ant. 2 is placed at different minimum points, the size of the antenna and its ground plane should be slightly modified.

Figure 4 shows the simulated *E*-field when Ant. 2 is placed at the minimum points ①-⑥, which indicates that both Ant. 1 and Ant. 2 are located at the minimum points excited by the other antenna.

The simulated *S*-parameters in this case are shown in Fig. 5. S_{11} and S_{22} at 2.4 GHz at each minimum point are below -18 dB, but the isolation level is different. When Ant. 2 is placed at the points ①, ②, and ③, the isolation is approximately 12.5 dB, 15 dB, and 15 dB, respectively. Therefore, one can conclude that when Ant. 2 is placed at the traveling minimum point, the *E*-field excited by Ant. 1 is nearly zero in some particular phases around Ant. 2. Ant. 2 can still be coupled via the *E*-field, and energy is still transmitted between the MIMO antennas, so the isolation is not well. As can be seen in Fig. 5 (b), when Ant. 2 is placed at the stable minimum point, the isolation of the dual-monopole MIMO antenna system has a better isolation level at around 2.4 GHz. Specifically, when Ant. 2 is placed at points ④ and ⑥, the isolation is better than 22.5 dB and 25 dB respectively. In addition, when the antenna is at minimum point ⑤, the isolation is approximately 25 dB. When Ant. 2 is placed at these positions, the *E*-field around Ant. 2 is always close to zero. In this case, the energy transferred between the antennas is very weak, so the isolation is largely improved. Hence, a significant improvement can be obtained by optimizing the positional isolation of the MIMO antennas.

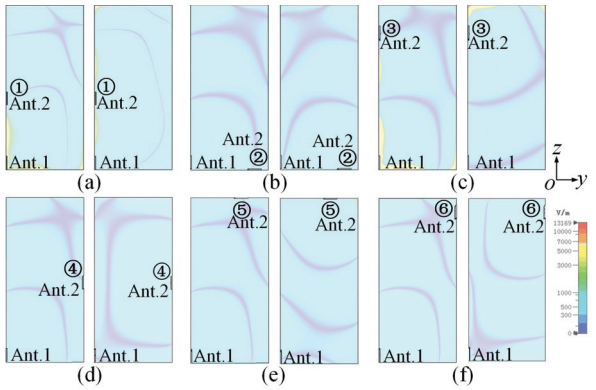

Fig. 4. Simulated E-field distribution when Ant.2 is placed at different points. (a) point ①. (b) point ②. (c) point ③. (d) point ④. (e) point ⑤. (f) point ⑥.

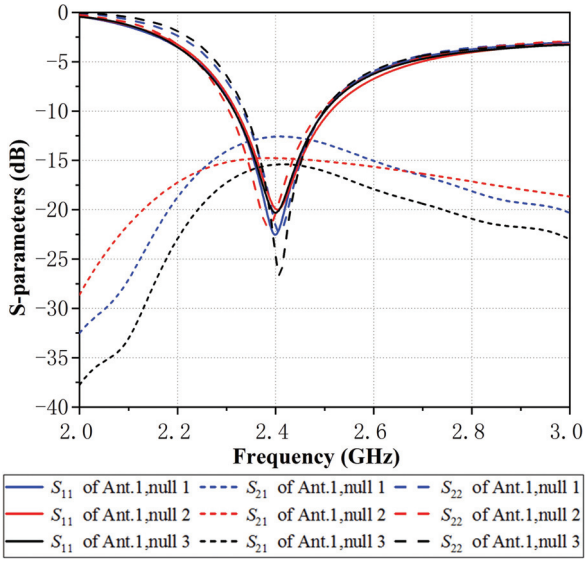

(a)

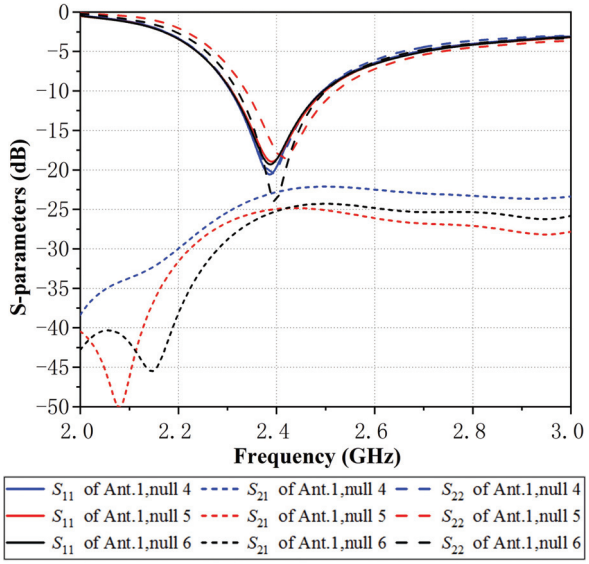

(b)

Fig. 5. Simulated S-parameters: Ant. 2 placed at the minimum points. (a) points ①-③. (b) points ④-⑥.

The simulated 3-D radiation patterns when Ant. 2 is placed at different minimum points are shown in Fig. 6, from which it can be observed that the radiations are not very stable when Ant. 2 is placed at the minimum points ①, ②, and ③. However, if Ant. 2 is placed at the points ④, ⑤, and ⑥, the radiation pattern is approximatively omnidirectional.

C. Parametric study

To in order to achieve the desired MIMO antenna system, the dimensions of the antenna radiator and the ground plane can be slightly modified to reach better isolation when Ant. 2 is moved to different minimum points.

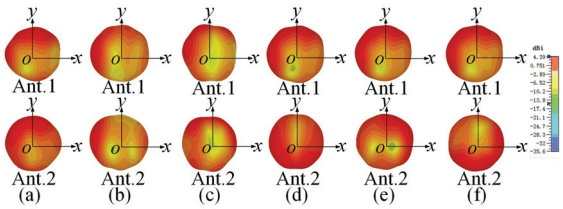

Fig. 6. The 3-D radiation patterns when Ant. 2 is placed at the minimum points ①-⑥.

This paper performs a parametric study to find the optimum antenna position with the best isolation. Figure 7 shows the simulated reflection coefficient and isolation at different ground plane lengths (L). As the length increases, the isolation first increases and then decreases. When L = 170 mm, the entire working frequency band has the best isolation. In contrast, the reflection coefficient of the two antennas has only a slight change, which shows that the length of the ground plane will only have a certain impact on the isolation. Figure 8 shows the simulated S-parameters of the different antenna spacings ($L6$). With the increase of L6, the reflection coefficient of the MIMO antennas basically does not change, but the isolation becomes worse. This shows that better isolation can be obtained only when Ant. 2 is placed at a proper position.

According to the previous analysis, it can be concluded that by changing the ground plane length, antenna spacing and other parameters, the reflection coefficient of the two antennas would not change significantly,

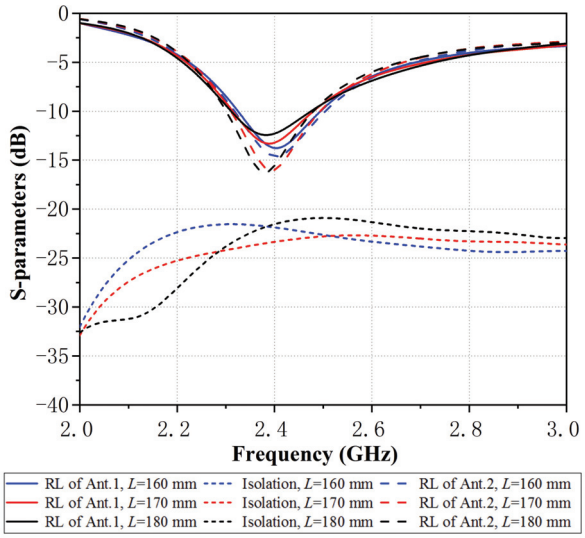

Fig. 7. Simulated S-parameters with different ground lengths *(L)*.

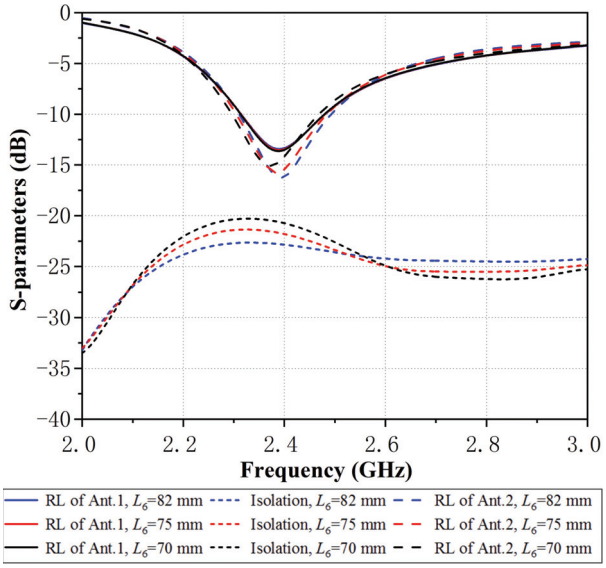

Fig. 8. Simulated S-parameters with different antenna spacings *(L6)*.

and their isolation could be affected to a certain extent. Therefore, it is necessary to select proper design parameters and ensure that there is the best isolation at 2.4 GHz to get the most compliant MIMO antenna system.

IV. RESULTS ANALYSIS

Figure 9 shows three prototypes of the proposed MIMO antennas for WLAN terminal application. The size of the prototypes is similar to a typical Wi-Fi router in the commercial market. The antennas' location corresponds to Ant. 2 placed at the minimum point ③, point ④, and point ⑥. As shown in Fig. 9, the two monopole antennas are printed on the FR-4 dielectric substrate and fed with SMA connectors. To verify the operational characteristics, the proposed MIMO antennas are fabricated and measured.

As shown by the comparison chart in Fig. 10, there is a good agreement between measured and simulated results. It can be seen from Fig. 10 (a) that if Ant. 2 is placed at the point ③, S_{11} and S_{22} are both greater than -10 dB, and the port-to-port isolation is better than 15 dB at the operating frequency. Figures 10 (b) and 10 (c) show that when Ant. 2 is placed at stable minimum point ④ and point ⑥, S_{11} and S_{22} are also both below -10 dB, while the isolation can be improved to 20 dB. Compared with Fig. 10 (a), S_{11} and S_{22} are almost identical, but the isolation is improved. Generally, a larger distance between the monopole antennas will result in a better isolation. However, in the proposed MIMO antenna system, compared with Ant. 2 placed at the point ③, the spacing between the antennas is obviously shorter when Ant. 2 is at minimum point ④, but its isolation is increasing.

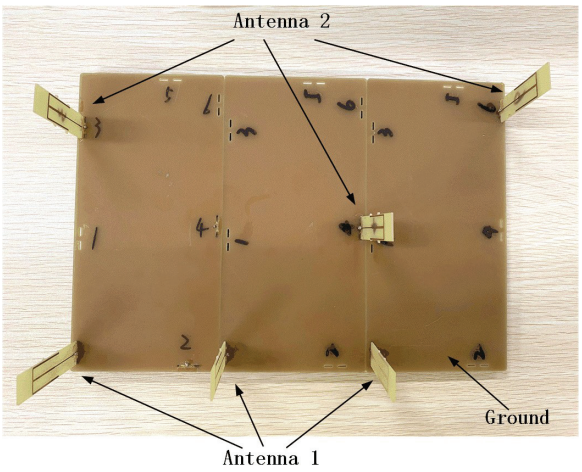

Fig. 9. Prototypes of the proposed MIMO antenna (three prototypes placed next to each other).

Figure 11 shows the comparison of the simulated and measured radiation pattern of proposed MIMO antennas in *E*-plane (*xoz*) and *H*-plane (*yo*u) at 2.4 GHz. It can be seen that the measurement result is approaching the simulation result. The results show that the peak achieved gain of Ant. 1 and Ant. 2 are both greater than 2.7 dBi.

To verify the diversity performance of the designed MIMO antenna system, Table 2 shows the envelope correlation coefficients (ECC) when Ant. 2 is placed at minimum point ③, point ④, and point ⑥. ECC describes the level of channel independence, which is frequently used to evaluate the performance of the MIMO antenna system. The larger mode diversity of different antenna elements will produce lower ECC values, so for the MIMO antenna system, the smaller the value of ECC is, the weaker the coupling between antennas would be. It can be seen from the table that when Ant. 2 is at minimum point ③, the ECC increases; on the contrary, when it is at stable minimum point ④ and ⑥, the ECC decreases, which means the coupling between antennas is weaker. This further verifies that Ant. 2 has better radiation performance when it is at the stable minimum point.

V. CONCLUSION

This paper proposes a method for efficiently decoupling the monopole antennas from the ground plane under the operation of high-order modes, which is suitable for WLAN MIMO platform applications. The monopole

Table 2: ECCs of the proposed MIMO antenna

	Minimum Point ③	Minimum Point ④	Minimum Point ⑥
ECC	0.057	0.024	0.018

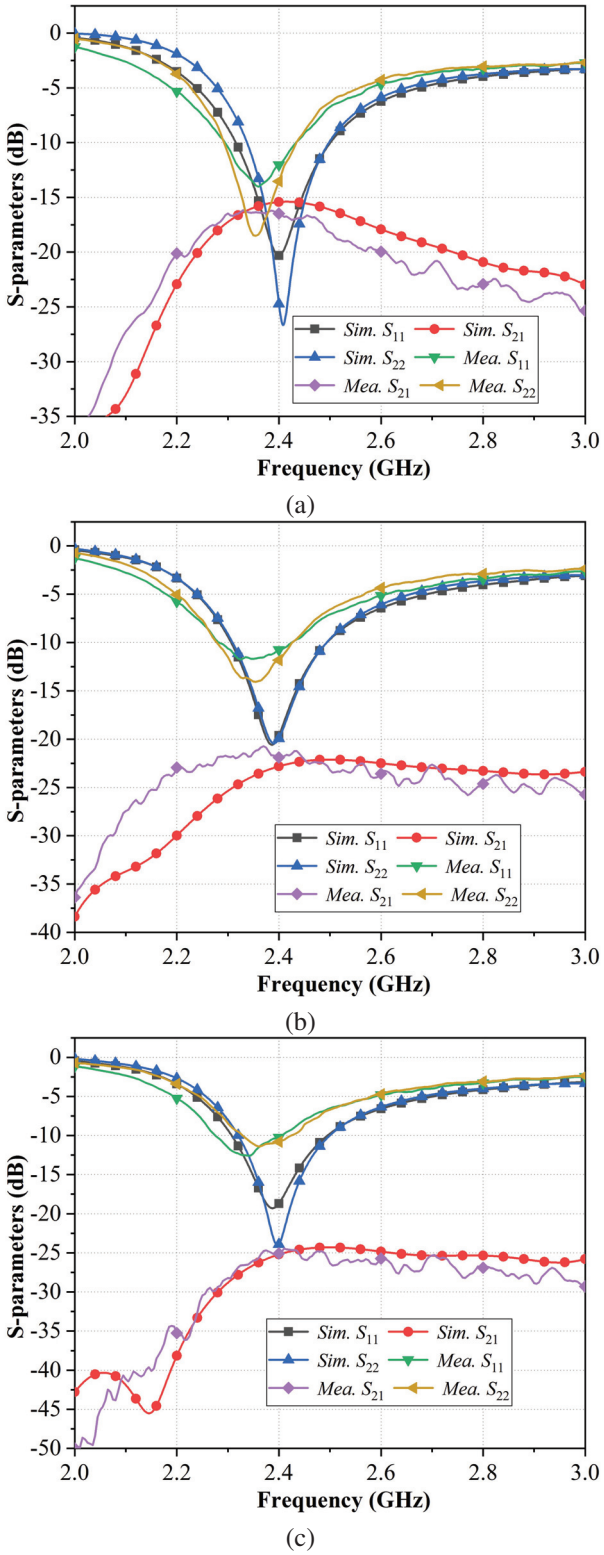

Fig. 10. S-parameters of measurement and simulation when Ant. 2 is placed at different points. (a) point ③. (b) point ④. (c) point ⑥.

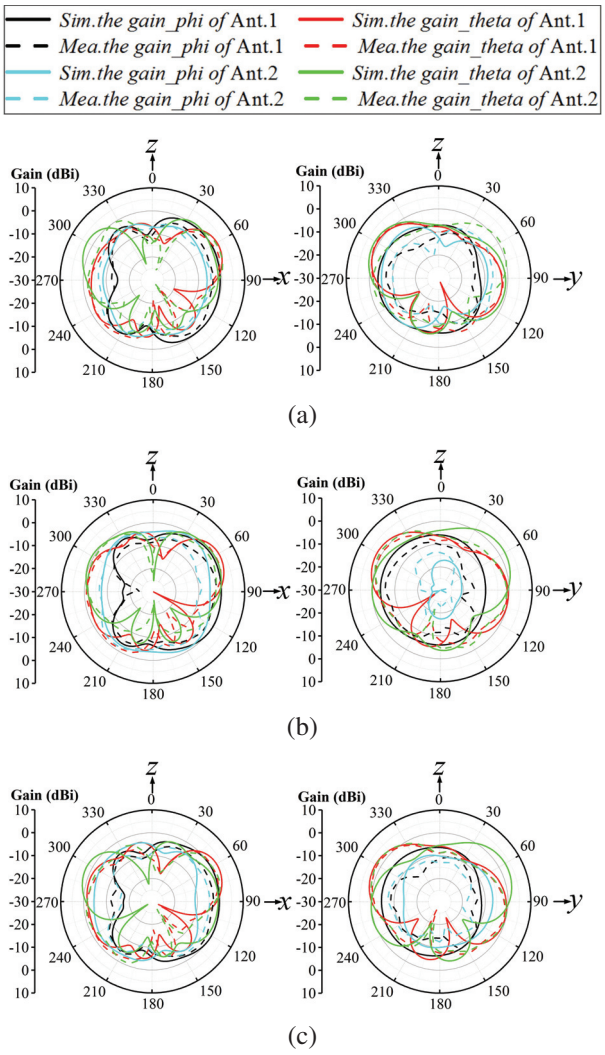

Fig. 11. The 2-D radiation patterns of measurement and simulation when Ant. 2 is placed at different points. (a) point ③. (b) point ④. (c) point ⑥.

antenna will generate a particular electric field distribution on the ground plane under the operation of high-order modes. These high-order modes will produce some stable E-field points. Then, by placing the other monopole antenna at these points, high isolation can be obtained between these two antennas without affecting their operation. This attractive method can realize the decoupling between antennas without utilizing extra elements or another decoupling network, which can make the decoupling mechanism simpler and also has a higher isolation value.

REFERENCES

[1] W. Shi, X. Liu, and Y. Li, "ULA fitting for MIMO radar," *IEEE Communications Letters*, vol. 26, 2022.

[2] W. Shi, S. A. Vorobyov, and Y. Li, "ULA fitting for sparse array design," *IEEE Transactions on Signal Processing*, vol. 69, pp. 6431-6447, 2021.

[3] F. Faraz, X. Chen, Q. Li, J. Tang, J. Li, T. A. Khan, and X. Zhang,, "Mutual coupling reduction of dual polarized low profile MIMO antenna using decoupling resonators," *Applied Computational Electromagnetics Society (ACES) Journal*, vol. 35, no. 1, pp. 38-43, 2020.

[4] X. Chen, M. Zhao, H. Huang, Y. Wang, S. Zhu, C. Zhang, J. Yi, and A. A. Kishk, "Simultaneous decoupling and decorrelation scheme of MIMO arrays," *IEEE Transactions on Vehicular Technology*, vol. 71, no. 2, pp. 2164-2169, Feb. 2022.

[5] B. Liu, X. Chen, J. Tang, A. Zhang, and A. Kishk, "Co- and cross-polarization decoupling structure with polarization rotation property between linearly polarized dipole antennas with application to decoupling of circularly polarized antennas," *IEEE Transactions on Antennas and Propagation*, vol. 70, no. 1, pp. 702-707, Jan. 2022.

[6] B. Qian, X. Chen, and A. Kishk, "Decoupling of microstrip antennas with defected ground structure using the common/differential mode theory," *IEEE Antennas and Wireless Propagation Letters*, vol. 20, no. 5, pp. 828-832, May 2021.

[7] Y. Wang, X. Chen, X. Liu, J. Yi, J. Chen, A. Zhang, and A. A. Kishk, "Improvement of diversity and capacity of MIMO system using scatterer array," *IEEE Transactions on Antennas and Propagation*, vol. 70, no. 1, pp. 789-794, Jan. 2022.

[8] K. Yu, Y. Li, and X. Liu, "Mutual coupling reduction of a MIMO antenna array using 3-D novel meta-material structures," *Applied Computational Electromagnetics Society (ACES) Journal*, vol. 33, no. 7, pp. 758-763, 2018.

[9] S. Luo, Y. Li, Y. Xia, and L. Zhang, "A low mutual coupling antenna array with gain enhancement using metamaterial loading and neutralization line structure," *Applied Computational Electromagnetics Society (ACES) Journal*, vol. 34, no. 3, pp. 411-418, 2019.

[10] J. Jiang, Y. Xia, and Y. Li, "High isolated X-band MIMO array using novel wheel-like metamaterial decoupling structure," *Applied Computational Electromagnetics Society (ACES) Journal*, vol. 34, no. 12, pp. 1829-1836, 2019.

[11] S. W. Cheung, Q. Li, D. Wu, C. Zhou, and B. Wang, "Defected ground structure with two resonances for decoupling of dual-band MIMO antenna," *IEEE International Symposium on Antennas and Propagation & USNC/URSI National Radio Science Meeting*, pp. 1645-1646, 2017.

[12] Z. Li, Z. Du, M. Takahashi, K. Saito, and K. Ito, "Reducing mutual coupling of MIMO antennas with parasitic elements for mobile terminals," *IEEE Transactions on Antennas and Propagation*, vol. 60, no. 2, pp. 473-481, Feb. 2012.

[13] C. Wu, C. Chiu, and T. Ma, "Very compact fully lumped decoupling network for a coupled two-element array," *IEEE Antennas and Wireless Propagation Letters*, vol. 15, pp. 158-161, 2016.

[14] X. Zhao, S. P. Yeo, and L. C. Ong, "Decoupling of inverted-F antennas with high-order modes of ground plane for 5G mobile MIMO platform," *IEEE Transactions on Antennas and Propagation*, vol. 66, no. 9, pp. 4485-4495, Sep. 2018.

[15] X.-Y. Ma, Z.-Y. Pang, G. Zhao, and G.-L. Huang, "An efficient decoupling technique for WLAN MIMO antenna applications," *IEEE Asia-Pacific Microwave Conference (APMC)*, Hong Kong, Hong Kong, pp. 75-77, 2020.

Bandwidth Enhancement of Slot Antenna Using Fractal Shaped Isosceles for UWB Applications

Djelloul Aissaoui[1,2], Abdelhalim Chaabane[3], Noureddine Boukli-Hacene[2], and Tayeb A. Denidni [4]

[1]Faculté des sciences Technologiques
Université Ziane-Achour de Djelfa, 17000, Algeria
djelloul.aissaoui@univ-djelfa.dz

[2]Laboratoire De Télécommunications
Université De Tlemcen, BP 230, Pole Chetouane, Tlemcen 13000, Algeria
abdelhafid.bouacha@gmail.com

[3]Laboratoire des Télécommunications, Département d'Electronique et Télécommunications
Faculté des Sciences et de la Technologie, Université 8 Mai 1945 Guelma, BP 401, Guelma 24000, Algeria
abdelhalim.chaabane@univ-guelma.dz

[4]Institut National de la Recherche Scientifique
Centre EMT, 800 Rue De La Gauchetiére West, Suite 6900, Montreal, Quebec, H5A-1K6, Canada
denidni@emt.inrs.ca

Abstract – In this paper, a coplanar waveguide (CPW) fed slot antenna using fractal shaped isosceles trapezoidal corrugations is designed and presented for Ultra-Wideband (UWB) applications. The proposed antenna is formed by a regular hexagonal patch fed through a CPW feed line and radiates amidst a notched wide hexagonal slot. The edge of the wide slot is shaped by a fractal structure that is formed by five trapezoidal notches. The antenna is printed on RO4350B substrate having a compact size of $0.305\lambda_0 \times 0.313\lambda_0 \times 0.012\lambda_0$ at 2.35 GHz. Good agreement is registered between the experimental results of the fabricated prototype and the calculated ones. By using an Agilent 8722ES vector network analyzer, the fabricated prototype confirms that the antenna has an excellent matching impedance over the bandwidth 2.35-10.65 GHz (127%) which covers the entire UWB band. Furthermore, good radiation performances are measured in an anechoic chamber. Consistent radiation patterns with a reasonable peak gain are measured over the entire working bandwidth. Therefore, the designed structure may be worthy considered for different wireless communications systems.

Index Terms – coplanar waveguide (CPW), fractal antenna, isosceles trapezoidal corrugations, slot antenna, ultra-wideband (UWB) antenna.

I. INTRODUCTION

Over the last few years, the appliance of the Ultra-wideband (UWB) technologies for modern wireless communication systems has received much appreciation owing to their promote features over a wide transmission capacity, such as low power level consuming, low signal disturbances, opportunity of low-cost transceivers, simplicity, and higher data transmission rate [1–3]. UWB systems have attracted enormous preoccupation due to the large bandwidth of 7.5 GHz extending from 3.1 to 10.6 GHz, which was attributed by the FederalCommunications Commission in February 2002 [4]. In today's world, UWB technology has been applied for several applications, such as radar detection, satellite communications, and vehicular communications systems [5]. Recently, enormous attempts have been concentrated on the expansion of UWB microwave components to become more compact and to improve their performances [6]. Typically, printed monopole planar antennas offer the main requirements and considered as excellent devices for UWB applications; dues to the characteristics that are proposed, such as low cost, low profile, compact sizes, possibility of incorporation with other RF devices, larger bandwidth, and consistent radiation patterns with acceptable gains over the considered bandwidths. For these reasons, the development of UWB antennas has spurred academic and industrial research. In recent few

Submitted On: January 28, 2022
Accepted On: September 30, 2022

https://doi.org/10.13052/2022.ACES.J.370907

years, several UWB planar antennas with miscellaneous configurations have been designed. In this respect, various techniques have been used to improve the main requested bandwidth such as the use of large etched slot in the ground plane as in [7]. Another method is to use fractal structures that are also able to diminish the attributed size and to enhance the antenna adaptation as in [8]. Unfortunately, most of the existing antennas in the literature don't cover the entire licensed UWB bandwidth and/or have complex and large configurations. In [9], an octagonal ring shaped antenna was proposed for UWB application. However, the main disadvantage of this antenna is that it doesn't cover the entire licensed UWB range. A bi-directional tapered slot antenna that has a large size of $55 \times 48 \times 1.5$ mm^3 has been proposed in [10]. A probe-fed hexagonal UWB antenna with AMC reflector having a complex structure and a bulky size of $100 \times 100 \times 15$ mm^3 has been proposed in [11]. A narrow-band Fabry Perot cavity UWB antenna that has a complex structure and a large size of $169 \times 169 \times 38.46$ mm^3 has been introduced in [12]. In [13], a narrow band antipodal UWB Vivaldi antenna that has a complex structure and a bulky size of $100 \times 104 \times 1.5$ mm^3 has been proposed. A closed loop resonator based compact UWB antenna that has a complex structure and a large size of $100 \times 100 \times 16$ mm^3 has been proposed in [14]. A complex geometry that covers only the frequency range of 1.31 – 6.81 GHz has been presented in [15].

II. ANTENNA CONFIGURATION AND DESIGN

The geometrical configuration of the proposed wide hexagonal slot fractal antenna is presented in Fig. 1. It is designed using RO4320B substrate having a relative permittivity ε_r= 3.66, a thickness of 1.524 mm and a loss tangent of 0.004. The proposed CPW-fed UWB slot antenna is basically composed of a wide-hexagonal-slot antenna and a parasitic hexagonal patch fed by a CPW. Thus, there are two radiating elements: the wide-hexagonal-slot and the hexagonal patch which acts as a tuning stub. Moreover, five trapezoidal slots are inserted symmetrically on the perimeter of the wide-hexagonal-slot antenna to improve the impedance characteristics. The hexagonal patch antenna has been designed by relating the areas of a circular patch with the one of the hexagonal patch structure. As given in [16], the side length B of a hexagonal patch can be calculated using the equation

$$B \approx 1.1\, r_e, \tag{1}$$

where r_e is the equivalent radius of a comparable circular patch given by the formula

$$r_e = \sqrt{r^2 - \frac{2hr}{\pi\varepsilon_r}\left(ln\frac{\pi r}{2h} + 1.7726\right)}\ , \tag{2}$$

where ε is the dielectric constant of the substrate, c is the speed of light in free space, h is the thickness of the substrate, and r is the radius of a comparable circular patch. The resonant frequency f_r of the hexagonal patch can be calculated using the formula (3).

$$f_r \approx \frac{Y_{mn}c}{2\pi r_e\sqrt{\varepsilon_r}}, \tag{3}$$

where Y_{mn} is the mth zero of the derivative of the Bessel function of order n. The values of $Y_{mn}$are given in Table 1.

Table 1: Values of Y_{mn}

Modes	Y_{mn}
TM01	0
TM11	1.841
TM21	3.054
TM02	3.832
TM31	4.201
TM41	5.317
TM51	6.415

The edge of the proposed wide slot is constituted by a fractal structure that is formed by notching a succession of five regular isosceles trapezoidal from the middle of the ribs constituting the hexagonal slot that having a length of A = 16.2 mm. The isosceles trapezoidal notches have three identical ribs of length h_1= 3.2 mm and one lengthy rib of length h_2= 6.4 mm.

The radiating element is lodged inside a ground plane having the same outer dimensions of the substrate of $0.305\lambda_0 \times 0.313\lambda_0$ at 2.35 GHz. The patch consists of a regular hexagon with a length of B = 10.5 mm and is fed by a CPW with an input impedance of value 50 Ω. The strip width W_f and the gap g between the feed line and the ground plane have of values 2.9 mm and

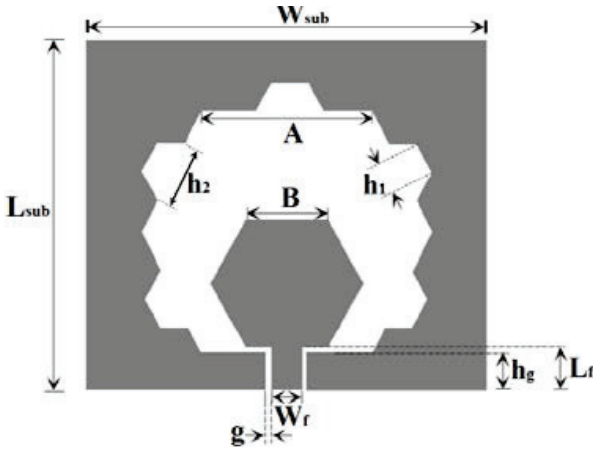

Fig. 1. Geometrical configuration of the proposed UWB slot antenna.

0.275 mm, respectively. As illustrated in Fig. 1, the designed antenna has a compact size of $0.305\lambda_0 \times 0.313\lambda_0 \times 0.012\lambda_0$ at 2.35 GHz. The detailed dimensions of the proposed UWB fractal antenna are listed in Table 1.

III. RESULTS AND PARAMETRIC STUDY

The electromagnetic solver, CST Microwave Studio [17], was used to numerically calculate and optimize the proposed fractal antenna. The reflection coefficient $|S_{11}|$of the simulated antenna, with the optimized parameters listed in Table 1, is depicted in Fig. 2. As a consequence of applying isosceles trapezoidal fractal elements on the proposed antenna the impedance bandwidth is enlarged by a 4.79 GHz; the high-frequency side is shifted up from 8.35 GHz to 12.75 GHz and the low-frequency side of the working bandwidth is also shifted down from 2.66 GHz to 2.27 GHz. Thereby, a 60.8% fractional bandwidth expansion is achieved (from 77.7% to 138.5%). Therefore, a UWB ranging from 2.27 to 12.75 GHz is exhibited which covers the entire UWB spectrum from 3.1 to 10.6 GHz. to show the effect of the antenna parameters on the bandwidth performance, a parametric study was carried out by changing one of the parameters while keeping all other parameters fixed as listed in Table 2. The first parametric study is on the length h_1 of the trapezoidal fractal notch elements. The influence of this parameter on the impedance bandwidth and the adaptation of the simulated antenna for different values 0.5, 1.5, 3.2, 4.5, and 5.5 mm are plotted in Fig. 3 (a). It can be seen that as the length h_1 augments from 0.5 to 3.2 mm the impedance bandwidth increases greatly by 36.52% (from 102.07% to 138.62%). However, the bandwidth decreases when the length h_1 exceeds 3.2 mm. Therewithal, the optimal length of the trapezoidal corrugations is found to be at h_1=3.2 mm. In addition, the lower frequencies of the bandwidth change slightly by increasing the length h_1 of the trapezoidal notches, while at the middle and the high frequencies, the augmentation of this parameter combines the resonances of the bandwidth that leads to improving the upper frequency of the bandwidth from 8.3 to 12.4 GHz

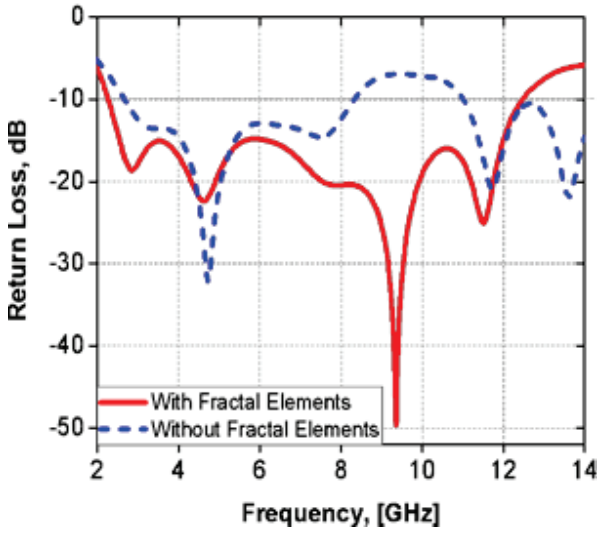

Fig. 2. Simulated return loss of the two antennas: for referenced antenna (dashed line); for the proposed UWB slot antenna (solid line).

Table 2: Optimized dimensions of the proposed slot antenna in term of wavelength at 2.35 GHz

Parameters	Dimensions [m]	Parameters	Dimensions [m]
A	$0.1269\lambda_0$	L_{sub}	$0.3055\lambda_0$
B	$0.0823\lambda_0$	W_{sub}	$0.3133\lambda_0$
h_1	$0.0251\lambda_0$	W_f	$0.0227\lambda_0$
h_2	$0.0501\lambda_0$	L_f	$0.0760\lambda_0$
h_g	$0.0204\lambda_0$	g	$0.0021\lambda_0$

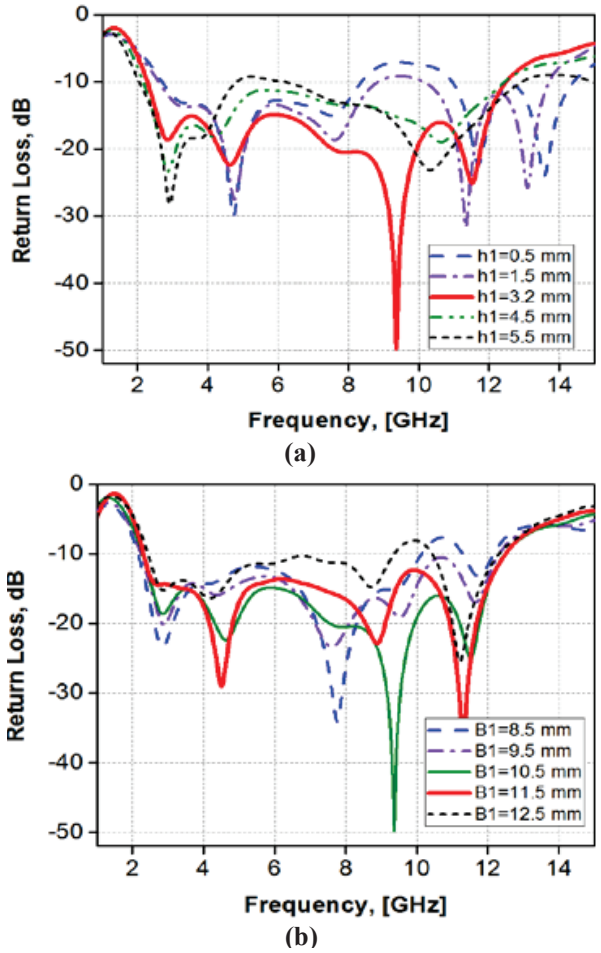

Fig. 3. *Continued*.

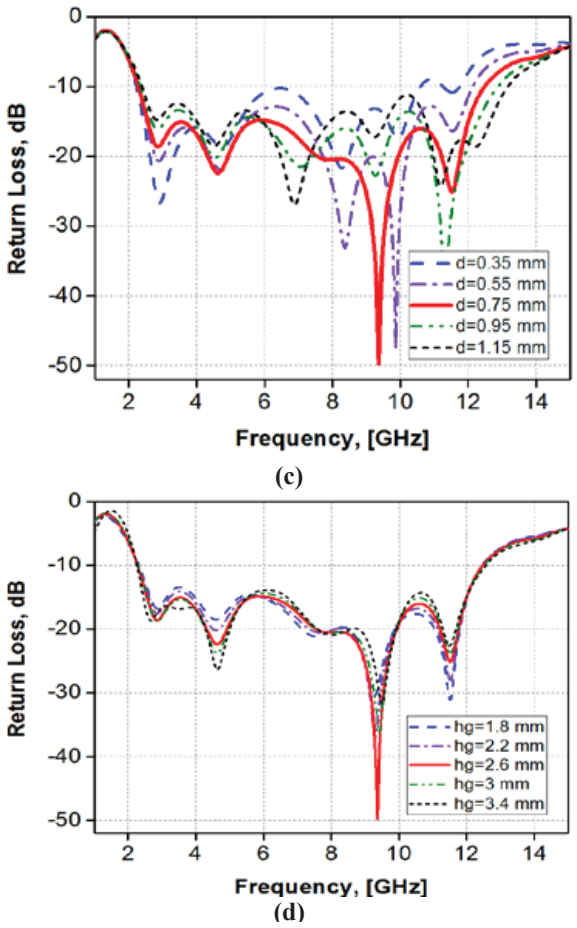

Fig. 3. Effect of different parameters on the reflection coefficient of the proposed antenna: (a) effect of the trapezoidal notch length; (b) effect of the parasitic patch length; (c) effect of the gap between the parasitic patch and the ground plane; (d) effect of the ground plane length.

and, consequently, the UWB characteristic of the proposed antenna is achieved. Therefore, the parameter h_1 represents a major impact on the impedance-matching performance of the proposed antenna. The impact of adjusting the patch side length B on the bandwidth performance is also studied. The antenna was calculated for different values of parameter B commencing from 7.5 to 11.5 mm with an increment of 1 mm, the obtained results are presented in Fig. 3 (b). As can be observed, the impact of patch length B on the impedance bandwidth and the adaptation performances is clearly visible. It is shown that the antenna bandwidth becomes wider by 9% (from 129.62% to 138.62%) when increasing the side length B from 7.5 to 10.5 mm. However, the bandwidth does not augment any further when the side length exceeds 10.5 mm. It can be noticed that as the patch augments in length a better adaptation performance is achieved over the working bandwidth. As illustrated in Fig. 3 (b), when B_1 exceeds 9.5 mm, the matching characteristics of the proposed antenna are enhanced at 10.7 GHz. When the length B_1 exceeds 10.5 mm, the $|S_{11}|$becomes narrower because of the growth of the capacitive coupling between the radiating element and the ground plane. Thus, the patch leads to augmenting greatly the upper frequency of the operating bandwidth. Thereby, the optimum value of the parameter B_1 is taken at 10.5 mm. The mutual coupling between the feed and the patch has an important impact on the antenna adaptation performance. For this reason, the impact of the gap d separating the patch and the ground plane is furthermore studied. Figure 3 (c) depicts the $|S_{11}|$for various values of gap d varying between 0.35 and 1.15 mm with an increment of 0.2 mm. As it is shown, this gap d augments the upper side of the bandwidth augments, whereas, the lower side is nearly invariable. Therefore, the adaptation improves and the total impedance bandwidth augments. The optimum distance separating the patch and the ground plane is obtained at 0.75 mm. When the gap d exceeds 0.75 mm, the $|S_{11}|$becomes narrower because the antenna impedance matching is going bad.

Figure 3 (d) presents the impact of the ground plane length h_g on the $|S_{11}|$. Its influence was studied for different lengths of the ground plane ranging from 1.8 to 3.4 mm with an increment of 0.4 mm. It can be seen that as the length h_g augments, the lower side of the impedance bandwidth as well as the upper side of the bandwidth changes slightly. Therefore, it is clearly observed that the length h_g has not a considerable impact on the antenna bandwidth. The optimum ground plane length for the proposed antenna was optimized at 2.6 mm.

IV. MEASURED RESULTS AND DISCUSSION

To give credence to the calculated results, a prototype of the proposed UWB slot antenna with the optimized geometrical dimensions were constructed and measured. Figure 4 presents a photograph of the realized prototype. The reflection coefficient $|S_{11}|$of the fabricated antenna is then measured using an Agilent 8722ES vector network analyzer. Figure 5 shows the measured reflection coefficient against their simulated results. It indicates that the fabricated antenna exhibits a measured impedance bandwidth as large as 8.32 GHz and covers the band ranging from 2.35 GHz to 10.67 GHz, relatively about 127%, which is suitable for UWB applications.

The comparison between simulated and measured results of the coefficient reflection indicates that there is a slight difference. At lower frequencies, an excellent concordance is observed between the calculated and measured results. Besides, there is a little disagreement at high frequencies which is mainly due to the fabrication tolerance and connector soldering.

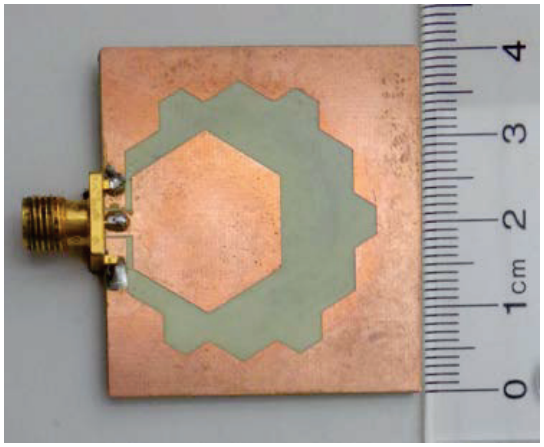

Fig. 4. Photograph of the proposed CPW-fed UWB slot antenna.

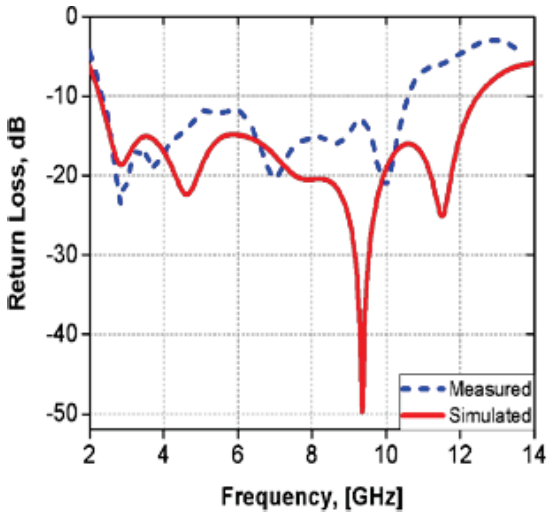

Fig. 5. Simulated and measured return loss S_{11} [dB] against frequency.

Furthermore, the H- and E- plane patterns of the fabricated antenna were measured in an anechoic chamber and compared with the predicted ones. Figure 6 shows the both measured and simulated 2-D far-field radiation patterns of the fabricated antenna in two principal planes, the E and H-planes for three respective frequencies 3, 5, and 9.5 GHz. Excellent agreements are achieved between the measured results and the calculated ones. In addition, the quasi-omnidirectional patterns can be observed in the H-plane at all frequencies, while in the E-plane, a bidirectional radiation pattern is achieved at the frequencies 3 and 5 GHz. At high frequencies around 9.5 GHz, the measured radiation pattern in the E-plane is no longer bidirectional. The small deformation at higher frequencies is probably due to the excitation of higher-order modes [18–19]. Figure 7 depicts the measured and

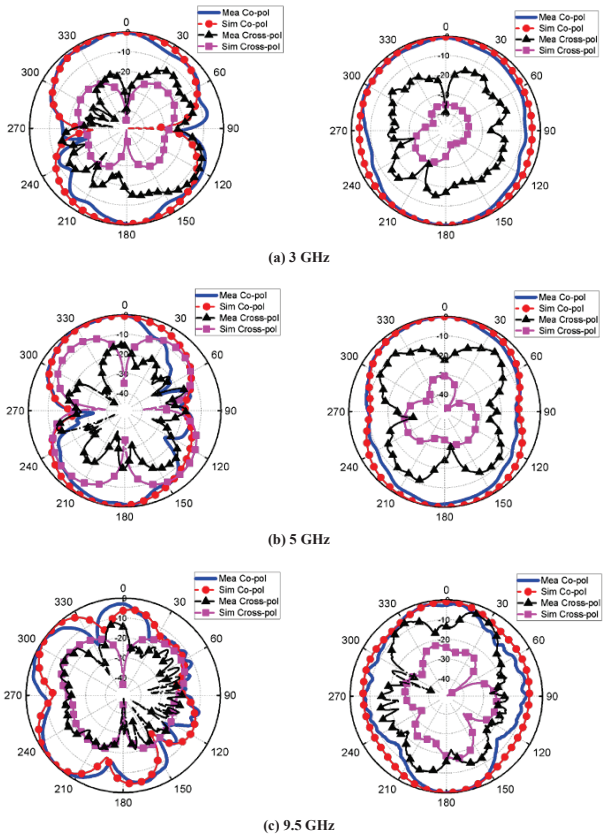

Fig. 6. Measured and simulated normalized radiation patterns of the proposed UWB slot antenna in E-plane (left) and H-plane (right) at three frequencies: (a) 3 GHz, (b) 5 GHz, and (c) 9.5 GHz.

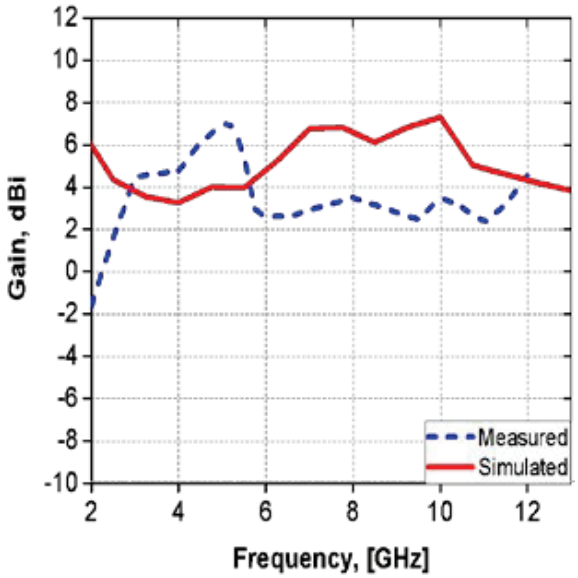

Fig. 7. Gain of the proposed UWB slot antenna versus frequency.

Table 3: Comparison of the fabricated antenna with other recently published antennas

Ref. No.	Antenna structure	Ground plane (GP)	Substrate/ permittivity	Electrical size	Bandwidth (GHz)	Bandwidth (%)	Peak Gain (dBi)	Ease of fabrication
[24]	Microstrip line-fed monopole antenna	Partial GP	FR4 ε_r=4.6	$0.338\lambda_0$ $\times 0.347\lambda_0$ $\times\ 0.014\lambda_0$	2.6-12.3	130.2	5.52	Easy
[25]	CPW-fed U-shaped monopole antenna	Partial GP	FR4 ε_r=4.4	$0.402\lambda_0$ $\times 0.435\lambda_0$ $\times\ 0.0201\lambda_0$	4.02-10.7	90.76	3.54	Easy
[26]	L-shaped feed line aperture antenna	Slotted GP	FR4 ε_r=4.4	$0.568\lambda_0$ $\times 0.568\lambda_0$ $\times 0.0116\lambda_0$	2.9-8	93.5	4.9	Easy
[27]	CPW-fed printed monopole antenna	Partial GP	FR4 ε_r=4.4	$0.358\lambda_0$ $\times 0.358\lambda_0$ $\times 0.0057\lambda_0$	2.15- 6.97	105.70	5	Easy
[28]	Metasurface-based microstrip-fed planar antenna	Partial GP	FR4 ε_r=4.4	$0.34\lambda_0$ $\times 0.34\lambda_0$ $\times 0.05\lambda_0$	3.1-10.6	109.49	6.8	Hard
[29]	Coaxial probe-fed microstrip patch with metamaterial-inspired reactive impedance surface	Full GP	RO4003 ε_r =3.38	$0.58\lambda_0$ $\times 0.58\lambda_0$ $\times 0.1\lambda_0$	4.64-7.3	44.5	7.2	Hard
[30]	CPW-fed cauliflower shaped antenna	Partial GP	RO-4350B ε_r=3.48	$0.368\lambda_0$ $\times\ 0.417\lambda_0$ $\times 0.015\lambda_0$	3.05-10.96	113	5.68	Hard
[31]	Microstrip line-fed question mark shaped antenna	Partial GP	FR4 ε_r=4.4	$0.347\lambda_0$ $\times 0.393\lambda_0$ $\times 0.017\lambda_0$	3.47-12.11	110.91	6	Easy
This work	CPW-fed slot antenna with fractal shaped isosceles trapezoidal	Slotted GP	RO-4350B ε_r=3.66	$0.305\lambda_0$ $\times\ 0.313\lambda_0$ $\times\ 0.012\lambda_0$	2.35-10.65	127	7.02	Easy

simulated peak gain of the fabricated prototype. Acceptable values are achieved in the whole UWB range with a maximum gain of 7.02 dBi attained at about the frequency of 5.15 GHz. The discrepancy between the simulated and measured gains may be due to many reflections into the electromagnetic waves between the tested antenna and reference antenna (double ridged horn antenna AH-118 operating between 1 and 18 GHz). The reflections may come from the room floor and ceiling, chamber scattering, and track inside the anechoic chamber. Figure 8 shows that the designed CPW-UWB slot antenna reveals acceptable values of efficiency within the operating band which are nearly over 80% that are superior to the ones achieved in [20–21]. The simulated group delay along the working bandwidth is plotted in Fig. 9 for a distance of 30cm between the front faces of two similar CPW-fed UWB slot antennas. A feeble variation below 1ns is obtained which is nearly comparable to the results presented in [22–23]. To demonstrate the usefulness of the fabricated model, the main parameters of the

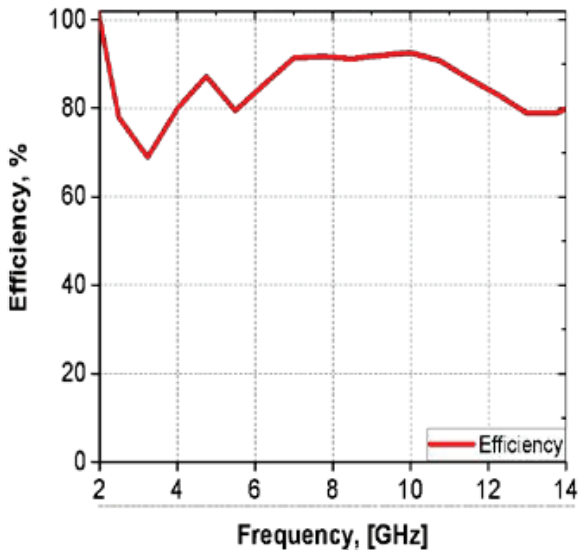

Fig. 8. Efficiency of the proposed UWB slot antenna versus frequency.

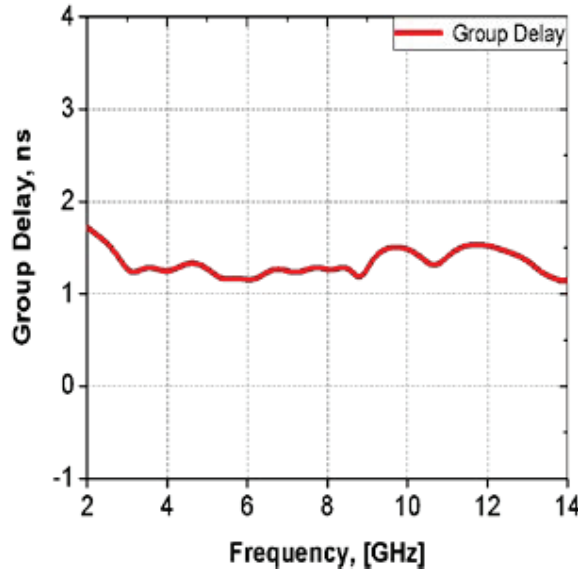

Fig. 9. Group delay of the proposed UWB slot antenna versus frequency.

proposed antenna are compared with the ones of some existing antennas in Table 3. It can be deduced that the parameters of the fabricated model are better or comparable to those of other existing antennas.

V. CONCLUSION

A compact printed CPW-fed slot antenna using fractal-shaped isosceles trapezoidal corrugations for UWB applications has been designed and measured in this work. The implementation of the isosceles trapezoidal fractal structure along the edge of the hexagonal slot has improved the working bandwidth. Experiments have been implemented to prove the antenna performances confirming that the fabricated antenna offers a large impedance bandwidth of about 127%, extending from 2.35 GHz to 10.67 GHz; which covers the entire UWB. Moreover, stable radiation patterns measured with an acceptable peak gain are measured over the whole working bandwidth. Thus, it can be concluded that the proposed design can be an advantageous candidate for many wireless communication systems.

ACKNOWLEDGMENT

This work was supported by the Directorate-General for Scientific Research and Technological Development (DG-RSDT) of Algeria.

REFERENCES

[1] D. Aissaoui, A. Chaabane, and A. Bouacha, "Compact super UWB elliptical antenna with corrugations for wireless communication systems," *IEEE IRASET 1st Int. Conf. Innov Res. App. Sci. Eng. Technol*., Meknes, MA, pp. 1-4, Apr. 2020.

[2] A. Chaabane and A. Babouri, "Dual band notched uwb MIMO antenna for surfaces penetrating application," *Adv. Electromagn.,* vol. 8, no. 3, pp. 6-15, 2019.

[3] A. Chaabane, O. Mahri, D. Aissaoui, and N. Guebgoub, "Multiband stepped antenna for wireless communication applications," *Inf. MIDEM.,* vol. 50, no. 4, pp. 275-284, 2020.

[4] E. Wang, W. Wang, X. Tan, Y. Wu, J. Gao, and Y. Liu, "A UWB MIMO slot antenna using defected ground structures for high isolation," *Int. J. RF Microw. Comput.-Aided Eng.,* vol. 30, no. 5, pp. 1-10, 2020.

[5] B. Hammache, A. Messai, I. Messaoudene, and T. A. Denidni, "Compact ultrawideband slot antenna with three notched-band characteristics," *Int. J. RF Microw. Comput.-Aided Eng.,* vol. 30, no. 5, pp. 1-10, 2020.

[6] A. F. Daw, M. A. Abdalla, and H. El-Henawy, "Wideband slow phase loaded inductor-composite right/left-handed transmission line for compact UWB power divider," *Microw. Opt. Technol. Lett.,* vol. 62, no. 6, pp. 1-5, 2020.

[7] R. Azim, M. T. Islam, and N. Misran, "Compact tapered shape slot antenna for UWB applications," *IEEE Antennas Wirel. Propag. Lett.,* vol. 10, pp. 1190-1193, 2011.

[8] M. A. Dorostkar, M. T. Islam, and R. Azim, "Design of a novel super wide band circular-hexagonal fractal antenna," *Prog. Electromagn. Res.,* vol. 139, pp. 229-245, 2013.

[9] P. Khanna, A. Sharma, A. K. Singh, and A. Kumar, "CPW - fed octagonal ring shaped ultra wide band antenna for wireless applications," *Adv. Electromagn.,* vol. 7, no. 3, pp. 87-92, 2018.

[10] Z. A. Abdul Hassain, A. R. Azeez, M. M. Ali, and T. A. Elwi, "A modified compact bi-directional UWB tapered slot antenna with double band-notch characteristic," *Adv. Electromagn.,* vol. 8, no. 4, pp. 74-79, 2019.

[11] A. Joshi and R. Singhal, "Gain enhancement in probe-fed hexagonal ultra wideband antenna using AMC reflector," *J. Electromagn. Waves Appl.,* vol. 33, no. 9, pp. 1185-1196, 2018.

[12] P. R. Prajapati and S. B. Khant, "Gain enhancement of UWB antenna using partially reflective surface," *Int. J. Microw. Wirel. Technol.,* vol. 10, no. 7, pp. 835-842, 2018.

[13] Z. Yang, H. Jingjianti and Y. Naichang, "An antipodal Vivaldi antenna with band-notched characteristics for ultra-wideband applications," *AEU - Int. J. Electron. Commun.,* vol. 76, pp. 152-157, 2017.

[14] D. Sankaranarayanan, D. Venkatakirand, and B. Mukherjee, "A novel compact fractal ring based cylindrical dielectric resonator antenna for ultra wideband application," *Prog. in Electromagn. Res*., vol. 67, pp. 71-83, 2016.

[15] A. Kumar, S. Dwari, G. P. Pandey, and B. K. Kanaujia, "A high gain wideband circularly polarized microstrip antenna," *Int. J. Microw. Wirel. Technol.,* vol. 74, pp. 125-130, 2018.

[16] V. Dinesh and G. Murugesan, "A CPW-fed hexagonal antenna with fractal elements for UWB applications," *Appl. Math. Inf. Sci.,* vol. 13, no. 1, pp. 73-79, 2019.

[17] CST Microwave Studio, ver. 2013, Computer Simulation Technology, Framingham, MA, 2013.

[18] M. Guerroui, A. Chaabane, and A. Boualleg, "Super UWB grooved and corrugated antenna for GPR application," *Period. Polytech. Electr. Eng. Comput. Sci.,*vol. 66, no. 1, pp. 31-37, 2022.

[19] A. Chaabane and M. Guerroui, "Printed UWB rhombus shaped antenna for GPR applications," *Iran. J. Electr. Electron. Eng.,* vol. 17, no. 4, 2021.

[20] R. Azim, M. T. Islam, and N. Misran, "Design of a planar UWB antenna with new band enhancement technique," *Applied Computational Electromagnetics Society (ACES) Journal,* vol. 26, no. 10, pp. 856-862, 2011.

[21] R. Azim, R. W. Aldhaheri, M. M. Sheikh, and M. T. Islam, "An effective technique based on off-set fed patch to enhance the bandwidth of microstrip planar antenna," *Microw. Opt. Technol. Lett.,* vol. 58, no. 5, pp. 1221-1226, 2016.

[22] Md. M. Alam, R. Azim, I. M. Mehedi, and A. I. Khan, "Coplanar waveguide-fed compact planar ultra-wideband antenna with inverted L-shaped and extended U-shaped ground for portable communication devices," *Chin. J. Phys.,* vol. 73, pp. 684-994, 2021.

[23] R. Azim, M. T. Islam, H. Arshad, Md. M. Alam, N. Sobahi, and A. I. Khan, "CPW-fed super-wideband antenna with modified vertical bow-tie-shaped patch for wireless sensor networks," *IEEE Access*, vol. 9, pp. 5343-5353, 2021.

[24] R. Azim, M. T. Islam, and N. Misran, "Microstrip line-fed printed planar monopole antenna for UWB applications," *Arab. J. Sci. Eng.,* vol. 38, no. 9, pp. 2415-2422, 2013.

[25] M. Guerroui, A. Chaabane, and A. Boualleg, "A CPW-fed amended U-shaped monopole UWB antenna for surfaces penetrating applications," *IEEE HORA 3rd Int. Cong. Hum. Comput. Int. Optim. Rob. Appl.,* Ankara, TR, Jun. 2021.

[26] Y. X. Zhang, Y. C. Jiao, H. Zhang, and Y. Gao, "A simple broadband flat-gain circularly polarized aperture antenna with multiple radiation modes," *Prog. Electromagn. Res. C*, vol. 81, pp. 1-10, 2018.

[27] T. Chen, J. Zhang, and W. Wang, "A novel cpw-fed planar monopole antenna with broadband circularly polarization," *Prog. Electromagn. Res. M,* vol. 84, pp. 11-20, 2019.

[28] P. Usha and C. Krishnan, "Epsilon near zero metasurface for ultrawideband antenna gain enhancement and radar cross section reduction," *AEU - Int. J. Electron. Commun.*, vol. 119, 2020.

[29] J. Chatterjee, A. Mohan, and V. Dixit, "Broadband circularly polarized h-shaped patch antenna using reactive impedance surface," *IEEE Antennas Wirel. Propag. Lett.,* vol. 17, no. 4, pp. 625-628, 2018.

[30] B. Guenad, A. Chaabane, D. Aissaoui, A. Bouacha, and T. A. Denidni, "Compact cauliflower-shaped antenna for ultra-wideband applications," *Applied Computational Electromagnetics Society (ACES) Journal*, vol. 37, no. 1, 2022, pp. 68-77, 2022

[31] A. Chaabane and M. Guerroui, "Circularly polarized UWB antenna with question mark shaped patch for GPR applications," *J. Appl. Res. Technol.,* vol. 20, no. 3, pp. 274-283, 2022.

Djelloul Aissaoui received his Magister degree in signals and systems and his Ph.D. degree in telecommunications science from the University of Tlemcen, Algeria, in 2007 and 2019, respectively. He is currently working as an associate professor in the Department of Electrical Engineering, Faculty of Science and Technology, University of Djelfa, Algeria. His current research areas of interest include fractal antennas, ultra-wideband antennas, and metamaterial antennas.

Abdelhalim Chaabane received his Ph.D. and completed his habilitation in Electronics in 2017 and 2020, respectively. He is currently working as an associate professor and a member of the Telecommunications Laboratory at the University 8 Mai 1945 Guelma. His current research areas of interest include fractal antennas, millimeter-wave high-gain, and wide-band antennas, UWB applications and radar, and biomedical engineering.

Noureddine Boukli-Hacene was born in 1959 in Tlemcen, Algeria. He received his Doctorate Degree (prepared at the "Centre National d'Etudes Spatiales" in Toulouse, France), in Electrical Engineering from the University of Limoges, France, in 1985. Then he joined the University of Tlemcen. Currerntly, he is a Professor in Electrical Engineering at the same university. His research interests include, among others, microstrip and miniaturized antennas, fractal antennas, ultra-wideband antennas, metamaterial antennas, and microwave circuits.

Tayeb A. Denidni received M.Sc. and Ph.D. degrees in Electrical Engineering from Laval University, Quebec City, QC, Canada, in 1990 and 1994, respectively. From 1994 to 2000, he was a Professor with the Engineering Department, Université du Quebec in Rimouski (UQAR), Rimouski, QC, Canada, where he founded the Telecommunications laboratory. Since August 2000, he has been with the Institut National de la Recherche Scientifique (INRS), Université du Quebec, Montreal, QC, Canada. His current research areas of interest include reconfigurable antennas using EBG and FSS structures, dielectric resonator antennas, metamaterial antennas, adaptive arrays, switched multi-beam antenna arrays, ultra-wideband antennas, microwaves, and development for wireless communications systems.

On the Coupling Imbalance of the UWB BLC in the 5G Low Noise Amplifier Design

Tamer G. Abouelnaga[1,2] and Esmat A. Abdallah[1]

[1]Microstrip Circuits Department
Electronics Research Institute ERI, Cairo, Egypt

[2]College of Industry and Energy Technology
New Cairo Technological University (NCTU)

Abstract – In this article, the design and the development of ultra-wideband UWB branch-line couplers BLCs with a novel method to control the coupling imbalance is proposed. The proposed UWB BLC is suitable for the 5G low-noise amplifier (LNA) design. UWB 4-branch BLC is designed using design curves developed using even and odd mode analyses to cover the 5G (3.3-5 GHz) frequency bands. The vertical branches of the UWB BLC are replaced by modified ones, and their effect on the coupling imbalance is investigated. The proposed BLC occupies an area of $33.9 \times 15.7\ mm^2$. Both conventional and modified BLC are fabricated, and their measured S-parameters are compared with analytical and simulated models. Based on the balanced amplifier topology, a 5G UWB low-noise amplifier is designed. The proposed BLCs and the MGF3022AM InGaP-HBT (Heterojunction Bipolar Transistor) are used to produce acceptable UWB performance. The balanced amplifier return loss, noise figure, and gain are investigated as BLCs coupling imbalance varies. The ultra-wideband LNA exhibits an acceptable small-signal gain, noise figure, input return loss, and output return loss across the 5G different frequency bands.

Index Terms – Branch-line coupler, balanced LNA amplifier, imbalance coupling, UWB.

I. INTRODUCTION

High data rates, spectral efficiency enhancement, shorter latency, and high Quality of Service (QoS) are the main requirements for 5G wireless communication networks [1–3]. For outdoor coverage, 5G sub-6 GHz bands are used [4]. The 5G frequency bands are classified as n46 (5.15-5.925), n47 (5.855-5.925), n77 (3.3 GHz–4.2 GHz), n78 (3.3 GHz–3.8 GHz), and n79 (4.4 GHz–5 GHz) [5]. These bands are within the ultra-wideband UWB frequency band (3.1 GHz - 10.6 GHz) that is authorized by Federal Communications Commission (FCC). Ultra-wideband refers to radio technology that is above 500 MHz or 20% bandwidth, depending on its center frequency [6]. In all RF and microwave receivers, the low noise amplifier (LNA) is the first level of the received signal amplification. There are two possible configurations for the LNA wideband operation. The first is the unbalanced structure, which consists of a multi-stage amplifier with inter-stage matching circuits. The second is a balanced amplifier, which employs 3 dB hybrid couplers to improve the matching across the wider bandwidth [7].

In this paper, an imbalanced coupling UWB BLC with an unbalanced structure is adopted to achieve a high-gain LNA over the UWB frequency range for the 5G applications. Other parameters such as input return loss, output return loss, noise figure (NF), and isolation are kept at an acceptable level. For that, both conventional UWB BLC and the proposed UWB imbalanced coupling BLC are designed, fabricated, and measured.

It had been shown in [8–12] that hybrid couplers may have arbitrary output power division by controlling the characteristic impedances of the $\frac{\lambda_g}{4}$ sections, where λ_g is the guided wavelength. Few researchers were concerned by the coupling imbalance CI of the couplers. Introducing a shorted stub, single section $\frac{\lambda_g}{4}$ transformers, circular sector patch, impedance varying, and phase inverter are the most used techniques, [13–18]. In [13], the vertical branch lines of the BLC were loaded by parallel-shorted stubs. In [14], single-section quarter-wave transformers at each port were integrated to achieve wideband and coupling imbalance operation. In [15], four circular sector patches were combined to form the coupler and the coupling imbalance was achieved by varying the impedance of the sectors. In [16], the conventional uniform transmission lines of BLC were replaced with nonuniform lines governed by a truncated Fourier series. In [17], a conventional two-section branch-line coupler with an additional phase inverter was used to control the coupling imbalance and the wideband operation. In [18],

Submitted On: July 10, 2022
Accepted On: October 27, 2022

https://doi.org/10.13052/2022.ACES.J.370908

the BLC's vertical branch lines were loaded with a short circuit stub. Parallel notches were also introduced at the T-junction of the BLC.

II. BLC DESIGN AND ANALYSIS PROCEDURE

In this section, even and odd mode analyses were used to obtain a developed design curve for the UWB BLCs over the entire frequency band of the 5G. Also, the S-parameters are calculated using a developed MATLAB code and then verified by CST and measured counterparts.

A. Even and odd mode analysis of conventional UWB BLC

Considering the analytical model of a one-section branch-line coupler [19], the analytical theory is extended to model four-branch BLC. Figure 1 shows a conventional four-branch BLC and its characteristic impedances of through and branch lines. The through lines' characteristic impedance are Z_1 and Z_3, and their lengths are θ_1 and θ_3 respectively. The branch lines' characteristic impedance is Z_2 and their length is θ_2. Both Port 1 and 4 are excited by in-phase and amplitude of $\frac{1}{2}$ signals which leads to an equivalent open circuit at the line of symmetry. Similarly, two out-of-phase and amplitudes of $\frac{1}{2}$ signals lead to an equivalent short circuit at the line of symmetry. By superposition, the sum of the two cases is a single signal of unit amplitude at Port 1. The resultant signals from the four ports are also the superposition of the results obtained in the even mode and odd mode cases. In each case, the problem reduces to that of a two-port network.

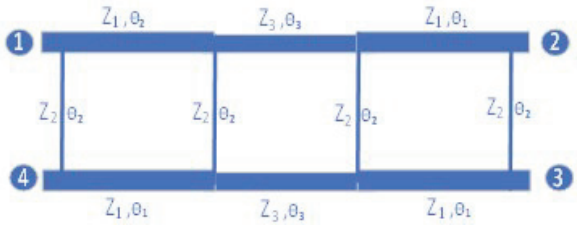

Fig. 1. Four branches of conventional BLC.

For the even mode, Figs. 2 (a) and (b) show the even mode excitation and the open stubs equivalent circuit, respectively. The even mode ABCD parameters are obtained in Equation (1). Similarly, Figs. 2 (c) and (d) show the odd mode excitation and the short stubs equivalent circuit, respectively. The odd mode ABCD parameters are obtained in Equation (2).

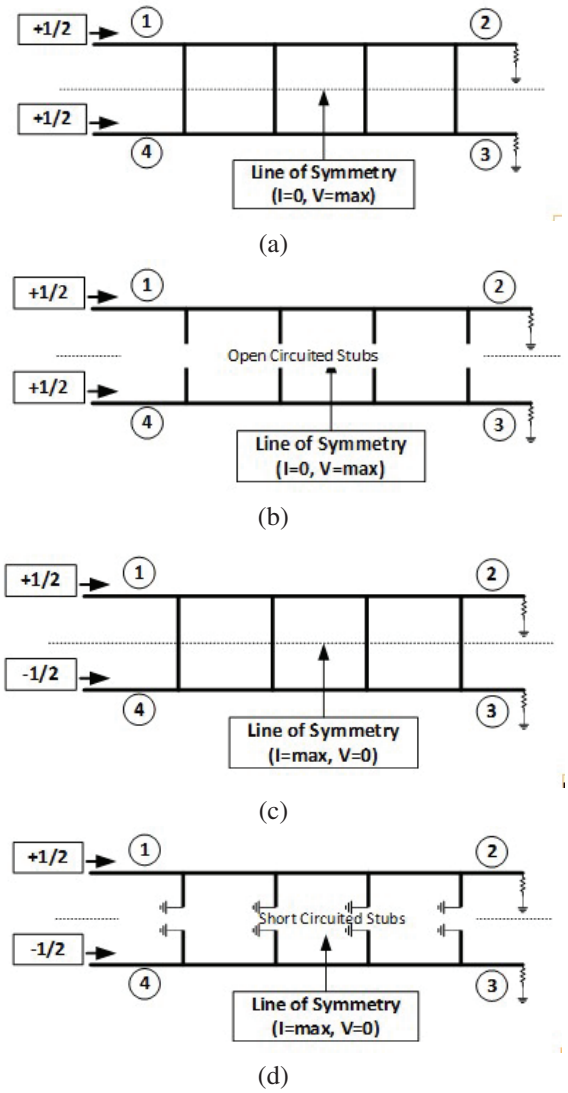

Fig. 2. Decomposition of BLC into (a) even–mode excitation; (b) even–mode equivalent circuit; (c) odd–mode excitation; (d) odd–mode equivalent circuit.

$$\begin{bmatrix} A & B \\ C & D \end{bmatrix}_e = \begin{bmatrix} 1 & 0 \\ \frac{jtan\left(\frac{\theta_2}{2}\right)}{Z_2} & 1 \end{bmatrix} \begin{bmatrix} cos(\theta_1) & jZ_1 sin(\theta_1) \\ \frac{jsin(\theta_1)}{Z_1} & cos(\theta_1) \end{bmatrix} \begin{bmatrix} 1 & 0 \\ \frac{jtan\left(\frac{\theta_2}{2}\right)}{Z_2} & 1 \end{bmatrix} \begin{bmatrix} cos(\theta_3) & jZ_3 sin(\theta_3) \\ \frac{jsin(\theta_3)}{Z_3} & cos(\theta_3) \end{bmatrix} \begin{bmatrix} 1 & 0 \\ \frac{jtan\left(\frac{\theta_2}{2}\right)}{Z_2} & 1 \end{bmatrix} \begin{bmatrix} cos(\theta_1) & jZ_1 sin(\theta_1) \\ \frac{jsin(\theta_1)}{Z_1} & cos(\theta_1) \end{bmatrix} \begin{bmatrix} 1 & 0 \\ \frac{jtan\left(\frac{\theta_2}{2}\right)}{Z_2} & 1 \end{bmatrix}, \quad (1)$$

$$\begin{bmatrix} A & B \\ C & D \end{bmatrix}_o = \begin{bmatrix} 1 & 0 \\ \frac{1}{jtan\left(\frac{\theta_2}{2}\right)Z_2} & 1 \end{bmatrix} \begin{bmatrix} cos(\theta_1) & jZ_1 sin(\theta_1) \\ \frac{jsin(\theta_1)}{Z_1} & cos(\theta_1) \end{bmatrix} \begin{bmatrix} 1 & 0 \\ \frac{1}{jtan\left(\frac{\theta_2}{2}\right)Z_2} & 1 \end{bmatrix} \begin{bmatrix} cos(\theta_3) & jZ_1 sin(\theta_3) \\ \frac{jsin(\theta_3)}{Z_3} & cos(\theta_3) \end{bmatrix} \begin{bmatrix} 1 & 0 \\ \frac{1}{jtan\left(\frac{\theta_2}{2}\right)Z_2} & 1 \end{bmatrix} \begin{bmatrix} cos(\theta_1) & jZ_1 sin(\theta_1) \\ \frac{jsin(\theta_1)}{Z_1} & cos(\theta_1) \end{bmatrix} \begin{bmatrix} 1 & 0 \\ \frac{1}{jtan\left(\frac{\theta_2}{2}\right)Z_2} & 1 \end{bmatrix}. \quad (2)$$

Using ABCD to S parameters transformation [20], and the fact that $AD - BC = 1$ and $A = D$, the S-parameter for the four-branch BLC is obtained. The required characteristic impedance, Z_2 of the branch line for the conventional four-branch, BLC is between 135 Ω and 264 Ω in Butterworth and Chebyshev designs [21]. In [22], the through characteristic impedance Z_1 and Z_3 are obtained as Equations (3) and (4).

$$Z_1 = \sqrt{\frac{Z_0 Z_2^3 \sqrt{1 - C_{factor}^2} - C_{factor}\, Z_0^2 Z_2^2}{C_{factor}\ \left(Z_2^2 - Z_0^2\right) + 2Z_0 Z_2 \sqrt{1 - C_{factor}^2}}}, \quad (3)$$

$$Z_3 = \sqrt{\frac{Z_1^4 \left(Z_2^4 - Z_0^2 Z_2^2\right)}{Z_1^4\ \left(Z_2^2 + Z_0^2\right) - Z_2^2 Z_0^2 \left(2Z_1^2 - Z_2^2\right)}}, \quad (4)$$

where the coupling factor C_{factor} is related to S_{21} and S_{31} in [4]:

$$S_{21} = \sqrt{1 - C_{factor}^2} and S_{31} = jC_{factor}.$$

For physical realizations, the branch characteristic impedance Z_2 is recommended to be within the range of 135 Ω to 145 Ω. MATLAB code was developed based on this assumption and Equations (3) and (4). Considering the frequency effect (3 GHz – 6 GHz), line-width-to-substrate-height ratio (w/h), and the effective dielectric constant ε_{eff}, Fig. 3 shows how to choose the through and the branch characteristic impedance values simultaneously, and then choose the aspect ratio (w/h) and the effective dielectric constant ε_{eff} of branch line Z_2 only. Figure 4 shows the aspect ratio (w/h) and the effective dielectric constant ε_{eff} of the through impedances Z_1 and Z_3 at different frequencies. In Table 1, the design process starts by choosing the branch characteristic impedance Z_2 between 135 Ω to 145 Ω lines shown in Fig. 3 (b) at 4 GHz. Z_2 is chosen to be 143 Ω with an aspect ratio $(\frac{w}{h})_2 = 0.1$ and $(\varepsilon_{reff})_2 = 3.23$. Also, Z_1 and Z_3 are found to be 54 Ω and 57.7 Ω, respectively. The through characteristic impedances aspect ratio and effective dielectric constant are extracted from Fig. 4 (b) and are shown in Table 2.

Figure 5 shows the calculated S-parameters of the UWB BLC using the developed MATLAB code. For

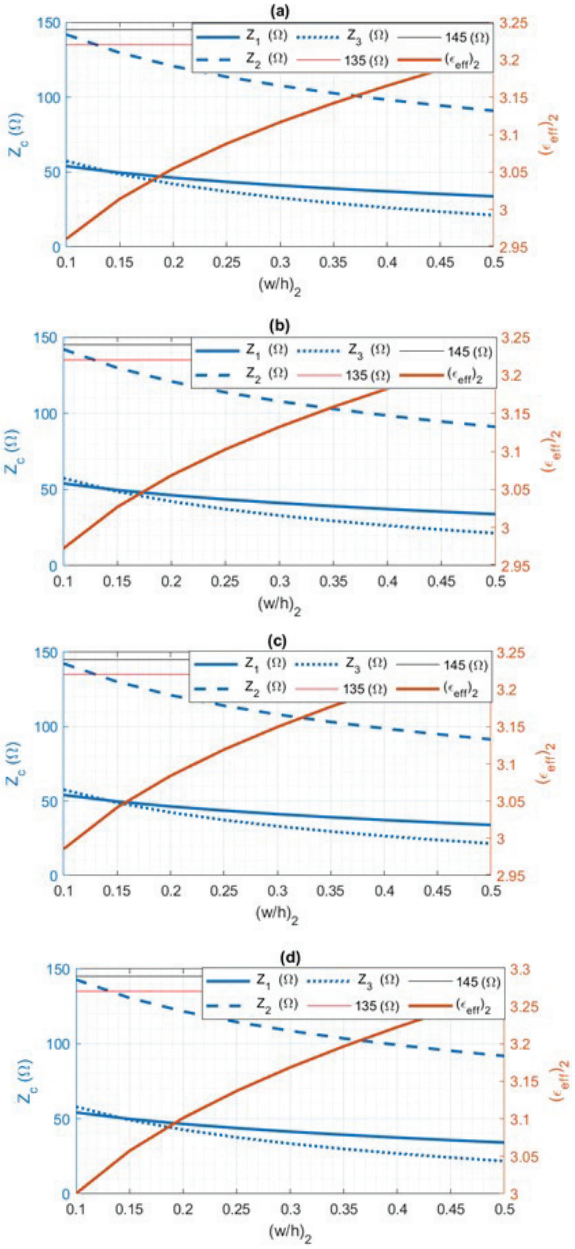

Fig. 3. Characteristic impedances of branch and through lines values at (a) 3 GHz; (b) 4 GHz; (c) 5 GHz; (d) 6 GHz.

verification purposes, the conventional UWB BLC is simulated using CST and then fabricated and both measured and simulated results are shown in Fig. 6. Good agreements were obtained between simulated and measured results over the frequency band, which extends from 3.3 GHz to 5 GHz. The conventional UWB coupler has simulated insertion loss and coupling of −3.77 dB and −3.15 dB while the measured insertion loss and coupling of −4 dB and −4.47 dB were obtained. The simulated and measured isolation and return loss are less than

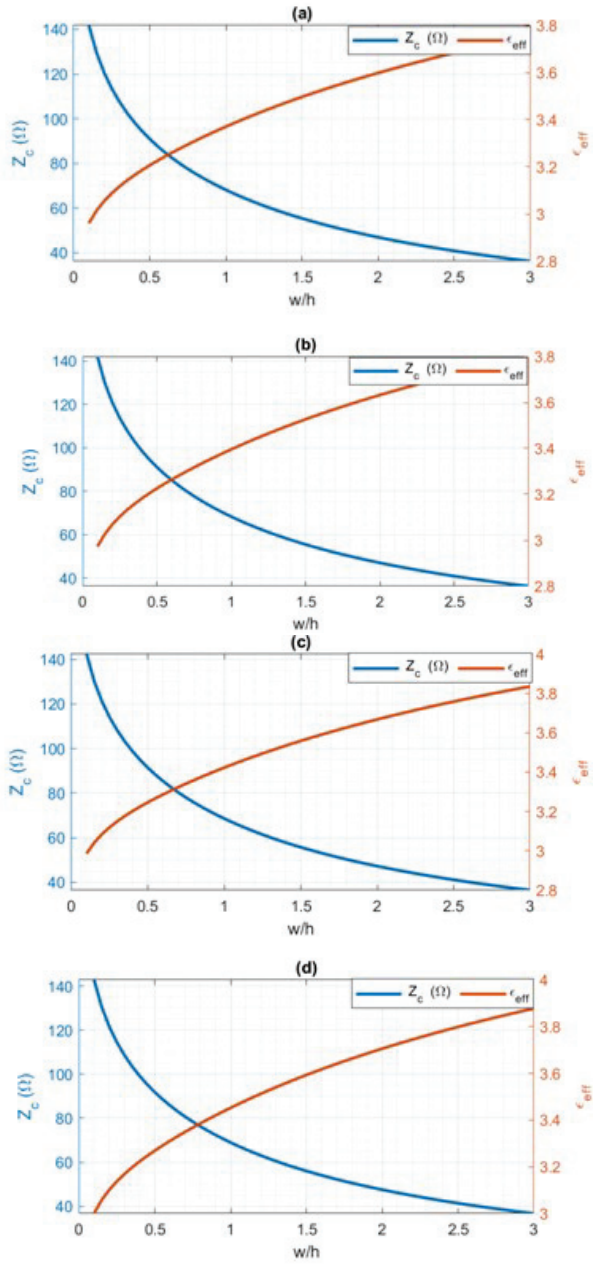

Fig. 4. Characteristic impedances of branch and through lines values versus aspect ratio w/h and effective dielectric constant at (a) 3 GHz; (b) 4 GHz; (c) 5 GHz; (d) 6 GHz.

-16.5 dB with fractional bandwidth of 56%, and phase imbalances less than 2^o over the operating bandwidth.

B. Proposed UWB BLC with different coupling imbalance

The UWB BLC coupling is controlled by replacing the uniform branch line with a proposed non-uniform one as shown in Fig. 7. The modified branch line has two circular discs with a radius R at its upper and lower

Table 1: Comparison of proposed BLC with previous works

Ref.	Technique	f_o (GHz)	BW $(\%)$	CI (dB)	PE (deg.)
13	Shorted stubs	3	30.5	4-10	4
14	Single section $\lambda/4$ transformer	3	50.9	6-14	2
15	Circular sector patch	10	22.2	3-10	5
16	Impedance varying	3	57	3-9	5
17	Phase inverter	2	48.2	3-10	5
18	Shorted stub and parallel notches	3.5	62	9-15	4
This work	Circular discs	3.19	103	1-12	2

Table 2: Conventional UWB BLC parameters

n	Z_n (Ω)	$(\frac{w}{h})_n$	$(\varepsilon_{reff})_n$	l_n (mm)
2	143	0.1	3.23	10.4
3	57.7	1.4	3.54	10
1	54	1.59	3.58	9.9
0	50	1.8	3.63	1.8

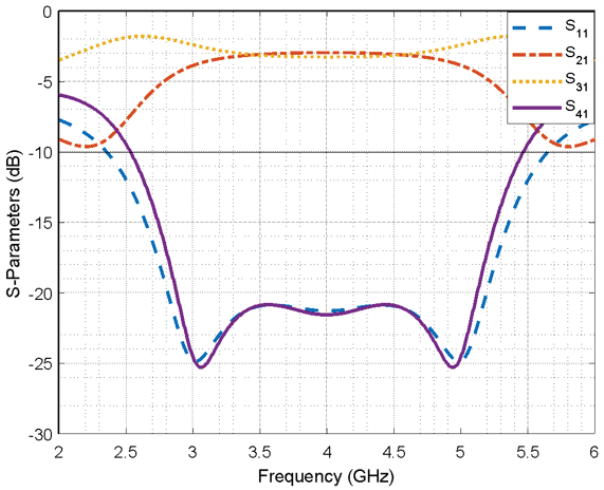

Fig. 5. Calculated S-parameters of conventional UWB BLC.

centers. As the disc radii increase the coupling imbalance increase. At 4 GHz the coupling imbalance increases from 0.8 dB to 12 dB as radius R increases from 0.25 mm to 1.25 mm, Table 3.

Figures 8 (a) to (e) show the S-parameters of the UWB BLC as discs radii increase. The proposed UWB

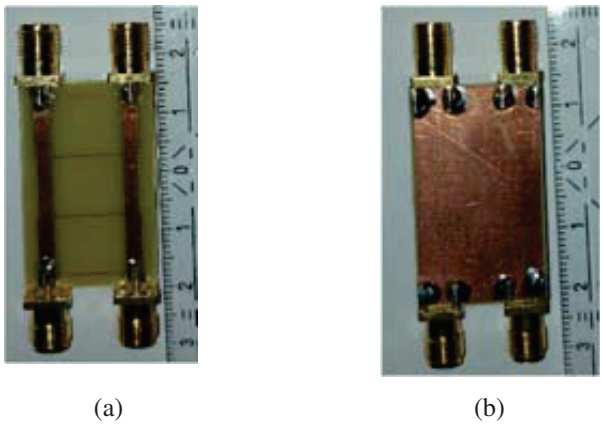

Fig. 6. Conventional UWB BLC (a) fabricated top view; (b) fabricated bottom view; (c) measured and simulated S-parameters.

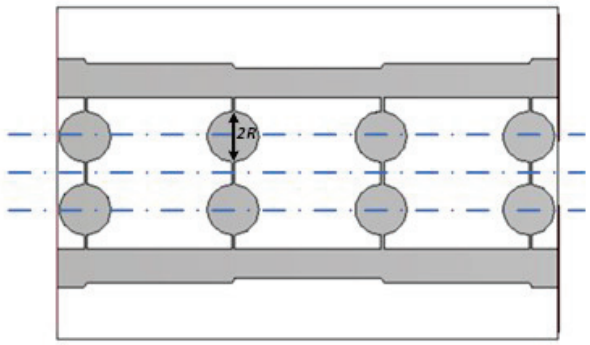

Fig. 7. Proposed UWB BLC with controllable coupling imbalance.

coupler has a coupling imbalance of 1 dB, 2 dB, 4 dB, 7 dB, and 12 dB over the bandwidth which ranges from 3.5 GHz to 5 GHz, 3.75 GHz to 4.65 GHz, 3.6 GHz to 4.5 GHz, 3.64 GHz to 4.2 GHz, and 3.5 GHz to 4 GHz as

Table 3: Coupling imbalance values at different disc radii at 4 GHz

R (mm)	0.25	0.5	0.75	1	1.25
CIR (dB)	1	2	4	7	12

circular discs have radii of 0.25 mm, 0.5 mm, 0.75 mm, 1 mm, and 1.25 mm, respectively.

For verification purposes, the proposed UWB BLC with a coupling imbalance of 7 dB is fabricated and measured. The top and bottom views of the proposed fabricated BLC are shown in Figs. 9 (a) and (b), respectively. Both measured and simulated results are shown in Fig. 9 (c). The simulated frequency band with a 7 dB imbalance extends from 3.5 GHz to 4.2 GHz while the

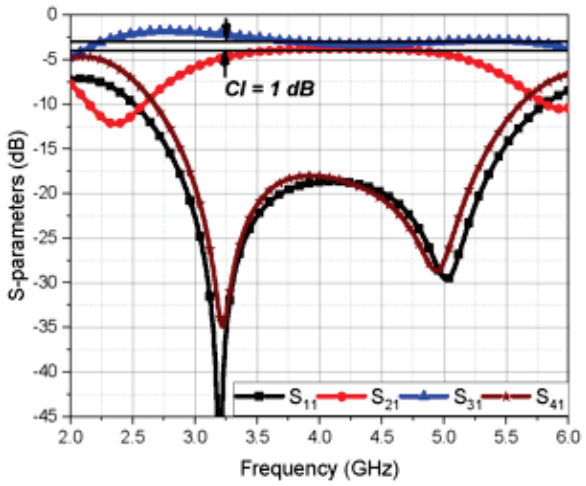

(a)

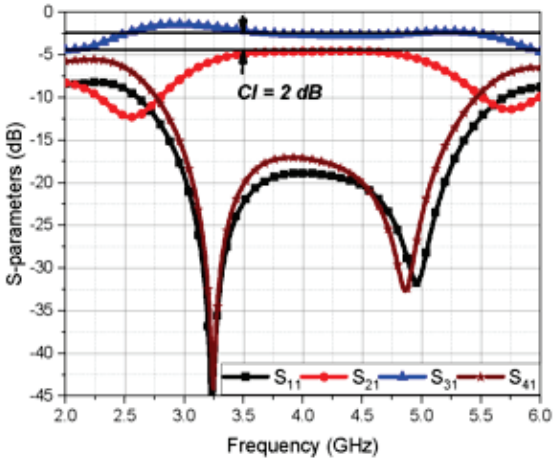

(b)

Fig. 8. *Continued.*

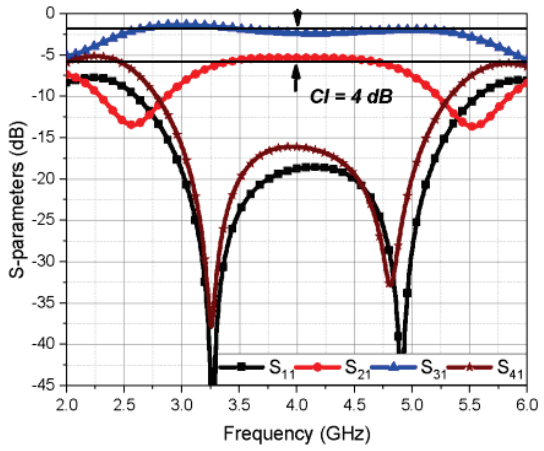

(c)

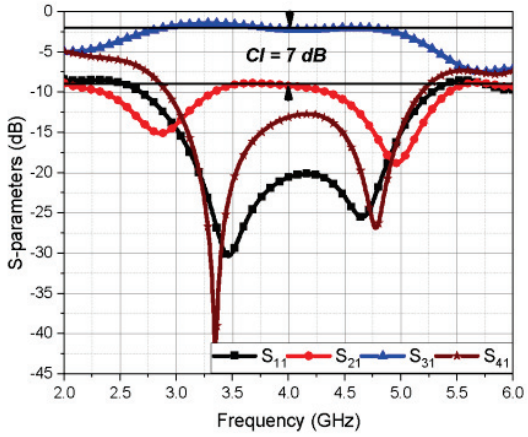

(d)

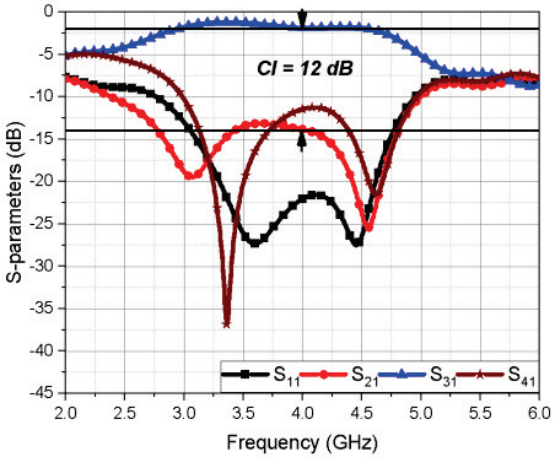

(e)

Fig. 8. UWB BLC with controllable coupling imbalance S-parameters at (a) $R = 0.25$ mm; (b) $R = 0.5$ mm; (c) $R = 0.75$ mm; (d) $R = 1$ mm; (e) $R = 1.25$ mm.

measured frequency band with a 7 dB coupling imbalance extends from 3.3 GHz to 4.48 GHz. The simulated insertion loss and coupling of 2.33 dB and −9.33 dB while the measured insertion loss and coupling of 2.2 dB and −8.1 dB are obtained, respectively. The simulated isolation and return loss are less than 13 dB and 20 dB with fractional bandwidth of 20.3%, and phase imbalances less than 2^o while the measured isolation and return losses are less than 14 dB and 16 dB with fractional bandwidth of 36%, and phase imbalances less than 10^o for the entire operating bandwidth.

III. BALANCED UWB LNA

In wireless communication systems, balanced amplifiers have been widely used due to their low noise figure, and better gain and stability as compared to a single amplifier. The proposed LNA circuit consists of four transistors with an impedance-matching network at the input and output of each transistor. MGF3022AM InGaP-HBT (Heterojunction Bipolar Transistor) has opted for the proposed LNA circuit. The MGF3022AM is designed for use in L-to-C-band amplifiers. Additional, two identical UWB BLC with different coupling

(a)

(b)

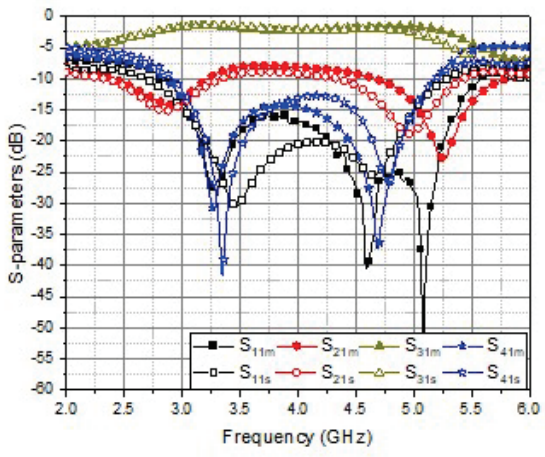

(c)

Fig. 9. Proposed fabricated UWB BLC (a) top view; (b) bottom view; (c) measured and simulated S-parameters.

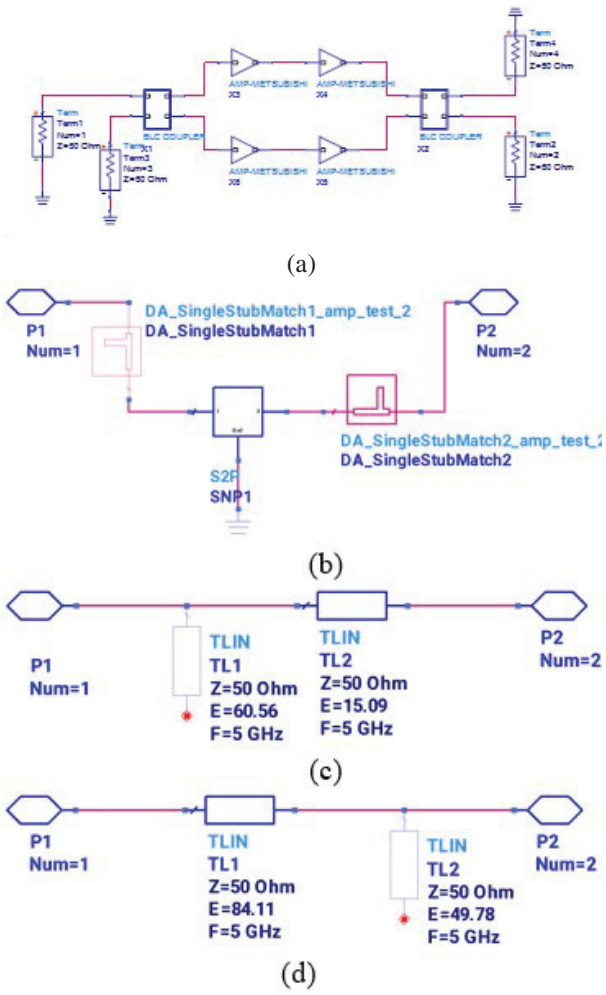

Fig. 10. Proposed UWB LNA (a) circuit diagram; (b) single transistor with input and output matching sections; (c) input matching section; (d) output matching section.

Table 4: $k-\mu$ factors of the MGF3022AM InGaP-HBT transistor

$F\ (GHz)$	μ	k
3.00	0.863	0.692
3.25	0.905	0.786
3.50	0.939	0.866
3.75	0.976	0.95
4.00	1.044	1.083
4.25	1.125	1.202
4.50	1.234	1.287
4.75	1.574	1.47
5.00	2.46	1.552
5.25	1.743	1.738
5.50	1.282	1.878
5.75	1.11	2.033
6.00	1.04	2.112

imbalanced designed in section II are included. Microwave transistors used to design UWB amplifiers are generally not well-matched across the operating frequency band. A wider bandwidth comes at the expense of low gain and more circuit complexity. Thus, we propseda circuit based on four amplifiers having a UWB coupler to provide a good adaptation for the gain and bandwidth. ADS simulator is used as a CAD tool to analyze the circuit performance. The balanced amplifier circuit is shown in Fig. 10 (a). Figure 10 (b) shows the transistor block, which has S-parameters of $V_{CE} = 3\ V$ and $I_C = 33\ mA$, and it's matching input and output circuits. Figures 10 (c) and (d) shows the equivalent input and output transmission line matching circuits designed at $F = 5\ GHz$, where Z is the line impedance in Ω and E is

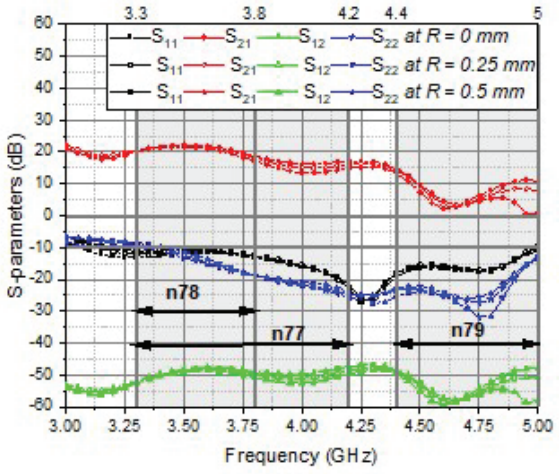

(a)

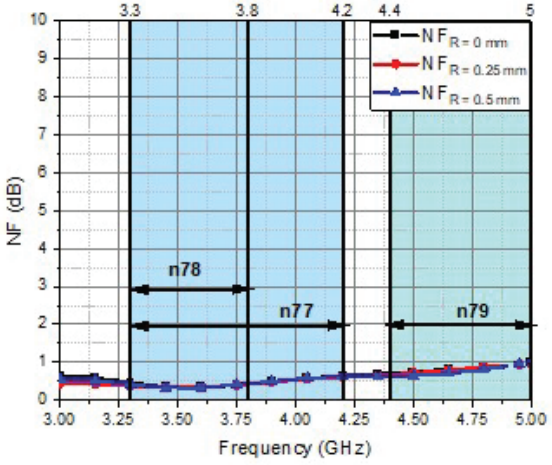

(b)

Fig. 11. Proposed LNA circuit (a) S-parameters at different coupling imbalances of the UWB BLC and (b) noise figure at different coupling imbalances of the UWB BLC.

Table 5: LNA parameters for different imbalance coupling associated with different discs' radii

R (mm)	I/P RL (dB)	O/P RL (dB)	Gain (dB)	NF (dB)	CI (dB)
n77 (3.7 GHz)					
0	11.9	17.2	19.5	0.38	0.99
0.25	11.7	17	20.3	0.38	2.2
0.5	11.4	16.3	20.7	0.38	3.3
0.75	13.2	17.8	20.1	1.1	4.1
1	13.3	16.9	20.6	1.1	7.2
1.25	14.8	16.1	21.2	1.1	11.8
n57 (3.5 GHz)					
0	11.9	13.2	21.5	0.34	1.4
0.25	11.5	12.5	22.1	0.35	2.8
0.5	10.7	11.5	22.3	0.32	3.8
0.75	12.7	11.9	20.23	1.1	4.6
1	11.9	10.8	19.98	0.97	7.6
1.25	11.97	10.01	18.9	0.99	12.4
n79 (4.7 GHz)					
0	17.4	25.9	4.6	0.83	0.79
0.25	17	26.7	3.6	0.83	2.1
0.5	17.2	29.1	3.7	0.74	3.8
0.75	16.1	22.9	8.3	1.69	5.2
1	18.1	20.5	6.8	1.8	11.7
1.25	16.1	13.7	10.7	2.13	15.5
4 GHz					
0	15.9	20.9	13.5	0.54	0.82
0.25	15.8	21.8	15	0.54	0.82
0.5	15.5	22	16.2	0.56	1.87
0.75	16.3	22.8	16.8	1.34	3.85
1	16.9	25.3	19.1	1.29	6.96
1.25	20	31.8	21.11	1.26	12.13

the electrical length of the open stub in degree. Table 4 shows the k and μ factors of the MGF3022AM InGaP-HBT transistor after adding the input and output matching sections. The k and μ factors are given by [5] as:

$$K = \frac{1-|S_{11}|^2-|S_{22}|^2+|\Delta|^2}{2|S_{12}S_{21}|}, |\Delta| = |S_{11}S_{22}-S_{12}S_{21}|,$$

$$\mu = \frac{1-|S_{11}|^2}{|S_{22}-\Delta S_{11}^*|+|S_{12}S_{21}|}. \quad (5)$$

The amplifier is nearly unconditionally stable across the 5G operating frequency band.

Different coupling imbalances associated with different discs' radii of UWB BLCs are used for the balanced LNA performance analysis. Figure 11 (a) shows the input return loss, output return loss, gain, and isolation for the first three coupling imbalances associated with the first three discs' radii of BLC balanced. Figure 11 (b) shows the associated noise figure of balanced LNA. Table 5 shows different LNA parameters for imbalances associated with six different discs' radii. For the 5G n77 center band, the gain varies from 19.5 dB to 21.2 dB while NF is better than 1.1. The input and output return loss, are better than 11.4 dB. For the 5G n57 center band, the gain varies from 18.9 dB to 22.3 dB, while NF is better than 1.1. The input and output return loss are better than 10 dB. For the 5G n79 center band, the gain varies from 3.6 dB to 10.7 dB, while NF is better than 2.3. The input and output return loss are better than 13.7 dB. Additionally, at 4 GHz (the center frequency of the UWB BLC), the gain varies from 13.5 dB to 21.11 dB while NF is better than 12.13. The input and output return loss are better than 15.5 dB.

IV. CONCLUSION

We introduced a simple and new method of controlling the coupling imbalance of the UWB BLC. For verification, a conventional UWB BLC was designed, fabricated, and measured. Additionally, a UWB BLC with a coupling imbalance of 7 dB was designed, fabricated, and measured. Both UWB BLC and UWB BLC with a 7 dB coupling imbalance were measured and simulated, and their results were founded to be in good harmony. The application of the proposed LNA-design BLC was verified. The proposed BLC added a degree of freedom in the design of the LNA considering gain and NF.

The UWB LNA that uses UWB BLC with an imbalance coupling is suitable for 5G sub−6 GHz applications as well as other wireless communication systems such as navigation and radar applications.

REFERENCES

[1] T. G. Abouelnaga, I. Zewail, and M. Shokair, "Design of 10 ×10 massive MIMO array in sub-6 GHz smartphone for 5G applications," *Progress in Electromagnetics Research B*, vol. 91, pp. 97-114, 2021.

[2] I. Al-Mejibli and S. Al-Majeed, "Sub-6 GHz quad-band reconfigurable antenna for 5G cognitive radio applications challenges of using MIMO channel technology in 5G wireless communication systems," *Applied Computational Electromagnetics Society (ACES) Journal*, vol. 36, no. 8, pp. 1015-1025, 2021.

[3] A. Junuthula and A. Prakasa, "A dual band AMC backed antenna for WLAN, WiMAX, and 5G wireless applications," *Applied Computational Electromagnetics Society (ACES) Journal*, vol. 36, no. 9, pp.1209-1214, 2021.

[4] A. Biswas and G. Vibha, "Design and development of low-profile MIMO antenna for 5G new radio smartphone applications," *Wireless Personal Communications*, vol. 111, no. 3, pp. 1695-1706, 2020.

[5] 5G NR specifications, document TS 38.101-1 V15.4.0 3GPP Release 15, 2018.
[6] R. S. Kshetrimayum, "An introduction to UWB communication systems," *IEEE Potentials*, vol. 28, pp. 9-13, 2009.
[7] D. K. Misra, *Radio Frequency and Microwave Communication Circuits; Analysis and Design,* John Wiley & Sons, 2004.
[8] C. Y. Pon, "Hybrid-ring directional coupler for arbitrary power division," *IEEE Trans. Microw. Theory Tech.*, vol. 19, no. 11, pp. 529-535, 1961.
[9] R. Levy and L. J. Lind, "Synthesis of symmetric branch line guide directional couplers," *IEEE Trans. Microw. Theory Tech.*, vol. 16, no. 12, pp. 80-89, 1968.
[10] G. L. Matthaei, L. Young, and E. M. T. Jones, *Microwave Filters, Impedance-Matching Network, and Coupling Structures*, Norwood, MA, Artech House, 1980.
[11] A. K. Agrawal and G. F. Mikucki, "A printed-circuit hybrid-ring directional coupler for arbitrary power divisions," *IEEE Trans. Microw. Theory Tech.*, vol. 34, no. 12, pp. 1401-1407, Dec. 1986.
[12] C. Hsu, J. Kuo, and C. Chang, "Miniaturized dual-band hybrid couplers with arbitrary power division ratios," *IEEE Transactions on Microwave Theory and Techniques*, vol. 57, no. 1, pp. 149-156, 2009.
[13] Z. Qamar, S. Y. Zheng, W. S. Chan, and D. Ho, "Coupling coefficient reconfigurable wide-band branch-line coupler topology with harmonic suppression," *IEEE Transactions on Microwave Theory and Techniques*, vol. 66, no. 4, pp. 1912-1920, 2018.
[14] S. Lee and Y. Lee, "Wideband branch-line couplers with single-section quarter-wave transformers for arbitrary coupling levels," *IEEE Microwave and Wireless Components Letters*, vol. 22, no. 1, pp. 19-21, Jan. 2012.
[15] S. Y. Zheng, J. H. Deng, Y. M. Pan, and W. S. Chan, "Circular sector patch hybrid coupler with an arbitrary coupling coefficient and phase difference," *IEEE Transactions on Microwave Theory and Techniques*, vol. 61, no. 5, pp. 1781-1792, 2013.
[16] K. A. Alshamaileh, V. K. Devabhaktuni, and N. I. Dib, "Impedance-varying broadband 90° branch-line coupler with arbitrary coupling levels and higher order harmonic suppression," *IEEE Transactions on Components, Packaging and Manufacturing Technology*, vol. 5, no. 10, pp. 1507-1515, 2015.
[17] L. Chiu and Q. Xue, "Investigation of a wideband 90-degree hybrid coupler with an arbitrary coupling level," *IEEE Transactions on Microwave Theory and Techniques*, vol. 58, no. 4, pp. 1022-1029, 2010.
[18] Q. Zeeshan, S. Y. Zheng, W. S. Chan, and H. Derek, "Coupling coefficient range extension technique for broadband branch-line coupler," *Journal of Electromagnetic Waves and Applications*, vol. 32, no. 1, pp. 92-112, 2018.
[19] T. G. Abouelnaga and A. S. Mohra, "Reconfigurable 3/6 dB novel branch line coupler," *Open Journal of Antennas and Propagation*, vol. 5, no. 1, pp. 1-7, 2017.
[20] M. Pozar, *Microwave Engineering,* John Wiley & Sons, 2011.
[21] M. Muraguchi, T. Yukitake, and Y. Naito, "Optimum design of 3-dB branch-line couplers using microstrip lines," *IEEE Trans. Microw. Theory Tech.*, vol. 31, no. 8, pp. 674-678, 1983.
[22] W. Yongle, J. Shen, and Y. Liu, Comments on "Quasi-Arbitrary Phase-Difference Hybrid Coupler," *IEEE Trans. Microw. Theory Tech.,* vol. 61, no. 4, pp. 1725-1727, 2013.

Tamer Gaber Abouelnaga was born November 1976. He received his B.Sc. degree (1994–1999, honors degree) in Electronics Engineering from Menofiya University, Egypt, and M.Sc. (2002–2007) and Ph.D. degrees (2007–2012) in Electronics and Communications from Ain Shams University, Egypt. He works at Microstrip Circuits Department, Electronics Research Institute, Egypt as a Researcher (2012–2017) and an Associate Professor (2018 to present). He also has worked as the Students Affairs Vice Dean (2018–2019) and the Community Service, Environmental Development Vice Dean (2019–2022) – Higher Institute of Engineering and Technology – Kafr Elsheikh City, as well as the Students Affairs Vice Dean (2022–2023) – College of Industry and Energy Technology, New Cairo Technological University (NCTU), Egypt. He has published 42 papers, 29 papers in peer-reviewed journals, and 13 papers in international conferences regarding antennas, couplers, filters, and dividers for different microwave applications.

Esmat A. Abdallah (Senior Member, IEEE) graduated from the Faculty of Engineering, Cairo University, Giza, Egypt in 1968. She received her M.Sc. and Ph.D. degrees from Cairo University in 1972 and 1975, respectively. She was nominated as an Assistant Professor, Associate Professor, and Professor in 1975, 1980, and 1985, respectively. In 1989, she was appointed President of the Electronics Research Institute (ERI), Cairo, Egypt, a position she held for approximately 10 years. She then became the Head of the Microstrip Department, ERI, from 1999 to 2006. Currently, she is at the Microstrip Department, Electronics Research Institute, Cairo, Egypt. She focuses on her research on microwave circuit designs, planar antenna systems, and nonreciprocal ferrite devices, and recently on EBG structures, UWB components, and antenna and RFID systems. She has been a single author or co-author on more than 285 research papers in highly cited international journals and proceedings of international conferences. She has 6 books and 7 patents. She supervised more than 85 Ph.D. and M.Sc. theses. She is a member of the National Council of Communication and Information Technology.

A Novel Compact Filtering Antenna for 5.0-GHz WLAN Communication System

Shujia Yan[1], Chongqi Zhang[1], Qiang Chen[1], and Mei Song Tong[2]

[1]School of Electronic and Electric Engineering
Shanghai University of Engineering Science, Shanghai, China

[2]Department of Electronic Science and Technology
Tongji University, Shanghai, China
mstong@tongji.edu.cn

Abstract – The proposed antenna presents a microstrip filter antenna with both filter out-of-band rejection characteristics and antenna radiation characteristics for WLAN communication system. The antenna consists of four U-shaped microstrip resonators, one Γ-shaped antenna, and one parallel coupling line. The Γ-shaped antenna has the filtering function as the last order resonator, and the parallel coupling line integrates the filter and antenna as the conductance converter. After simulation and test, the results show that the center frequency of the filter antenna is 5.25 GHz, the fractional bandwidth is 8.0% (5.0 − 5.42 GHz), the in-band gain changes smoothly, the maximum in-band gain is 3.059 dBi, the gain at 150 MHz outside the passband rapidly decreases to 10.0 dBi, and the overall out-of-band gain drops to below −24 dBi. The filter antenna has a simple structure and thin substrate, which optimizes the overall size of the filter and antenna, reduces the transmission loss between them, and is applicable to the RF front-end of wireless communication systems.

Index Terms – compact design; filter antenna; microstrip antenna; WLAN communication system

I. INTRODUCTION

In recent years, the rapid development of wireless communications has led to an exponential growth in the demand for passive devices. As one of the most widely used wireless communication systems, WLAN technology has become more and more mature. The data transmission rate in the 5.0-GHz band (5.15 − 5.35 GHz) of the IEEE802.11a standard is relatively high, so it is able to meet the needs of most high-speed communications and, therefore, has been widely used. As an important part of wireless communication system, antennas and filters play a very important role in the performance of the whole wireless communication system, but their size is often much larger than other devices. If antennas and filters are integrated in a compact module that provides both radiation and filtering functions, the size of the communication system could be effectively reduced and the communication quality could be improved by reducing mutual interference. Therefore, filtering antennas [1] that combine filters and antennas closely together have been widely studied.

In the traditional design method of filtering antenna, the antenna and filter are designed separately based on the reference impedance, which is 50 Ω or 75 Ω, and then they are connected directly because they share a common characteristic impedance. However, this will easily cause impedance mismatch and increase the insertion loss of the circuit, leading to the deterioration of the entire system. To eliminate this problem, an additional structure for impedance transformation is used between the filter and the antenna [2, 3], so that the filter can be correctly integrated with the antenna in the required bandwidth with good impedance matching. However, this structure increases the circuit area and transmission loss in the frequency range. Also, Bailey proposed a microstrip antenna with filtering characteristics by coupling four layers of patches to each other [4]. However, none of the above methods use an integrated design approach and there is no generality. In 2016, Fakharian *et al.* proposed an open/short-ended digital E-type resonator by using two integrated PIN diodes and realized the coupling connection between the filter and the antenna [5], but it cannot be printed directly. Moreover, the method of deploying simple parasitic elements was proposed to expand the working bandwidth of the antenna by improving the roll-off performance of the upper edge of the radiator and the selectivity of the upper and lower edges [6–8]. Nevertheless, the above antenna only has one polarization.

More advanced filtering antennas based on the substrate integrated waveguide were proposed in [9, 10] and they have shown good filtering effects, but

Submitted On: January 16, 2022
Accepted On: October 30, 2022

https://doi.org/10.13052/2022.ACES.J.370909

manufacturing the antenna becomes more difficult and requires a much higher cost. Although the comprehensive design method is adopted, the coupling structure between the antenna and filter is more complicated and manufacturing it is not easy [11]. In addition, a filter antenna consisting of a sector patch antenna and a bandpass filter is proposed in [12], which has a smooth in-band gain but very limited out-of-band rejection. More recently, a 2×2 integrated filtering antenna array with good out-of-band suppression characteristics was proposed, but unfortunately, its impedance bandwidth cannot cover the entire 5.0-GHz band of the WLAN communication system [13].

Given the above problems, this paper proposes a new type of microstrip filtering antenna for WLAN communication systems. The filtering antenna is designed through a comprehensive design method and integrates four U-shaped open-loop resonators, a Γ-shaped antenna, and a section of coupling line. The Γ-shaped antenna, as the last resonator of the filter, has both radiation characteristics and filtering characteristics. Simulation and measurement results show that the filtering antenna has a center frequency of 5.25 GHz and a maximum gain of 3.059 dBi. Also, it has a gentle change of in-band gain and the maximum gain difference is 0.7 dBi. Furthermore, its out-of-band gain can decrease rapidly and stabilize at -24 dBi finally, showing an excellent filtering feature. The filtering antenna not only presents good radiation and filtering characteristics, but also has a compact size. The overall size is 41.49 mm $\times$ 26.25 mm $\times$ 0.288 mm, which is much smaller than that of other structures [13]–[15]. With the attractive performance, the filtering antenna could be very useful in the 5.0-GHz band of WLAN communication system.

II. CONFIGURATION OF ANTENNA

A. Filter selection

An open-circuit resonator with a length that is an integer multiple of the half wavelength has the characteristics of a parallel resonant circuit. To realize the integrated design of the filtering antenna, the U-shaped filter is selected. The filter has a compact structure with good indicators and has been widely used in RF and microwave engineering. Moreover, the U-shaped filter uses a traditional open-loop resonator as the basic resonance unit and the open-loop resonator is equivalent to a half-wavelength resonator. A fifth-order bandpass filter is designed by using the design method of integrated filter. The filter has a center frequency of 5.25 GHz, a fractal bandwidth of 10.0%, and a ripple coefficient of 0.01 dB, respectively. The dielectric plate is Rogers 5880 with a dielectric constant of 2.2 and a plate thickness of 0.254 mm. The coupling coefficient C of the resonator and the external quality factor Q_{ext} at the input and output can be calculated by [16].

Table 1: Chebyshev Normalized Component Values

n	g_1	g_2	g_3	g_4	g_5	g_6
1	0.096	1.0				
2	0.4489	0.4078	1.0			
3	0.6292	0.9703	0.6292	1.0		
4	0.7129	1.2004	1.3213	0.6476	1.0	
5	0.7563	1.3049	1.5773	1.3049	0.7563	1.0

$$C_{i,i+1} = \frac{FBW}{\sqrt{g_i g_{i+1}}}, \tag{1}$$

$$Q_{ext,in} = \frac{g_0 g_1}{FBW}, \tag{2}$$

$$Q_{ext,out} = \frac{g_5 g_6}{FBW}. \tag{3}$$

In the above equations, $C_{i,i+1}$ represents the coupling coefficient between i-th and $(i+1)$-th resonators, FBW represents the fractal bandwidth, and g_i with $g_0 = 1$ represent the Chebyshev normalized component values as shown in Table 1 [16], where $Q_{ext,in}$ represents the external figure of merit at the input and $Q_{ext,out}$ represents the external figure of merit at the output, respectively. From the formulas, we can obtain the coupling coefficients as $C_{12} = C_{45} = 0.1$ and $C_{23} = C_{34} = 0.07$, and the Q-factors at the input and output as $Q_{ext,in} = Q_{ext,out} = 7.56$, respectively.

B. Determination of the filter's sizes

To determine the physical sizes of the open-loop resonator, a single-port simulation model is created by using the well-known simulation tool HFSS, and the simulation is performed in an eigenmode. The resonant frequencies of the resonator with different values of L_1 are obtained and shown in Fig. 1. It can be seen from the figure that the resonant frequency decreases as the length of the resonator increases. To achieve a resonant frequency of 5.25 GHz, the length L_1 of the resonator is initially set to be 8.18 mm.

After the length of the resonator is set, the coupling coefficient between the resonator and the external quality factor of the output resonator is extracted by the comprehensive design method, and then the specific sizes of the filter can be determined with the simulations of HFSS. For mutual coupling resonators, the required coupling coefficient can be obtained by adjusting the coupling structure's parameters. Because the U-shaped filter keeps aligned up and down, the coupling strength of the resonators is determined by the size of gap between the resonators. The coupling coefficient C can be calculated by [16].

$$C = \frac{f_H^2 - f_L^2}{f_H^2 + f_L^2}, \tag{4}$$

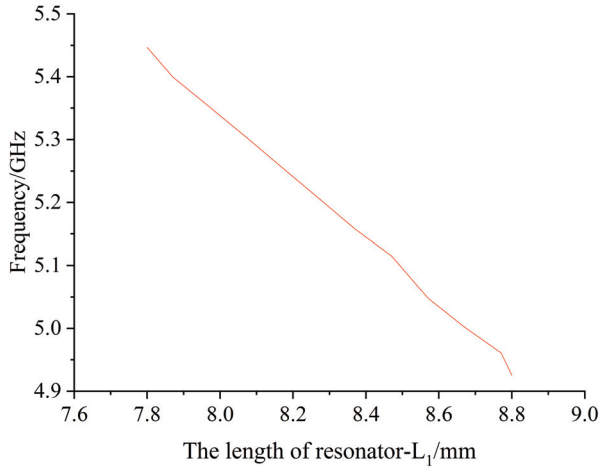

Fig. 1. Change of resonant frequency in terms of L_1.

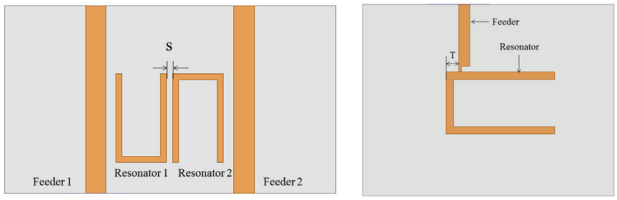

Fig. 2. Simulated parameters for (a) the gap of resonators S and (b) the tap position T.

where f_H and f_L are the upper and lower resonant frequency of the coupled resonator, respectively. Also, the center frequency is $f_c = \sqrt{f_H f_L}$ and the coupling coefficient is positively related to the distance between the two resonance peaks [17].

A simulation is performed with the length of $L_1 =$ 8.18 mm and the simulation model is shown in Fig. 2 (a). The relationship between the gap of filtering resonators and the coupling coefficient is obtained and shown in Fig. 3. It can be seen that the coupling coefficient increases as the coupling gap decreases. When the gap between the resonators is 0.23 mm and 0.34 mm, the corresponding resonance curves are shown in Fig. 4. The calculated coupling coefficients are 0.1 and 0.07, respectively, which can meet the need very well.

Because the fractal bandwidth of the filter is designed to be 10.0%, which is relatively wide, and the traditional slot-coupled feeding structure is thought of as complicated, we use a tap line to feed directly in the filter design so that the external figure of merit can be adjusted by changing the parameters of feeding structure. The external figure of merit of a resonator is mainly determined by the tap's feeding position at both ends in the filter.

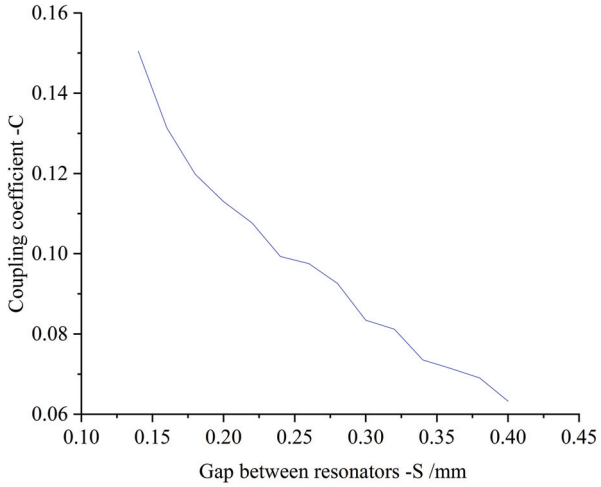

Fig. 3. Relationship between the gap of resonators S and coupling coefficient C.

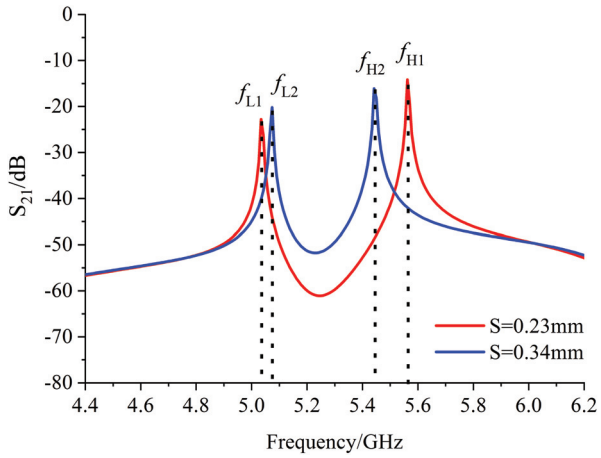

Fig. 4. Resonant responses of the two open-loop resonators.

To obtain the required figure of merit, a single-port simulation is performed with a single resonator and the simulation model is shown in Fig. 2 (b). The external figure of merit Q_{ext} is calculated by [16].

$$Q_{ext} = \frac{f_0}{\triangle f_{\pm 90^\circ}}, \tag{5}$$

where f_0 represents the resonant frequency of the resonator and $\Delta f_{\pm 90^\circ}$ represents the difference of frequencies corresponding to the phases of higher and lower 90° than the phase at f_0. When the resonator's length is determined, the single-port simulations are performed by taking different values for the tap position T. The changing curve of the external quality factor Q_{ext} in terms of the tap position T is shown in Fig. 5 and it can be seen

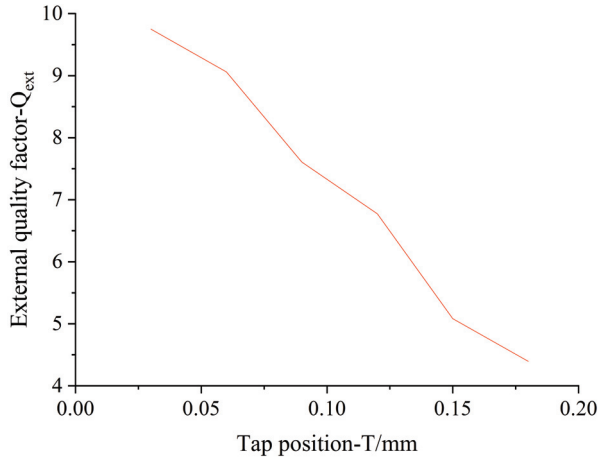

Fig. 5. Relationship between Q_{ext} and T.

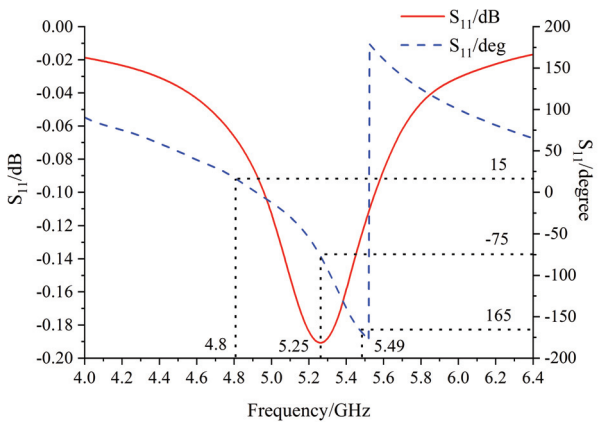

Fig. 6. Amplitude and phase of S_{11} when T = 0.09 mm.

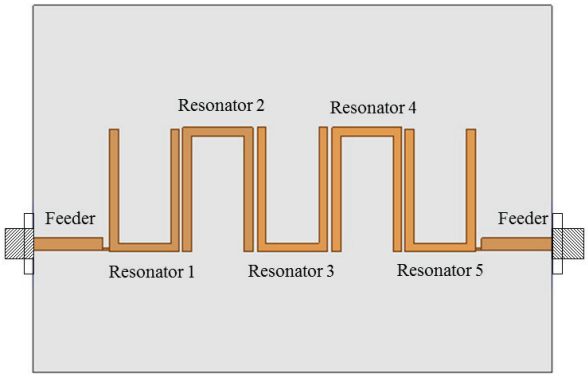

Fig. 7. Structure of the optimized filter.

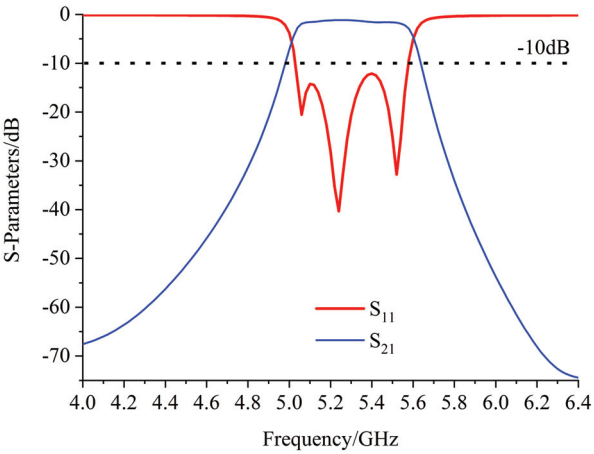

Fig. 8. *S* parameter of the optimized fifth-order filter.

that Q_{ext} is inversely related to T. When $T = 0.09$ mm, the changing curve of the amplitude and phase of the S_{11} is shown in Fig. 6. According to Equation (5), the external figure of merit is 7.60, which basically meets the requirement.

C. Optimization of the filter

In the previous design and analysis, the structural parameters of the filter are preliminarily determined, i.e., the resonator's length is $L_1 = 8.18$ mm, the tap position is $T = 0.09$ mm, and the coupling gaps are $S_1 = 0.23$ mm and $S_2 = 0.34$ mm, respectively. The model of initial filter is established in the HFSS and then optimized for each structural parameter. The optimized structure is shown in Fig. 7 and its *S*-parameter is plotted in Fig. 8. It can be seen that the range of -10 dB bandwidth is from 5.03 GHz to 5.57 GHz, the center frequency is 5.25 GHz, the reflection coefficient is greater than -15 dB, and the insertion loss is less than -1.5 dB, which can meet the design requirements fully.

D. Γ-shaped antenna and its integration with the filter

The Γ-shaped antenna is a deformed monopole antenna, the structure and equivalent circuit of which are shown in Fig. 9. In the figure, R_a is the radiation resistance of the antenna, C_a is the resonance capacitance, L_a is the resonance inductance, and C_g is the added parallel capacitance which is used to maintain the same impedance characteristic as that of the antenna in a wider bandwidth [17]. The antenna and the filter's circuit board have a common ground, and an impedance conversion line is connected to the microstrip antenna. The line can adjust the resonance characteristic of the antenna at 5.25 GHz and the antenna actually becomes the last resonator of the filter. The antenna needs to have the same figure of merit Q_{ext} as the filter, and the external figure of merit

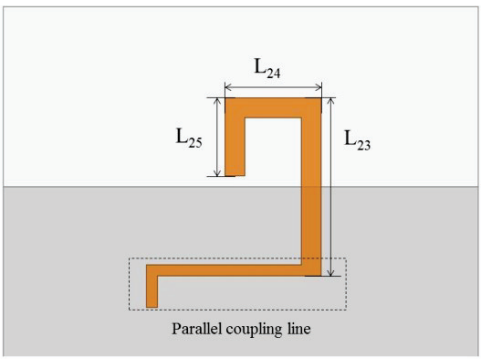

Fig. 9. Antenna part of the proposed filtering antenna. (a) Structure. (b) Equivalent circuit.

Q_a of the antenna can be extracted by [17].

$$Q_a = \frac{f_0}{2\mathrm{Re}[Z_{in}(f_0)]} \frac{d[\mathrm{Im}(Z_{in})]}{df}\bigg|_{f=f_0} \tag{6}$$

where f_0 is the corresponding frequency with the maximum value of resistance and Z_{in} is the input impedance at the antenna's feeding point. The resonance frequency of the Γ-shaped antenna is determined by the total length of L_{23}, L_{24}, and L_{25}, and it is approximately the half wavelength at the center frequency. From the simulations, we find that the current density in the vertical arm connected to the coupling line is the strongest and it is shown in Fig. 10. Also, the length L_{23} can be adjusted to obtain a matching figure of merit while keep the total length unchanged approximately. After designing the bandpass filter and the Γ-shaped antenna, we then use a couple of parallel coupling lines as an admittance transformer to connect the filter with the antenna. The parallel coupling lines and their equivalent circuit are shown in Fig. 11 [18].

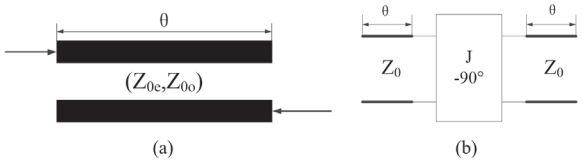

Fig. 10. Current density distribution of the antenna.

The parity analysis method is used to analyze the parallel coupling lines. If the two structures have the same electrical properties, the ABCD matrices of the two structures should be equal. When the electrical length is $\theta = \frac{\pi}{2}$, we can obtain the following relationship

$$\frac{Z_{0e}}{Z_0} = 1 + JZ_0 + (JZ_0)^2, \tag{7}$$

$$\frac{Z_{0o}}{Z_0} = 1 - JZ_0 + (JZ_0)^2, \tag{8}$$

$$JZ_0 = \frac{2FBW\theta}{\sqrt{g_4 g_5}}, \tag{9}$$

where Z_{0e} and Z_{0o} are the even- and odd-mode impedances, respectively, Z_0 is the input impedance, and g_4 and g_5 are the original values of the filter. The even- and odd-mode impedances can be obtained when Z_0 is given, and the physical dimensions of the parallel coupling lines can then be determined. When all structural parameters of the filtering antenna are determined, the overall optimization can be performed in the HFSS. The complete structure of the filtering antenna is shown in Fig. 12 and it has three layers. The middle layer is the substrate and the bottom of the substrate is a ground plate which is made of copper. Also, the copper's resonance unit and the antenna are attached to the upper layer of the substrate. The parameters of overall structure are shown in Fig. 13, and the specific values of those parameters are listed in Table 2.

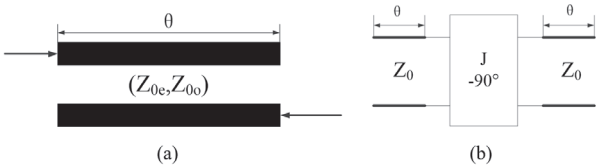

Fig. 11. A couple of parallel coupling lines. (a) Structure. (b) Equivalent circuit.

Table 2: Structural Parameters of the Filtering Antenna (unit: mm)

L	L_b	L_0	L_{01}	L_{11}	L_{12}	L_{13}	L_{21}	L_{22}
41.49	31.59	5	0.47	8.17	8.23	8.3	2.34	9.66
L_{23}	L_{24}	L_{25}	W	W_0	W_{01}	W_1	W_2	S_1
9.84	5.34	2.34	26.25	0.9	0.2	0.6	1.1	0.26
S_2	S_3	T	B					
0.37	0.18	0.08	5					

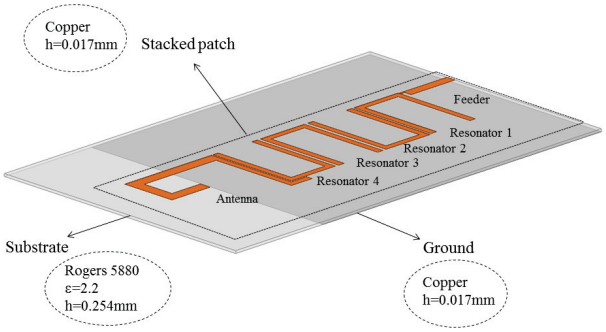

Fig. 12. Complete structure of the filtering antenna.

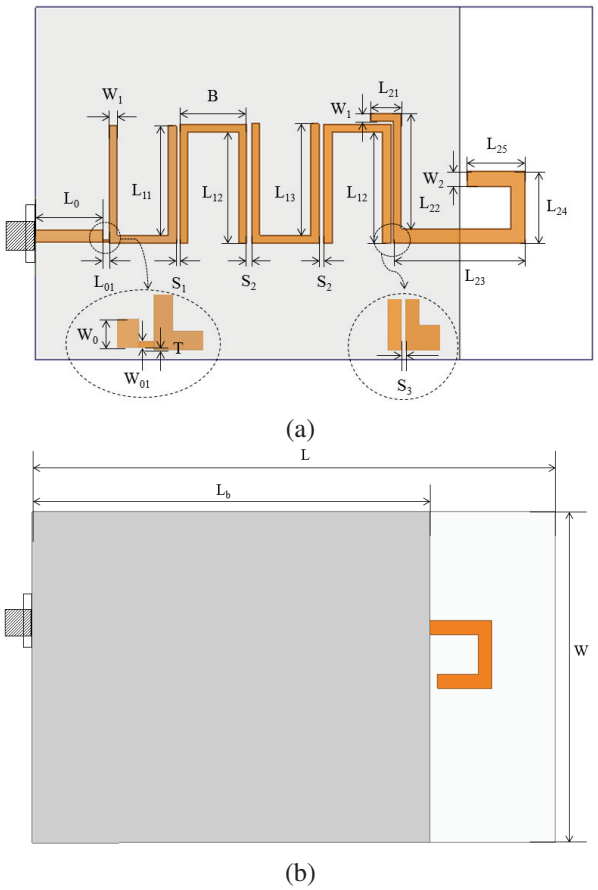

Fig. 13. Structural parameters of the filtering antenna. (a) Top view. (b) Back view.

III. PERFORMANCE OF THE FILTERING ANTENNA

The physical PCB board of the filtering antenna is manufactured according to the structural parameters obtained from the optimization simulations and it is shown in Fig. 14. The S_{11} parameter and gain of the filtering antenna are measured using a vector network analyzer and the comparison between the simulation results and

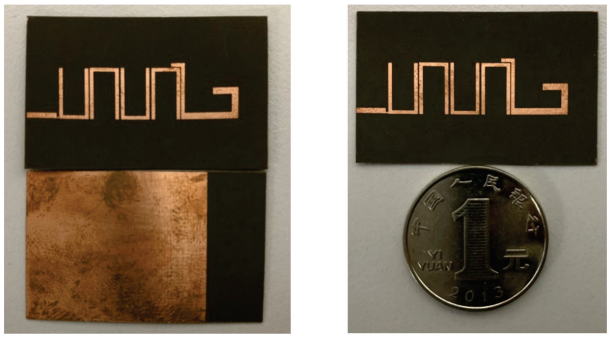

Fig. 14. Proposed filtering antenna. (a) Physical image. (b) Size comparison.

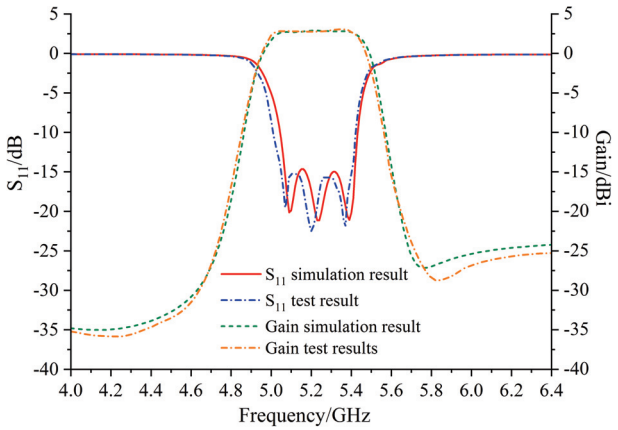

Fig. 15. S_{11} parameter and gain of the filter antenna.

measurement results are illustrated in Fig. 15. From the figure, we can see that the center frequency of the filtering antenna is 5.25 GHz, the fractal bandwidth at −10.0 dB is 8.0% (5.0 − 5.42 GHz), and the return loss is lower than −15.0 dB. There is a small frequency offset in the measurement result due to the inevitable errors in the experimental setup and manufacturing of PCB board. In addition, the gain of the filtering antenna is 2.79 dBi at the frequency of 5.25 GHz and the change of in-band gain is gentle because the maximum deviation of gain is only 0.7 dBi. Outside the band, the gain drops to −10 dBi at 150 MHz and the gain drops overall to −24 dBi finally.

We also present the radiation patterns of the filtering antenna at 5.25 GHz by simulations and they are shown in Fig. 16. In the XOY plane, there is an 8-shaped pattern similar to that of a monopole antenna. Moreover, there is a depression in the direction of 260° and it is mainly caused by the coupling loss between the antenna's end and the ground plate.

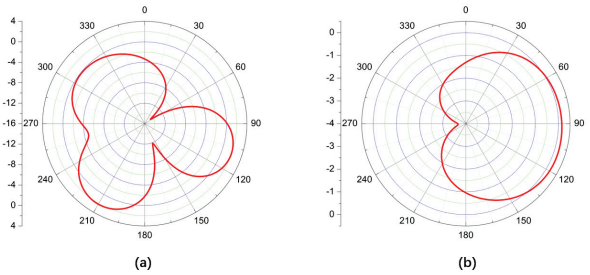

Fig. 16. Simulated radiation patterns of the filtering antenna. (a) XOY plane. (b) YOZ plane.

Table 3: Comparison on the Performances od Antennas

Reference	BW (GHz)	Size (mm)	Gain* (dBi)
[14]	3.1-10.6	40 × 30	3.05
[19]	3.5-5.97	49 × 37.85	4.177
[20]	5.15-5.825	64.3 × 34.8	3.5
[21]	5.15-5.825	98.93 × 42.93	7.40
[22]	5.15-5.825	93.53 × 38.82	7.30
[23]	5.25-5.35	21.075 × 17	3.93-4.45
This work	5-5.42	41.49 × 26.25	3.059

*The gain is obtained in the band of $5 - 5.42$ GHz.

We compare the antenna proposed in this paper with the typical antennas proposed in previous papers and the result is shown in Table 3. It can be seen that the filter antenna proposed in this paper has higher gain than the antenna proposed in [14], much smaller physical size than those antennas proposed in [19]–[22], and wider bandwidth than the antenna proposed in [23]. The bandwidth of proposed antenna can cover the 5.0- GHz band to meet the requirements of practical applications.

IV. CONCLUSION

This paper proposes a microstrip filtering antenna for WLAN communication system in the 5.0-GHz band by using an integration design method of filters. The antenna becomes the fifth-order resonator of the filter through the integration of parallel coupling lines, which realize the combination of antenna's radiation property and filter's out-of-band rejection characteristic. The simulation and measurement results show that the filtering antenna has a smooth in-band gain and good out-of-band suppression feature. Also, the antenna has a compact structure whose overall size is much smaller than that of other structures. Based on the excellent performance, the proposed filtering antenna can be a good candidate for WLAN communication system in the 5.0-GHz working band.

REFERENCES

[1] Y. F. Cao, Y. Zhang, and X. Y. Zhang, "Filtering antennas: from innovative concepts to industrial applications," *Frontiers of Information Technology & Electronic Engineering*, vol. 21, no. 1, pp. 116-127, 2020.

[2] M. Troubat, S. Bila, M. Thévenot, D. Baillargeat, T. Monédière, S. Verdeyme, and B. Jecko, "Mutual synthesis of combined microwave circuits applied to the design of a filter-antenna subsystem," *IEEE Transactions on Microwave Theory and Techniques*, vol. 55, no. 6, pp. 1182-1189, Jun. 2007.

[3] W.-J. Wu, S.-L. Zuo, X.-M. Huang, D.-E. Wen, and R. Fan, "Compact dual-band loop-loaded monopole with integrated band-select filter for WLAN application," *IEEE International Symposium on Antennas, Propagation and EM Theory*, Xi'an, China, Oct. 2012.

[4] M. C. Bailey, "A stacked patch antenna design with strict bandpass filter characteristics," *2004 IEEE International Symposium on Antennas and Propagation and USNC/URSI National Radio Science Meeting*, vol. 2. Monterey, CA, USA, Jun. 2004.

[5] M. M. Fakharian, P. Rezaei, A. A. Orouji, and M. Soltanpur, "A wideband and reconfigurable filtering slot antenna," *IEEE Antennas and Wireless Propagation Letters*, vol. 15, pp. 1610-1613, 2016.

[6] G. Sun, S. Wong, L. Zhu, and Q. Chu, "A compact printed filtering antenna with good suppression of upper harmonic band," *IEEE Antennas and Wireless Propagation Letters*, vol. 15, pp. 1349-1352, 2016.

[7] J. Wu, Z. Zhao, Z. Nie, and Q. H. Liu, "A broadband unidirectional antenna based on closely spaced loading method," *IEEE Transactions on Antennas and Propagation*, vol. 61, no. 1, pp. 109-116, Jan. 2013.

[8] J. Wu, Z. Zhao, Z. Nie, and Q. Liu, "A printed unidirectional antenna with improved upper band-edge selectivity using a parasitic loop," *IEEE Transactions on Antennas and Propagation*, vol. 63, no. 4, pp. 1832-1837, Apr. 2015.

[9] H. Cheng, Y. Yusuf, and X. Gong, "Vertically integrated three-pole filter/antennas for array applications," *IEEE Antennas and Wireless Propagation Letters*, vol. 10, pp. 278-281, 2011.

[10] H. Chu and Y.-X. Guo, "A filtering dual-polarized antenna subarray targeting for base stations in millimeter-wave 5G wireless communications," *IEEE Transactions on Components, Packaging and Manufacturing Technology*, vol. 7, no. 6, pp. 964-973, Jun. 2017.

[11] X. Y. Zhang, W. Duan, and Y.-M. Pan, "High-gain filtering patch antenna without extra circuit," *IEEE Transactions on Antennas and Propagation*, vol. 63, no. 12, pp. 5883-5888, Dec. 2015.

[12] X. Chen, F. Zhao, L. Yan, and W. Zhang, "A compact filtering antenna with flat gain response within the passband," *IEEE Antennas and Wireless Propagation Letters*, vol. 12, pp. 857-860, 2013.

[13] A. K. Sahoo, R. D. Gupta, and M. S. Parihar, "Slot antenna array with integrated filter for WLAN application at 5.2 GHz," *Wireless Personal Communications*, vol. 101, no. 2, pp. 931-941, Feb. 2018.

[14] A. Alhegazi, Z. Zakaria, N. A. Shairi, A. Salleh, and S. Ahmed, "Compact UWB filtering-antenna with controllable WLAN band rejection using defected microstrip structure," *Radioengineering*, vol. 27, no. 1, pp. 110-117, Apr. 2018.

[15] H. Md Maqubool, S. Kumari, and A. K. Tiwary, "Sunflower shaped fractal filtenna for WLAN and ARN application," *Microwave and Optical Technology Letters*, vol. 62, no. 1, pp. 346-354, Jan. 2020.

[16] J.-S. Hong and M. J. Lancaster, *Microstrip Filters for RF/Microwave Applications*. John Wiley & Sons, New York, 2004.

[17] Y. Yusuf and X. Gong, "Compact low-loss integration of high-3-D filters with highly efficient antennas," *IEEE Transactions on Microwave Theory and Techniques*, vol. 59, no. 4, pp. 857-865, Apr. 2011.

[18] D. M. Pozar, *Microwave Engineering*. John Wiley & Sons, New York, 2009.

[19] M. C. Lim, S. K. A. Rahim, M. R. Hamid, A. A. Eteng, and M. F. Jamlos, "Frequency reconfigurable antenna for WLAN application," *Microwave and Optical Technology Letters*, vol. 59, no. 1, pp. 171-176, Jan. 2017.

[20] M. M. Hosain, S. Kumari, and A. K. Tiwary, "Sunflower shaped fractal filtenna for WLAN and ARN application," *Microwave and Optical Technology Letters*, vol. 62, no. 1, pp. 346-354, Jan. 2020.

[21] M. R. Jena, S. Sahoo, G. P. Mishra, and B. B. Mangaraj, "Miniaturised band notched printed LPDA design with meander fractal dipole for UWB communication," *International Journal of Electronics*, vol. 108, no. 1, pp. 21-44, Jan. 2021.

[22] S. Sahoo, G. P. Mishra, M. R. Jena, and B. B. Mangaraj, "Sub-sectional tapered printed-LPDA design with WLAN, WiMAX notch bands for UWB communication systems," *International Conference on Intelligent Computing and Communication Technologies*, pp. 717-727, Singapore, Jan. 2019.

[23] A. B. Sahoo, G. P. Mishra, and B. B. Mangaraj, "Optimal design of compact dual-band slot antenna using particle swarm optimization for WLAN and WiMAX applications," *Recent Advances in Electrical & Electronic Engineering (Formerly Recent Patents on Electrical & Electronic Engineering)*, vol. 12, no. 5, pp. 425-431, May 2019.

Shujia Yan received the B.S. degree in Electrical Engineering and Automation from Tongji University, Shanghai, China, in July 2004, and the M.S. degree in control theory and control engineering from Dalian Maritime University, Dalian, China, in April 2008, and the Ph.D. degree in detection technology and automatic equipment from Tongji University, Shanghai, China, in June 2014. She is currently working in Shanghai University of Engineering Science as a lecturer. Her research interest is mainly in Applied Computational Electromagnetics,intelligent detection and inductively coupled power transfer.

Chongqi Zhang received the B.S. degree in Rail traffic signal and control from Changzhou University, Changzhou, China, in July 2018, and the M.S. degree in Intelligent Perception and Control from Shanghai University of Engineering Science, Shanghai, China, in April 2021. He is currently working in Shenzhen Huiding Technology Co., Ltd. as an electronic engineer. He won the second place of the 16th "HUAWEI CUP" National Postgraduate Mathematical Contest in Modeling in 2019. His research interest is mainly in Application of Radio Frequency Identification.

Qiang Chen received his B.S. degree in Geophysics and Computer Science from Yangtz University, Hubei, China, in 1986, and the M.S. degree in Geophysics from Yangtz University, Hubei, China, in 1997, and Ph.D. degree in Geophysics from Tongji University, Shanghai, China, in 2001. He is currently working in Shanghai University of Engineering Science as a Professor. Her research interest is mainly in theory and method of urban pipe network detection underground resource detection, and the development of electromagnetic detection instrument and equipment.

Mei Song Tong received the B.S. and M.S. Degrees from Huazhong University of Science and Technology, Wuhan, China, respectively, and Ph.D. degree from Arizona State University, Tempe, Arizona, USA, all in electrical engineering. Currently, he is the Distinguished/Permanent Professor, Head of Department of Electronic Science and Technology, and Vice Dean of College of Microelectronics, Tongji University, Shanghai, China. He has also held an adjunct professorship at the University of Illinois at Urbana-Champaign, Urbana, Illinois, USA, and an honorary professorship at the University of Hong Kong, Hong Kong, China. He has published more than 500 papers in refereed journals and conference proceedings and co-authored six books or book chapters. His research interests include electromagnetic field theory, antenna theory and technique, modeling and simulation of RF/microwave circuits and devices, interconnect and packaging analysis, inverse electromagnetic scattering for imaging, and computational electromagnetics.

Prof. Tong is a Fellow of the Electromagnetics Academy, Fellow of the Japan Society for the Promotion of Science (JSPS), and Senior Member (Commission B) of the USNC/URSI. He has been the chair of Shanghai Chapter since 2014 and the chair of SIGHT committee in 2018, respectively, in IEEE Antennas and Propagation Society. He has served as an associate editor or guest editor for some well-known international journals, including IEEE Antennas and Propagation Magazine, IEEE Transactions on Antennas and Propagation, IEEE Transactions on Components, Packaging and Manufacturing Technology, International Journal of Numerical Modeling: Electronic Networks, Devices and Fields, Progress in Electromagnetics Research, and Journal of Electromagnetic Waves and Applications, etc. He also frequently served as a session organizer/chair, technical program committee member/chair, and general chair for some prestigious international conferences. He was the recipient of a Visiting Professorship Award from Kyoto University, Japan, in 2012, and from University of Hong Kong, China, 2013. He advised and coauthored 12 papers that received the Best Student Paper Award from different international conferences. He was the recipient of the Travel Fellowship Award of USNC/URSI for the 31th General Assembly and Scientific Symposium (GASS) in 2014, Advance Award of Science and Technology of Shanghai Municipal Government in 2015, Fellowship Award of JSPS in 2016, Innovation Award of Universities' Achievements of Ministry of Education of China in 2017, Innovation Achievement Award of Industry-Academia-Research Collaboration of China in 2019, Chapters Award of IEEE New Jersey Section, USA, in 2019, "Jinqiao" Award of Technology Market Association of China in 2020, and Baosteel Education Award of China in 2021. In 2018, he was selected as the Distinguished Lecturer (DL) of IEEE Antennas and Propagation Society for 2019–2022.

A Novel Comb-line Leaky-wave Antenna for 77 GHz FMCW Automotive Radar System and Comparison with Buttler Beamformers

Masoud Sarabi and Warren F. Perger

Department of Electrical & Computer Engineering
Michigan Technological University, Houghton, 49931 USA
msarabi@mtu.edu, wfp@mtu.edu

Abstract – For a typical frequency modulated continuous wave automotive radar system, a design using a novel leaky-wave antenna is proposed that has a simple, cheap and easy manufacturing structure whose performance is compared with two different antenna arrays. The software used were MATLAB and CST Microwave Studio. The first antenna system was an inset-fed patch array, and the second antenna system was a circular patch array with a Buttler beamforming network as a beam scanning mechanism. The simulation results of the three proposed designs are obtained using the range-Doppler method for multi-target scenarios. The proposed leaky-wave antenna excels the antenna arrays, which offer cheaper and simpler solutions for the automotive industry.

Index Terms – buttler beamforming network, frequency modulated continuous wave (FMCW), inset-fed patch antenna array, leaky-wave antenna (LWA), multi-target detection

I. INTRODUCTION

Road safety has always been a challenging issue all around the world. The National Highway Traffic Safety Administration (NHTSA) is an agency that provides annual statistics on road casualties as shown in Fig. 1 As we see, in 2019 alone there were 36,096 fatalities on US roads [1].

Different solutions have been so far proposed to increase road safety. But amongst the proposed methods, frequency-modulated continuous wave (FMCW) radars are one of the most promising solutions compared to other types of automotive radar systems. These radars are low-cost, simple in architecture, and have robustness in foggy or rainy weather, which makes them more appealing compared to LIDAR or cameras. In general, there are two types of radars: pulse radars and continuous wave (CW) radars. In pulse radars, we transmit a very short pulse accompanied by high average power.

Radar resolution ΔR is equal to $c/2BW$, where C is the speed of light and BW is the system bandwidth. Continuous wave radars, as the name implies, continuously send radar signals toward targets, and thus provide

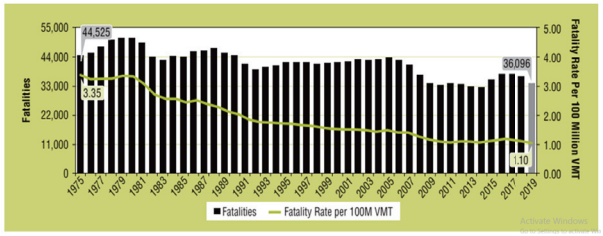

Fig. 1. US Road's Fatality Rate per 100 million VMT, 1975-2019 [1].

continuous radar updates on the target. In CW radars the peak-to-average power is quite low (a few watts) and this factor makes such radars more economical for automotive applications compared to pulse-waveform radars [2].

There are many interesting applications or aspects of FMCW radars to be improved such as in [3], where authors mention improving the low resolution of FSK radars using LFM waveforms. In [3] and [4], the emphasis is on the design of a baseband signal processing system for FMCW radar where a three-ramp chirp is used to increase radar accuracy and shorten the measurement time without complicating the RF front-end. In [5] the authors have introduced a 60GHz LWA to do a simultaneous estimation of the direction of arrival (DOA) and ranging of objects providing 60° beam steering by sweeping from 50GHz to 60GHz. Human tracking is a vital research area. There is already a proposed microstrip LWA for tracking humans as shown in [6]. In [7] the authors have assessed different ways of walking such as slow or fast walking using the FMCW radar system. One of the most challenging issues of the multi-target FMCW radar systems is the existence of ghost targets. Any radar detection other than the main targets is considered a ghost target. It could have different causes and so the solutions are as diverse as the types of ghost targets themselves. For example, in [8] the ghost targets are caused by inter-radar interference and to suppress such ghost targets, authors use a carrier sensing method and interference replica to suppress the ghosts. In our proposed system there is an easy solution which

Submitted On: March 14, 2022
Accepted On: October 9, 2022

https://doi.org/10.13052/2022.ACES.J.370910

will be discussed in section IV. The antenna used in any radar system is one of the main factors that determine the overall cost of the system. In this work, we have studied the application of a comb-line leaky-wave antenna for radar systems to explore the interesting characteristics of these antennas. In fact, leaky-wave antennas are modified waveguiding structures which might have modifications such as periodic slots or stubs. They allow electromagnetic waves to leak through them as they travel along the structure, giving leaky-wave antennas interesting properties [9]. The mechanism of wave leakage through each periodic slot is explained in [10]. The Floquet periodicity theorem [11] was applied to periodic leaky-wave antennas whereby the field of each slot could be expanded as a multiplication of a periodic function by the general exponential wave function of the form $e^{-j\beta z}e^{-\alpha z}$, in which β is propagation constant and α is attenuation factor. In a recent work [12], a periodic LWA has been used in a joint communication radar. In [13], a circularly polarized periodic LWA has been used for radar imaging.

II. FMCW WAVEFORMS

A typical FMCW radar system is shown in Fig. 2 which includes the following block diagrams of the transmitter, receiver, mixer, and analog to digital converter (A/D).

In simple words, an FMCW signal is generated at the transmitter side and sent via the transmitter antenna toward the receiver. At the receiver's side, after receiving the echo signal reflected from a target, a mixer combines the chirp signal (reference signal) and the reflected signal. A low pass filter removes the higher frequency harmonics and keeps the intermediate frequency (IF) signal which then goes to the analog-to-digital converter and finally to the signal processing block for detection and range-Doppler mapping.

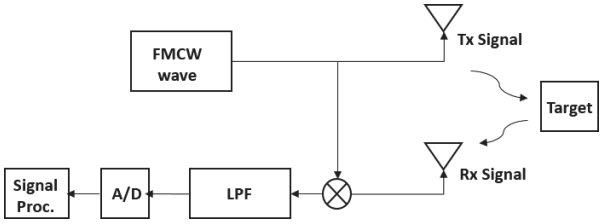

Fig. 2. Schematic of a generic FMCW Radar system.

A. FMCW signal model

The transmitted signal can be considered as equation(1):

$$s_{tx}(t) = A_{tx}cos(2\pi f_c t + 2\pi \int_0^t f_{tx}(\tau)\, d\tau), \qquad (1)$$

in which, $f_{tx}(\tau)$ is the linear chirp function of the transmit frequency equal to $B\tau/T$ while chirp could be exponential, quadratic, etc. but in this work, the linear chirp has been used. f_c is the working frequency of radar, B is the bandwidth, A_{tx} is the signal amplitude and T is pulse duration. On the other hand, the receiving frequency is described in equation (2).

$$f_{rx}(t) = \frac{B}{T}(t - t_d) + f_D, \qquad (2)$$

where t_d is the time delay. A target moving with the velocity v gives the Doppler shift described by f_{rx} as $f_{rx}(t)$=$-2f_c$ v/c. The received signal is expressed by equation (3):

$$\begin{aligned} f_{rx}(t) &= A_{rx}cos(2\pi f_c(t - t_d) + 2\pi \int_0^t f_{rx}(\tau)\, d\tau), \\ &= A_{rx}cos\{2\pi f_c(t - t_d) + \frac{B}{T}(\frac{1}{2}t^2 - t_d t) + t_d t), \end{aligned} \qquad (3)$$

where A_{rx} is the amplitude of the received signal that is influenced by the radar cross section (RCS), the distance of the target, gains of transmitting and receiving antennas and the power used for the transmission. As Fig. 2 illustrates, once the FMCW signal is generated at the transmitter's side, a branch of this signal is injected into the mixer that is at the receiver's side. In this mixer, the reference signal and the received signal (echo from the target) are mixed or in other words, they are multiplied together, leading to higher-frequency components in addition to lower-frequency ones. To suppress the higher frequency components and get the IF signal (intermediate frequency signal), a low-pass filter is used right after the mixer. The IF signal is represented by $s_{IF}(t)$. If a triangular waveform composed of two ramps (a positive and negative ramp) is used, then two beat frequencies f_{bu} and f_{bd} will emerge after the low pass filter (LPF) expressed by equations(4) and (5):

$$f_{bu}(t) = \frac{2R_0}{C}\frac{B}{T} + 2\frac{f_c v}{C}, \qquad (4)$$

$$f_{bd}(t) = \frac{-2R_0}{C}\frac{B}{T} + 2\frac{f_c v}{C}, \qquad (5)$$

The reflected signal that returnsfrom a given target looks like the transmitted signal but in fact, it is the shifted version of the reference signal both in time and frequency. Figure 3 illustrates the sent and the received spectrograms (Tx and Rx chirps correspondingly). A chirp could also be in form of a sawtooth waveform as shown in Fig. 4. Based on this figure, we can write the following equations of the upbeat and downbeat frequencies:

$$f_b^+ = \frac{4\Delta f R}{CT_s} - f_D, \qquad (6)$$

$$f_b^- = \frac{-4\Delta f R}{CT_s} - f_D, \qquad (7)$$

Then solving for the equations (6) and (7) for R and f_D, will result in equations (8) and (9):

$$R = \frac{cT_s}{8\Delta f}\,\frac{(f_b^+ - f_b^-)}{2}\,, \tag{8}$$

$$f_D = -\frac{(f_b^+ + f_b^-)}{2}\,. \tag{9}$$

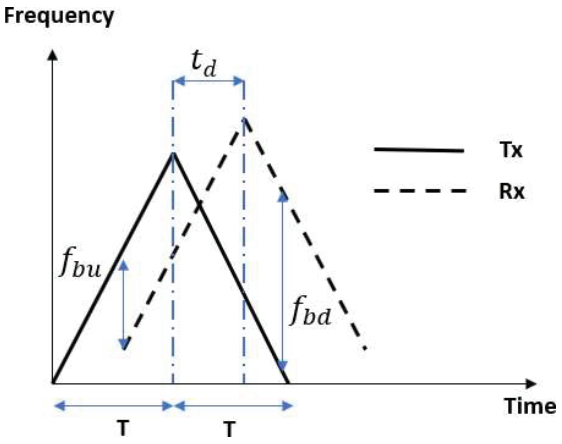

Fig. 3. Spectrogram of triangular chirp for transmittedand received signals.

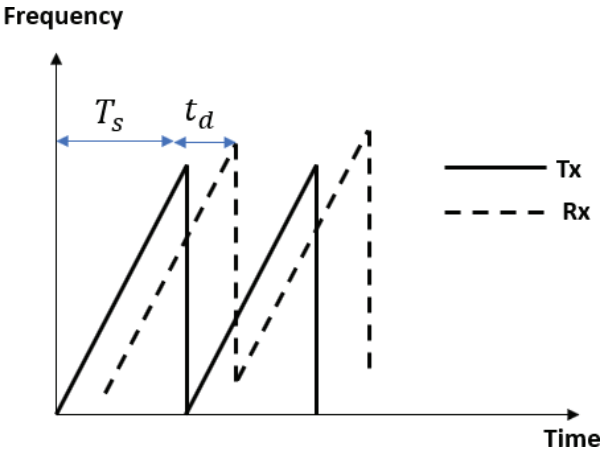

Fig. 4. Spectrogram of triangular chirp for transmittedand received signals.

III. THE PROPOSED RADAR STRUCTURE

The proposed 77 GHz automotive FMCW radar system is shown in Fig. 5. The design parameters of the RF components of this system, such as system bandwidth, antenna gain, noise figure, etc. are summarized in Table 1. The system design has been implemented using MATLAB Simulink. The main design parameters of the radar system are summarized in Table 1 which are chosen from [3].

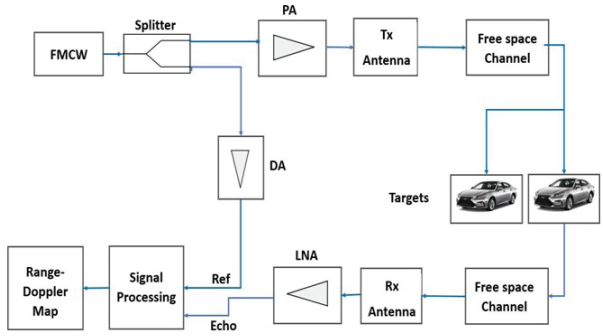

Fig. 5. The architecture of the multi-target FMCW automotive radar.

Table 1: Design parameters of the radar system

Parameter	Explanation	Value
Fs	Sampling frequency	150 MHz
BW	Bandwidth	150 MHz
Tx Gain	Transmitter's gain	36 dB
Rx Gain	Receiver's gain	42 dB
NF	Noise figure	4.5

A. FMCW signal block

This block generates FMCW signal of 77 GHz frequency which is a typical frequency for automotive applications. We could use any type of chirp including linear, quadratic, etc. The linear chirp itself could be up, down, or triangular. We have used both triangular and up-chirp in our proposed radar system.

B. Splitter

A splitter is a three-port and non-directional component that has the task of directing the input signal to two different outputs. A common type of splitter is the Wilkinson splitter.

C. Power amplifier

This component is used to boost a weak signal into a strong signal and denoise it.

D. Transmitter/ receiver antenna

In this research, we propose the application of a leaky-wave antenna as a substitute for antenna array which is shown in Fig. 6 with the main dimensions summarized in Table 2. As we know, the automotive industry uses antenna array as a transmitting and receiving system. leaky-wave antennas have interesting properties that make them quite attractive for radar systems. By using the frequency scanning property of the leaky-wave antennas, we could control the antenna beam in different directions as described by [10]:

$$sinsin\ (\theta_m) = \beta(f)/k_0. \tag{10}$$

Once the frequency changes, the propagation constant changes and so does the direction of the main

beam. The antenna proposed for this radar system is a comb-line leaky-wave antenna with the substrate Arlon AD 350 with permittivity ε_r=3.5. This comb-line leaky-wave antenna provides a simple beamforming structure and right/left-handed beam-scanning. The antenna structure is composed of 31 stubs to introduce periodicity and generate Floquet modes [4] and it is excited through two ports situated at both sides of the antenna.

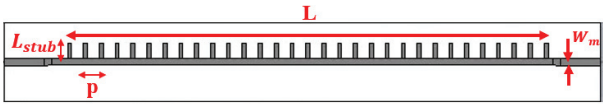

Fig. 6. Comb-line leaky-wave antenna as FMCW radar antenna.

The design parameters for our proposed comb-line leaky-wave antenna are summarized in Table 2. The wavelength $\lambda = 3.89$ *mm* corresponds to the radar frequency of 77 GHz. Microstrip width W_m is set on 1mm which is in an appropriate range for width trace of antenna that works in 77 GHz. Antenna length is chosen to be approximately 20λ to be long enough for the leakage factor to be small. Stub width and length are correspondingly 0.5 and 2mm that are chosen by running iterative simulations of CST software to achieve optimal values. The period p is chosen to be smaller than wavelength to minimize grating lobes.

Table 2: Design parameters of comb-line leaky-wave antenna

Parameter	Symbol	Value (mm)
Wavelength	λ	3.89
Microstrip width	W_m	1
Antenna length	L	75
Stub width	W_{stub}	0.5
Stub length	L_{stub}	2
Period	p	2
Substrate thickness	H_s	0.38

The following figure shows the propagation patterns of the comb-line leaky-wave antenna that proves the frequency scanning capability of it. By looking at the propagation patterns we can see that the comb-line leaky-wave antenna has both left and right-handed propagations and there are beams with decent gains at these frequencies.

E. Propagation channel

The propagation channel is a free space medium that is modeled by applying time delay as well as attenuation of the transmitted FMCW signal because of the path loss

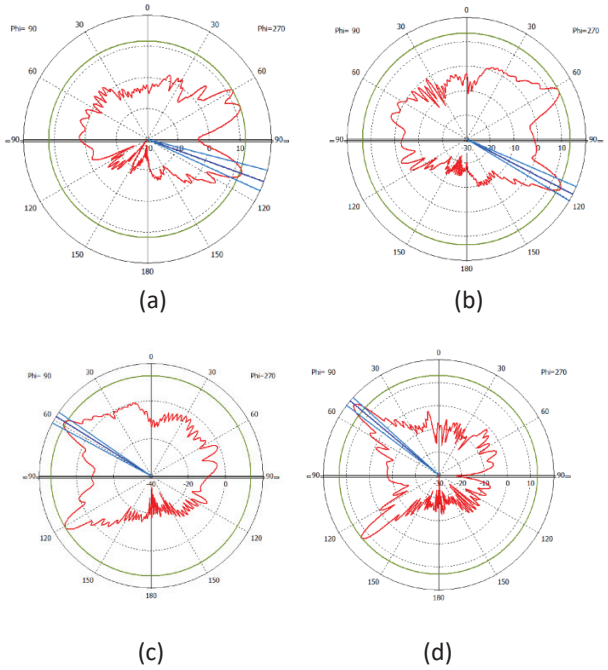

Fig. 7. Radiation patterns of the proposed comb-line leaky-wave antenna at $\varphi = 0^\circ$ showing right & left-handed beam scanning for frequencies a = 75 GHz, b = 77 GHz, c = 77.5 GHz and d = 79 GHz.

expressed in the following equation:

$$L_{pl} = (4\pi R/\lambda)^2, \tag{11}$$

where R is the propagation distance and λ the signal wavelength.

F. Target RCS

Every target could be attributed a radar cross section (δ) value at a given frequency. This parameter specifies how much the backscatter power per steradian is echoed from the target. In our radar design we considered four road targets that are a truck, a car, a motorcycle, and a bike. Table 3 summarizes the RCS values considered for the targets at 77 GHz.

Table 3: Radar cross sections of targets in at f = 77 GHz

Target	Truck	Car	Motorcycle	Bike
RCS	1000	50	25	15

G. Preamplifier

Preamplifier is a device for amplification and noise suppression of the echo signal. In the corresponding Simulink block, the attributed noise figure of this block is NF = 4.5 for the ambient temperature of T = 290°K and the gain is 42.

H. Signal processing

The signal processing block is composed of four subblocks of a mixer, pulse buffer, range-Doppler response, and range-speed estimation. The mixer multiplies the reference signal with the echo signal which then generates IF signal. The pulse buffer block converts scalar samples to frame structure. The range-Doppler block receives the input IF signal and calculates the range-Doppler map using the FFT transform. The number of FFT points is 2048 in our platform. For range processing FFT windowing as well as Doppler processing FFT windowing we can use any of the 5 types of windows such as Hamming, Chebyshev, Hanning, Kaiser, and Taylor. Figure 8 summarizes the signal processing block and its subblocks.

Fig. 8. Subblocks of the signal processing block.

IV. SIGNAL PROCESSING AND DETECTION

The proposed radar system was tested using 2 different FMCW chirps of sawtooth and triangular. The corresponding equations of both cases were discussed in section II (equations 4 - 9). In each case, the evaluation of the radar system was done using a range-Doppler map. In our simulations, we assume that the radar system is installed on a reference vehicle that is moving with a speed of 27.77 m/s and an initial range of 0 m. The range–Doppler map gives us the relative velocity of a vehicle in reference to the radar as well as the relative range as equations (12) and (13) express:

$$\Delta v = v_{radar} - v_{vehicle}, \tag{12}$$

$$\Delta R = R_{radar} - R_{vehicle}. \tag{13}$$

At the first stage, the triangular FMCW chirp was used in the radar system and the ghost target issue was challenging in this case. Since by increasing the number of actual targets, the number of ghost targets also increases. Based on our simulations, for example in the four-target scenario, we observed 12 ghost targets as shown in Fig. 9. For our proposed radar system when we use triangular chirp there is a linear equation that could be used to predict the number of ghost targets (G) which is G = 3 ∗ N, in which (N) is the number of targets. There are different methods for suppressing ghost targets as was briefly pointed out in the introduction section. But not every method works for every radar system. The authors think that in the triangular chirp the down-ramp causes some additional echoes and creates a scenario of "mirror ghosts". If we closely observe Fig. 9, we notice that there are two groups of ghost targets, the ghost targets that appear right below the actual targets marked as Group I and the ghost targets that appear on the left- and right-hand side of the range-Doppler map marked as Group II. The ghost targets of Group I are exactly the mirror of actual targets with reference to the range axis (axis of symmetry) and thus the velocities of Group I's ghost targets are the same, but the ranges are the opposite of the actual ones.

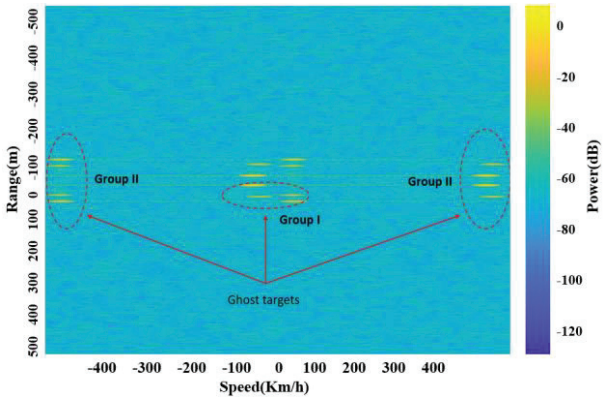

Fig. 9. Range-Doppler map for the 4-target scenario using triangular sweep.

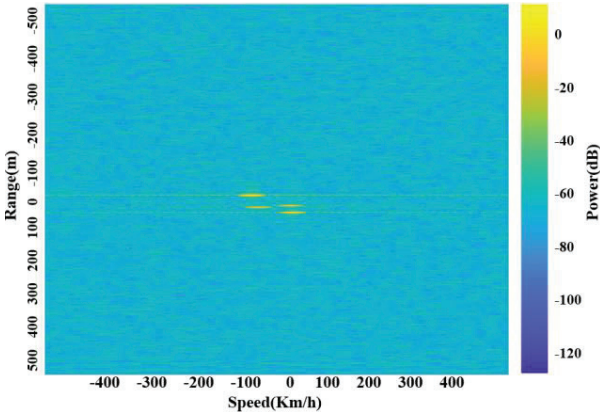

Fig. 10. Range-Doppler map using sawtooth sweep.

It is even more interesting to see the ghost targets of Group II. We can observe that some actual targets' echoes project themselves onto the left- and right-hand side of the range-Doppler map. By looking at the ghost targets of Group II, we can see that they emerge on the two far ends of the map and mark very high velocities such as 400 Km/h which can't be attributed to any vehicle, at least in the automotive perspective. Thus, they can be easily neglected. But the ghost targets of Group I could cause confusion in automotive scenarios since they are exactly within the same range of values or velocities

as actual targets are. For our proposed system there is an easy fix and that is switching to the use of sawtooth chirp instead of the triangular chirp. Figure 10 illustrates that by switching to the sawtooth chirp the issue of the ghost targets is resolved.

As a figure of merit for the range-Doppler graphs in our radar system, we can compare the power of the echo signal with the power of the background noise using the right-hand side color bars in Figs. 9 and 10. We can observe that basically our target returns have power of about -20dB or higher which is an easily detectable value against the background noise which is about -80dB.

V. PERFORMANCE OF ANTENNA ARRAYS VERSUS SINGLE LWA

In this paper, several antenna arrays were designed, and their performances were evaluated compared to our proposed leaky-wave antenna. The small-signal S-parameters of each design was extracted as Touchstone file since as we know, we can get the S-parameters of any microwave device with n ports, as snp file where n shows the number of ports. CST Studio Microwave has the capability to extract the S-parameters in Touchstone format. For example, for our case, since we have only 2 feeding ports, the s2p file was extracted and directly plugged into the antenna blocks (transmitter and receiver) of the FMCW radar's architecture in Simulink. In the following section we are going to introduce three antenna systems designed for our proposed FMCW radar system.

A. Inset feed microstrip patch array

This structure is composed of an array of 77 GHz antennas as illustrated on Fig. 11. The substrate used was Arlon AD 350 with permittivity value of εr = 3.5.

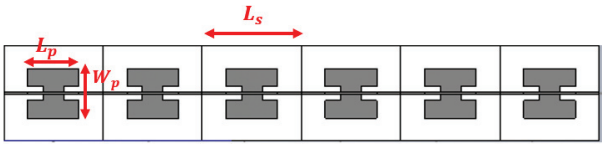

Fig. 11. Inset feed microstrip patch array.

B. Circular patch array with Buttler beamforming network

Buttler beamforming networks are very common structures for beam scanning. These networks are comprised of branch-line couplers, crossovers, and phase shifters. Figure 12 shows the different blocks of the Buttler matrix. Block A is a branch-line coupler which is a 90° hybrid coupler, and we have four of the same couplers on the structure. Block B is showing a microwave crossover which simply routes the signals. Block C is showing a 45° phase shifter and we have two phase shifters on the matrix. Block D is showing the circular patch antenna array designed for operation at 77GHz. The ports 1 to 4, on the left side of the Buttler matrix are the feed ports. At a given time, only one port is excited and three other ports are terminated using 50 Ω terminators.

Table 4: Design parameters of a single cell of patch array

Parameter	Explanation	Value (mm)
L_s	Substrate length	2.07
W_s	Substrate length	2.07
L_p	Patch length	1.08
W_p	Patch width	1.10
L_i	Indentation length	0.32
W_i	*Indentation width*	0.12

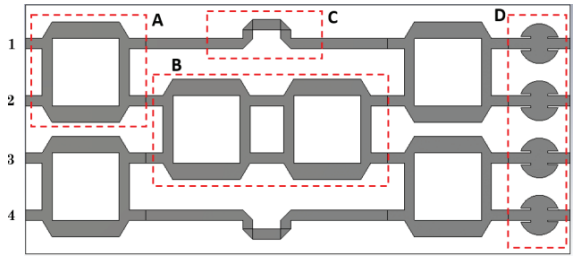

Fig. 12. Circular patch array with Buttler beamforming network.

Figure sets 13 to 15 summarize the beamforming behavior of Buttler beamforming network on the circular patch array as the structure is fed through any of the ports 1 to 4 on plane $\varphi = 0^{\circ}$.

By paying close look to the propagation patterns, we can observe the left-handed and right-handed beam patterns. The frequency range changes from 76.5 GHz to 77.5 GHz.

At the central frequency of $f_c = 77\ GHz$ the angular directions of the main beam by switching between ports 1 to 4 are correspondingly $+149^{\circ}$, $+14^{\circ}$,-14° and -149° Tables 5, 6, and 7 summarize the range-Doppler data of the three antenna systems in the proposed FMCW radar system. The first four columns in each table correspondingly show the real velocity v_{real}, real range (R_{real}), real relative velocity of the target to the radar (Δv_{real}), and the real relative range of the target to the radar (ΔR_{real}) and these are fixed values in all three tables. The last two columns show the estimated relative velocity and the estimated relative range of each target. As was the case with the inset-fed patch antenna array, we believe by doing some antenna tuning and optimization in the designed array, we could possibly improve the gain. In

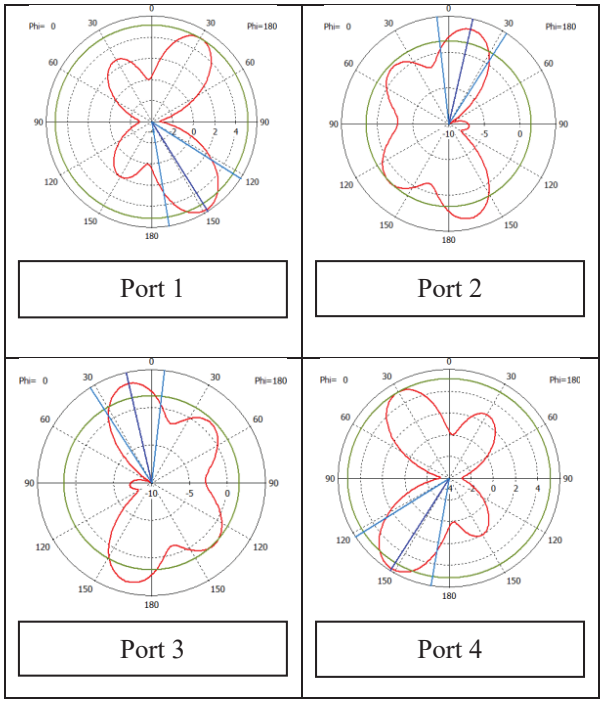

Fig. 13. Propagation patterns of the circular patch array with Buttler beamforming network at frequency of f =76.5 GHz.

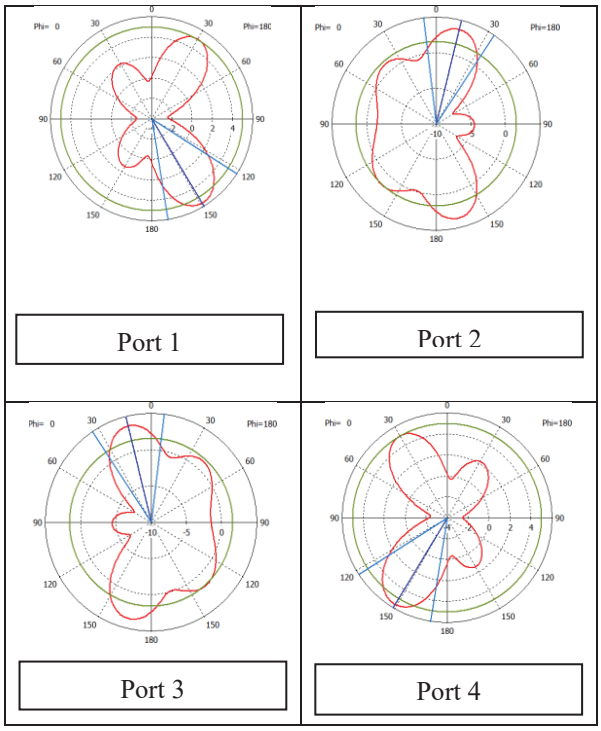

Fig. 14. Propagation patterns of the circular patch array with Buttler beamforming network at frequency of f =77 GHz.

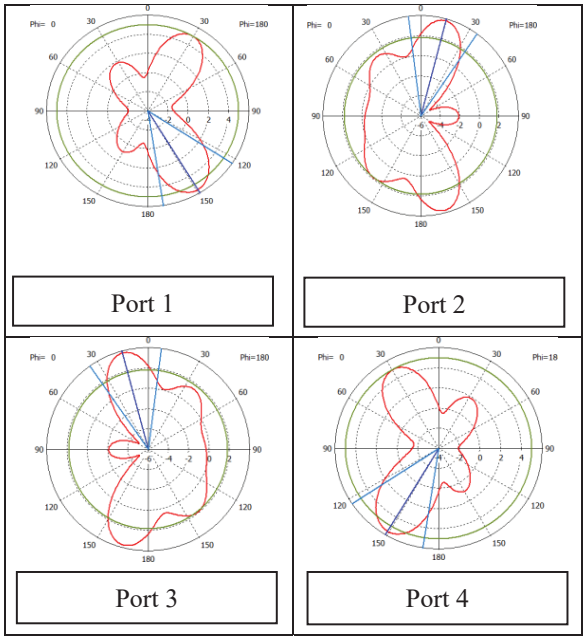

Fig. 15. Propagation patterns of the circular patch array with Buttler beamforming network at frequency of f =77.5 GHz.

this case, the radar returns have the power of −30dB to −35dB which are still detectable against the background noise with −80dB power.

In addition to the Tables 5, 6, and 7, the range-Doppler data of the three proposed antenna systems have been shown as graphs on Fig. 16. In this figure the

Table 5: Range-Doppler results of circular patch array with Buttler Beamformer

Target	Truck	Car	Motorcycle	Bike
V_{real} (Km/h)	129.9	59.9	126	46.8
R_{real} (m)	65	65	45	20
Δv_{real} (Km/h)	+32.7	−37.2	28.8	−50.4
ΔR_{real} (m)	65	65	45	20
ΔV_{est} (Km/h)	+32.1	−38.5	+29.8	−57.7
ΔR_{est} (m)	63.0	63	44.5	18.5

Table 6: Range-Doppler results of the Inset-fed patch array

Target	Truck	Car	Motorcycle	Bike
V_{real} (Km/h)	129.9	59.9	126	46.8
R_{real} (m)	65	65	45	20
Δv_{real} (Km/h)	+32.7	−37.2	28.8	−50.4
ΔR_{real} (m)	65	65	45	20
ΔV_{est} (Km/h)	+29.9	−49.2	+29.9	−53.5
ΔR_{est} (m)	59.3	59.3	40.8	22.2

Table 7: Range-Doppler results of the Comb-line leaky-wave antenna

Target	Truck	Car	Motorcycle	Bike
V_{real} (Km/h)	129.9	59.9	126	46.8
R_{real} (m)	65	65	45	20
Δv_{real} (Km/h)	+32.7	−37.2	28.8	−50.4
ΔR_{real} (m)	65	65	45	20
ΔV_{est} (Km/h)	+32.1	−40.6	+27.8	−55.6
ΔR_{est} (m)	63.0	63.0	44.5	20.7

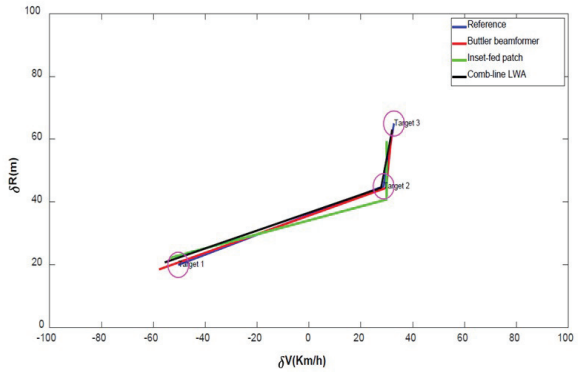

Fig. 16. Range-Doppler performance of the Buttler beamformer network, Inset-fed patch array and comb-line leaky-wave antenna.

horizontal axis is the speed of a target relative to the radar (δV) and the vertical axis is the position of a target relative to the radar system (δR). There are four curves in the figure. The blue curve is the reference curve, the red, green, and black curves show the range-Doppler responses of the circular patch array with Buttler beamforming network, the inset-fed patch array, and the comb-line leaky-wave antenna correspondingly. The pink circles show the range-Doppler margin of 3 targets. We can see that the Buttler beamformer's performance is the best but at the cost of more complexity in design. The comb-line leaky-wave antenna has decent range-Doppler performance and is showing a better margin than the inset-fed patch array for target 2. Overall, the comb-line leaky-wave antenna shows a successful performance in range-Doppler detection of the proposed FMCW radar system.

VI. CONCLUSION

In this work, we proposed a comb-line leaky-wave antenna and compared the performance against the inset-fed patch antenna array and circular patch array controlled with a Buttler beamforming network. The main contribution of this work is introducing a novel frequency scanning system for the automotive industry by using a combline leaky-wave antenna. The proposed antenna is simple in structure and cheap to manufacture because most importantly unlike other antenna arrays, it does not need any phase shifters or, couplers or complex beamforming networks. Based on the results in section V, the authors believe that the functionality of the proposed leaky-wave antenna results in acceptable range and velocity margins for road safety and automotive applications. Observing the range-Doppler map in Fig. 9 shows that the ghost-target problem could be a critical issue in FMCW radars, especially if we use triangular chirp. The negative ramp of the triangular chirp creates images of the main targets in a symmetrical fashion and thus artificial and unreal echoes appear on the range-Doppler map. We discussed and categorized the ghost targets. Ghost targets of type II can be easily ignored because their range and velocity values are beyond real automotive scenarios. But ghost targets of type I, emerge exactly within the same velocity values of the genuine target returns and have the negated range values of real targets, which makes them significant to detect and suppress. The fix was using a sawtooth chirp to cancel out the effect of the negative ramp in the triangular chirp.

REFERENCES

[1] https://www.nhtsa.gov/

[2] M. Jankiraman, *FMCW Radar Design*, Artech House, 2018.

[3] C. Kärnfelt, A. Péden, A. Bazzi, G. El Haj Shhadé, M. Abbas, T. Chonavel, and F. Bodereau, "77 GHz ACC radar simulation platform," *9th International Conference on Intelligent Transport Systems Telecommunications, (ITST)*, IEEE, 2009.

[4] J.-Jr Lin, Y.-P. Li, W. C. Hsu, and T. S. Li, "Design of an FMCW radar baseband signal processing system for automotive application," *SpringerPlus*, vol. 5, no. 1, pp. 1-16, 2016.

[5] M. Steeg, A. Al Assad, and A. Stöhr, "Simultaneous DoA estimation and ranging of multiple objects using an FMCW radar with 60 GHz leaky-wave antennas," *43rd International Conference on Infrared, Millimeter, and Terahertz Waves (IRMMW-THz)*, IEEE, 2018.

[6] S.-T. Yang and H. Ling, "Application of a microstrip leaky wave antenna for range–azimuth tracking of humans," *IEEE Geoscience and Remote Sensing Letters*, vol. 10, no. 6, pp. 1384-1388, 2013.

[7] E. Gambi, G. Ciattaglia, A. De Santis, and L. Senigagliesi, "Millimeter wave radar data of people walking," *Data in Brief*, vol. 31, pp. 105996, 2020.

[8] D. Ammen, M. Umehira, X. Wang, S. Takeda, and H. Kuroda, "A ghost target suppression technique using interference replica for automotive FMCW

radars," *IEEE Radar Conference (RadarConf20)*, IEEE, 2020.

[9] F. B. Gross, *Frontiers in Antennas: Next Generation Design & Engineering*, McGraw-Hill Education, 2011.

[10] D. R. Jackson, C. Caloz, and T. Itoh, "Leaky-wave antennas," *Proceedings of the IEEE*, vol. 100, no. 7, pp. 2194-2206, 2012.

[11] L. Brillouin, *Wave Propagation in Periodic Structures*, Dover Publications, 2003.

[12] M. Steeg, F. Exner, J. Tebart, A. Czylwik, A. Stöhr, "OFDM joint communication–radar with leaky-wave antennas," *Electronics Letters*, vol. 56, no. 21, pp. 1139-1141, 2020.

[13] A. Zandamela, A. Al-Bassam, and D. Heberling, "Circularly polarized periodic leaky-wave antenna based on dielectric image line for millimeter-wave radar applications," *IEEE Antennas and Wireless Propagation Letters*, vol. 20, no. 6, pp. 938-942, 2021.

Masoud Sarabi has received his PhD in Electrical Engineering from the Michigan Tech university in 2021. His research interests are antenna design for biomedical hyperthermia, beamformers, and FMCW radar systems for road safety applications.

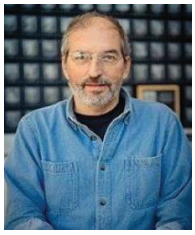

Warren F. Perger is a professor of Electrical and Computer Engineering department at Michigan Tech university and has been a faculty member since 1987.